

Bulk and surface engineering to improve performance and stability of perovskite solar cells

Présentée le 30 septembre 2022

Faculté des sciences de base
Laboratoire de photonique et interfaces
Programme doctoral en chimie et génie chimique

pour l'obtention du grade de Docteur ès Sciences

par

Thomas Paul BAUMELER

Acceptée sur proposition du jury

Prof. D. L. Emsley, président du jury
Prof. M. Graetzel, Dr S. M. Zakeeruddin, directeurs de thèse
Prof. E. Sargent, rapporteur
Dr S. Stranks, rapporteur
Prof. K. Sivula, rapporteur

“Because you have seen me, you have believed; blessed are those who have not seen and yet have believed.”

The Holy Bible, John 20:29

Acknowledgments

First of all, I would like to express my deepest gratitude to both my thesis directors, Professor Michael Grätzel, Director of the Laboratory of Photonics and Interfaces (LPI), and Dr. MER Shaik M. Zakeeruddin, for giving me the privilege to pursue my doctoral studies within this world-renowned research group. I am particularly grateful for their unconditional support throughout my thesis, their trust, and the freedom I had regarding the research I wanted to conduct.

I am also particularly grateful to Dr. MER Christophe Roussel for having me as his principal teaching assistant throughout my Ph.D. Not only did the level of trust he showed to me push me forward and boost my confidence, but it also allowed me to deeply develop my pedagogical skills and build a strong teaching experience. I particularly enjoyed helping in the education of generations of young scientists from both UNIL and EPFL. Also, the relationship that we developed throughout the years evolved from a mentoring figure to a friendship. Thank you also to Stéphane Thonney and Frédéric Gumy for the help and good time during the experimental teaching tasks I completed in their labs.

I thank Carmen Martinez, Heidi Francelet, Cécile Prébandier, and Anne Lene Odegaard for their precious help regarding administrative matters, for introducing me to the doctoral program of EDCH and the LPI facilities and daily life. I particularly thank Carmen for all the help, patience, and kindness regarding the chemicals management and all the tiring procedures related to it.

I also give big thanks to the ISIC team, from the CH Magasin crew members (Jacky, Roxane, Loïc) for their help in ordering, receiving, sending chemicals and equipment on a daily basis, to the electronical and mechanical workshop people, namely Gil Corbaz, Benjamin Le Geyt,

and Grégoire, for their help with the maintenance of our equipment and Biagio Greco for the help regarding the maintenance of our facilities.

I express my gratitude to Dr. Mounir Mensi for his help, kindness, and pedagogy regarding the XPS measurements and surface characterization discussions in general, to George Fish and Etienne Socie for the THz measurements, coffees, and discussions, both scientific or about personal matters (YNWA Reds !) and to Grégoire Baroz for introducing me to the SEM facilities and measurements.

Of course, I would like to thank all my colleagues at LPI, all the people I met and shared laboratories with within the course of my Ph.D., with special greetings to my office mate Algirdas Dučinskas, to Dr. Olivier Ouellette, Vincent Dufoulon, Dr. Georgios Kakavelakis, Dr. Anurag Krishna, with whom I had a privileged relationship and passionate discussions about both science and non-scientific topics such as world politics, sports, etc.

I would like to give some special thanks to Dr. Essa Alharbi, Dr. Marko Stojanovic, and Jean-David Décoppet for the deep relationship we developed throughout the years at LPI. I shared many working moments, coffee breaks, daily struggles, and the excitement of getting new, good, promising results with Essa; we traveled here and there, sometimes for work, to certify excellent results, and sometimes for private business. All these moments were filled with interesting discussion and exchange, both on scientific and personal levels, which developed my understanding of PV technology but also of Arabic culture amongst others. Marko, Jean-David, and I formed the small Swiss subgroup within LPI and we had lots of laughs, good memories, and hangouts which were of prime importance to bring some joy and fun to the workplace.

To Dr. Albert Daubry, I want to express my gratitude as well. Thank you for the shared struggle of the daily life of a Ph.D. student and all the pints of beers related, but mainly for introducing

me to so many new people and things outside EPFL and beyond science, in other words for opening my mind to new horizons, escaping from the academic world and being an amazing friend. Thank you for all the good times and laughs.

Thank you to Aline Schaub for her unconditional support during the first 3 years of my Ph.D., to my flat mate Timur Senyuz for the good atmosphere we created at home, to Vivien Michel for the sports sessions together, and Dr. Ibrahim M. Dar and Dr. Neha Arora for lightning the spark of my interest in perovskite solar cells research. Thank you to the group of friends that were a constant support in Lausanne, in no particular order André Douverny Roque Dos Santos, Aurélien Borst and all the Babylonians team (Nicolas, Gil, Stéphanie, Vincent, Helder, Benjamin and Cyrille), Aurélien Willauer, Gontran Sangouard, Aaron Terpstra.

Finally, last but not least, I also want to take the opportunity to thank some very important people outside of the Lausanne area, EPFL, and research. These are the people who are here for me and support me on a daily basis, no matter what: my friends, Mélissa Gigon, Julien Paupe, and Pierre Gobin, Aurélie Baume & Davin Willemin, Zoé & Antoine Jeandupeux, Lionel Jobin, Lucien Ourny, Nathanaël Marie as well as Carole Bigler very recently and Kevin Tschann; and, of course, my family: my parents Violaine and Ded, my brother Quentin, my sister Eve and my grandmothers Marie-Thérèse and Nicole. Thank you for all your love, patience, and support throughout my Ph.D., and beyond!

Lausanne, March 2021

Abstract

Human society is craving new and renewable energy sources. Indeed, the need for novel sources is an obligation in order to cope with the exponentially increasing global energy demand. Also, environmentally friendly alternatives to fossil fuels are more crucial than ever in order to limit the effects of global warming. Finally, the current gas and oil crisis underlies the importance for each state to have some alternatives in case of shortage, i.e. to gain some energetic independence. In that regard, solar energy represents the best candidate, given its huge potential and its universal character. In particular, perovskite solar cells (PSCs) show the highest promise amongst emerging technologies. From their first report in 2009, the power conversion efficiency rocketed, to cross 25 % recently. Unfortunately, several important issues remain.

Chapter 2. Its lower bandgap makes formamidinium lead iodide (FAPbI₃) a more suitable candidate for single-junction solar cells than pure methylammonium lead iodide (MAPbI₃). However, its structural and thermodynamic stability is improved by introducing a significant amount of MA and bromide, both of which increase the bandgap and amplify trade-off between the photocurrent and photovoltage. Here, we simultaneously stabilized FAPbI₃ into a cubic lattice and minimized the formation of photoinactive phases, such as hexagonal FAPbI₃ and PbI₂, by introducing 5% MAPbBr₃, as revealed by synchrotron X-ray scattering. We were able to stabilize the composition (FA_{0.95}MA_{0.05}Cs_{0.05})Pb(I_{0.95}Br_{0.05})₃, which exhibits a minimal trade-off between the photocurrent and photovoltage. This material shows low energetic disorder and improved charge-carrier dynamics as revealed by photothermal deflection spectroscopy (PDS) and transient absorption spectroscopy (TAS), respectively. This allowed the fabrication of operationally stable perovskite solar cells yielding reproducible efficiencies approaching 22%.

Chapter 3. Herein, we successfully engineered a multi-cation halide composition of perovskite solar cells via the two-step sequential deposition method. Strikingly we find that adding mixtures of 1D polymorphs of orthorhombic δ -RbPbI₃ and δ -CsPbI₃ to the PbI₂ precursor solution induces the formation of porous mesostructured hexagonal films. This porosity greatly facilitates the heterogeneous nucleation and the penetration of FA/MA cations within the PbI₂ film. Thus, the subsequent conversion of PbI₂ into the desired multication cubic α -structure by exposing it to a solution of formamidinium methylammonium halides is greatly enhanced. During the conversion step, the δ -CsPbI₃ also is fully integrated into the 3-D mixed cation perovskite lattice, which exhibits high crystallinity and superior optoelectronic properties. The champion device shows a power conversion efficiency (PCE) over 22%, with an open-circuit voltage of 1.15V, a short-circuit photocurrent of 24.82 mA·cm⁻², and a fill factor of 78% at a bandgap of 1.55 eV. Furthermore, these devices exhibit enhanced operational stability, with the best device retaining more than 90% of its initial value of PCE under 1-Sun illumination with maximum power point tracking for 400 h.

Chapter 4. A promising approach for the production of highly efficient and stable hybrid perovskite solar cells is employing mixed ion materials. Remarkable performances have been reached by materials comprising a stabilized mixture of methylammonium (MA⁺) and formamidinium (FA⁺) as the monovalent cation. We compare and quantify the methods of stabilizing FA-based perovskites involving the additional blending of the smaller inorganic cations cesium (Cs⁺) and rubidium (Rb⁺), which can lead to an improvement in phase purity of the black cubic perovskite modification. Even under excess lead iodide conditions, the presence of a separate PbI₂ phase as well as hexagonal phases, which are very common for formamidinium-containing perovskites, can be drastically reduced or even completely prevented. In this respect, adding both Cs⁺ and Rb⁺ showed greater effectivity than only adding Cs⁺, enabling an increase in the percentage of cubic phase within the material from 45 % in the

double cation FA:MA mixture to 97.8 % in the quadruple composition. The impact of admixing inorganic cations on the perovskite crystal structure resulted in enlarged homogeneous crystallite sizes, a less pronounced orientational order and indicated also minor modifications of unit cell sizes. Finally, we discuss the impact of phase purity on charge-carrier recombination dynamics and solar cell performance.

Chapter 5. The need for facile and stable ways to mitigate MHPs imperfections without modifying their elemental composition is crucial. Herein, we removed Cs^+ from the bulk of the perovskite and applied it on the surface, as a passivation agent via a cesium iodide (CsI) solution. We study the effect of CsI passivation on the perovskite films' structural and optoelectronic properties by X-ray diffraction (XRD) and X-Ray photoelectron spectroscopy (XPS, ARXPS), scanning electron (SEM) and Kelvin Probe Force (KPFM) microscopies, steady-state and time-resolved photoluminescence (PL, TRPL), and electroabsorption (TREAS) spectroscopy. Specifically, XRD and XPS demonstrate the total conversion of precursors into the photoactive phase of FA-perovskite upon CsI passivation, and KPFM, TRPL, and TREAS measurements show the high quality of the as-prepared film, reaching an impressive photoluminescence quantum yield (PLQY) of over 8 % and improved charge carriers mobility and lifetimes. Devices prepared using this method reached over 24 % power conversion efficiency and 1.17 open-circuit voltage (V_{OC}), compared to 22.7 % PCE and 1.11 V V_{OC} for the control devices. Also, their operational stability at maximum power point was improved, from less than 80 % to over 90 % of initial efficiency still delivered after more than 600 hours of light-soaking tests.

Keywords.

Sustainability, solar energy, perovskite solar cells, compositional engineering, defect engineering, phase purity, stability.

Résumé

Plus que jamais, la société humaine a besoin de nouvelles sources d'énergie renouvelables et bon marché. En effet, afin de lutter contre le réchauffement climatique et répondre à la demande énergétique croissant de manière exponentielle au niveau mondial, il est primordial de développer des sources d'énergies alternatives à celle existantes. De plus, la crise actuelle (gaz et pétrole) souligne aussi l'importance pour les états d'une indépendance énergétique vis-à-vis des gros producteurs d'énergies fossiles. Dans cette perspective, l'énergie solaire représente un candidat de choix, de par son potentiel énorme et de par son universalité. En particulier, les cellules photovoltaïques à pérovskites (PSCs, pour « *perovskite solar cells* ») se sont établies comme la technologie émergente la plus prometteuse. Depuis leur découverte en 2009, leur efficacité a connu une impressionnante ascension, s'établissant déjà au-delà de 25% aujourd'hui. Cependant, et ce en dépit de leurs performances impressionnantes, d'important défis demeurent. Notamment, la stabilité de la couche de pérovskite reste trop faible de par les défauts intrinsèques qu'elle présente et, dans une certaine mesure, l'utilisation d'éléments toxiques dans leur composition pourrait être un obstacle quant à leur commercialisation à grande échelle. Le présent travail se veut un exemple de pistes à suivre pour l'amélioration des PSCs et présente différentes stratégies d'ingénierie avec des résultats encourageants.

Chapitre 2. Sa bande d'énergie interdite fait du formaldéhyde d'iodure de plomb (FAPbI₃) un candidat plus approprié pour les cellules photovoltaïques à jonction simple que son analogue de méthylammonium (MAPbI₃). Cependant, sa stabilité structurelle et thermodynamique nécessite d'être améliorée par l'introduction d'une quantité significative de MA et de bromure, qui causent tous les deux une augmentation de la bande d'énergie interdite et amplifient la disparité entre le photocourant et la phototension. Ici, nous avons

simultanément stabilisé le FAPbI_3 sous sa forme photoactive cubique et minimisé la formation de phases photo-inactives (telles que le FAPbI_3 hexagonal et le PbI_2) en introduisant 5% de MAPbBr_3 , comme révélé par diffusion des rayons X (source : synchrotron). Nous avons pu stabiliser la composition $(\text{FA}_{0.95}\text{MA}_{0.05}\text{Cs}_{0.05})\text{Pb}(\text{I}_{0.95}\text{Br}_{0.05})_3$, qui présente un compromis minimal entre le photocourant et la photovoltage. Cette composition présente un faible désordre énergétique et une meilleure dynamique des porteurs de charge, comme le révèlent respectivement la spectroscopie de déviation photothermique (PDS) et la spectroscopie d'absorption transitoire (TAS). Ceci a permis la fabrication de cellules solaires à pérovskite opérationnellement stables et offrant des performances reproductibles proches de 22%.

Chapitre 3. Dans ce chapitre, nous avons modifié avec succès la méthode séquentielle (en 2 étapes) de préparation des cellules solaires à pérovskites. Nous révélons de manière frappante que l'ajout de polymorphes 1D de $\delta\text{-RbPbI}_3$ et $\delta\text{-CsPbI}_3$ orthorhombiques à la solution précurseur de PbI_2 induit la formation de films hexagonaux mésostructurés poreux. Cette porosité ainsi créée facilite grandement la nucléation hétérogène et la pénétration des cations FA/MA dans le film de PbI_2 . Ainsi, la conversion ultérieure du PbI_2 en la structure pérovskite souhaitée est grandement améliorée lors de l'exposition aux sels FAI, MABr. Au cours de l'étape de conversion, le $\delta\text{-CsPbI}_3$ est également entièrement intégré dans le réseau de pérovskite, qui présente une cristallinité élevée et des propriétés optoélectroniques supérieures. Il en résulte des cellules solaires présentant une efficacité supérieure à 22 %, avec une tension en circuit ouvert de 1,15 V, un photocourant en court-circuit de $24,82 \text{ mA.cm}^{-2}$ et un facteur de remplissage de 78 %, pour une bande interdite de 1,55 eV. En outre, ces dispositifs présentent une meilleure stabilité opérationnelle, le meilleur dispositif conservant plus de 90 % de son efficacité initiale après plus de 400 h d'exposition sous un éclairage de un soleil (AM1.5G).

Chapitre 4. Une approche prometteuse pour la production de cellules solaires à pérovskite très efficaces et stables consiste à utiliser des matériaux à ions mixtes. Des performances remarquables ont été atteintes par des matériaux comprenant un mélange stabilisé de méthylammonium (MA^+) et de formamidinium (FA^+) en tant que cation monovalent. Nous comparons et quantifions les méthodes de stabilisation des pérovskites à base de FA en impliquant le mélange supplémentaire des cations inorganiques plus petits que sont le césium (Cs^+) et le rubidium (Rb^+), et qui peuvent conduire à une amélioration de la pureté de phase du pérovskite. Même dans des conditions d'excès d'iodure de plomb, la présence d'une phase de PbI_2 distincte ainsi que de phases hexagonales détriminales, très courantes pour les pérovskites contenant du formamidinium, peut être considérablement réduite ou même complètement empêchée. À cet égard, l'ajout de Cs^+ et de Rb^+ s'est révélé plus efficace que l'ajout de Cs^+ seul, permettant une augmentation du pourcentage de phase cubique (photoactive) dans le matériau de 45 % dans le mélange FA:MA à double cation à 97,8 % dans la composition quadruple. L'impact du mélange de cations inorganiques sur la structure cristalline de la pérovskite s'est traduit par une augmentation de la taille des cristaux, un ordre d'orientation moins prononcé et des modifications mineures de la taille des cellules unitaires. Enfin, nous discutons de l'impact de la pureté de phase sur la dynamique de recombinaison des porteurs de charge et les performances des cellules solaires.

Chapitre 5. Il est crucial de développer de simples méthodes afin d'atténuer les imperfections des pérovskites sans en modifier leur composition élémentaire. Dans cet article, nous avons retiré le Cs^+ du pérovskite et l'avons appliqué à sa surface, comme agent de passivation, via une solution d'iodure de césium (CsI). Nous étudions l'effet de la passivation au CsI sur les propriétés structurales et optoélectroniques des films de pérovskite par diffraction des rayons X (XRD) et spectroscopie photoélectronique des rayons X (XPS, ARXPS), microscopie électronique à balayage (SEM) et microscopie de force à sonde Kelvin

(KPFM), photoluminescence à l'équilibre et résolue dans le temps (PL, TRPL) et spectroscopie d'électroabsorption (TREAS). En détails, la XRD et la XPS démontrent la conversion totale des précurseurs vers la phase préovskite photoactive après passivation par le CsI, et les mesures KPFM, TRPL et TREAS démontrent la haute qualité du film ainsi préparé, atteignant un rendement quantique de photoluminescence (PLQY) impressionnant de plus de 8 % et une mobilité et une durée de vie des porteurs de charge nettement améliorées. Les cellules solaires préparées via cette méthode atteignent un rendement de conversion de puissance de plus de 24 % et une tension en circuit ouvert (V_{OC}) de 1,17 V, contre 22,7 % d'efficacité et 1,11 V pour les dispositifs de contrôle. En outre, la stabilité opérationnelle au point de puissance maximale est améliorée, passant de moins de 80 % à plus de 90 % de l'efficacité initiale encore délivrée après plus de 600 heures de tests d'exposition au soleil.

Mots-clés.

Durabilité, énergie solaire, cellules solaires à pérovskites, ingénierie compositionnelle, ingénierie des défauts, pureté de phase, stabilité.

Table of Contents

Acknowledgments.....	2
Abstract	5
Résumé.....	8
Chapter 1: Introduction	15
Energy challenges of the XXIst century	15
The sun: a bright and radiative energy provider	18
Semiconductors: ideal light-harvesting materials?	19
Recombination : overview of an efficiency-killer.....	23
Solar cells: basics & evolution of PV technology.....	25
Working principle.....	25
PV technology evolution	32
Perovskite solar cells.....	35
Historical perspective	35
Working principle.....	37
Crystal structure and electronic properties of hybrid metal halides perovskites.....	37
Defects and losses in PSCs.....	46
Conclusion.....	49
References	50
Chapter 2 Minimizing the Trade-Off between Photocurrent and Photovoltage in Triple-Cation Mixed-Halide Perovskite Solar Cells.....	69
Introduction	69

Results and Discussion.....	71
Conclusion.....	81
Supplementary Information.....	83
References	94
Chapter 3 Formation of High-Performance Multi-Cation Halide Perovskites Photovoltaics by d-CsPbI ₃ / d-RbPbI ₃ Seed-assisted Heterogeneous Nucleation	
Introduction	101
Results and Discussion.....	103
Conclusion.....	114
Experimental Section	115
Supplementary Information.....	118
References	127
Chapter 4 Quantifying Stabilized Phase Purity in Formamidinium-Based Multiple-Cation Hybrid Perovskites.....	
Introduction	141
Results and discussion.....	143
Conclusion.....	151
Experimental section	152
Supporting Information	154
References	158
Chapter 5 Post-engineering via inorganic salts to reach highly efficient and stable perovskite solar cells	
	166

Introduction	166
Results and Discussion.....	166
Conclusion.....	168
Supporting Information	181
References	185
Conclusion	189
Curriculum Vitae	194

Chapter 1: Introduction

Energy challenges of the XXIst century

The Industrial Revolution, which took place during the XVIIIth and XIXth centuries, marked an important turning point in human history. Along with the development of machines, tools, and mechanized factory systems, the living standards of the population considerably improved, in the West especially. As a result, the world's population growth rate drastically increased and so did global energy demand (Fig. 1).

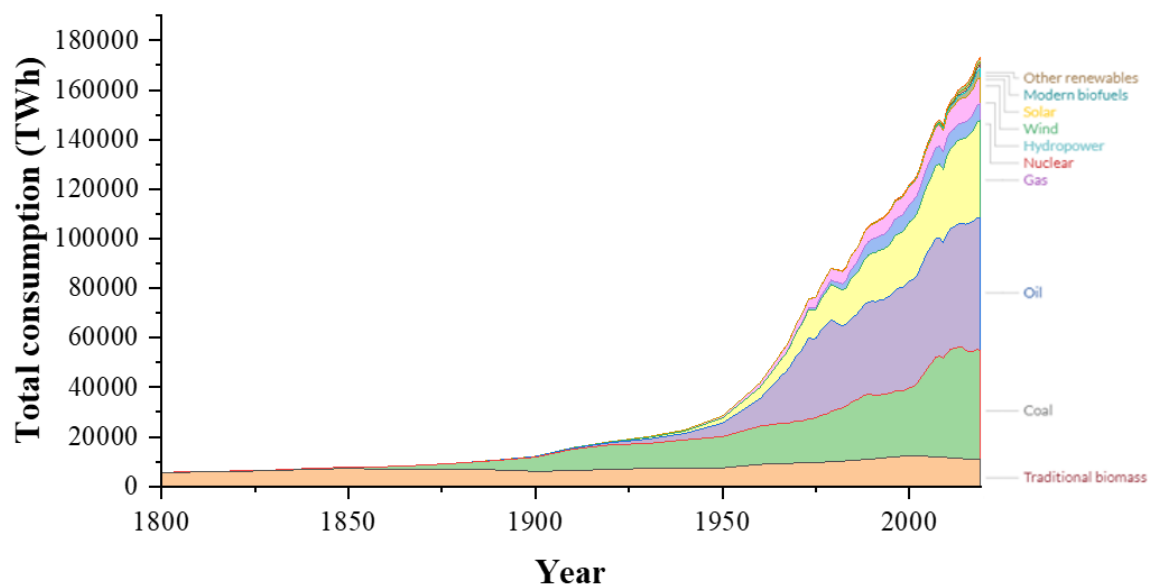


Figure 1. Global primary energy consumption over the years by source. Plotted with data available at ourworldindata.org¹

Following the establishment of the first commercially successful steam-powered engine in 1712 (Newcomen's atmospheric engine),² global coal consumption drastically increased, replacing traditional biomass (wood). It was soon followed by oil after the discovery of the first commercial oil well in Pennsylvania in 1859.³ The XXth century saw the continuous rise of both these energy sources together with the emergence of novel sources such as gas, nuclear power, and hydropower.⁴ At the time, there were no specific concerns other than “simply”

being able to supply for the exponentially growing energy demand which directly resulted from the modernization of society and population growth. And already then the task was quite challenging, as the world population doubled between 1950 and 1987.⁵ However, the beginning of the XXIst century marked an important turning point, with growing concerns about global warming and the very strong impact of human activities on it, especially regarding the consumption of fossil energy (coal, oil, gas) which are responsible for most of the overall greenhouse gases (GHGs) emissions.

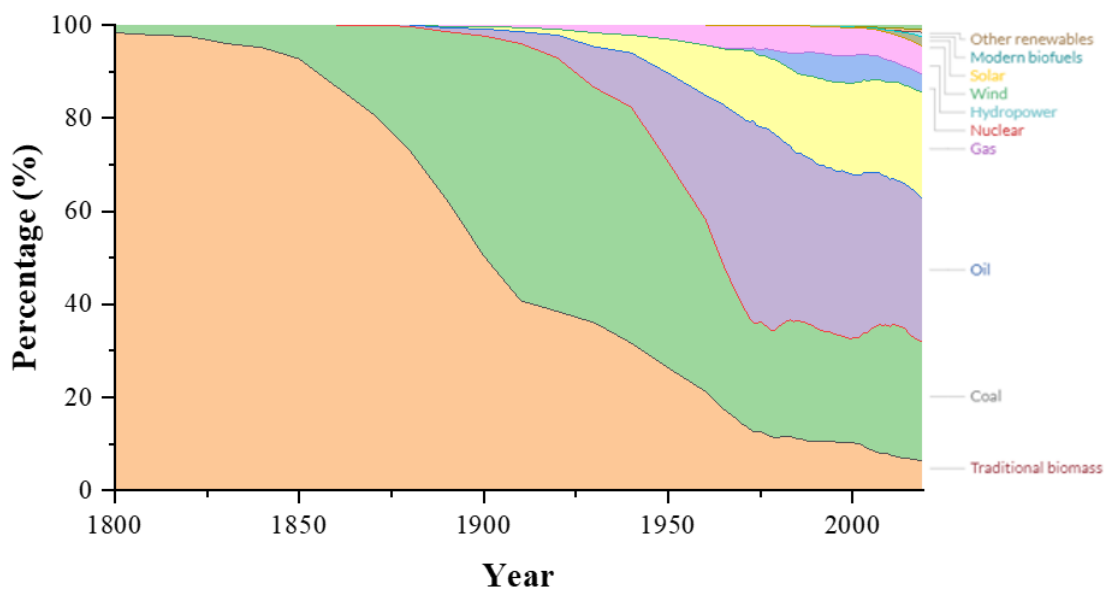


Figure 2. Relative share of the global energy consumption per energy source over the years. Plotted with data available at ourworldindata.org¹

Current estimates demonstrate that global energy demand will further double in the next 30 years and triple by 2100, jumping from around 16 TW nowadays to above 50 TW at the end of the century.⁶ In order to cope with the demand, but in a desperate effort to limit the effect of global warming, enormous strains are put on the development of renewable energy sources.

Among the several renewable energy sources, solar power represents the candidate with the most potential. To get an idea of the immensity of its potential, if we were to capture all the solar energy that our planet receives in 90 minutes, we would have harvested more energy than

what human society consumes in a calendar year.⁷ Or said differently, planet Earth receives from the Sun in one year more than 400 times the predicted global energy demand of the 2100 horizon. A graphic illustration of the potential of the different renewable and non-renewable energy sources is shown in Fig. 3 and it compares these potentials to today's annual global energy consumption. It is clear from the figure that solar energy has the most potential amongst all energy sources. Actually, its potential is even bigger than all other energy sources combined.

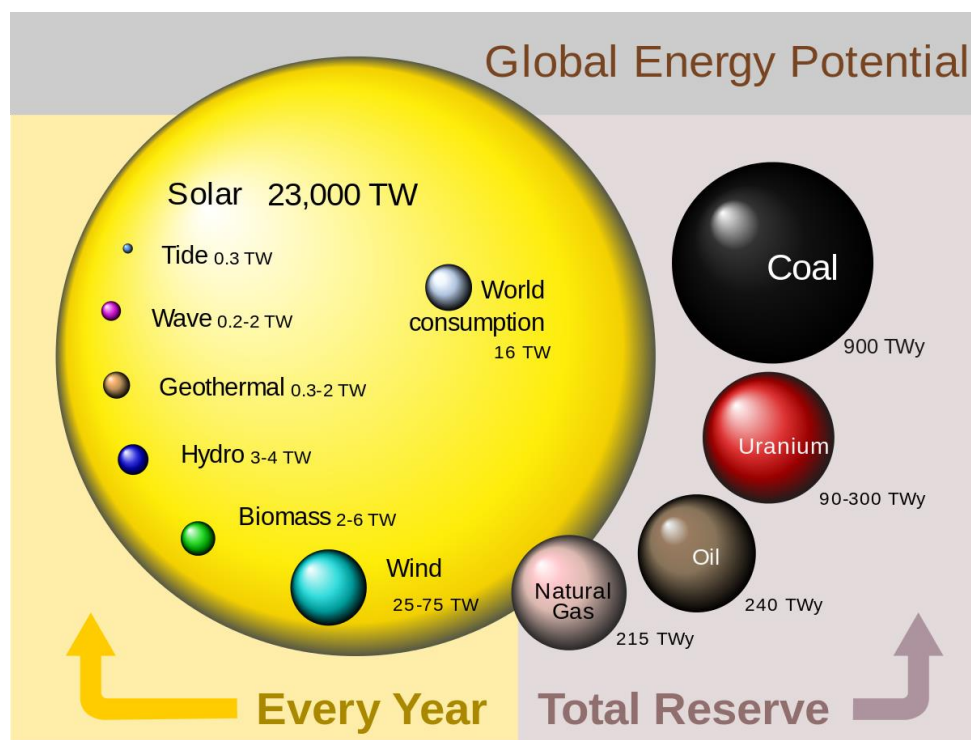


Figure 3. Comparing finite and renewable planetary energy reserves (Terawatt-years). Total recoverable reserves are shown for the finite resources. Yearly potential is shown for renewables.⁸

The importance of developing efficient devices capable of harvesting solar energy is thus crucial and represents the most-promising technology towards establishing renewable energy as the new benchmark.

Furthermore, and on top of pure ecological/sustainable reasoning, solar energy also represents a wise choice regarding the current energy crisis. Indeed, as sunlight radiates all over the world (and even if some areas exhibit preferential conditions regarding PV development), solar energy also represents a possible solution for each state to improve their independence

regarding energy supply. For instance, the current invasion of Ukraine from Russia is causing an energy crisis. Currently, crude oil price around \$100 a barrel (and even reached \$125), and Europe is fearing from gas shortages as trouble is happening on the Russian Yamal-Europe pipeline (one major route for Russian gas supply to Europe).^{9,10} In this regard, solar power would represent the best candidate to solve energy independence globally. Also, assuming a global integration of wide-scale solar power in the grid, the prospect of an infinite and reliable energy source would benefit the economy as well in bringing confidence in a viable and permanent source of energy, preventing shortages and speculation.

The sun: a bright and radiative energy provider

Solar energy is created by nuclear fusion that takes place in the Sun. It generates heat and light which flows away in the form of electromagnetic radiation (photons), which behave like a wave, moving through space, but can also behave as a particle, with a discrete amount of energy that can be absorbed, transmitted, or emitted. The energy associated with a photon depends on its frequency ν or wavelength λ as given by the Planck-Einstein relation:¹¹

$$E_{\text{photon}} = h\nu = \frac{hc}{\lambda} \quad (1)$$

where h is the Planck's constant ($6.626 \cdot 10^{-34} \text{ m}^2 \text{ kg s}^{-1}$).

Strictly speaking, light is defined as electromagnetic radiations with a wavelength comprised between 200 nm and 2500 nm. Eventually part of it reaches our planet. Part of this energy coming from the Sun can be harnessed and converted into another form of energy, electricity (solar power, solar PV) or heat (solar thermal energy, STE). Even though the power conversion efficiency of STE (up to 90%)^{12,13} is much higher than for solar PV, the enormous advantage of solar PV over STE is that it readily produces electrical power. And regarding power plants,

PV design is much simpler than that of thermal. Indeed, a conventional solar PV farm only consists of a solar panels installation connected to the grid

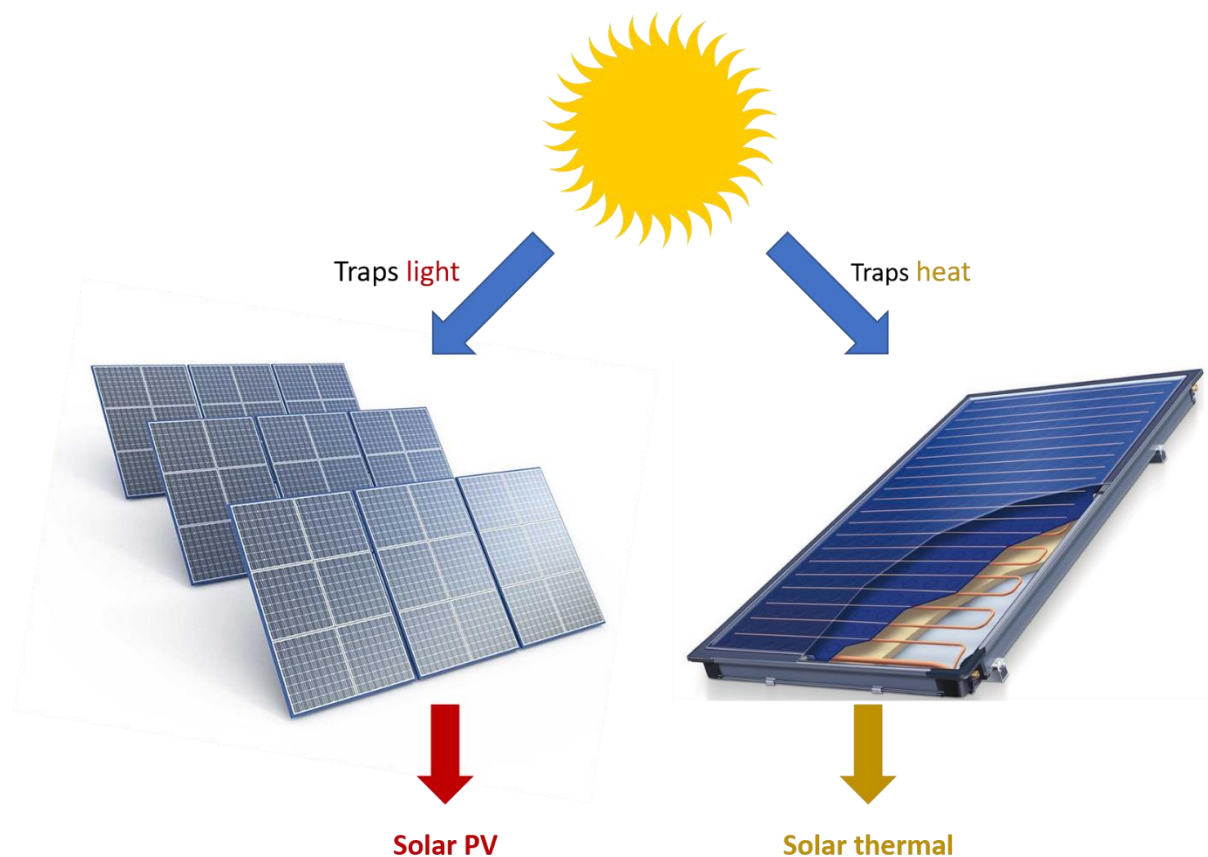


Figure 4. *Difference between solar PV and solar thermal energy technologies*

Solar power relies on the photovoltaic effect, where a semiconductor material, exposed to photons (light), generates an electrical current and a voltage. This phenomenon was first described by Edmond Becquerel in 1839 in the *Comptes rendus de l'Académie des Sciences*, where he described the first electrochemical cell producing power upon exposure to light.¹⁴

Semiconductors: ideal light-harvesting materials?

Semiconductors are materials that have an electrical conductivity that lies between that of a conductor and that of an insulator. Electrons are thus present in energy bands that can be separated by “forbidden” regions, that is regions for which no wavelike electron orbitals exist. The outermost electron orbital filled with the electron is defined as the valence band (VB) and

the first empty electron orbital is defined as the conduction band (CB). The energy difference between the highest (occupied) state of the VB and the lowest (unoccupied) state of the CB is defined as the bandgap energy (E_g). In conductive materials (metals, electrolytes, superconductors, plasmas), molecular orbitals become a series of continuous energy levels as part of VB and CB overlap, allowing charges to flow. In the case of insulators, the energy gap is huge; photons can still be absorbed, the generated electron is lost due to the high resistance of insulators. Semiconductors lie in-between the two, exhibiting properties of both conductors and insulators, rendering them interesting materials regarding light-harvesting and energy capture.¹⁵

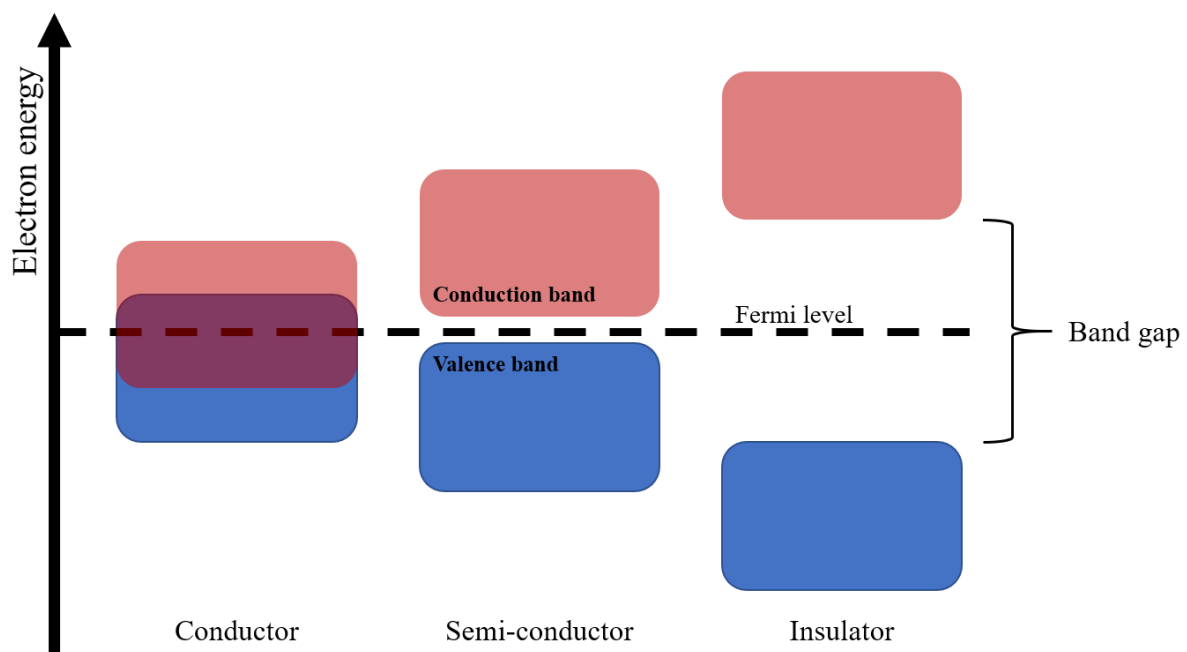


Figure 5. Schematics of band theory explanation of the difference between conductors, semiconductors, and insulators

Photovoltaic technologies are constituted of diverse semiconductor materials depending on the type of photovoltaic technology. Some are called *direct bandgap* to semiconductors and some others are referred as *indirect bandgap* semiconductors. The difference lies in the electron momentum: direct semiconductors exhibit VB and CB with the same electron momentum, meaning that upon light exposure, the photovoltaic material will absorb photons with an energy

greater than the band gap ($E = h\nu \geq E_g$) and, upon excitation, electrons (e^-) will be directly promoted from the VB to the CB, leaving a positive charge in the conduction band, a hole (h^+). But in the case of indirect bandgap semiconductors, VB and CB do not share the same electron momentum and thus, an electron cannot jump directly from the VB to the CB. It needs also the involvement of a phonon (lattice vibration) in order to change its electron momentum to attain the same as for the VB. Then only, a transition can occur.

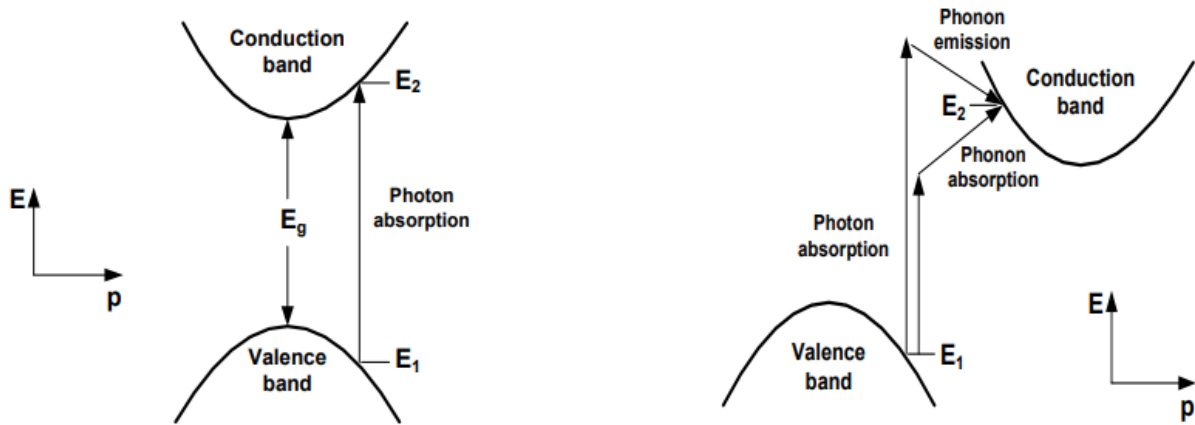


Figure 6. Illustration of the difference in the absorption process between a direct (left) and indirect (right) semiconductor.¹⁶

The absorption rate depends on two parameters: the thickness of the material (x), and its absorption coefficient α . When the light of intensity I_0 strikes the material's surface, its intensity at any distance x in the semiconductor is:

$$I = I_0 e^{-\alpha x} \quad (2)$$

Light propagates within the medium depending on the material's complex refractive index n' :

$$n' = n + ik \quad (3)$$

n is the real part of the refractive index and determines the propagation velocity (v and wavelength λ) in the medium:

$$n = \frac{c}{v} = \frac{\lambda_0}{\lambda} \quad (4)$$

where c is the speed of light in vacuum (299,792,458 meters per second) and assuming ambient is vacuum having wavelength λ_0 .

The imaginary part of the extinction coefficient is k . It is an intrinsic property of the material related to the absorption coefficient as follows:

$$a = \frac{4\pi k}{\lambda} \quad (5)$$

Thus, the absorption coefficient of a material depends on the wavelength λ . This suggests that semiconductors preferentially absorb light at a particular wavelength.

Finally, photons of energy less than the bandgap that strikes the material cannot excite an electron and are thus transmitted. These phenomena are called absorption and transmission, respectively (described in Fig. 6 below). Photovoltaic technologies will then take advantage of the charge separation process and collect the flow of electrons to use them in an external circuit to produce some work. The recombination of photogenerated electron-hole pairs can happen in radiative or non-radiative pathways and represent efficiency losses for the photovoltaic device. When recombining radiatively, an electron-hole pair emits a photon of energy corresponding to the bandgap. The whole point is to prevent photogenerated charges to recombine, as their collection is what drives the power conversion efficiency of the associated photovoltaic devices.

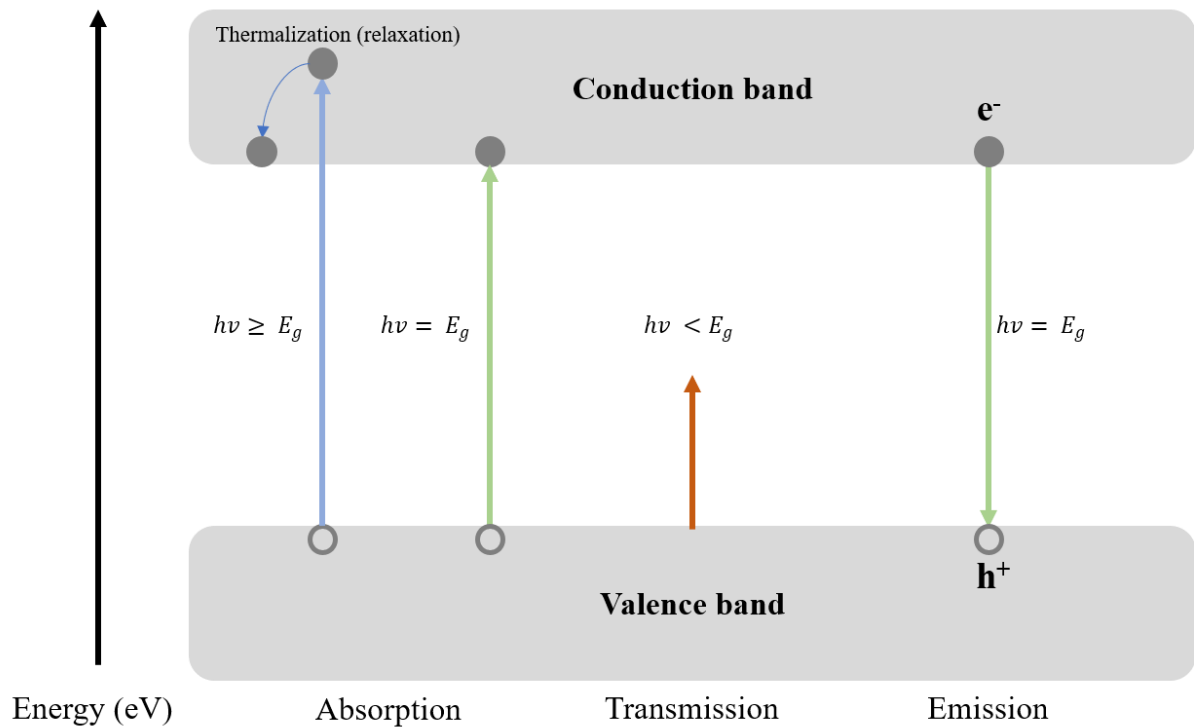


Figure 7. Schematics of the energy bands and associated processes in photovoltaics

Recombination : overview of an efficiency-killer

As mentioned above, light absorption can promote electrons from the VB to the CB, creating an electron-hole pair. If not collected, the electron relaxes its extra, just absorbed energy, and recombine with the hole in the VB. This phenomenon is called recombination. Two major types of recombination processes are distinguished:

1. radiative recombination (generates photons as e^- and h^+ recombine)
2. non-radiative recombination: trap (Shockley-Read-Hall) recombination and Auger recombination

As aforementioned, radiative recombination is simply the opposite of the absorption process: the excited electron relaxes to the VB by emitting a photon of energy corresponding to the bandgap. This is typically the working principle of LEDs and LASERS. Non-radiative recombination corresponds to the relaxation of excited electrons through other processes than the emission of a photon. Most often, the light-harvesting material used in solar cells is not

perfect in terms of crystallinity. Indeed, defects or impurities can be present, and this creates energetic defects in the electronic structure of the material. In other terms, photogenerated electrons in the CB might relax to discrete defect levels of lower energy and then relax to the VB, recombining with a hole. In this phenomenon called trap (or Shockley-Read Hall) recombination, the electron relaxes through lattice vibration, which results mainly in phonons emission that gets lost as heat. Another recombination method that also occurs in semiconductors is known as Auger recombination. It is similar to radiative recombination, apart from the fact that the relaxation energy is not expressed via the emission of a photon but is given to other charge carriers which subsequently get excited to higher energy states within the same energy band, before thermally relaxing via phonons generation.¹⁷

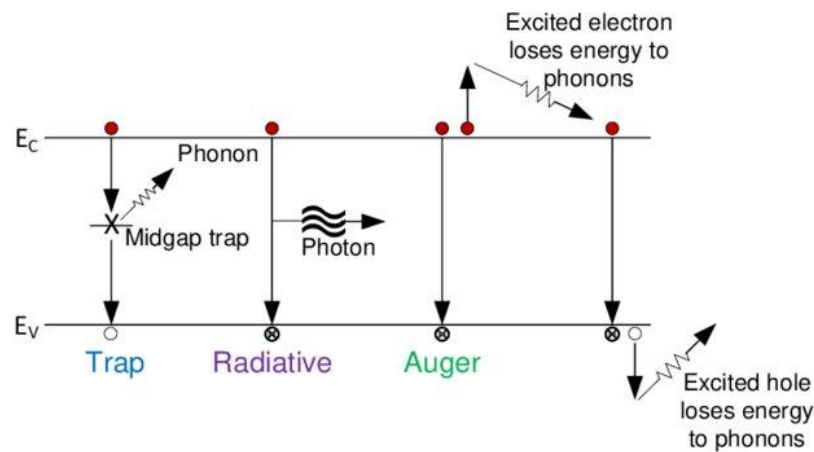


Figure 8. Illustration of the three recombination processes occurring in solar cells¹⁸

Auger recombination mostly occurs in case of high charge carrier concentrations, following heavy doping or a high injection rate, which is likely to happen under exposure to a concentrated light.

The time between the photogeneration and the recombination of electron-hole pairs is defined as the minority carrier lifetime of a material, and it is a crucial parameter for solar cells performance. It is directly proportional to the charge carrier concentration Δn and inversely proportional to the recombination rate R :

$$\tau = \frac{\Delta n}{R} \quad (6)$$

and the overall charge carrier lifetime is defined as:

$$\frac{1}{\tau} = \frac{1}{\tau_{radiative}} + \frac{1}{\tau_{trap}} + \frac{1}{\tau_{Auger}} \quad (7)$$

This equation shows that any recombination process competing with radiative recombination reduces the effective lifetime of charge carriers and is therefore detrimental.¹⁹

Solar cells: basics & evolution of PV technology

Now that we had a look at semiconductors and the photogeneration of charges as well as the associated recombination mechanisms, let's have a closer look at solar cells.

Working principle

In a typical solar cell, two doped semiconductors are brought into contact and put under illumination to take advantage of the photogeneration of charges. Doped semiconductors are regular semiconductors whose conductivity has been tuned through the introduction of impurities (= doping). The nature of the dopant determines the nature of the doping: *n*-doping consists in introducing additional donor (free electrons) impurities in the bulk of the material whereas *p*-type doping refers to the introduction of acceptor states (free holes). As an example, silicon, which is part of the group IV of chemical elements, is doped into an *n*-type semiconductor by introducing group V atoms such as phosphorus (P) and *p*-doped using group III atoms such as boron (B).

The doping of a semiconductor implies changes in its energy levels: indeed, undoped (or intrinsic) semiconductors exhibit an equal amount of electrons in the VB and holes in the CB, which establish the energy of the Fermi level (E_F) almost exactly in the middle of the gap between VB and CB edges. Fermi level represents the average work needed to remove an

electron from the material (work function). The introduction of extra electrons (n-doping) disrupts the equilibrium, lowering in energy the Fermi level closer to the VB ($E_{F,n}$); whereas less electrons (p-doping) will have the exact opposite effect, with the extra holes shifting the Fermi level towards the edge of the CB ($E_{F,p}$).

$$E_{F,n} = E_F + k_b T \ln\left(\frac{N_D}{n}\right) \quad (8)$$

$$E_{F,p} = E_F - k_b T \ln\left(\frac{N_A}{n}\right) \quad (9)$$

where k_B is the Boltzmann constant ($1.38 \cdot 10^{-23} \text{ m}^2 \text{ kg s}^{-2} \text{ K}^{-1}$), N_D and N_A are the donor and acceptor concentrations respectively, and n is the intrinsic charge carriers concentration.

When an n -type and a p -type semiconductors are brought into contact, what is called a p - n junction is formed, and the Fermi level of both will equilibrate by diffusing the excess electrons from the n -type towards the p -type SC and holes diffusion in the opposite direction. This phenomenon creates a bending of the respective VB and CB of each material and an internal electrical field is formed in the area where electrons and holes diffuse, called the depletion region. A built-in potential (V_{bi}) is also created, which simply corresponds to the difference in the Fermi levels in n - and p -type SC before they were joined.

$$qV_{bi} = E_{F,n} - E_{F,p} \Rightarrow V_{bi} = \frac{k_B T}{q} \ln\left(\frac{N_D N_A}{n^2}\right) \quad (10)$$

The charge carriers' transport is ruled by diffusion and drift. Diffusion has been discussed here above and is caused by the gradient in charge carrier concentration whereas the drift corresponds to the process where charged particles move under the influence of an electric field. This pushes electrons towards the n -type part and holes towards the p -type part. Thus, diffusion and drift mechanisms are opposed. At equilibrium, the net current is null, as drift and diffusion currents cancel each other.

Under the application of an external voltage, the p - n junction equilibrium is disturbed: considering the positive pole of the voltage connected on the p -side and the negative on the n -side, applying a forward bias leads to the reduction of the built-in potential V_{bi} and of the internal electric field, which shrinks the depletion region. As a result, the drift of photogenerated charge carriers is diminished, ultimately allowing charges to flow. This is the creation of a photocurrent. In opposition, when a backward bias is applied, the built-in potential increases as well as the internal electric field, preventing any movement of charges. And if no bias is applied, a residual saturation current (J_0) flows across the cell to compensate for the charge carriers' diffusion.

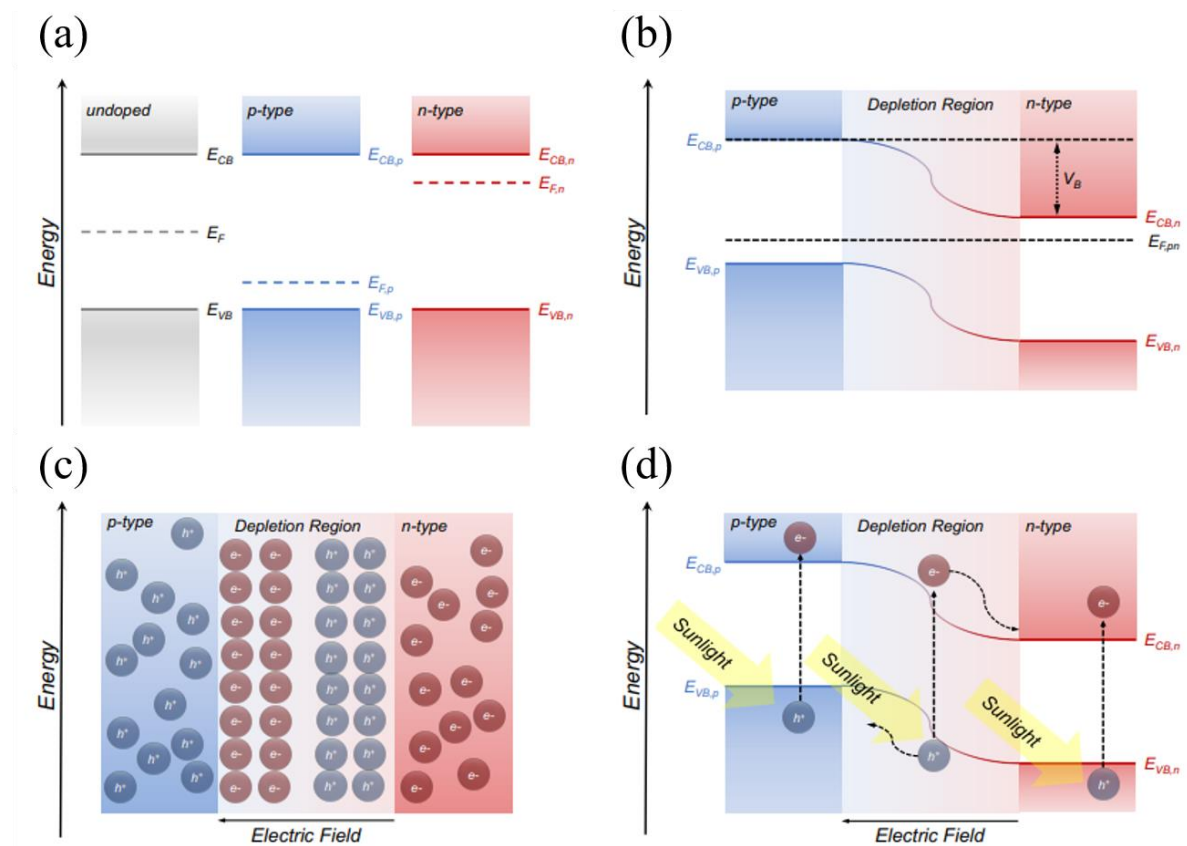


Figure 9. (a) Schematic representation of energy levels in undoped (left), p-doped (middle), and n-doped (right) semiconductors, with their corresponding Fermi levels. (b) Formation of a p-n junction with the depletion zone and band bending resulting from the Fermi levels adjustment. (c) Schematic representation of electrons and holes distribution in a p-n junction and the resulting internal electric field. (d) Schematic representation of a p-n junction operation principle under illumination

The current variation in the dark is described as follows:

$$J(V) = J_0 \left(\exp \left(\frac{qV}{k_B T} \right) - 1 \right) \quad (11)$$

All in all, it is only possible to create a photocurrent in a single direction. This is the definition of a semiconductor diode. And a photovoltaic solar cell under dark is actually similar to that, with light acting as the external applied bias.

When such a device is placed under illumination, photons absorption processes (as explained above) take place in the depletion region. The photogenerated electron-hole pairs will then be separated thanks to the internal electric field: electrons in the CB will flow towards the n -type SC and holes will flow towards the p -type SC. This leads to the splitting of Fermi level into $E_{F,n}$ and $E_{F,p}$ (quasi-Fermi level splitting, ΔE_F). Charges generated outside of the depletion region will recombine or diffuse to the depletion region and eventually be separated. When no external voltage is applied (i.e. at $V = 0$), short-circuit conditions are reached and short-circuit photocurrent (J_{sc}), that is the maximal current that the device can deliver, can be measured. It depends on the illumination of the solar cell and the charge photogeneration rate.²⁰ The photocurrent under illumination is described as:

$$J(V) = J_{sc} - J_0 \left(\exp \left(\frac{qV}{k_B T} \right) - 1 \right) \quad (12)$$

When the photocurrent is null ($J = 0$), open-circuit conditions are attained. The voltage under such conditions is defined as open-circuit photovoltage (V_{oc}) and corresponds to the quasi-Fermi level splitting potential:

$$V_{oc} = \frac{E_{F,n} - E_{F,p}}{q} = \frac{\Delta E_F}{q} \quad (13)$$

Or solving equation (11) for $J=0$ gives:

$$V_{oc} = \frac{k_B T}{q} \ln \left(\frac{J_{sc}}{J_0} - 1 \right) \quad (14)$$

However, solar cells are only non-ideal diodes, and several detrimental processes and elements are to be considered. First of all, shunt and series resistances: shunts resistance (R_{sh}) are typically due to manufacturing defects which provide alternative ways for the photogenerated charges to flow, leading to a leakage current (J_{sh}) and thus, lower performance, whereas series resistances (R_{series}) corresponds to electrical losses at interfaces/metal contacts.^{20–22} Finally, the current-voltage dependence is non-ideal and thus, a non-ideality factor m needs to be considered.^{23,24} The realistic version of equation YY is:

$$J(V) = J_{sc} - J_0 \left(\exp \left(\frac{q(V + JAR_{series})}{mk_B T} \right) - 1 \right) - \frac{V + JAR_{series}}{R_{sh}} \quad (15)$$

where A corresponds to the illuminated area (active area) of the solar cell. It is clear from equation (15) that lowering both shunt and series resistances improves the photocurrent J and thus the performance. All in all, they represent non-radiative recombination pathways, which we already discussed, have tremendously bad consequences for the solar cells performance.

A practical way to determine the non-radiative voltage losses is the measurement of the photoluminescence quantum yield (PLQY) or equivalently the electroluminescence quantum efficiency (EQE), and combination of both can also experimentally determine V_{oc} :

$$V_{oc} = \frac{\Delta E_F}{q} = V_{oc,rad} + \frac{k_B T}{q} \ln(PLQY) \quad (16)$$

$$V_{oc} = \frac{\Delta E_F}{q} = V_{oc,rad} + \frac{k_B T}{q} \ln(EQE) \quad (17)$$

Thus, voltage losses are:

$$\Delta V = V_{oc,rad} - V_{oc} = -\frac{k_B T}{q} \ln(PLQY) = -\frac{k_B T}{q} \ln(EQE) \quad (18)$$

The power conversion efficiency (PCE) of solar cells is measured via the recording of photocurrent-photovoltage (J - V) measurements under AM1.5G illumination (that is, the global standard spectrum, which is a reproduction of sunlight striking Earth's surface with an angle of 41.81° above horizon, passing through the atmosphere (air mass = 1.5), and with a total irradiance of 1000 W/m^2 and with solar cells exposed frontally to it, that is with a tilt angle of 37° from the horizon and shown in Fig. 10).²⁵

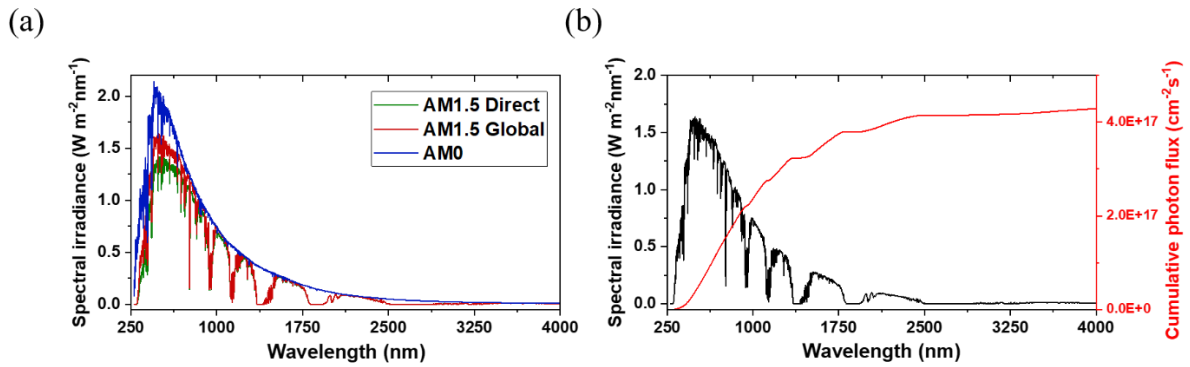


Figure 10. (a) Spectral irradiance of AM1.5G, AM1.5D, and AM0 and (b) spectral irradiance and cumulative photon flux of AM1.5G plotted with data acquired from the US National Renewable Energy Laboratory (NREL) website²⁶

The PCE of any solar cell is simply the ratio of the output electrical power given by the solar cell compared to the input power received from the sun:

$$PCE (\%) = \frac{P_{out}}{P_{in}} \cdot 100 \quad (19)$$

In 1961, Shockley and Queisser determined that the maximum theoretical PCE for a single-junction solar cell, considering an ideal case, lies at 30% for an absorber layer with a band gap energy of 1.1 eV. However, this calculation used a simplified model of the solar spectrum and more estimations determine it at 33.7 % for a band gap of 1.34 eV.^{27,28} This is referred as the Shockley-Queisser limit in their honor and represent the perfect case for which all of the solar power falling on the solar device would be converted into electricity, with no non-radiative

losses. Thus, material with a band gap energy as close as possible to 1.34 eV represent the most-suitable candidate regarding single-junction photovoltaic devices.

To calculate the power delivered by the solar cells, three parameters are taken into account from the J - V measurements: the short-circuit photocurrent (J_{sc}) and the open-circuit photovoltage (V_{oc}) which were already discussed and represent the maximum theoretical photocurrent and photovoltage of the solar cell respectively, and the fill factor (FF):

$$PCE (\%) = \frac{V_{oc}J_{sc}FF}{P_{in}} \cdot 100 \quad (20)$$

The fill factor is defined as the ratio between the actual maximum power delivered by the cells and the product of J_{sc} and V_{oc} :

$$FF = \frac{P_{max}}{J_{sc}V_{oc}} \quad (21)$$

It can help to approximate the ideality of the solar cells (how far experimental performance are from the maximal, theoretical ones) and evaluate resistive losses (losses due to series resistance). In Figure 11, FF corresponds to the ratio of the red rectangle over the blue one.

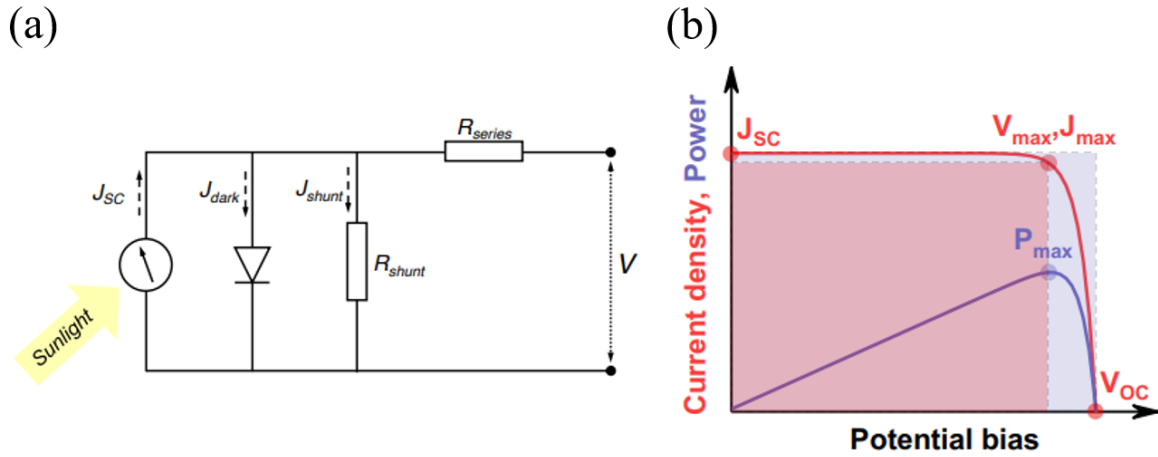


Figure 11. (a) Equivalent circuit of a solar cell under illumination, with all the other electrical elements: generated short-circuit photocurrent J_{sc} , dark current (J_{dark}), shunt leakage current (J_{sh}), series resistance (R_{series}) and shunt resistance (R_{sh}). (b) Graphical representation of a J - V curve. The important parameters are highlighted. The fill factor (FF) represents the ratio of the area of the red rectangle over the blue rectangle.

PV technology evolution

Even though Becquerel was the first to report on an electrochemical photovoltaic cell in 1839, it is not before the middle of the 20th century that photovoltaic devices really kicked in: p - n junctions were discovered in 1941 by V.E. Lashkaryov²⁹ and the first modern junction solar cell was patented in 1946 by R. Ohl.³⁰ Finally, it is in 1954 that the first practical silicon solar cell was demonstrated by Chapin *et al.* at Bell laboratories, reaching a PCE of 6%.³¹ Monocrystalline Silicon (mc-Si, PCE = 26.1%³²) and polycrystalline silicon (pc-Si, PCE = 23.3%³²) represent the first generation of solar cells, together with gallium arsenide (GaAs, PCE = 29.1%³²). They all correspond to high efficiency solar cells with excellent stability, but their production is highly energy-intensive, rendering them costly and environmentally harmful to some extent.³³ Amorphous silicon (a-Si) ones, on the other hand, are less energy-intensive in their manufactory, but their efficiency is only marginal compared to mc-Si and pc-Si. Their higher relative efficiency at low light intensities make them interesting for indoor purposes, though.³⁴ The bandgap of mc-Si and pc-Si cells lie around 1.1 eV, 1.7 eV for a-Si and 1.42 eV for GaAs.^{35,36}

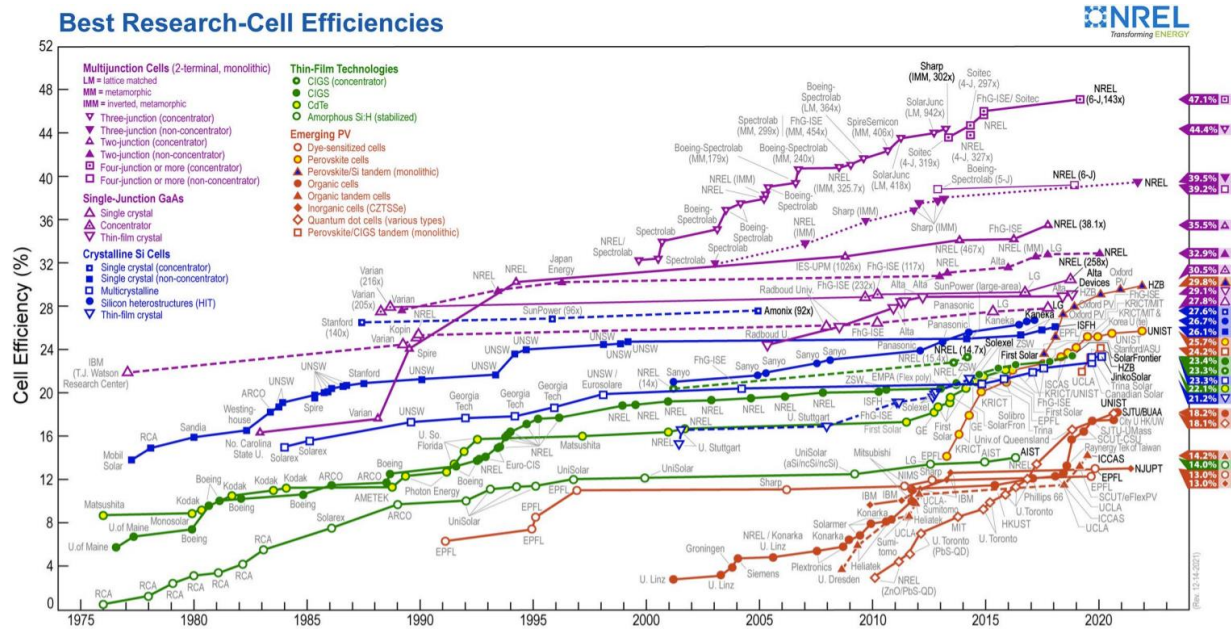


Figure 12. Best Research-Cell Efficiencies chart from the U.S. National Renewable Energy Laboratory (NREL)

The second generation of solar cells emerged in the 1970s with the apparition of thin film technologies, such as copper indium gallium selenide (CIGS, bandgap = 1.13 eV, PCE = 23.35%)³⁷, cadmium telluride (CdTe, bandgap = 1.45 eV, PCE = 22.1%)^{38–40}, gallium indium phosphide (GaInP, PCE = 20.8%)^{41,42}, copper zinc tin sulfide (CZTS/Se, bandgap 1.05-1.2 eV, PCE = 12.6%).^{43,44} CIGS technology shows the highest performance, but GaInP solar cells exhibit the advantage of having particularly low voltage losses, enabling high V_{oc} up to 1.41 V. Unfortunately, and even if they have the advantage to avoid the use of silicon wafers as well as using less materials than first generation photovoltaic devices, these devices still exhibit the same drawbacks than first-generation solar cells, i.e. their production is highly energy-consuming, require some Earth-rare materials and is not so energy-friendly.³³

Third generation of solar cells arose from the late 1990s, taking advantage of innovation (notably in the deposition methods that followed the second generation of PV, but also from engineering as a whole), with the ultimate aim to develop simpler processes and lower their environmental footprint by involving more Earth-abundant elements. Diverse device's architecture can be found amongst the several different types of third-generation PV cells. The

most-promising technologies are dye-sensitized solar cells (DSSCs), perovskite solar cells (PSCs) and organic solar cells (OPVs). DSSCs are developed following the discovery of Prof. Michael Grätzel and mimic the natural photosynthesis. The technology is simple and environmentally friendly, but their PCE is limited ($< 14\%$). Still, DSSCs are already manufactured on a multi-megawatt scale, and their excellent efficiency at lower light intensities render them extremely interesting for other purposes than high efficiency solar energy generation though, such as integrated PV for indoor purposes or detectors, amongst other. PSCs are derived from solid-state DSSCs and use a light-absorbing layer made of tin/lead perovskites. They demonstrated an incredible raise in their PCE, starting from an initial 3.8% PCE in 2009 up to 25.7% nowadays, already competing with silicon cells within 15 years from their discovery!^{45,46} Unfortunately, PSCs lack operational stability to date, but they are poised to conquer the market in the near future. Finally, OPVs represent a major candidate to establish the next benchmark PV technology, especially regarding the fact they involve low-cost, non-toxic, Earth-abundant materials and already demonstrate to be promising regarding their industrialization, with easy manufacturing schemes made possible thanks to the high flexibility of OPVs. In terms of efficiency, the record PCE established so far lies at about 18% PCE.⁴⁷

Perovskite solar cells

Historical perspective

Historically, the name of "perovskite" first referred to the mineral calcium titanate (CaTiO_3), described by Gustav Rose (1798 - 1873) in the 1830s' and who named it after the Russian mineralogist Count Lev Alekseyevich von Perovski (1792-1856, Figure 13).⁴⁸



Figure 13. Count Lev Alekseyevich von Perovski

By extension, the "perovskite" denomination was then applied to any material of empirical formula ABX_3 which adopts the same atomic structure as CaTiO_3 , with A being a rather large monovalent cation (A^+), B a

smaller divalent cation (B^{2+}) and X a divalent anion (X^{2-}). The ideal perovskite lattice arrangement is shown below (Figure 14). It corresponds to a cubic perovskite phase, also referred to as alpha phase (α -phase). As with many structures in crystallography, it can be represented in several ways. The simplest way to think about a perovskite is the following: B^{2+} cations are 6-fold coordinated to X^- anions, forming a system of ordered octahedra where B^{2+} cations lie in the center of the octahedra and X^- anions forming the corners. The bigger, 12-fold coordinated A^+ cations fill the gap between the octahedra and balance the charge of the whole network.

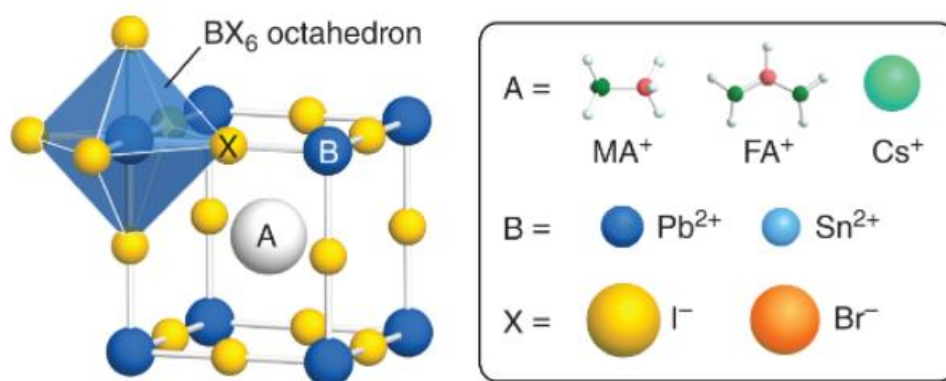


Figure 14. Schematics of a 3D ABX_3 perovskite structure with an emphasis on the chemical elements used in each A, B or X position respectively for solar cells applications⁴⁹

Depending on the elemental nature of A, B and X ions, respectively, perovskites can offer a broad array of properties, such as superconductivity,⁵⁰ catalytic properties,⁵¹ strong magnetoresistance,⁵² or spintronics,⁵³ rendering them interesting for diverse applications. A real breakthrough occurred in 2006, though, when Prof. Miyasaka's group (in collaboration with *Peccell Technology Inc.*) presented at the *Electrochemical Society (ECS)* meeting the use metal-halide perovskites (MHPs), and more precisely of methylammonium lead bromide (MAPbBr_3) as light-harvesting material to fabricate solar cells of 2.19% PCE.⁵⁴ In 2009 finally, the first research article was published by the same group. They reported the use of methylammonium lead iodide (MAPbI_3), to produce PSCs of 3.8% PCE.⁴⁵ Since then, the interest of researchers worldwide was triggered, and constant improvements were reported, to attain nowadays a record PCE of 25.7%.⁴⁶ Thus, the photovoltaic potential of MHPs material is immense, and lots of research groups are competing worldwide to push PSCs to the next stage. This phenomenon is reflected in Figure 15, which displays the amount of research papers published every year for each type of solar cells. As it is clear, soon after 2010 marked a turning point, as PSCs research exploded, at the expense of other technologies, and in particular DSSCs.

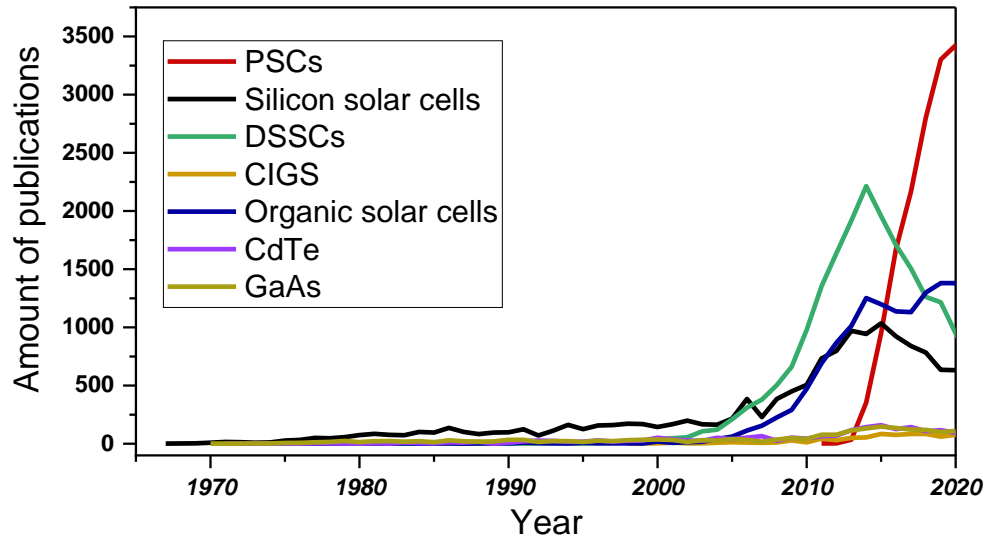


Figure 15. Number of research papers published for each photovoltaic technology plotted as a function of years

Working principle

In a conventional PSC, the perovskite light-absorbing layer is sandwiched between an electron transporting layer (ETL) and a hole transport material (HTM), which are then connected to the outer circuit via electrodes (gold, generally). The working mechanism of a PSC depends on three distinguished processes: (1) charge generation (2) charge separation and (3) charge collection.

Crystal structure and electronic properties of hybrid metal halides perovskites

MHPs used in the fabrication of photovoltaic devices are direct band gap semiconductors which exhibit high absorption coefficients ($\sim 10^5 \text{ cm}^{-1}$), allowing them to absorb most of the incident sunlight.⁵⁵ They exhibit a 3D perovskite structures which present the general formula APbX_3 , where A-site is occupied by organic and/or inorganic cations such as formamidinium ($\text{FA}^+ = \text{HC}(\text{NH}_2)_2^+$), methylammonium ($\text{MA}^+ = \text{CH}_3\text{NH}_3^+$), guanidinium ($\text{GA}^+ = \text{C}(\text{NH}_2)_3^+$), imidazolium ($\text{IA}^+ = \text{C}_3\text{H}_5\text{N}_2^+$), ethylammonium ($\text{EA}^+ = \text{CH}_3\text{CH}_2\text{NH}_3^+$), cesium (Cs^+), rubidium (Rb^+) and X-site is comprised of iodide (I^-) and/or bromide (Br^-). B-site is most commonly

made of post-transition (group-14) metal lead (Pb^{2+}), but research involving more environmentally-friendly elements is growing, with tin (Sn^{2+})⁵⁶ the most-promising candidate and to minor extent germanium (Ge^{2+}),⁵⁷ bismuth (Bi^{3+}),⁵⁸ antimony (Sb^{2+})⁵⁹ or (copper, Cu^{2+})⁶⁰ (*nb: when employing metalloid elements, perovskite material take the empirical formula $\text{A}_3\text{B}_2\text{X}_9$*).

Perovskite's structure impacts drastically both the photovoltaic performances and its stability. Depending on the chemical nature of the ions used in the A, B or X position, the structure and even the dimensionality of the perovskite can change, and accordingly its optoelectronic properties. For example, if the ion used in the A-position is a small monovalent cation, a well-ordered three-dimensional perovskite framework can be obtained, whereas the use of a larger cation can induce two-dimensional layered or even single-dimensional chain perovskite materials.

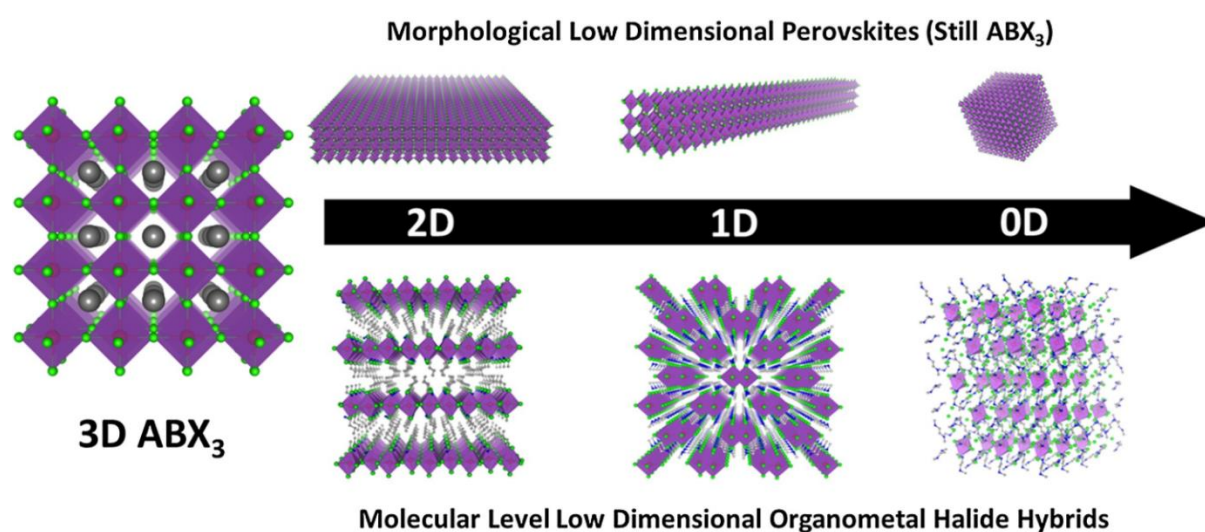


Figure 16 3D ABX_3 metal halide perovskites and perovskite-related materials with different dimensionalities at both morphological and molecular levels.⁶¹

Thus, only limited combinations of elements/ions are able to form ideal 3D MHP structures. Ideality of perovskite structures can be estimated by Goldschmidt's tolerance factor T and an octahedral factor μ .

Goldschmidt's tolerance factor T

Goldschmidt's tolerance factor was firstly used to predict and describe the structure of oxide perovskites.⁶² It has been shown that it can equally describe and predict, in a very simple and empirical way, the structure and stability of MHPs and fully-inorganic perovskites as well, using the following formula:

$$T = \frac{r_A + r_X}{\sqrt{2}(r_B + r_X)}$$

where r_A , r_B and r_X correspond to the ionic radii of A, B and X, respectively. For compositions with a mixture of cations for A or B, or a mixture of halides for X, an effective ionic ratio is estimated by using the weighted average of the atomic ratio, as described by G. Kieslich *et al.*⁶³ Theory states that cubic perovskite structures should be attained for T values comprised between 0.71 and 1.00, however experimental data showed that the actual interval for which stable cubic perovskite structures are formed is $0.85 < T < 1.00$ and is referred to as the *Goldilock's zone*. For $T > 1.00$, hexagonal structures are formed and tilted BX_6 octahedra arose for $T < 0.9$, disorganizing the overall structure.⁶⁴ Interestingly, for an ABX_3 structure, only Cs^+ , MA^+ and FA^+ can be used in the A-site to fulfill Goldschmidt's rules, with Rb^+ , IA^+ and EA^+ being on the limit (Figure 17(a)).

Also, with a band gap energy of 1.43-1.5 eV, α -FAPbI₃ is closer to the optimum value of 1.4 eV calculated by Schokley-Queisser for a single-junction solar cell. Therefore, it is almost ideal for light-harvesting and it is not surprising that it has proven to be the most efficient MHP composition to date.^{46,65} Unfortunately, the photoactive active phase of FAPbI₃ is unstable with respect to the photoinactive yellow δ -phase at room temperature and it is therefore a tremendous challenge to stabilize the photoactive black α -phase in order to yield sustainable, long-performing PSCs.

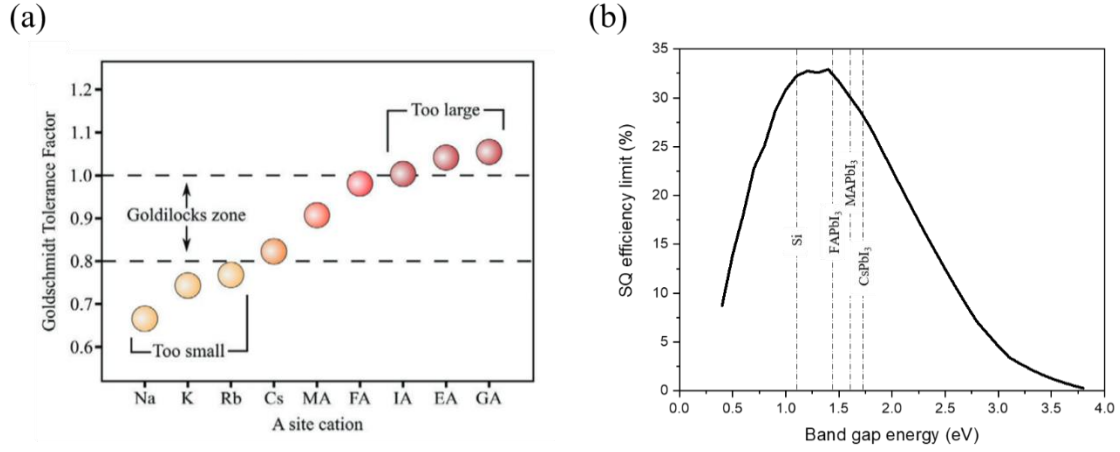


Figure 17 (a) Examples of the influence of the A-cation on Goldschmidt's factor and thus, on the perovskite structure. According to the predictions, only Cs, FA and MA are to be used in the A-site from the current list⁶⁶(b) SQ limit as function of the band gap energy for a single-junction solar cell at 298K.

Octahedral factor

Goldschmidt's factor, even if able to provide an easy and rapid evaluation of the potential of perovskite compositions, is not sufficient to predict the formation of perovskite structures in reality, though, as shown by Li *et al.* in 2004.⁶⁷ To further classify distorted perovskites, one has to take into account the tilting of the BX₆ octahedra by employing Glazer's octahedral factor μ . The octahedral factor is equal to the ratio of r_B with r_X :

$$\mu = \frac{r_B}{r_X}$$

Indeed, depending on the angle of B-X-B bonds, which depends on both atomic radii and thus can be represented by the octahedral factor, the overall perovskite structure might be distorted compared to the ideal cubic one (this is the case for when B-X-B angle is not flat (180°)), as shown in Figure 17.

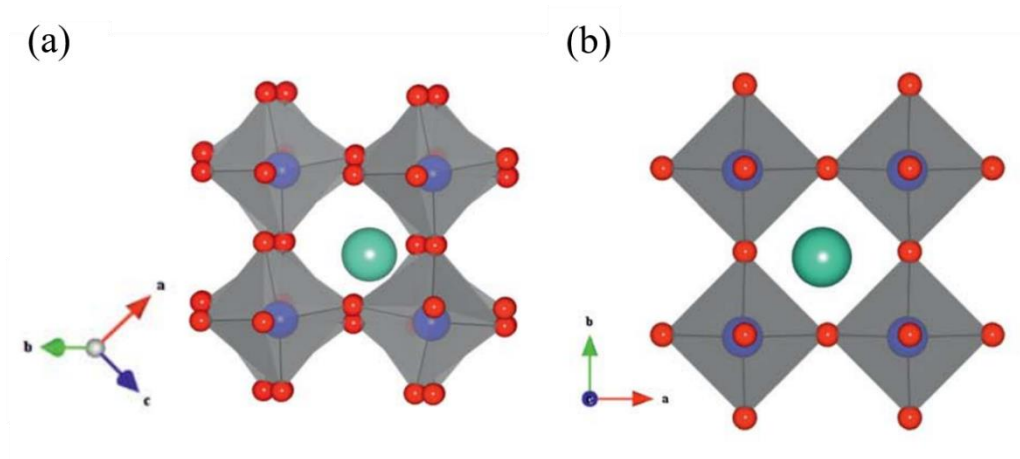


Figure 18. Comparison between tilted (a) and non-tilted (b) perovskite structures.⁶⁸ A ions are in green, B in red and X in blue. It is clearly observable, notably on the bottom part of picture (a) that the B-X-B angle is not flat anymore in this tilted configuration.

Li et al. proposed in 2008 to build a two-dimensional tolerance factor-octahedral structure map model to explore the regularities governing the formation of halide perovskites and investigated 186 complex halide compounds of empirical formula ABX_3 .⁶⁹ They found out that 96% of the perovskite structures lie in the same and well-defined area of the t - μ map, that is for $0.81 \leq t \leq 1.11$ and $0.44 \leq \mu \leq 0.90$, while almost all the non-perovskite structures are found in the other part of the map (Figure 19). This is, therefore, a very strong tool to predict whether a compound of empirical formula ABX_3 will form a perovskite structure or not.⁷⁰

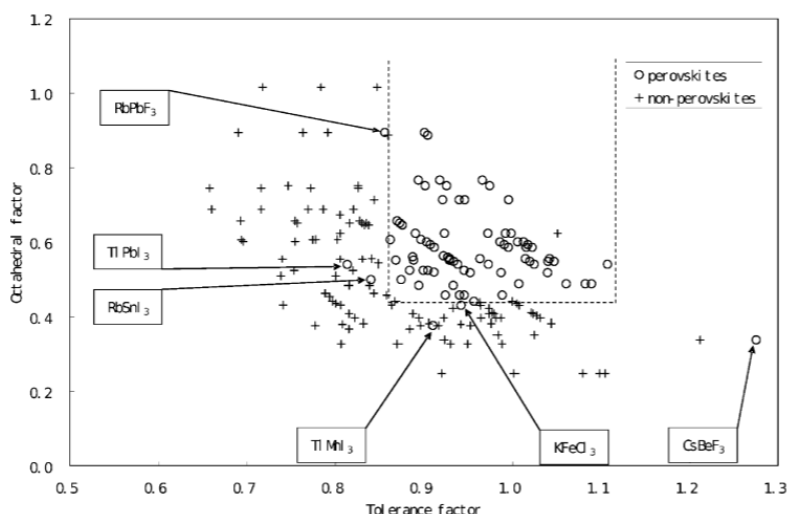


Figure 19. Classification of halide perovskite compounds of empirical formula ABX_3 in the T - μ structure map as reported by Li et al.⁶⁹ Compounds with a perovskite structure are denoted by a ring and non-perovskite compounds are denoted with a cross. The perovskite formability threshold is clearly

observable and is shown here with dotted lines. Apart from the few exceptions that are highlighted, all the perovskite structures are found within the formability threshold.

Electronic structure

The electronic structure of ABX_3 perovskites is also highly dependent on their composition. The interactions between A, B and X elements give rise to the optoelectronic properties that made PSCs such a hit in the photovoltaic research. Most interestingly, MHPs exhibit films low trap density and with easily tunable bandgaps.

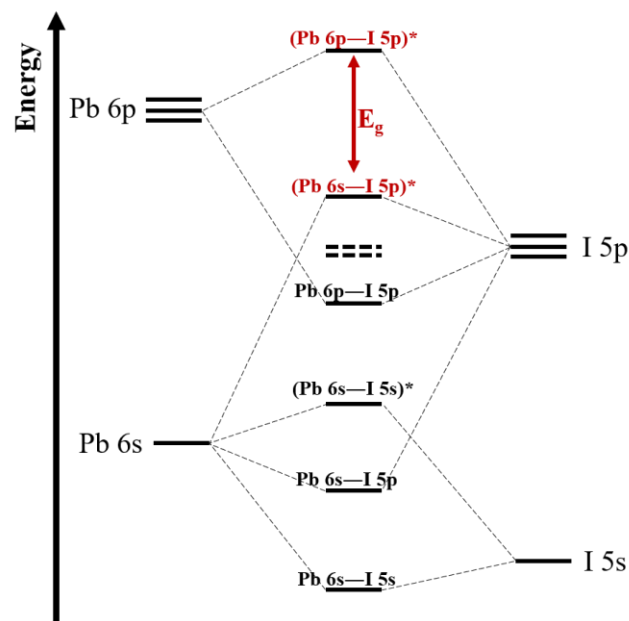


Figure 20. Band structure of lead iodide based MHPs

Umebayashi *et al.* demonstrated in 2003 already by ultraviolet photon spectroscopy (UPS) and density functional theory (DFT) calculations that states close to band edges (thus, responsible of the band gap) of MHPs is almost exclusively driven by contributions from metal and halide ions only, with very small and indirect effects arising from A cation as it lies deep (5 eV) below Fermi level energy).^{71,72} The valence band is formed by antibonding (σ^*) interactions between the halide 5p and metal 6s orbitals, and the conduction band by antibonding interaction between halide 5p and metal 6p orbitals interactions (see example for $MAPbI_3$ displayed in Figure 20).

Crucially, in Pb-based perovskites, the valence band maximum (VBM) is dictated by the halide 5p orbitals, which makes MHPs VBM position (and thus, the resulting bandgap) highly sensitive to the halide ions.⁶⁴ The atomic weight of the metallic cation also plays an important role on the band structure of MHPs: elements with lower atomic weights relative to Pb (Sn, Ge, and Sb) provide greater ns² contribution to the σ^* characteristic of the VBM, raising its energy.^{73,74} By contrast, replacing Pb with the heavier atom Bi results in increased spin-orbital coupling that favorably lowers the CBM.⁷⁵

Crystallography of photoactive perovskite structures

As aforementioned, the properties of perovskite materials highly depends on their elemental composition, as this will define the band structure but also the symmetry of the perovskite crystal network. In particular, 3D hybrid organic-inorganic MHPs are used for solar cells applications due to their excellent optoelectronic properties. The most promising candidate in terms of band gap energy is α -FAPbI₃.

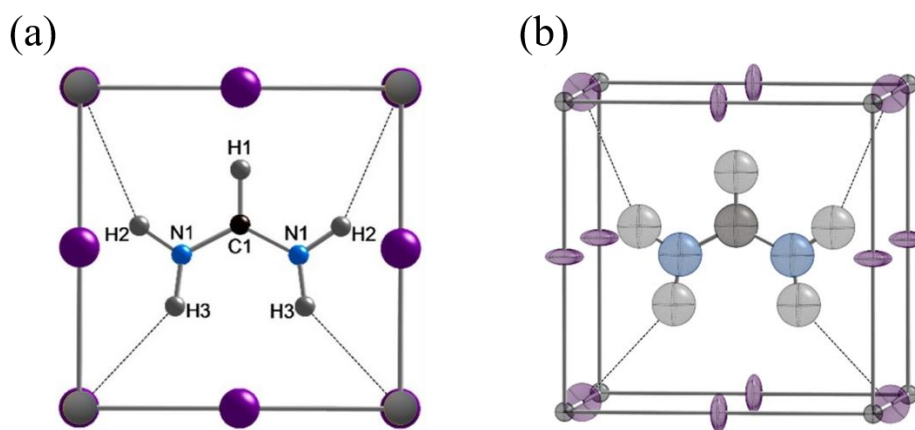


Figure 21. FAPbI₃ unit cell structure of α -FAPbI₃ (a) in 2D and (b) in 3D; dark grey represents lead at all corners, claret stands for iodide along cell edges, black for carbon, blue for nitrogen and light gray for hydrogen. Dotted lines represent hydrogen NH...I bonding

3D MHPs are unique crystal structures of ABX₃ formula with corner-sharing lead-halide octahedra forming an ionic network counterbalanced by A-cation in the cavities between the octahedra. However, MHPs can exhibit a variety of different polymorphs depending on the energy of the system: cubic, orthorhombic, tetragonal, hexagonal, etc (Figure 21). The ideal

perovskite structure is the cubic structure, referred as α -phase, and corresponds to the most symmetrical (non-tilted) and ordered polymorph (space group $Pm\bar{3}m$), with Pb-X-Pb angles at 180° and the A-cation lying in the middle of the void between PbX_3^- octahedra, as is the unit cell depicted in Figure 21 with formamidinium as A-cation.⁷⁶ It corresponds to the photoactive black phase of MHPs. Unfortunately, it is only stable at high temperatures (> 330 K). Indeed, below that, the most-promising perovskite composition α -FAPbI₃ undergoes a phase transition to the photoinactive hexagonal yellow phase (δ -FAPbI₃, space group $P6_3mc$), which exhibit a large band gap of approx. 2.48 eV and another one for $T < 130$ K, where it is converted to tetragonal and photoinactive β -phase (space group $P4mm$). Similar behavior apply to MAPbI₃, which translates from cubic to the tetragonal phase (β -MAPbI₃, space group $I4mcm$) below 330 K and to an orthorhombic phase for $T < 130$ K (γ -phase, space group $Pnma$).^{77–79}

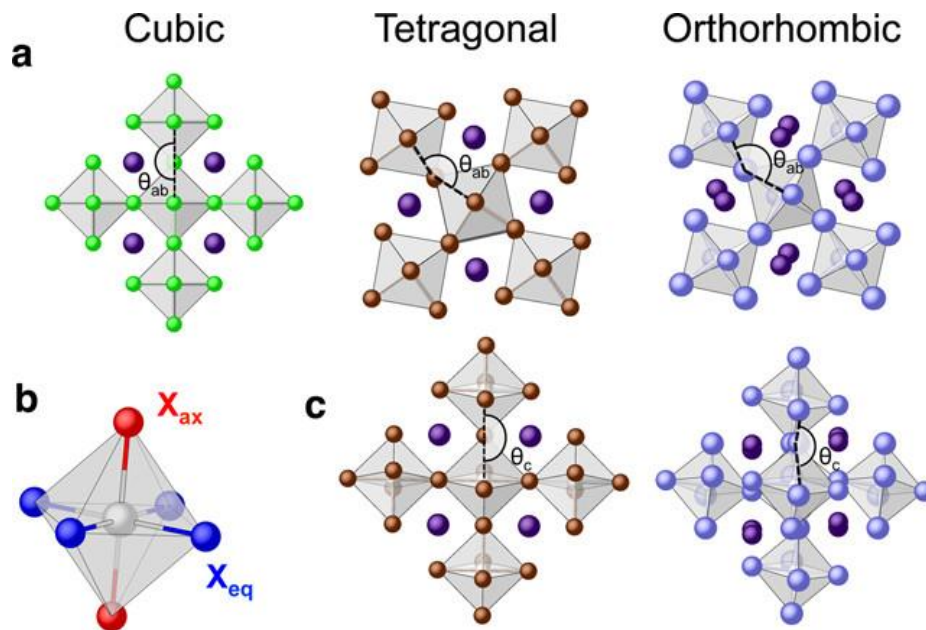


Figure 22. (a) Sketch of the 3D arrangement of the PbX_6 exhibiting a cubic (C), tetragonal (T), or orthorhombic (O) structure; the symmetry descent is related to small coherent displacements of halides, leading to bending of Pb–X–Pb angles with $\theta_{ab} = \theta_c = 180^\circ$ (C), $\theta_{ab} < 180^\circ$ and $\theta_c = 180^\circ$ (T), and $\theta_{ab} = \theta_c < 180^\circ$ (O). Atomic species in the top (a) and side (c) views are Cs = violet, Pb = gray, X = green, brown, cyan. (b) Equatorial (X_{eq}) and axial (X_{ax}) halides in the PbX_6 octahedron are highlighted in blue and red, respectively.⁸⁰

As different polymorphs correspond to different unit cells, it thus interacts differently with light and other particles (as shown by the band gap energies difference for instance). Hence, a

straightforward way to determine the structure of prepared perovskite films is x-ray diffraction (XRD) measurements. Indeed, different polymorphs diffract x-ray beams differently and thus, recording diffraction patterns gives solid information on the perovskite film's crystal phase composition. α -FAPbI₃ typically diffracts x-rays at $\sim 13.9^\circ$, 19.8° , 24.3° , 28.1° , 31.4° , 34.6° , 40.1° and 42.7° , corresponding to the (0 0 1), (0 1 1), (1 1 1), (0 0 2), (0 1 2), (1 1 2), (0 2 2) and (0 3 3) diffraction planes, respectively.⁸¹ Most intense peaks are found at 13.9° , 28.1° and 34.6° . On the other hand, δ -FAPbI₃ shows a strong and typical diffraction signal at around 11.8° and PbI₂ at 12.6° . Figure 23 displays the XRD patterns of FAPbI₃ perovskite at different temperatures. The transition from δ -FAPbI₃ to α -FAPbI₃ starts at around 130°C (403 K) and is complete at 150°C (423 K), as shown by the respective diffraction significative peaks.

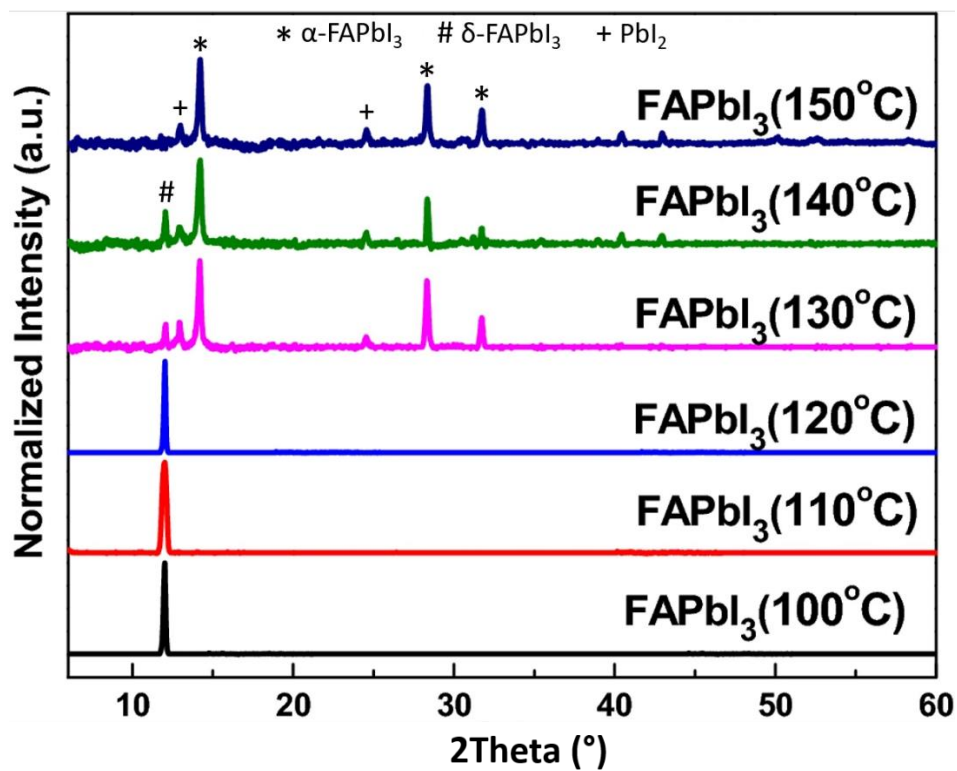


Figure 23. Temperature effect on FAPbI₃ polymorphism: for temperature $> 130^\circ\text{C}$, δ -FAPbI₃ converts into α -FAPbI₃, and pure α -FAPbI₃ is attained for $T > 150^\circ\text{C}$

To attain phase purity is a challenge in α -FAPbI₃-based PSCs. Often, only part of δ -FAPbI₃ is successfully converted into α -FAPbI₃, with some percentage remaining in the yellow phase, or even forming PbI₂ + FAI. Moreover, over time at RT, α -FAPbI₃ tends to translate back to the

yellow phase (phase instability), and this represents one of the most-challenging drawbacks of PSCs to date. Some strategies to stabilize α -FAPbI₃ include mixing halide (iodide and bromide) and A-cation (FA⁺, MA⁺, Cs⁺) or post-film formation treatments (passivation, vapor treatment, etc).

All in all, XRD measurements are a very powerful tool to assess phase composition and purity of perovskite films and can be especially useful in order to study their long-term compositional stability.

Defects and losses in PSCs

Phase impurities constitute a source of performance loss, as other phases than α -FAPbI₃ are less performing. But in practice, even if high phase purity is achieved, the preparation of ideal perovskite films, showing no defects, remains a sweet illusion. Indeed, different types of defects arise when preparing PSCs.

To put it in simple words, defects in crystallography are defined as any disruption of the ideal crystal lattice, by the formation of irregularities, the adjunction of impurities or simply by vacancies in the crystal network. In semiconductors, four types of defects are relevant and defined according to their dimensionality: (i) zero-dimensional defects (point defects); (ii) one-dimensional defects (line defects, dislocation); (iii) two-dimensional defects (surface defects, grain boundaries) and (iv) three-dimensional defects (voids, precipitates, clusters, etc). A point defect is an imperfection that occurs at a specific location in a crystal, such as an atom vacancy (an atom missing from the lattice), an interstitial defect (an atom irregularly placed in the lattice) or an anti-site substitution (an atom sitting on the site of another element). If an atom is responsible for both a vacancy and an interstitial defect, it is referred as a Frenkel defect, and in the case where two ions (cation and anion) are missing simultaneously, it is called a Schottky defect.⁸² In contrast, extended defects are not confined to a specific lattice site; a dislocation,

for example, is a one-dimensional “line” defect. When there is an extra plane of atoms in the lattice, the edge of that plane is a line and is referred to as an edge dislocation. A stacking fault, where a plane of atoms is in the wrong sequence, is an example of a two-dimensional defect.

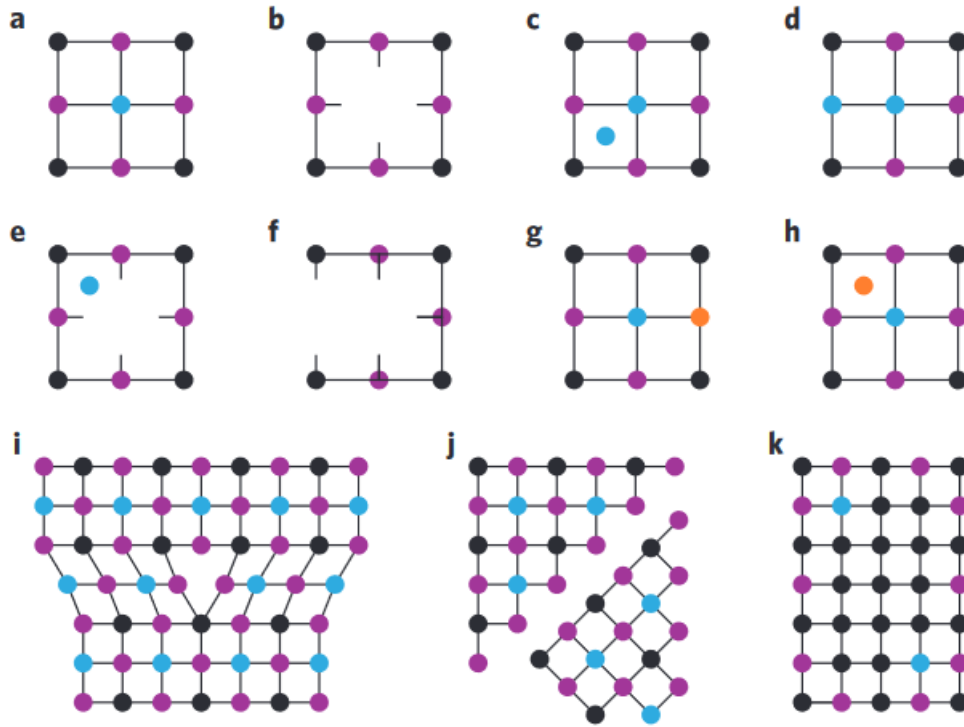


Figure 24 Illustration of different defects types that can be found in semiconductors and especially in perovskite films (a) perfect lattice (b) vacancy (c) interstitial (d) anti-site substitution (e) Frenkel defect (interstitial and vacancy created from the same ion) (f) Schottky defect (anion and cation vacancies occurring together) (g) substitutional impurity (h) interstitial impurity (i) edge dislocation (line defect propagating along the axis perpendicular to the page) (j) grain boundary and (k) precipitate.⁸³

Regarding our material of interest, MHPs, the most occurring defects (and thus the most problematic ones) originate from both the bulk of the material and from interfaces with the charge transport layers, as main defects arise at grain boundaries and at the surface of the perovskite films.^{83–86} This compromises the power conversion efficiency and the long-term stability by creating intermediate energy states that will promote non-radiative recombination pathways and irregularities in the crystal lattice that will catalyze further degradation.⁸²

Regarding FAPbI₃, DFT calculations showed there are 12 different types of defects that can arise: iodide, FA⁺ or lead vacancies (V_I , V_{FA} , V_{Pb}), interstitial point defects (I_i , FA_i , Pb_i) and

anti-site point defects (I_{FA} , I_{PB} , FA_I , FA_{Pb} , Pb_I , Pb_{FA}).⁸⁷ In another words, MHPs can suffer from different irregularities in their crystal structure and composition. The most deleterious defects form deep trap with high energy formation and thus, they seldom form. Defects with low formation energy are also commonly found in MHPs, but they are mostly shallow and thus only give a negligible contribution to non-radiative recombination. They could heavily contribute to the poor stability of MHPs, though. Indeed, MHPs are mixed conductors, that is both electronic but also ionic conductors. Thus, low formation energy shallow trap can promote ion migration, which is detrimental to the performance of PSCs to some extent (considered as one of the major reason behind hysteresis)⁸⁸, but most importantly drastically impacts the long-term stability of MHPs and thus, of PSCs.

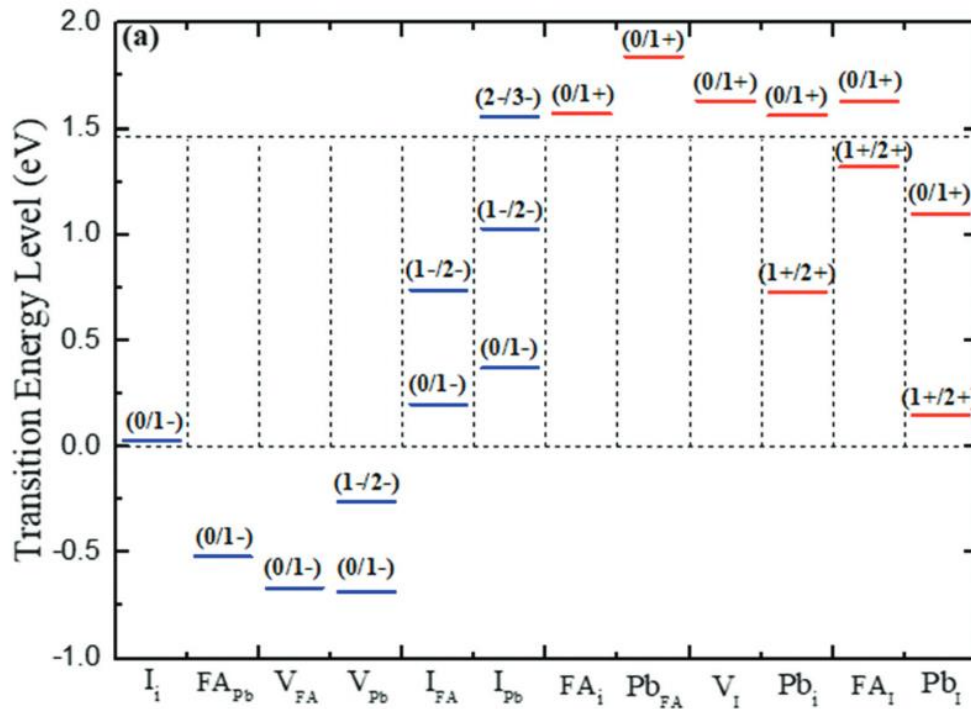


Figure 25. The charge transition energy levels of intrinsic defects in $FAPbI_3$ derived from DFT calculations⁸⁷

Table 1. *FAPbI₃ defects formation energies of point (in eV) calculated via DFT⁸⁷*

Condition	I _i	FA _{Pb}	V _{FA}	V _{Pb}	I _{FA}	I _{Pb}	FA _i	Pb _{FA}	V _i	Pb _i	FA _i	Pb _i
I-poor	0.60	1.02	0.14	0.86	0.34	0.72	2.36	2.28	1.69	3.38	2.30	4.63
Pb-rich	1.60	2.08	1.09	2.97	2.45	3.89	1.31	1.22	0.63	1.27	0.19	1.46
Moderate	1.13	1.61	0.54	1.95	1.37	2.34	1.86	1.69	1.16	2.29	1.27	3.01

Thus, controlling the growth of the perovskite crystals in order to prevent defects formation is crucial towards highly efficient and stable PSCs. Also, the passivation of interfacial/surface defects has to be undertaken seriously, as it is also a key parameter for viable devices. Such features are still preventing PSCs to flood the market.

Conclusion

In this thesis, we focused in further developing PSCs to get them one step closer to an industrial reality. We tackled some key issues found in PSCs with regards to the phase purity and defects mitigation. We notably simplified the perovskite composition and engineered the deposition method in order to yield highly efficient, stable and reproducible PSCs. The outcome of this thesis results in the successful preparation of solar cells achieving over 24 % PCE, with improved operational stability. This work also shines lights on different but simple engineering strategies that can be undertaken to further develop PSCs. It can be used as an example to guide future researchers in bringing PSCs closer to a commercial product.

References

1. Global primary energy consumption by source.
https://ourworldindata.org/grapher/global-energy-consumption-source?country=~OWID_WRL.
2. Morris, C. R. The dawn of innovation : the first American Industrial Revolution. 368 (2012).
3. Britannica, E. of the encyclopedia. 'Edwin Drake - American oil driller'. *Encyclopedia Britannica*.
4. Deese, D. A. Energy: Economics, Politics, and Security. *Int. Secur.* **4**, 140 (1979).
5. Hawks, J., Hunley, K., Lee, S. H. & Wolpoff, M. Population bottlenecks and Pleistocene human evolution. *Mol. Biol. Evol.* **17**, 2–22 (2000).
6. van Ruijven, B. J., De Cian, E. & Sue Wing, I. Amplification of future energy demand growth due to climate change. *Nat. Commun.* **10**, 1–12 (2019).
7. Watari, T. *et al.* Total material requirement for the global energy transition to 2050: A focus on transport and electricity. *Resour. Conserv. Recycl.* **148**, 91–103 (2019).
8. Perez, R. & Perez, M. A fundamental look at energy reserves for the planet.
9. Twidale, S. Flows through Russia's Yamal-Europe gas pipeline turn eastwards | Reuters. *Reuters* <https://www.reuters.com/business/energy/russias-yamal-europe-gas-pipeline-halts-westbound-flows-data-2022-03-15/> (2022).
10. Crude oil - 2022 Data - 1983-2021 Historical - 2023 Forecast - Price - Quote - Chart.
<https://tradingeconomics.com/commodity/crude-oil>.
11. De Broglie, L. Recherches sur la théorie des Quanta.
12. Singh, N., Kaushik, S. C. & Misra, R. D. Exergetic analysis of a solar thermal power system. *Renew. Energy* **19**, 135–143 (2000).
13. *Thermal, Mechanical, and Hybrid Chemical Energy Storage Systems*. (Elsevier, 2021).

doi:10.1016/C2019-0-00430-X.

14. Becquerel, E. Comptes rendus hebdomadaires. *Comptes rendus l'Académie des Sci.* (1839).
15. Kuzemsky, A. L. Band Theory and Electronic Properties of Solids. *Stat. Mech. Phys. Many-Particle Model Syst.* 297–318 (2017) doi:10.1142/9789813145641_0012.
16. Luque, A. & Hegedus, S. Handbook of Photovoltaic Science and Engineering. *Handb. Photovolt. Sci. Eng.* (2005) doi:10.1002/0470014008.
17. Kirk, A. P. Solar Photovoltaic Cells: Photons to Electricity. *Sol. Photovolt. Cells Photons to Electr.* 1–123 (2014) doi:10.1016/C2014-0-03052-3.
18. Jobayer Hossain, M., Hossain, J. & Mohammad. Novel High Efficiency Quadruple Junction Solar Cell with Current Matching and Optimized Quantum Efficiency. *arXiv arXiv:1904.01108* (2019).
19. Tress, W. Perovskite Solar Cells on the Way to Their Radiative Efficiency Limit – Insights Into a Success Story of High Open-Circuit Voltage and Low Recombination. *Adv. Energy Mater.* **7**, 1602358 (2017).
20. Nelson, J. The Physics of Solar Cells. *Phys. Sol. Cells* (2003) doi:10.1142/P276.
21. Drud Nielsen, L. Distributed Series Resistance Effects in Solar Cells. *IEEE Trans. Electron Devices* **29**, 821–827 (1982).
22. Araújo, G. L., Cuevas, A. & Ruiz, J. M. The Effect of Distributed Series Resistance on the Dark and Illuminated Current-Voltage Characteristics of Solar Cells. *IEEE Trans. Electron Devices* **33**, 391–401 (1986).
23. Charles, J. P., Abdelkrim, M., Muoy, Y. H. & Mialhe, P. A practical method of analysis of the current-voltage characteristics of solar cells. *Sol. Cells* **4**, 169–178 (1981).
24. Lorenzo, E. *et al.* Solar Electricity: Engineering of Photovoltaic Systems. 316 (1994).
25. Gueymard, C. A., Myers, D. & Emery, K. Proposed reference irradiance spectra for

solar energy systems testing. *Sol. Energy* **73**, 443–467 (2002).

26. Solar Spectra | Grid Modernization | NREL. <https://www.nrel.gov/grid/solar-resource/spectra.html>.

27. Shockley, W., Queisser, H. J. & ell, R. Detailed Balance Limit of Efficiency of pn Junction Solar Cells Additional information on J. Appl. Phys. JOURNAL OF APPLIED PHYSICS Detailed Balance Limit of Efficiency of p-n Junction Solar Cells*. *Cit. J. Appl. Phys* **32**, 510 (1961).

28. Rühle, S. Tabulated values of the Shockley–Queisser limit for single junction solar cells. *Sol. Energy* **130**, 139–147 (2016).

29. Lashkaryov, V. E. INVESTIGATIONS OF A BARRIER LAYER BY THE THERMOPROBE METHOD. *Izv. Akad. Nauk SSSR, Ser. Fiz* **5**, 442–446 (1941).

30. Ohl, R. S. Light-sensitive electric device. (1941).

31. Chapin, D. M., Fuller, C. S. & Pearson, G. L. A new silicon p-n junction photocell for converting solar radiation into electrical power [3]. *Journal of Applied Physics* vol. 25 676–677 (1954).

32. Green, M. *et al.* Solar cell efficiency tables (version 57). *Prog. Photovoltaics Res. Appl.* **29**, 3–15 (2021).

33. Stoppato, A. Life cycle assessment of photovoltaic electricity generation. *Energy* **33**, 224–232 (2008).

34. Kim, G. *et al.* Transparent Thin-Film Silicon Solar Cells for Indoor Light Harvesting with Conversion Efficiencies of 36% without Photodegradation. *ACS Appl. Mater. Interfaces* **12**, 27122–27130 (2020).

35. Muteri, V. *et al.* Review on Life Cycle Assessment of Solar Photovoltaic Panels. *Energies* 2020, Vol. 13, Page 252 **13**, 252 (2020).

36. Luceño-Sánchez, J. A., Díez-Pascual, A. M. & Capilla, R. P. Materials for

Photovoltaics: State of Art and Recent Developments. *Int. J. Mol. Sci.* 2019, Vol. 20, Page 976
20, 976 (2019).

37. Nakamura, M. *et al.* Cd-Free Cu(In,Ga)(Se,S)₂ thin-film solar cell with record efficiency of 23.35%. *IEEE J. Photovoltaics* **9**, 1863–1867 (2019).

38. National Renewable Energy Laboratory of the United States of America (NREL) National Center for Photovoltaics. Best Research-Cell Efficiencies chart. <https://www.nrel.gov/pv/assets/pdfs/best-research-cell-efficiencies.20200925.pdf>.

39. First Solar, Inc. - First Solar Achieves Yet Another Cell Conversion Efficiency World Record. <https://investor.firstsolar.com/news/press-release-details/2016/First-Solar-Achieves-Yet-Another-Cell-Conversion-Efficiency-World-Record/default.aspx>.

40. Ali, A. M. *et al.* A computational study on the energy bandgap engineering in performance enhancement of CdTe thin film solar cells. *Results Phys.* **7**, 1066–1072 (2017).

41. Geisz, J. F., Steiner, M. A., García, I., Kurtz, S. R. & Friedman, D. J. Enhanced external radiative efficiency for 20.8% efficient single-junction GaInP solar cells. *Appl. Phys. Lett.* **103**, 041118 (2013).

42. Kotulak, N. A. & Barner, K. E. Growth and analysis of gallium phosphide on silicon for very high efficiency solar cells. (2011).

43. Wang, W. *et al.* Device Characteristics of CZTSSe Thin-Film Solar Cells with 12.6% Efficiency. *Adv. Energy Mater.* **4**, 1301465 (2014).

44. Bag, S. *et al.* Low band gap liquid-processed CZTSe solar cell with 10.1% efficiency. *Energy Environ. Sci.* **5**, 7060–7065 (2012).

45. Kojima, A., Teshima, K., Shirai, Y. & Miyasaka, T. Organometal halide perovskites as visible-light sensitizers for photovoltaic cells. *J. Am. Chem. Soc.* **131**, 6050–6051 (2009).

46. Kim, M. *et al.* Conformal quantum dot–SnO₂ layers as electron transporters for efficient perovskite solar cells. *Science* (80-.). **375**, 302–306 (2022).

47. Liu, F. *et al.* Organic Solar Cells with 18% Efficiency Enabled by an Alloy Acceptor: A Two-in-One Strategy. *Adv. Mater.* **33**, (2021).
48. Hazen, R. M. Perovskites. *Sci. Am.* **258**, 74–80 (1988).
49. Miyasaka, T. Hybrid Perovskite Solar Cells. *Hybrid Perovskite Sol. Cells* (2021) doi:10.1002/9783527825851.
50. Schooley, J. F., Hosler, W. R. & Cohen, M. L. Superconductivity in Semiconducting SrTi₃. *Phys. Rev. Lett.* **12**, 474–475 (1964).
51. Pedersen, L. A. & Libby, W. F. Unseparated rare earth cobalt oxides as auto exhaust catalysts. *Science* (80-.). **176**, 1355–1356 (1972).
52. Kobayashi, K. I., Kimura, T., Sawada, H., Terakura, K. & Tokura, Y. Room-temperature magnetoresistance in an oxide material with an ordered double-perovskite structure. *Natur* **395**, 677–680 (1998).
53. Philipp, J. B. *et al.* Spin-dependent transport in the double-perovskite Sr₂CrWO₆. *Appl. Phys. Lett.* **79**, 3654 (2001).
54. Kojima, A., Teshima, K., Miyasaka, T. & Shirai, Y. Novel Photoelectrochemical Cell with Mesoscopic Electrodes Sensitized by Lead-halide Compounds (2).
55. Stranks, S. D. *et al.* The Physics of Light Emission in Halide Perovskite Devices. *Adv. Mater.* **31**, 1803336 (2019).
56. Hao, F. *et al.* Solvent-Mediated Crystallization of CH₃NH₃SnI₃ Films for Heterojunction Depleted Perovskite Solar Cells. *J. Am. Chem. Soc.* **137**, 11445–11452 (2015).
57. Sun, P. P., Li, Q. S., Yang, L. N. & Li, Z. S. Theoretical insights into a potential lead-free hybrid perovskite: substituting Pb²⁺ with Ge²⁺. *Nanoscale* **8**, 1503–1512 (2016).
58. Park, B.-W. *et al.* Bismuth Based Hybrid Perovskites A₃Bi₂I₉ (A: Methylammonium or Cesium) for Solar Cell Application. *Adv. Mater.* **27**, 6806–6813 (2015).
59. Saparov, B. *et al.* Thin-Film Preparation and Characterization of Cs₃Sb₂I₉: A Lead-

Free Layered Perovskite Semiconductor. *Chem. Mater.* **27**, 5622–5632 (2015).

60. Cortecchia, D. *et al.* Lead-Free MA₂CuCl_xBr_{4-x} Hybrid Perovskites. *Inorg. Chem.* **55**, 1044–1052 (2016).

61. Zhou, C. *et al.* Low dimensional metal halide perovskites and hybrids. *Mater. Sci. Eng. R Reports* **137**, 38–65 (2019).

62. Goldschmidt, V. M. Die Gesetze der Krystallochemie. *Naturwissenschaften* **14**, 477–485 (1926).

63. Kieslich, G., Sun, S. & Cheetham, A. K. Solid-state principles applied to organic–inorganic perovskites: New tricks for an old dog. *Chem. Sci.* **5**, 4712–4715 (2014).

64. Rudd, P. N. & Huang, J. Metal Ions in Halide Perovskite Materials and Devices. *Trends Chem.* **1**, 394–409 (2019).

65. Jono, R. & Segawa, H. Theoretical Study of the Band-gap Differences among Lead Triiodide Perovskite Materials: CsPbI₃. *Chem. Lett* **48**, 877–880 (2019).

66. Goetz, K. P., Taylor, A. D., Paulus, F. & Vaynzof, Y. Shining Light on the Photoluminescence Properties of Metal Halide Perovskites. *Adv. Funct. Mater.* **30**, (2020).

67. Li, C., Soh, K. C. K. & Wu, P. Formability of ABO₃ perovskites. *J. Alloys Compd.* **372**, 40–48 (2004).

68. Dolgos, M. *et al.* Chemical control of octahedral tilting and off-axis A cation displacement allows ferroelectric switching in a bismuth-based perovskite. *Chem. Sci.* **3**, 1426–1435 (2012).

69. Li, C. *et al.* Formability of ABX₃ (X = F, Cl, Br, I) halide perovskites. *Acta Crystallogr. B.* **64**, 702–707 (2008).

70. Filip, M. R. & Giustino, F. The geometric blueprint of perovskites. *PNAS* **115**, 5397–5402 (2018).

71. Umebayashi, T. *et al.* Electronic structures of lead iodide based low-dimensional

crystals. *Phys. Rev. B* **67**, 155405 (2003).

72. Walsh, A. Principles of Chemical Bonding and Band Gap Engineering in Hybrid Organic–Inorganic Halide Perovskites. *J. Phys. Chem. C* **119**, 5755–5760 (2015).

73. Zhao, B. *et al.* High Open-Circuit Voltages in Tin-Rich Low-Bandgap Perovskite-Based Planar Heterojunction Photovoltaics. *Adv. Mater.* **29**, 1604744 (2017).

74. Stoumpos, C. C. *et al.* Hybrid germanium iodide perovskite semiconductors: Active lone pairs, structural distortions, direct and indirect energy gaps, and strong nonlinear optical properties. *J. Am. Chem. Soc.* **137**, 6804–6819 (2015).

75. Abdelhady, A. L. *et al.* Heterovalent Dopant Incorporation for Bandgap and Type Engineering of Perovskite Crystals. *J. Phys. Chem. Lett.* **7**, 295–301 (2016).

76. Weller, M. T., Weber, O. J., Frost, J. M. & Walsh, A. Cubic Perovskite Structure of Black Formamidinium Lead Iodide, α -[HC(NH₂)₂]PbI₃, at 298 K. *J. Phys. Chem. Lett.* **6**, 3209–3212 (2015).

77. Lu, H. *et al.* Vapor-assisted deposition of highly efficient, stable black-phase FAPbI₃ perovskite solar cells. *Science* (80-.). **370**, (2020).

78. Kim, B., Kim, J. & Park, N. First-principles identification of the charge-shifting mechanism and ferroelectricity in hybrid halide perovskites. *Sci. Reports 2020 101* **10**, 1–7 (2020).

79. Breternitz, J., Tovar, M. & Schorr, S. Twinning in MAPbI₃ at room temperature uncovered through Laue neutron diffraction. *Sci. Rep.* **10**, 16613 (2020).

80. Bertolotti, F. *et al.* Coherent Nanotwins and Dynamic Disorder in Cesium Lead Halide Perovskite Nanocrystals. *ACS Nano* **11**, 3819–3831 (2017).

81. Murugadoss, G. *et al.* Crystal stabilization of α -FAPbI₃ perovskite by rapid annealing method in industrial scale. *J. Mater. Res. Technol.* **12**, 1924–1930 (2021).

82. Kim, J., Lee, S. H., Lee, J. H. & Hong, K. H. The role of intrinsic defects in

methylammonium lead iodide perovskite. *J. Phys. Chem. Lett.* **5**, 1312–1317 (2014).

83. Ball, J. M. & Petrozza, A. Defects in perovskite-halides and their effects in solar cells. *Nat. Energy* 2016 111 **1**, 1–13 (2016).

84. Yang, S. *et al.* Stabilizing halide perovskite surfaces for solar cell operation with wide-bandgap lead oxysalts. *Science* (80-.). **365**, 473–478 (2019).

85. Wang, F., Bai, S., Tress, W., Hagfeldt, A. & Gao, F. Defects engineering for high-performance perovskite solar cells. *npj Flex. Electron.* 2018 21 **2**, 1–14 (2018).

86. Lei, Y., Xu, Y., Wang, M., Zhu, G. & Jin, Z. Origin, Influence, and Countermeasures of Defects in Perovskite Solar Cells. *Small* **17**, (2021).

87. Liu, N. & Yam, C. Y. First-principles study of intrinsic defects in formamidinium lead triiodide perovskite solar cell absorbers. *Phys. Chem. Chem. Phys.* **20**, 6800–6804 (2018).

88. Bi, E., Song, Z., Li, C., Wu, Z. & Yan, Y. Mitigating ion migration in perovskite solar cells. *Trends Chem.* **3**, 575–588 (2021).

89. Liu, M., Johnston, M. B. & Snaith, H. J. Efficient planar heterojunction perovskite solar cells by vapour deposition. *Nature* **501**, 395–398 (2013).

90. Zhou, H. *et al.* Interface engineering of highly efficient perovskite solar cells. *Science* (80-.). **345**, 542–546 (2014).

91. Chen, Q. *et al.* Planar heterojunction perovskite solar cells via vapor-assisted solution process. *J. Am. Chem. Soc.* **136**, 622–625 (2014).

92. Green, M. A., Ho-Baillie, A. & Snaith, H. J. The emergence of perovskite solar cells. *Nature Photonics* vol. 8 506–514 (2014).

93. Zhao, Y. & Zhu, K. CH₃NH₃Cl-assisted one-step solution growth of CH₃NH₃PbI₃: Structure, charge-carrier dynamics, and photovoltaic properties of perovskite solar cells. *J. Phys. Chem. C* **118**, 9412–9418 (2014).

94. Saliba, M. *et al.* Cesium-containing triple cation perovskite solar cells: Improved

stability, reproducibility and high efficiency. *Energy Environ. Sci.* **9**, 1989–1997 (2016).

95. Saliba, M. *et al.* Incorporation of rubidium cations into perovskite solar cells improves photovoltaic performance. *Science* (80-.). **354**, 206–209 (2016).

96. Alharbi, E. A. *et al.* Perovskite Solar Cells Yielding Reproducible Photovoltage of 1.20 V. *Research* **2019**, 8474698 (2019).

97. Alharbi, E. A. *et al.* Atomic-level passivation mechanism of ammonium salts enabling highly efficient perovskite solar cells. *Nat. Commun.* **10**, 1–9 (2019).

98. Mahesh, S. *et al.* Revealing the origin of voltage loss in mixed-halide perovskite solar cells. *Energy Environ. Sci.* **13**, 258–267 (2020).

99. Kadro, J. M., Nonomura, K., Gachet, D., Grätzel, M. & Hagfeldt, A. Facile route to freestanding CH₃NH₃PbI₃ crystals using inverse solubility. *Sci. Rep.* **5**, 1–6 (2015).

100. Burschka, J. *et al.* Sequential deposition as a route to high-performance perovskite-sensitized solar cells. *Nature* **499**, 316–319 (2013).

101. Malinkiewicz, O. *et al.* Perovskite solar cells employing organic charge-transport layers. *Nat. Photonics* **8**, 128–132 (2014).

102. Ball, J. M., Lee, M. M., Hey, A. & Snaith, H. J. Low-temperature processed meso-superstructured to thin-film perovskite solar cells. *Energy Environ. Sci.* **6**, 1739–1743 (2013).

103. Kim, J. H., Williams, S. T., Cho, N., Chueh, C. C. & Jen, A. K. Y. Enhanced Environmental Stability of Planar Heterojunction Perovskite Solar Cells Based on Blade-Coating. *Adv. Energy Mater.* **5**, (2015).

104. Jeon, N. J. *et al.* Solvent engineering for high-performance inorganic-organic hybrid perovskite solar cells. *Nat. Mater.* **13**, 897–903 (2014).

105. Yang, W. S. *et al.* High-performance photovoltaic perovskite layers fabricated through intramolecular exchange. *Science* (80-.). **348**, 1234–1237 (2015).

106. Im, J. H., Jang, I. H., Pellet, N., Grätzel, M. & Park, N. G. Growth of CH₃ NH₃ PbI₃

cuboids with controlled size for high-efficiency perovskite solar cells. *Nat. Nanotechnol.* **9**, 927–932 (2014).

107. Seo, J. *et al.* Benefits of very thin PCBM and LiF layers for solution-processed p-i-n perovskite solar cells. *Energy Environ. Sci.* **7**, 2642–2646 (2014).

108. Kim, Y. Y. *et al.* Fast two-step deposition of perovskite via mediator extraction treatment for large-area, high-performance perovskite solar cells. *J. Mater. Chem. A* **6**, 12447–12454 (2018).

109. Eperon, G. E. *et al.* Formamidinium lead trihalide: A broadly tunable perovskite for efficient planar heterojunction solar cells. *Energy Environ. Sci.* **7**, 982–988 (2014).

110. Li, Z. *et al.* Stabilizing Perovskite Structures by Tuning Tolerance Factor: Formation of Formamidinium and Cesium Lead Iodide Solid-State Alloys. *Chem. Mater.* **28**, 284–292 (2016).

111. Jeon, N. J. *et al.* Compositional engineering of perovskite materials for high-performance solar cells. *Nature* **517**, 476–480 (2015).

112. Lee, J. W. *et al.* 2D perovskite stabilized phase-pure formamidinium perovskite solar cells. *Nat. Commun.* **9**, 1–10 (2018).

113. Yoo, H. S. & Park, N. G. Post-treatment of perovskite film with phenylalkylammonium iodide for hysteresis-less perovskite solar cells. *Sol. Energy Mater. Sol. Cells* **179**, 57–65 (2018).

114. Liu, G. *et al.* Efficient solar cells with enhanced humidity and heat stability based on benzylammonium-caesium-formamidinium mixed-dimensional perovskites. *J. Mater. Chem. A* **6**, 18067–18074 (2018).

115. Niu, T. *et al.* High performance ambient-air-stable FAPbI₃ perovskite solar cells with molecule-passivated Ruddlesden-Popper/3D heterostructured film. *Energy Environ. Sci.* **11**, 3358–3366 (2018).

116. Yi, C. *et al.* Entropic stabilization of mixed A-cation ABX₃ metal halide perovskites for high performance perovskite solar cells. *Energy Environ. Sci.* **9**, 656–662 (2016).
117. Stranks, S. D. & Snaith, H. J. Metal-halide perovskites for photovoltaic and light-emitting devices. *Nature Nanotechnology* vol. 10 391–402 (2015).
118. Liu, T. *et al.* Cesium Halides-Assisted Crystal Growth of Perovskite Films for Efficient Planar Heterojunction Solar Cells. *Chem. Mater.* **30**, 5264–5271 (2018).
119. Kim, M. *et al.* Methylammonium Chloride Induces Intermediate Phase Stabilization for Efficient Perovskite Solar Cells. *Joule* **3**, 2179–2192 (2019).
120. Duong, T. *et al.* Structural engineering using rubidium iodide as a dopant under excess lead iodide conditions for high efficiency and stable perovskites. *Nano Energy* **30**, 330–340 (2016).
121. Zhang, M. *et al.* High-Efficiency Rubidium-Incorporated Perovskite Solar Cells by Gas Quenching. *ACS Energy Letters* vol. 2 438–444 (2017).
122. Zhou, N. *et al.* CsI Pre-Intercalation in the Inorganic Framework for Efficient and Stable FA_{1-x}Cs_xPbI₃(Cl) Perovskite Solar Cells. *Small* **13**, (2017).
123. Zhou, W. *et al.* Thermal Conductivity: Thermal Conductivity of Amorphous Materials (Adv. Funct. Mater. 8/2020). *Adv. Funct. Mater.* **30**, 2070048 (2020).
124. Xu, Y. *et al.* The Effect of Humidity upon the Crystallization Process of Two-Step Spin-Coated Organic-Inorganic Perovskites. *ChemPhysChem* **17**, 112–118 (2016).
125. Pathak, S. *et al.* Atmospheric influence upon crystallization and electronic disorder and its impact on the photophysical properties of organic-inorganic perovskite solar cells. *ACS Nano* **9**, 2311–2320 (2015).
126. Ko, H. S., Lee, J. W. & Park, N. G. 15.76% efficiency perovskite solar cells prepared under high relative humidity: Importance of PbI₂ morphology in two-step deposition of CH₃NH₃PbI₃. *J. Mater. Chem. A* **3**, 8808–8815 (2015).

127. Yan, K. *et al.* Hybrid Halide Perovskite Solar Cell Precursors: Colloidal Chemistry and Coordination Engineering behind Device Processing for High Efficiency. *J. Am. Chem. Soc.* **137**, 4460–4468 (2015).
128. Zhao, Y. *et al.* Perovskite seeding growth of formamidinium-lead-iodide-based perovskites for efficient and stable solar cells. *Nat. Commun.* **9**, 1–10 (2018).
129. Jung, M. H., Rhim, S. H. & Moon, D. TiO₂/RbPbI₃ halide perovskite solar cells. *Sol. Energy Mater. Sol. Cells* **172**, 44–54 (2017).
130. Lim, D.-H., Ramasamy, P., Kwak, D.-H. & Lee, J.-S. Solution-phase synthesis of rubidium lead iodide orthorhombic perovskite nanowires. *Nanotechnology* **28**, 255601 (2017).
131. Zhang, T. *et al.* Bication lead iodide 2D perovskite component to stabilize inorganic a-CsPbI₃ perovskite phase for high-efficiency solar cells. *Sci. Adv.* **3**, e1700841 (2017).
132. Wang, Y. *et al.* Thermodynamically stabilized β -CsPbI₃-based perovskite solar cells with efficiencies >18%. *Science* **365**, 591–595 (2019).
133. Meng, H. *et al.* Chemical Composition and Phase Evolution in DMAI-Derived Inorganic Perovskite Solar Cells. *ACS Energy Lett.* **5**, 263–270 (2020).
134. Burwig, T., Fränzel, W. & Pistor, P. Crystal Phases and Thermal Stability of Co-evaporated CsPbX₃ (X = I, Br) Thin Films. *J. Phys. Chem. Lett.* **9**, 4808–4813 (2018).
135. Trots, D. M. & Myagkota, S. V. High-temperature structural evolution of caesium and rubidium triiodoplumbates. *J. Phys. Chem. Solids* **69**, 2520–2526 (2008).
136. Han, B. *et al.* Stable, Efficient Red Perovskite Light-Emitting Diodes by (α , δ)-CsPbI₃ Phase Engineering. *Adv. Funct. Mater.* **28**, 1804285 (2018).
137. Lim, D.-H., Ramasamy, P., Kwak, D.-H. & Lee, J.-S. Solution-phase synthesis of rubidium lead iodide orthorhombic perovskite nanowires. *Nanotechnology* **28**, 255601 (2017).
138. Mohammed, M. S., Salman, G. D. & Hassoon, K. I. Growth and Characterizes of PbI₂ Films By Vacuum Evaporation Method. *Al-Mustansiriyah J. Sci.* **30**, 60 (2019).

139. Xu, X. *et al.* Porous and Intercrossed PbI₂-CsI Nanorod Scaffold for Inverted Planar FA-Cs Mixed-Cation Perovskite Solar Cells. *ACS Appl. Mater. Interfaces* (2019) doi:10.1021/acsami.8b20933.
140. Yang, W. S. *et al.* Iodide management in formamidinium-lead-halide-based perovskite layers for efficient solar cells. *Science* (80-.). **356**, 1376–1379 (2017).
141. Jiang, Q. *et al.* Enhanced electron extraction using SnO₂ for high-efficiency planar-structure HC(NH₂)₂ PbI₃-based perovskite solar cells. *Nat. Energy* **2**, 1–7 (2017).
142. Kubicki, D. J. *et al.* Phase Segregation in Cs-, Rb- and K-Doped Mixed-Cation (MA)_x(FA)_{1-x}PbI₃ Hybrid Perovskites from Solid-State NMR. *J. Am. Chem. Soc.* **139**, 14173–14180 (2017).
143. Yadav, P. *et al.* The Role of Rubidium in Multiple-Cation-Based High-Efficiency Perovskite Solar Cells. *Adv. Mater.* **29**, 1701077 (2017).
144. Uchida, R. *et al.* Insights about the Absence of Rb Cation from the 3D Perovskite Lattice: Effect on the Structural, Morphological, and Photophysical Properties and Photovoltaic Performance. *Small* **14**, 1802033 (2018).
145. Lee, J. W. *et al.* Formamidinium and cesium hybridization for photo- and moisture-stable perovskite solar cell. *Adv. Energy Mater.* **5**, (2015).
146. Xia, X. *et al.* Spray reaction prepared FA_{1-x}Cs_xPbI₃ solid solution as a light harvester for perovskite solar cells with improved humidity stability. *RSC Adv.* **6**, 14792–14798 (2016).
147. Kirchartz, T., Márquez, J. A., Stolterfoht, M. & Unold, T. Photoluminescence-Based Characterization of Halide Perovskites for Photovoltaics. *Adv. Energy Mater.* **10**, 1904134 (2020).
148. Abdi-Jalebi, M. *et al.* Potassium-and rubidium-passivated alloyed perovskite films: Optoelectronic properties and moisture stability. *ACS Energy Lett.* **3**, 2671–2678 (2018).
149. Jong, U.-G. *et al.* First-principles study on the chemical decomposition of inorganic

perovskites CsPbI₃ and RbPbI₃ at finite temperature and pressure. (2018).

150. Philippe, B. *et al.* Chemical Distribution of Multiple Cation (Rb⁺, Cs⁺, MA⁺, and FA⁺) Perovskite Materials by Photoelectron Spectroscopy. *Chem. Mater.* **29**, 3589–3596 (2017).

151. Jiang, Q. *et al.* Enhanced electron extraction using SnO₂ for high-efficiency planar-structure HC(NH₂)₂ PbI₃-based perovskite solar cells. *Nat. Energy* **2**, 1–7 (2017).

152. Yang, W. S. *et al.* High-performance photovoltaic perovskite layers fabricated through intramolecular exchange. *Science* (80-.). **348**, 1234–1237 (2015).

153. Domanski, K., Alharbi, E. A., Hagfeldt, A., Grätzel, M. & Tress, W. Systematic investigation of the impact of operation conditions on the degradation behaviour of perovskite solar cells. *Nat. Energy* **3**, 61–67 (2018).

154. Tress, W. *et al.* Performance of perovskite solar cells under simulated temperature-illumination real-world operating conditions. *Nat. Energy* **4**, 568–574 (2019).

155. Grätzel, M. The light and shade of perovskite solar cells. *Nature Materials* vol. 13 838–842 (2014).

156. Park, N. G., Grätzel, M., Miyasaka, T., Zhu, K. & Emery, K. Towards stable and commercially available perovskite solar cells. *Nature Energy* vol. 1 1–8 (2016).

157. Correa-Baena, J. P. *et al.* Promises and challenges of perovskite solar cells. *Science* vol. 358 739–744 (2017).

158. Sorialtin, H., Geyer, R. & Zafer, C. Life cycle assessment of hole transport free planar-mesoscopic perovskite solar cells. *J. Renew. Sustain. Energy* **12**, 23502 (2020).

159. Han, Q. *et al.* Single Crystal Formamidinium Lead Iodide (FAPbI₃): Insight into the Structural, Optical, and Electrical Properties. *Adv. Mater.* **28**, 2253–2258 (2016).

160. Amat, A. *et al.* Cation-induced band-gap tuning in organohalide perovskites: Interplay of spin-orbit coupling and octahedra tilting. *Nano Lett.* **14**, 3608–3616 (2014).

161. Smecca, E. *et al.* Stability of solution-processed MAPbI₃ and FAPbI₃ layers. *Phys.*

Chem. Chem. Phys. **18**, 13413–13422 (2016).

162. Stoddard, R. J. *et al.* Enhancing Defect Tolerance and Phase Stability of High-Bandgap Perovskites via Guanidinium Alloying. *ACS Energy Lett.* **3**, 1261–1268 (2018).

163. Park, N. G. & Zhu, K. Scalable fabrication and coating methods for perovskite solar cells and solar modules. *Nature Reviews Materials* vol. 5 333–350 (2020).

164. Turren-Cruz, S. H., Hagfeldt, A. & Saliba, M. Methylammonium-free, high-performance, and stable perovskite solar cells on a planar architecture. *Science* (80-.). **362**, 449–453 (2018).

165. Tavakoli, M. M. *et al.* Controllable Perovskite Crystallization via Antisolvent Technique Using Chloride Additives for Highly Efficient Planar Perovskite Solar Cells. *Adv. Energy Mater.* **9**, (2019).

166. Shi, L. *et al.* Gas chromatography-mass spectrometry analyses of encapsulated stable perovskite solar cells. *Science* (80-.). **368**, (2020).

167. Yun, Y. *et al.* A Nontoxic Bifunctional (Anti)Solvent as Digestive-Ripening Agent for High-Performance Perovskite Solar Cells. *Adv. Mater.* **32**, (2020).

168. Jeong, J. *et al.* Pseudo-halide anion engineering for α -FAPbI₃ perovskite solar cells. *Nature* **592**, 381 (2021).

169. Merten, L. *et al.* Quantifying Stabilized Phase Purity in Formamidinium-Based Multiple-Cation Hybrid Perovskites. *Chem. Mater.* acs.chemmater.0c04185 (2021) doi:10.1021/acs.chemmater.0c04185.

170. Zheng, X. *et al.* Defect passivation in hybrid perovskite solar cells using quaternary ammonium halide anions and cations. *Nat. Energy* 2017 27 **2**, 1–9 (2017).

171. Koh, T. M. *et al.* Formamidinium-containing metal-halide: An alternative material for near-IR absorption perovskite solar cells. *J. Phys. Chem. C* **118**, 16458–16462 (2014).

172. Pellet, N. *et al.* Mixed-Organic-Cation Perovskite Photovoltaics for Enhanced Solar-

Light Harvesting. *Angew. Chemie* **126**, 3215–3221 (2014).

173. Shahiduzzaman, M. *et al.* Ionic liquid-assisted growth of methylammonium lead iodide spherical nanoparticles by a simple spin-coating method and photovoltaic properties of perovskite solar cells. *RSC Adv.* **5**, 77495–77500 (2015).

174. Salado, M. *et al.* Extending the lifetime of perovskite solar cells using a perfluorinated dopant. *Wiley Online Libr.* **9**, 2708–2714 (2016).

175. Shahiduzzaman, M. *et al.* Viscosity effect of ionic liquid-assisted controlled growth of CH₃NH₃PbI₃ nanoparticle-based planar perovskite solar cells. *Org. Electron.* **48**, 147–153 (2017).

176. Baumeler, T. *et al.* Minimizing the Trade-Off between Photocurrent and Photovoltage in Triple-Cation Mixed-Halide Perovskite Solar Cells. *J. Phys. Chem. Lett.* **11**, 10188–10195 (2020).

177. Alharbi, E. A. *et al.* Formation of High-Performance Multi-Cation Halide Perovskites Photovoltaics by δ -CsPbI₃/ δ -RbPbI₃ Seed-Assisted Heterogeneous Nucleation. *Adv. Energy Mater.* 2003785 (2021) doi:10.1002/aenm.202003785.

178. Alharbi, E. A. *et al.* Methylammonium Triiodide for Defect Engineering of High-Efficiency Perovskite Solar Cells. *ACS Energy Lett.* **6**, 3650–3660 (2021).

179. Zheng, X. *et al.* Defect passivation in hybrid perovskite solar cells using quaternary ammonium halide anions and cations. *Nat. Energy* **2**, (2017).

180. Jiang, Q. *et al.* Surface passivation of perovskite film for efficient solar cells. *Nat. Photonics* **13**, 460–466 (2019).

181. Santhosh, N. *et al.* Fabrication of hole-transport-free perovskite solar cells using 5-ammonium valeric acid iodide as additive and carbon as counter electrode. *Mater. Lett.* **236**, 706–709 (2019).

182. Duong, T. *et al.* Rubidium Multication Perovskite with Optimized Bandgap for

Perovskite-Silicon Tandem with over 26% Efficiency. *Adv. Energy Mater.* **7**, 1700228 (2017).

183. Lee, M. M., Teuscher, J., Miyasaka, T., Murakami, T. N. & Snaith, H. J. Efficient hybrid solar cells based on meso-superstructured organometal halide perovskites. *Science* (80-.). **338**, 643–647 (2012).

184. Lin, Y. *et al.* π -Conjugated Lewis Base: Efficient Trap-Passivation and Charge-Extraction for Hybrid Perovskite Solar Cells. *Adv. Mater.* **29**, 1604545 (2017).

185. Niu, T. *et al.* Stable High-Performance Perovskite Solar Cells via Grain Boundary Passivation. *Adv. Mater.* **30**, 1706576 (2018).

186. Noel, N. K. *et al.* Enhanced Photoluminescence and Solar Cell Performance via Lewis Base Passivation of Organic-Inorganic Lead Halide Perovskites. **08**, 27 (2021).

187. Qin, P.-L. *et al.* Stable and Efficient Organo-Metal Halide Hybrid Perovskite Solar Cells via π -Conjugated Lewis Base Polymer Induced Trap Passivation and Charge Extraction. *Adv. Mater.* **30**, 1706126 (2018).

188. Wang, S. *et al.* High-Performance Perovskite Solar Cells with Large Grain-Size obtained by using the Lewis Acid-Base Adduct of Thiourea. *Sol. RRL* **2**, 1800034 (2018).

189. Wang, Y. *et al.* Stabilizing heterostructures of soft perovskite semiconductors. *Science* (80-.). **365**, 687–691 (2019).

190. Wang, S. *et al.* Lewis acid/base approach for efficacious defect passivation in perovskite solar cells. *J. Mater. Chem. A* **8**, 12201–12225 (2020).

191. Kim, M., Motti, S. G., Sorrentino, R. & Petrozza, A. Enhanced solar cell stability by hygroscopic polymer passivation of metal halide perovskite thin film. *Energy Environ. Sci.* **11**, 2609–2619 (2018).

192. Liu, Y. *et al.* Ultrahydrophobic 3D/2D fluoroarene bilayer-based water-resistant perovskite solar cells with efficiencies exceeding 22%. *Sci. Adv.* **5**, eaaw2543 (2019).

193. Wu, W. Q. *et al.* Bilateral alkylamine for suppressing charge recombination and

improving stability in blade-coated perovskite solar cells. *Sci. Adv.* **5**, (2019).

194. Zhao, Y. *et al.* Correlations between Immobilizing Ions and Suppressing Hysteresis in Perovskite Solar Cells. *ACS Energy Lett.* **1**, 266–272 (2016).

195. Wang, R. *et al.* Caffeine Improves the Performance and Thermal Stability of Perovskite Solar Cells. *Joule* **3**, 1464–1477 (2019).

196. Zhang, S. *et al.* Solvent engineering for efficient inverted perovskite solar cells based on inorganic CsPbI₂Br light absorber. *Mater. Today Energy* **8**, 125–133 (2018).

197. Zheng, X. *et al.* Dual functions of crystallization control and defect passivation enabled by sulfonic zwitterions for stable and efficient perovskite solar cells. *Wiley Online Libr.* **30**, 1803428 (2018).

198. Zuo, C., Vak, D., Angmo, D., Ding, L. & Gao, M. One-step roll-to-roll air processed high efficiency perovskite solar cells. *Nano Energy* **46**, 185–192 (2018).

199. Yang, M. *et al.* Facile fabrication of large-grain CH₃NH₃PbI₃–xBr_x films for high-efficiency solar cells via CH₃NH₃Br-selective Ostwald ripening. *Nat. Commun.* **7**, 12305 (2016).

200. Son, D.-Y. *et al.* Self-formed grain boundary healing layer for highly efficient CH₃NH₃PbI₃ perovskite solar cells. *Nat. Energy* **1**, 16081 (2016).

201. Xin, C. *et al.* Defects Healing in Two-Step Deposited Perovskite Solar Cells via Formamidinium Iodide Compensation. *ACS Appl. Energy Mater.* **3**, 3318–3327 (2020).

202. Luo, D., Su, R., Zhang, W., Gong, Q. & Zhu, R. Minimizing non-radiative recombination losses in perovskite solar cells. *Nat. Rev. Mater.* **2019 51** **5**, 44–60 (2019).

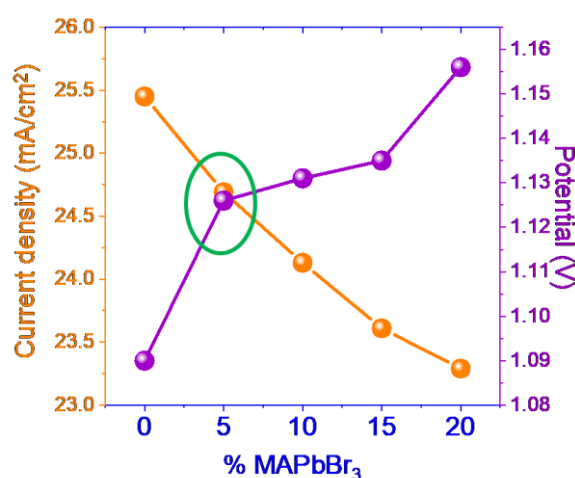
203. De Mello, J. C., Wittmann, H. F. & Friend, R. H. An improved experimental determination of external photoluminescence quantum efficiency. *Adv. Mater.* **9**, 230–232 (1997).

204. Paraecattil, A. A., De Jonghe-Risse, J., Pranculis, V., Teuscher, J. & Moser, J. E.

Dynamics of Photocarrier Separation in MAPbI₃ Perovskite Multigrain Films under a Quasistatic Electric Field. *J. Phys. Chem. C* **120**, 19595–19602 (2016).

Chapter 2 Minimizing the Trade-Off between Photocurrent and Photovoltage in Triple-Cation Mixed-Halide Perovskite Solar Cells

*This work has been published: T. Baumeler, N. Arora, A. Hinderhofer, S. Akin, A. Greco, M. Abdi-Jalebi, R. Shivanna, R. Uchida, Y. Liu, F. Schreiber, S. M. Zakeeruddin, R. H. Friend, M. Grätzel, M. I. Dar, *J. Phys. Chem. Lett.* **2020**, 11, 23, 10188-10195*



Introduction

Hybrid perovskite materials exhibit the ABX_3 structure, where A generally stands for a monovalent cation such as methylammonium $(MA)=CH_3NH_3^+$, cesium (Cs^+) or formamidinium $(FA)=CH_3(NH_2)_2^+$, B for a divalent metal cation (Pb^{2+}, Sn^{2+}) and X for a monovalent halide anion (I^-, Br^-, Cl^-) .¹⁻³ These perovskite semiconductors exhibit outstanding optoelectronic properties, including a high absorption coefficient over a wide range of the solar spectral irradiance, a direct bandgap, low exciton binding energy, large charge-carrier diffusion lengths and ambipolarity.⁴⁻⁸

Initially, Kojima *et al.* demonstrated $MAPbBr_3$ and $MAPbI_3$ perovskite materials for photovoltaic applications.¹ With the substitution of bromide by iodide, the bandgap decreases

and the spectral sensitivity towards longer wavelengths (up to 800 nm) increases, leading to the amplification of short-circuit photocurrent (J_{sc}) but reducing the open-circuit photovoltage (V_{oc}).⁹ This tunability feature of perovskite materials was further extended to the A-site cation by Koh *et al.* who demonstrated FAPbI₃ perovskite as a potential light absorber with a bandgap of 1.47 eV.¹⁰ Although a low bandgap makes FAPbI₃ a more desired light absorber, the thermodynamic instability of the photoactive trigonal phase of FAPbI₃ (α -FAPbI₃) under ambient conditions poses a serious challenge to materials scientists and the photovoltaics community. To address this issue, different strategies have been envisaged by the scientific community. For example, methylammonium chloride-induced stabilization of α -FAPbI₃ phase,¹¹ and surface coating via a molecularly tailored two-dimensional (2D) overlayer rendering the back conversion of α -FAPbI₃ to δ -FAPbI₃ less favorable has been reported recently.¹²

At the beginning, Pellet *et al.* stabilized the photoactive phase by mixing MA and FA cations to form multi-cation MA_xFA_{1-x}PbI₃ perovskites.¹³ In a similar direction, Jeon *et al.* reasoned that the incorporation of MAPbBr₃ into FAPbI₃ stabilizes the perovskite phase of latter and simultaneously improves the power conversion efficiency (PCE) of the perovskite solar cells (PSCs).¹⁴ Subsequently, the compositional engineering of perovskite materials attracted tremendous attention to develop highly efficient and stable PSCs.¹⁵⁻²⁴

By introducing Cs⁺ cation into (FAMA)PbX₃ perovskite structures, further improvement in the thermal stability and reduction in phase impurities was shown.^{25,26} The resulting state-of-the-art triple-cation perovskite composition contains >15% of MAPbBr₃ in an FA-dominant lattice exhibiting a bandgap of 1.63 eV, which is larger than that of pure MAPbI₃.¹⁴ Therefore, optimization of MAPbBr₃ content within the FAPbI₃ perovskite structure is critical, primarily, to minimize the trade-off between the photocurrent and photovoltage which can consequently enhance the PCE of resulting PSCs. Arguably, this will lead to the fabrication of more efficient

devices, which will pave the way towards stable and reproducible devices, a key factor towards the industrialization of PSCs.¹¹

Herein, we aimed to minimize the MAPbBr₃ content in order to ensure high PCE while still benefiting from the stability features of MAPbBr₃. We probed the PCE and stability of PSCs in order to find out the composition, which demonstrates the best compromise between the stabilization features and the loss of photocurrent associated with MAPbBr₃, while simultaneously improving the overall photovoltaic performance of FA-dominant PSCs.

Results and Discussion

We deposited CsI_{0.05}(FA_{1-y}MA_y)_{0.95}Pb(I_{1-y}Br_y)₃ (y=0, 0.05, 0.10, 0.15, 0.20) (denoted as P + y% MAPbBr₃) perovskite films using one-step solution-based anti-solvent method. See the experimental methods for further details.

To investigate the composition of perovskite films and to establish the effectiveness of the experimental methodology, we explored X-ray photoelectron spectroscopy (XPS). As shown in Figure S1 and Table S1, Pb and Cs experimental concentrations are relatively stable across the series while the iodide and bromide concentrations follow the expected trend. The relative contents of halides determined from the XPS data correlate with the values calculated for each condition (Table S1), which confirms the effective introduction of the desired amounts of MAPbBr₃ into the CsI containing FAPbI₃ perovskite lattice system. In addition, the peaks attributed to lead (Pb 4f_{5/2} and Pb 4f_{7/2}), iodide (I 3d_{3/2} and I 3d_{5/2}) and bromide (Br 3d_{3/2} and Br 3d_{5/2}) display a shift, which could be associated with the binding energy as a function of composition.²⁷⁻²⁹

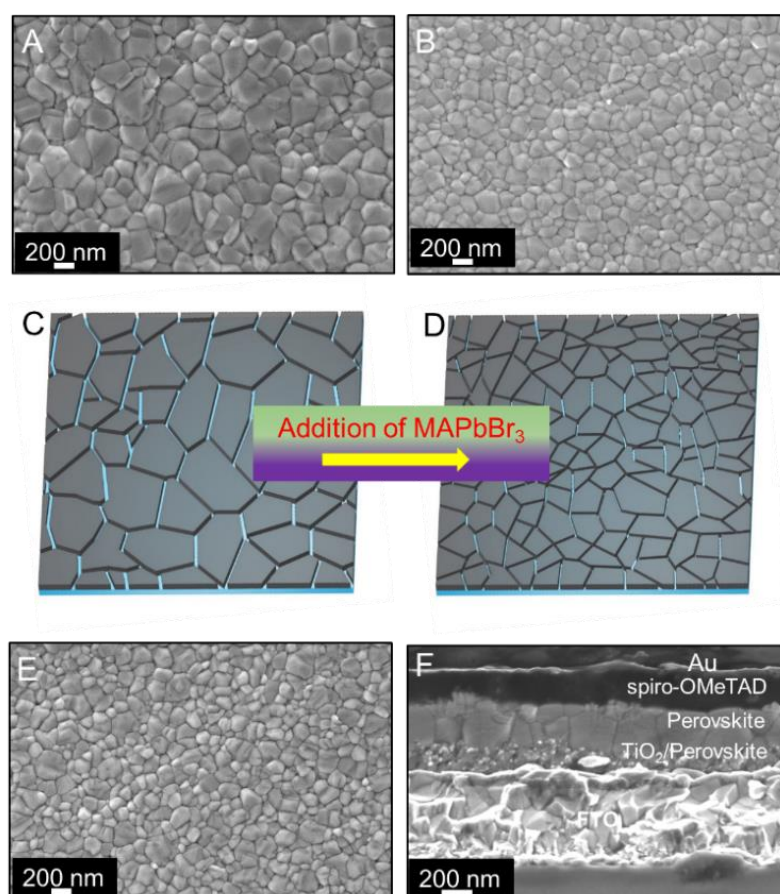


Figure 1. Morphological analysis of perovskite films and fully assembled perovskite solar cell: Top-view SEM micrograph of (A) P + 0% MAPbBr₃; (B) P + 5% MAPbBr₃; (C) and (D) Schematic illustration showing the reduction in grain size upon introduction of MAPbBr₃; ; (E) Top-view SEM micrograph of P + 20% MAPbBr₃ and (F) cross-sectional SEM micrograph of P + 5% MAPbBr₃ based device.

The effect of perovskite composition on the morphology and thickness of the film was investigated through field-emission scanning electron microscopy (FE-SEM) (Figure 2, Figure S2-S4). Top view SEM micrographs reveal that MAPbBr₃-free perovskite film (Figure 1A) is composed of sub-micron sized structures, while with the introduction of 5% MAPbBr₃, the grain size decreases dramatically to ~200-300 nm (Figure 1B) and remains invariant of MAPbBr₃ concentration (Figure. 1E). Such growth behavior can be explained by invoking an increase in the nucleation density induced by MAPbBr₃ (Figure 1C-D). Cross-sectional SEM reveals that the composition insignificantly influences the perovskite film thickness as all the MAPbBr₃ containing perovskite film exhibit a thickness of approximately 500 nm (Figure 1F).

To gain deeper insight into the growth and formation of the perovskite structures, we recorded grazing-incidence x-ray scans³⁰ of the perovskite film samples containing different mixtures of MAPbBr₃ and FAPbI₃. In addition to peaks corresponding to the perovskite phase, we also observed the features that can be attributed to the hexagonal (yellow) FAPbI₃ phase and lead iodide as well as insignificant traces of other phases (Figure 2A). By fitting the perovskite peaks with a Gaussian, we determined the peak position as well as the width of each peak (Figure 2B). Assuming a cubic perovskite structure, an average lattice parameter was determined. Figure 2C shows that the average lattice parameter depends linearly on the amount of added MAPbBr₃, which is an intuitive result since MA⁺ and Br⁻ are both smaller than FA⁺ and I⁻, respectively.³¹ The linear dependence is also in agreement with Vegard's law. From the peak-width, we determine that the size of coherently scattering domains is on average at least ~55 nm for all films, which means that the defect density in the crystal lattice is relatively low and not strongly reduced upon mixing.³²

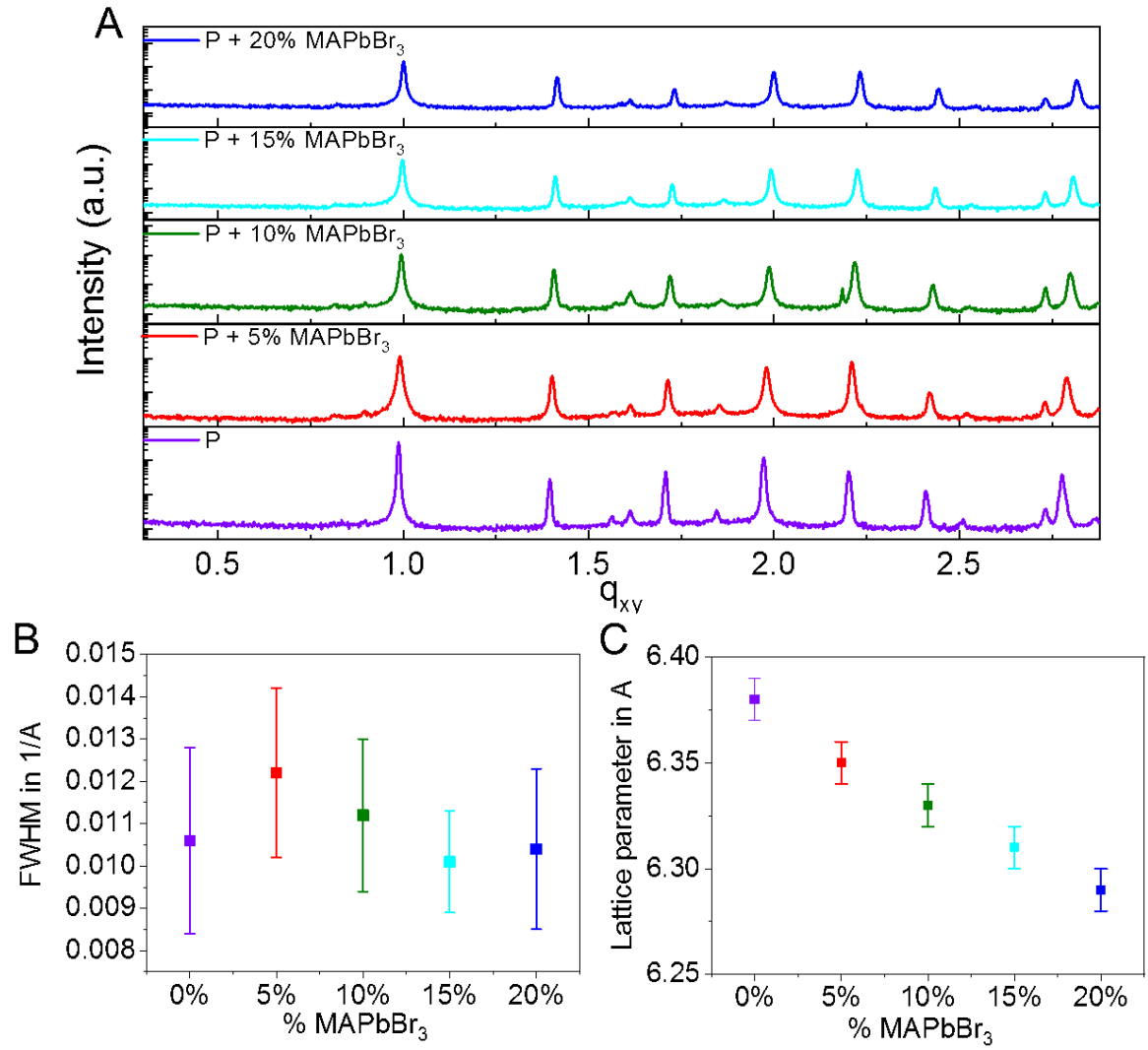


Figure 2. (A) Grazing-incidence X-ray diffraction patterns of the perovskite for different percentages of MAPbBr₃; (B) Average full width at half maximum (FWHM) of the fitted perovskite peaks for different percentages of MAPbBr₃. The FWHM correlates with the size of the coherently scattering domains, which is not strongly affected by the amount of added MAPbBr₃; (C) Average cubic lattice parameter of the fitted perovskite for different MAPbBr₃ percentages.

We performed grazing-incidence X-ray diffraction at different angles of incidence using an area detector. Figure 3A-C and Figure S5 show examples of the obtained reciprocal space maps (RSMs) for different perovskite films at an angle of incidence of 0.06° . By analyzing the azimuthal intensity distribution of the Debye-Scherrer rings, we observed that for different amounts of added MAPbBr₃, the preferred orientation of the perovskite crystallites differs with respect to the substrate plane. Figure 3D shows that for MAPbBr₃-free perovskite films, the

angular distribution of the first Debye-Scherrer ring shows only one maximum at 45° . We analyzed the relative angles between the maxima of different diffraction rings and determined that the preferred orientation parallel to the substrate plane is $\langle 111 \rangle$ (Figure 3E). Thus, we attribute the maximum in Figure 3A to the (100) plane.

With the addition of 5% MAPbBr₃, we observe that the angular intensity distribution of the first ring changes from a single maximum to two different maxima at 54° and 23° (Figure 3D, red trace). We determined that the preferred orientation parallel to the substrate is $\langle 211 \rangle$ and thus, we attribute the two maxima on the first ring to the (100) and (010)/(001) planes, respectively (Figure 3F). For the 10% MAPbBr₃ sample, this distribution becomes even narrower, but for amounts higher than 10%, we observe an almost homogeneous distribution, indicating that there is no preferred orientation of the perovskite crystallites. We further determined the relative amount of impurities in the samples, in particular, the photoinactive hexagonal phase and lead iodide, at different angles of incidence.

Figure 3G shows the integrated peak intensity of the PbI₂ (001) ring and the (100) ring of the hexagonal phase for different amounts of MAPbBr₃ at angles of incidence of 0.06° and 0.14° normalized to the perovskite (100) intensity. We observe that overall, an increase of the MAPbBr₃ content leads to an increase of the amounts of the hexagonal phase as well as PbI₂ in the bulk except for a MAPbBr₃ content of 5%. However, near to the surface, we observe for a MAPbBr₃ content of 5% a strong reduction of the impurities to less than half compared to pure FAPbI₃.

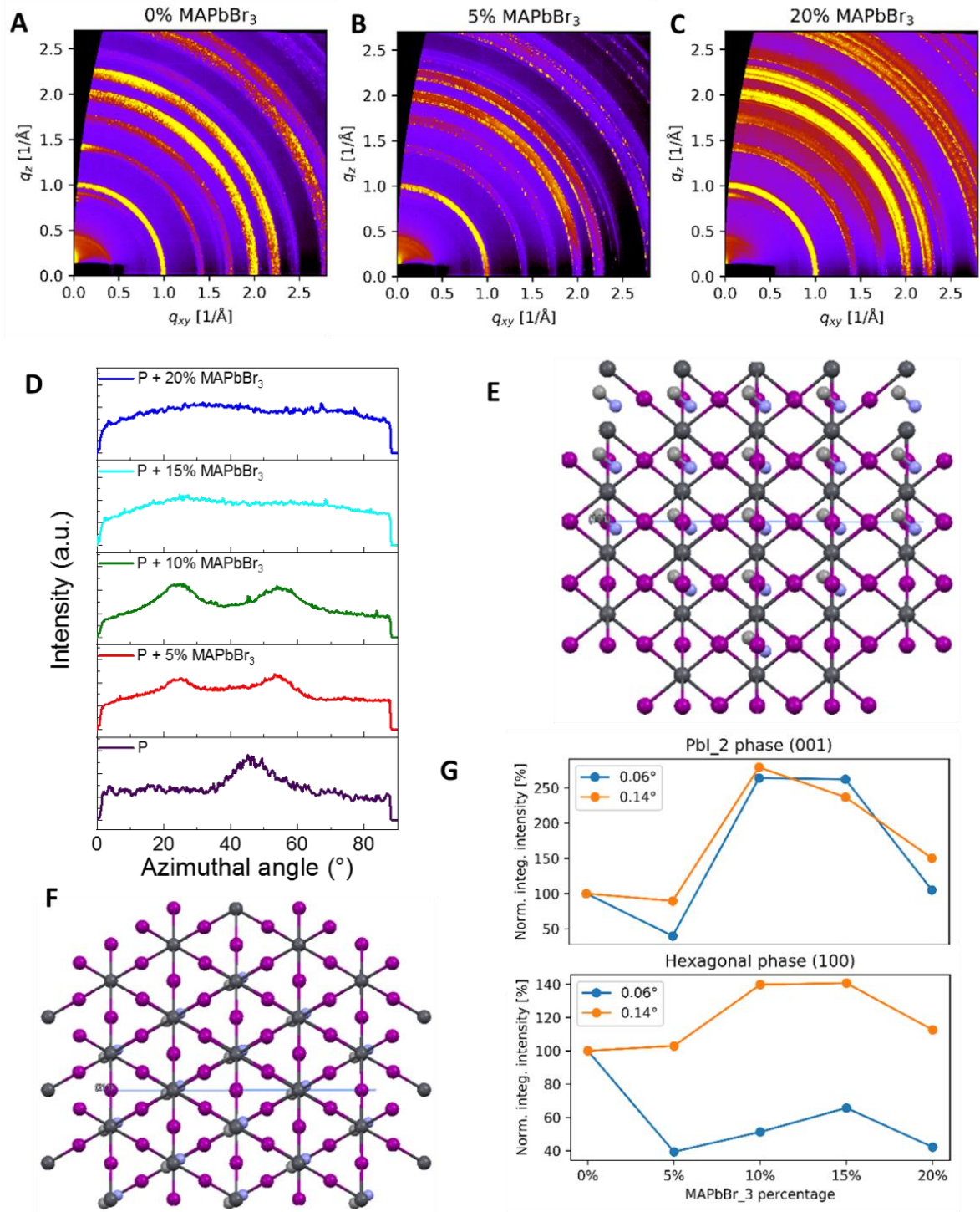


Figure 3. Reciprocal space maps obtained from GIWAXS of perovskite films with different amounts of MAPbBr₃ at an angle of incidence of 0.06° (A) P + 0% MAPbBr₃; (B) P + 5% MAPbBr₃; (C) P + 20% MAPbBr₃; (D) Radially integrated intensity plots along the ring at $q_z \approx 2 \text{ Å}^{-1}$ for the different perovskite compositions derived from the corresponding 2D-GIWAXS patterns.; (E) sketch of <111> unit cell orientation for P - alternating layers of lead cations (grey) and I⁻ anions (purple); (F) sketch of <211> unit cell orientation for P + 5% MAPbBr₃ and higher – alternating mixed layers, P = Cs_{0.05}(FA_{1-y}MA_y)_{0.95}Pb(I_{1-y}Br_y)₃. (G) The integrated intensity of the (001) and (100) Debye-Scherrer ring of PbI₂ and the hexagonal phase normalized to the perovskite (100) intensity for different percentages of MAPbBr₃ at an angle of incidence of 0.06° and 0.14°. The intensity is given relative to 0% MAPbBr₃.

Therefore, we infer that by adding 5% of MAPbBr₃ to FAPbI₃, the number of phase impurities at the surface can be reduced, which might have an impact on the performance of the perovskite as an absorber material.³³ Furthermore, introducing more than 5% MAPbBr₃ seems to strongly increase the amount of PbI₂ in the sample both in the bulk and near to the top surface, which might also be detrimental to the photovoltaic performance.

The influence of MAPbBr₃ incorporation on the optoelectronic properties of mixed-halide perovskite films was investigated using PDS, a highly sensitive optical absorption measurement. With the introduction of MAPbBr₃ into FAPbI₃ perovskite lattice, the bandgap energy shifted towards higher energies (Figure 4A), which can be explained by considering the substitution of larger ions including FA⁺ and I⁻ with smaller ions like MA⁺ and Br⁻. From the PDS spectrum, we measure an Urbach energy of 15.4 meV for the FA_{0.95}Cs_{0.05}PbI₃ film (Figure 4B). The Urbach energy arises through defects and structural disorder in the crystalline structure, and thermal fluctuation of constituent atoms or ions.^{34,35} By introducing MAPbBr₃ into the CsI-containing FAPbI₃ lattice, the Urbach energy decreases systematically to 13 meV and 11 meV, respectively, for 10% and 20% compositions (Figure 4B), clearly establishing lower energetic disorder associated with the MAPbBr₃ containing films. Figure 4C shows the normalized transient absorption spectra at 1 ns acquired after exciting the perovskite films with 500 nm pump pulse. The spectra consist of ground-state bleach ($\Delta T/T > 0$) centred around band edge and refractive index change ($\Delta T/T < 0$) above the bandgap. Increasing MAPbBr₃ content monotonically increases the bandgap as evident from the blueshift of the ground state bleach (GSB), consistent with the PDS data. The normalized decay dynamics (Figure S7) reveals that mixed-halide perovskite films exhibit slow GSB decay as compared to MAPbBr₃-free films. By adding 5% of MAPbBr₃ into the FA-dominant lattice, the charge-carrier lifetime increases remarkably exponentially from 10 ns to 100 ns. Interestingly, we do not observe any shift in the GSB with the delay in time, establishing that the films are phase pure, and ruling out any

phase segregation. The time-resolved photoluminescence (Figure S8) and the full transient absorption contour maps (Figure S9) recorded for each perovskite film further confirm the presence of long-lived charge carriers in MAPbBr₃ containing perovskite films.³⁶ The relatively poor optoelectronic quality of bromide-free perovskite films could be due to the low-structural stability of the FA-dominant phase, which eventually renders them more prone to the formation of defects and energetic disorder.³⁷

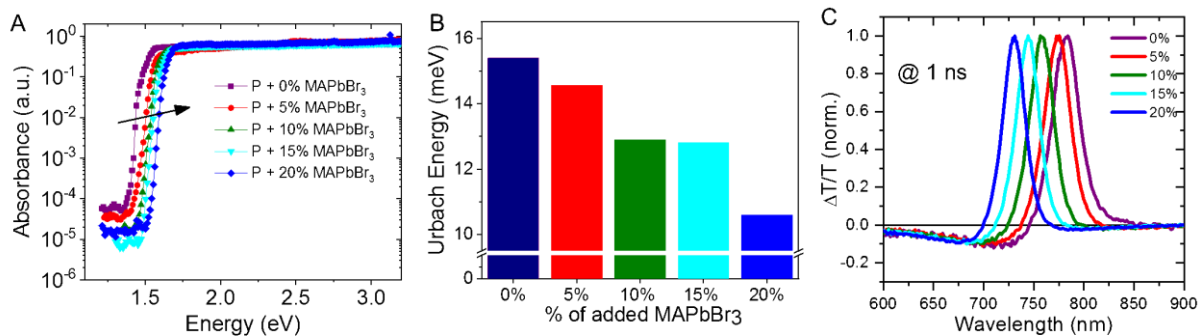


Figure 4. (A) Photothermal deflection absorption spectra of the perovskite with different amounts of MAPbBr₃; (B) histograms of the Urbach Energy measured on the different perovskite films and (C) transient absorption spectrum at 1 ns representing different ground state bleach corresponding to a band edge of the perovskites.

The introduction of MAPbBr₃ into the FAPbI₃ perovskite system should raise the bandgap and thus decrease the J_{SC} and/or increase the V_{OC} . As the PCE of a photovoltaic cell depends on both parameters, therefore, the best trade-off between high J_{SC} (low MAPbBr₃ content) and high V_{OC} (high MAPbBr₃ content) needs to be determined for different perovskite compositions. We investigated the photovoltaic performance of PSCs based on CsI_{0.05}(FA_{1-y}MA_y)_{0.95}Pb(I_{1-y}Br_y)₃ films using conventional n-i-p device architecture with a mesoporous TiO₂ layer as an electron transporting material (ETM) and spiro-OMeTAD as a hole transporting material (HTM). The J - V plots corresponding to the most efficient devices for each composition are displayed in Figure 5A and the corresponding extracted PV parameters are summarized in Table 1. The bromide-free PSC yielded a J_{SC} of 25.4 mA cm⁻², a V_{OC} of 1.090 V and a fill factor (FF) of 0.73, resulting in a PCE of 20.4%. However, the perovskite

composition containing 5% MAPbBr₃ exhibits better photovoltaic performances with a PCE of 21.6% ($J_{SC} = 24.7 \text{ mA cm}^{-2}$, $V_{OC} = 1.126 \text{ V}$, and FF of 0.77), indicating this composition to be the best compromise between high photocurrent and high photovoltage among all the compositions. By increasing the MAPbBr₃ content to 10%, the PCE drops to 21.2% and PSCs containing 15% MAPbBr₃ yielded a PCE = 20.9% closely followed by the 20% MAPbBr₃ perovskite composition which showed a PCE = 20.8%. Relatively low photovoltage displayed by bromide-free PSC could be due to the less structural stability of MAPbBr₃-free FAPbI₃ phase, which apparently leaves the film more susceptible to defects and trap states.^{38,39} We further determined the stabilized (scan-speed independent) PCEs of these devices by probing at their maximum power point (MPP) under full-sun illumination for 60 seconds (Figure 5B), and the results are shown in Table 1. Remarkably, the stabilized PCEs measured with MPP-tracking are in excellent agreement to the values obtained via J - V measurements, suggesting low hysteretic behaviour,⁴⁰ which is further supported by the J - V hysteresis measurements (Figure S10). From all these results, it is particularly interesting to note that the stabilized PCE values of the 5% MAPbBr₃ composition not only surpasses the performance of other PSCs but is also higher than that of state-of-the-art triple-cation PSCs (Figure S11).

MAPbBr ₃ conc. (%)	J_{SC} (mA cm ⁻²)	V_{OC} (V)	FF	PCE (%)	Stabilized PCE (%)	IPCE Onset (nm)	Bandgap (eV)
0	25.45	1.090	0.727	20.4	20.1	843	1.487
5	24.69	1.126	0.768	21.6	21.4	829	1.503
10	24.13	1.131	0.768	21.2	21.0	811	1.537
15	23.61	1.135	0.777	20.9	20.7	803	1.546
20	23.29	1.156	0.765	20.8	20.6	795	1.572

Table 2. Photovoltaic parameters extracted from the J - V curves corresponding to the most efficient PSCs for each perovskite composition ($P + y\%$ MAPbBr₃) and bandgap values estimated from IPCE spectra.

The integrated photocurrent densities obtained from the incident photon-to-electron conversion efficiency (IPCE) spectra (Figure 5C) are in excellent agreement with those obtained from the J - V curves, indicating that the spectral mismatch between our simulator and AM-1.5 standard solar radiation is negligible. Furthermore, the sharp IPCE onset shifted from 843 nm to 829 nm after introducing 5% MAPbBr₃ as summarized together with J_{SC} and V_{OC} in Table 1 and vice-versa. The photovoltaic results revealed that the higher the J_{SC} and the lower the V_{OC} . Interestingly, the perovskite composition containing 5% MAPbBr₃ shows the best trade-off between the J_{SC} and V_{OC} . To investigate the reproducibility of our results, which is a key factor for large-scale deployment of PSCs, it is crucial to not only look at the most efficient device for each composition but also to investigate the averaged PCE of several devices from different batches. Table S2 summarizes the averaged data of several cells of each composition ($n > 10$) from different batches and Figure 5D shows the PCE distribution for each composition. Evidently, 5% MAPbBr₃ shows a good reproducibility with an average PCE exceeding 21% while remaining the most efficient composition. The other MAPbBr₃ containing compositions displayed PCEs in the range of 20-21%, whereas MAPbBr₃-free PSCs exhibit poor reproducibility, with PCEs ranging from 17.5%-20%. The poor reproducibility of P + 0% MAPbBr₃ could be asserted with the inherent structural and thermodynamic instability of FAPbI₃ system.¹⁰

Finally, to evaluate the long-term viability of these devices, the operational stability of devices (unencapsulated) was tested under continuous full-sun illumination at their MPP at 60°C in an inert atmosphere (Figure 5E).^{35,41} The PSCs containing 5% MAPbBr₃, demonstrated the best operational stability which is comparable to that of state-of-the-art PSCs containing 17% MAPbBr₃ (Figure S12). In contrast, MAPbBr₃-free PSC exhibits a very poor operational stability, losing more than 50% of its initial PCE after 100 hours, which underlines the crucial

role of MAPbBr₃ towards stabilizing the FAPbI₃ system into the perovskite structure.¹² All MAPbBr₃ containing devices showed comparable and excellent operational stability.⁴²

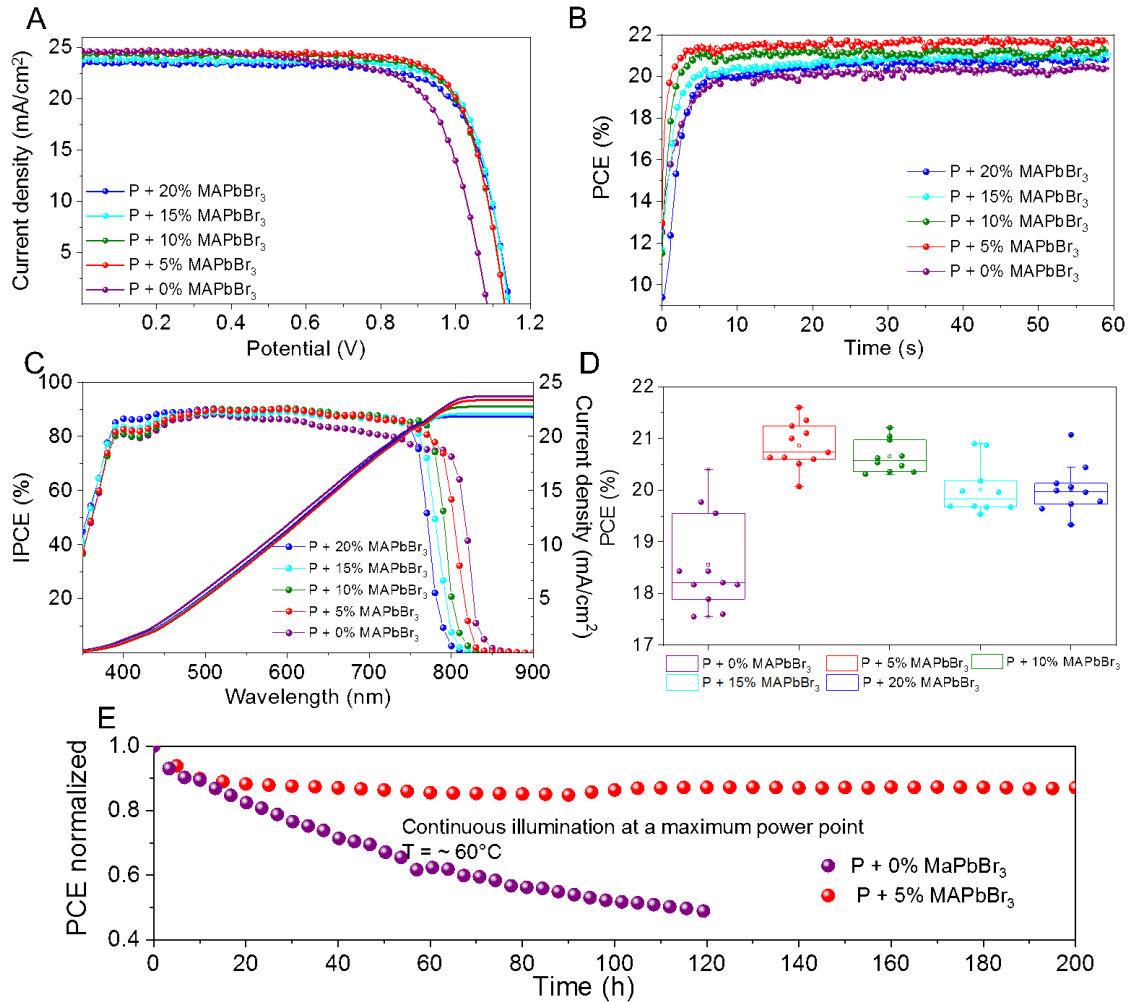


Figure 5. Photovoltaic characterization of devices based on different perovskite composition (P + y% MAPbBr₃) (A) Current density-voltage (*J*–*V*) curves (reverse scan) recorded at a scan rate of 0.05 V/s under the irradiation of simulated AM 1.5G; (B) Maximum power point tracking for 60 s, yielding stabilized efficiencies summarized in Table 1; (C) IPCE spectra as a function of monochromatic wavelength recorded for different perovskite composition-based devices; also shown are integrated current densities obtained from the respective IPCE spectrum; (D) Statistical analysis of the PCE for each perovskite composition; (E) Plot of the operational stability of an unencapsulated (P + 0% MAPbBr₃) and (P + 5% MAPbBr₃)-based device examined at a maximum power point under continuous full-sun illumination at 60°C in a nitrogen atmosphere.

Conclusion

In summary, we demonstrate that the optoelectronic quality and structural stability of the FAPbI₃ films are strongly dependent on the presence and content of MAPbBr₃. Crucial guiding principles for designing stable and high-quality perovskite films exhibiting direct correlation

with the solar cell performance have been put forth as (1) minimizing energetic disorder, (2) improving charge-carrier dynamics, and (3) reducing surface phase impurities. The introduction of MAPbBr₃ decreases the perovskite grain size by increasing the nucleation density, besides influencing the preferred orientation of perovskite grains. For MAPbBr₃-free system, the introduction of 5–10% MAPbBr₃ changes the preferred orientation from the (111) to (211) with respect to the substrate. Also, we find a strong reduction of the hexagonal non-perovskite phase for films with MAPbBr₃ compared to results for MAPbBr₃-free films at the top surface. Consequently, the introduction of MAPbBr₃ reduces the energetic disorder and prolongs the lifetime of photogenerated charge carrier. Finally, by benefiting from the positive effects of MAPbBr₃ on the optoelectronic quality and structural stability, we obtained remarkable photovoltaic performance and excellent operational stability without sacrificing much of the light-harvesting properties of FAPbI₃. To further improve the performance of PSCs, we would need to increase the crystallinity of absorber layer exhibiting an optimal bandgap and minimize defect/trap states in the bulk and/or at the interfaces and parasitic recombination including nonradiative and interfacial recombination without compromising on the energetic or band alignment within a fully assembled device.^{43,44} Fundamentally, the same set of rules could be extended to other perovskite systems. Arguably our comprehensive study will contribute to a fundamental understanding of PSCs and could help in designing new and stable light absorbers with tailored optoelectronic properties for efficient devices.

Supplementary Information

Experimental Section

Materials and Methods

All the chemicals and solvents used were stored in a glove box under inert and dry atmosphere to prevent any contamination of the reactants and/or products with moisture or

Reagent	Details	Supplier
Methylammonium bromide (CH ₃ NH ₃ Br)		GreatCell Solar
Formamidinium iodide (CH ₅ IN ₂)		GreatCell Solar
Lead iodide (PbI ₂)	Specified purity > 98%	TCI
Lead bromide (PbBr ₂)	Specified purity > 98%	TCI
Cesium iodide	Ultra dry (99.998%)	Abcr, GmbH
Spiro-OMeTAD		Merck
LiTFSI		Sigma-Aldrich
FK 209 Co(III) TFSI		Dyename AB

oxygen.

Solvent	Details	Supplier
N, N -Dimethylformamide (CH ₃) ₂ NC(O)H)	≥ 99.8%	Acros Organics
Dimethyl Sulfoxide (CH ₃) ₂ SO)	≥ 99.7%	Acros Organics
Chlorobenzene (C ₆ H ₅ Cl)	≥ 99.8%	Acros Organics
Acetonitrile (CH ₃ CN)	≥ 99.0%	Sigma-Aldrich
Anhydrous ethanol (EtOH)	≥ 99.8%	Fisher Chemical
Titanium diisopropoxidebis(75 % (w/w) in iPrOH	Sigma-Aldrich

acetylacetonate)		
Acetylacetone	$\geq 99.0\%$	Sigma-Aldrich

Perovskite solar cells were fabricated in the conventional n-i-p mesoscopic architecture using the solution deposition technique. Mesoporous titanium dioxide (TiO_2) was used as semiconductor electron transport material on FTO-coated glass and perovskite of empirical formula $\text{Cs}_{0.05}(\text{FA}_{1-y}\text{MA}_y)_{0.95}\text{Pb}(\text{I}_{1-y}\text{Br}_y)_3$ were used a light-harvesting material. Spiro-OMeTAD was used as hole-transport material and gold was used to form the electrode of the photovoltaic devices.

Substrate preparation

Glass substrates (transparent conducting oxide (TCO) glass, NSG 10, Nippon sheet glass, Japan) coated with conductive fluorine-doped tin oxide (FTO) were cleaned by ultrasonication in a 2% (v/v) Hellmanex® III (HellmaAnalytics) cleaning solution (30 min sonication) in deionized water (30 min sonication), with ethanol (20 min sonication) and lastly with acetone (5 minutes sonication) before being treated in oxygen plasma for 15 minutes.

Compact TiO_2 spray pyrolysis

A ~30-nm thick compact TiO_2 layer was deposited on FTO via aerosol spray pyrolysis at 450°C from a precursor solution of titanium diisopropoxide bis(acetylacetonate) (75% in 2-propanol) diluted in ethanol (1: 9, volume ratio) with oxygen as a carrier gas.

Mesoporous TiO_2 layer

A 200-nm thick mesoporous TiO_2 film was deposited onto the compact layer by spin-coating a solution of a diluted paste of 30 NR-D (Dyesol) in anhydrous ethanol (1:6 weight ratio) at 4,000 r.p.m. for 20 s with a ramp-up of 2,000 r.p.m. Mesoporous films were annealed at 450°C for 30 min under dry airflow. After cooling down to 150°C the substrates were immediately transferred in a nitrogen atmosphere glove box for depositing the perovskite films.

Perovskite solutions preparation

Perovskite films were deposited from the precursor solution of 1.38 M FAPbI₃ and 1.38 M MAPbBr₃ in dimethylformamide/dimethylsulphoxide (4: 1/v/v) using a single-step deposition method. Thereafter, CsI (abcr, GmbH, ultra-dry; 99.998%), (5% volume, 1.5 M DMSO) was added to the precursor solution. The desired solutions were prepared to obtain perovskites of formula CsI_{0.05}(FAPbI₃)_{1-y}MAPbBr₃)_y.

Hole transport material preparation

Spiro-OMeTAD [2,2',7,7'-tetrakis (N, N-di-p-methoxyphenyl-amine)9,9'-spirobifluorene] was dissolved in 1 mL chlorobenzene (70 mM) and doped at a molar ratio of 0.5, 0.03 and and 3.3 with lithium bis(trifluoromethanesulfonyl)imide (LiTFSI) (stock solution of 520 mg Li-TFSI in 1 mL acetonitrile), tris(bis(trifluoromethylsulfonyl)imide) (FK209, Dynamo) (stock solution of 40 mg in 100 μ L) and 4-tert-Butylpyridine (TBP), respectively.

Perovskite deposition

Perovskite solution was deposited on the meso-TiO₂ films in a two-step process: first at 2,000 r.p.m. for 10 s with a ramp-up of 200 r.p.m followed by spinning at 4,000 r.p.m. for 20 s with a ramp-up of 2,000 r.p.m. During the second step chlorobenzene (200 μ L) was dropped on the spinning substrate 5 s prior to the end of the spinning procedure The substrates were then annealed at 100°C for 1 h on a hotplate.

Hole transport material deposition

After the substrates were cooled down, 40 μ L of the Spiro-OMeTAD solution was subsequently deposited on top of the perovskite layer by spin coating at 4,000 r.p.m. for 20 s with a ramp-up of 2,000 r.p.m.

Electrode deposition

The device fabrication was completed by thermal evaporation of ~80 nm thick gold layer in high-vacuum using a Leica evaporator. Shadow masks were used to pattern the electrodes.

Structural Characterization

X-ray diffraction spectroscopy (XRD) measurements were carried out using a high power ceramic X-Ray tube from an Empyrean system (Theta-Theta, 240mm) equipped with a pixel-1D detector, Bragg-Brentano beam optics and parallel beam optics. GIXD data was measured under an angle of incidence of 0.08° with a point detector. GIWAXS data was measured with a PILATUS 300k area detector under the same angle of incidence. Calculation of powder diffraction data was done with mercury.

Morphological characterization

A field-emission scanning electron microscope (Merlin) was used to examine the morphology of the perovskite films and the thickness of various layers. Scanning electron microscopy (SEM) measurements were performed using an ultrahigh-resolution Merlin (Carl Zeiss, Germany) scanning electron microscope composed of a GEMINI II column, a process chamber with a 5-axes motorized stage (X, Y, Z, Tilt and Rotation) and a semi-automatic airlock. Measurements were taken using an in-lens detector. The SEM was controlled by the ZeissSmartSEM software operated via a graphical user interface. A high vacuum was reached during measurement.

X-ray photoelectron spectroscopy

X-ray photoelectron spectroscopy (XPS) measurements were carried out using a PHI VersaProbe II scanning XPS microprobe (Physical Instruments AG, Germany). The analysis was performed using a monochromatic Al Ka X-ray source of 24.8 W power with a beam size of 100 μm .

Photothermal deflection absorption measurement (PDS)

PDS is a scatter-free surface-sensitive absorption measurement capable of measuring 5-6 orders of magnitude weaker absorbance than the band edge absorption. For the measurements, a monochromatic pump light beam was shined on the sample (film on Quartz substrate), which on absorption produced a thermal gradient near the sample surface via non-radiative relaxation induced heating. This resulted in a refractive index gradient in the area surrounding the sample surface. This refractive index gradient was further enhanced by immersing the sample in an inert liquid FC-72 Fluorinert® (3M Company) which has a high refractive index change per unit change in temperature. A fixed wavelength CW laser probe beam was passed through this refractive index gradient producing a deflection proportional to the absorbed light at that particular wavelength, which was detected by a photo-diode and lock-in amplifier combination. Scanning through different wavelengths gave us complete absorption spectra. Because this technique makes use of the non-radiative relaxation processes in the sample, it is immune to optical effects like interference and scattering.

Transient absorption spectroscopy

The pump-probe transient absorption spectroscopy was carried out in a home-built setup. An 800nm (90 fs) fundamental pulses generated by Ti: Sapphire amplifier system (Spectra-Physics Solstice) operating at 1 kHz were passed through Optical parametric amplifier (TOPAS, Light Conversion) to generate pump pulses (500nm, FWHM of 10nm). The broadband probe beam was generated by a supercontinuum laser (Disco, Leukos). The electronic delay generator obtained the delay between the pump and probe pulses. The pump and probe beams were overlapped from the same side of the sample. An InGaAs dual-line array detector (Hamamatsu G11608-512) coupled to a calibrated monochromator is used to collect the transmitted probe pulses. The difference in transmission was acquired using lock-in board from Stresing Entwicklungsbüro.

Photovoltaic studies

Current-voltage characteristics (J - V curves) were recorded by applying an external potential bias to the cell while recording the generated photocurrent with a digital source meter (Keithley model 2400). The light source used was a 450-W xenon lamp (Oriel) equipped with a Schott K113 Tempax sunlight filter (Prazisions Glas & Optik GmbH) to match the emission spectrum of the lamp with the AM 1.5 G standard. Before each measurement, the exact light intensity was determined using a calibrated Si reference diode equipped with an infrared cutoff filter (Schott KG-3). To specify the illuminated area, a shadow mask with an area of 0.16 cm² was used.

Quantum efficiency measurements

The Incident Photon to Current Conversion Efficiency (IPCE), data were collected using a modulated light intensity of 1 Hz frequency. An Arkeo-Ariadne apparatus (Cicci Research s.r.l.) based on a 300 Watts Xenon lamp was used to focus light through a monochromator (from JobinYvon Ltd., UK). The light was directed to the device being tested. To specify the illuminated area a shadow mask with an area of 0.16 cm² was used.

Stability test

Photo-stability tests were carried out at a maximum power point under one-sun illumination at 60 °C using a home-built electronic board with an eight-channel maximum power point capability. The channels were equipped with DACs (DAC7563), level shifters (INA2132), and an output line driver (OPA2192). The driving line had a 12-bit resolution in the ± 2.048 V range (1 mV per bit). The buffer output was connected to the cells through a 0.5 Ohm sense resistor. The voltage drop was amplified (INA188) to sense the current. The voltage was buffered (OPA2188) to sense the voltage. The signal lines were multiplexed (CD54HC4051) into a fourth-order active Butterworth filter with its pole set at 500 Hz. Data conversion was performed at 430 SPS by an analog to digital converter (ADS1118). The DACs and the ADC were interfaced by an Atmega328 microcontroller. The light source consisted of an array of

white LEDs was powered by a constant current and no filters (UV) were used. Equivalent sun intensities were calibrated using a calibrated Si reference diode equipped with a KG-3 filter. The setup was calibrated periodically using a Keithley 2602B source-measuring unit.

Table S1. Quantification of iodide, bromide, lead and cesium in different perovskite films measured by XPS.

Element	0% MAPbBr ₃	5% MAPbBr ₃	10% MAPbBr ₃	15% MAPbBr ₃	20% MAPbBr ₃
Br (%)	0	4.3	11.0	13.9	20.0
I (%)	100	95.7	89.0	86.1	80.0
Pb (%)	13.81	14.14	14.05	14.02	13.50
Cs (%)	0.76	1.18	0.89	1.01	1.13

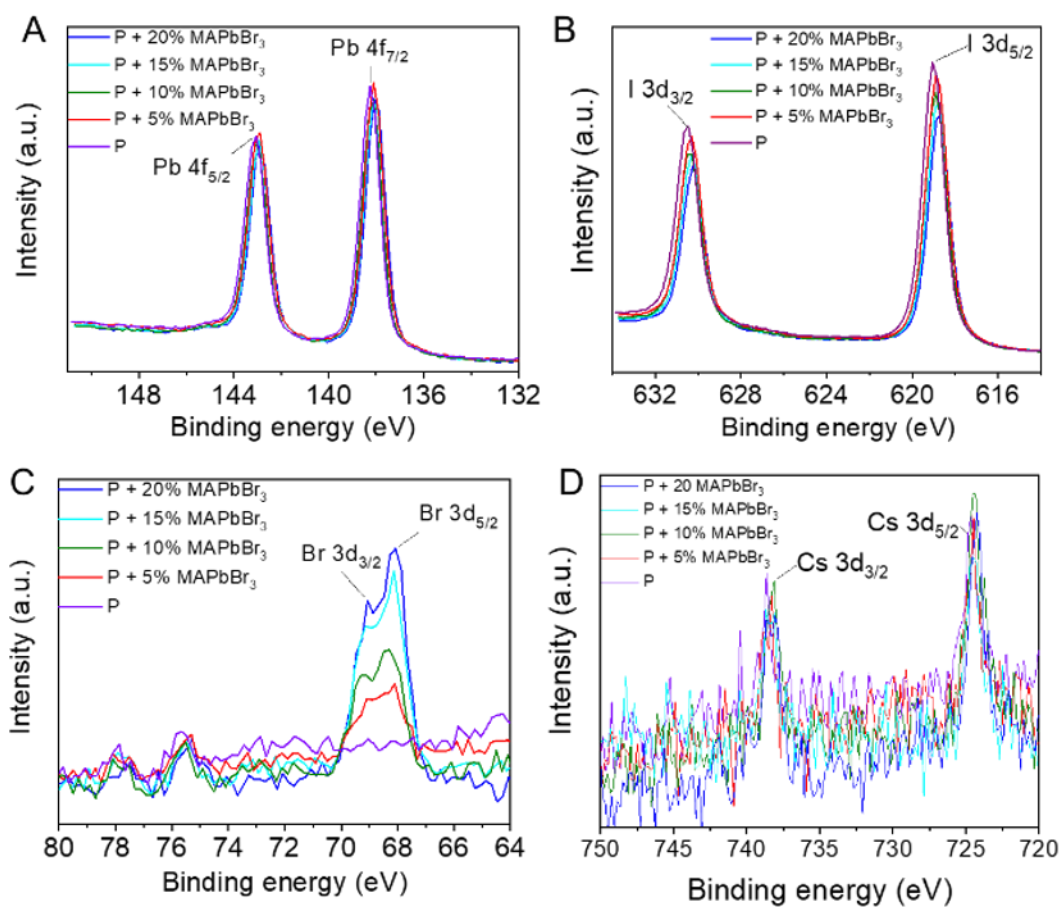


Figure S1. Compositional analysis of perovskite films: High-resolution core level XPS spectra corresponding to (A) Pb 4f states; (B) I 3d states, (C) Br 3d states and (D) Cs 3d states for different perovskite compositions ($P + y\%$ MAPbBr₃, $y = <0, 0.05, 0.10, 0.15, 0.20$).

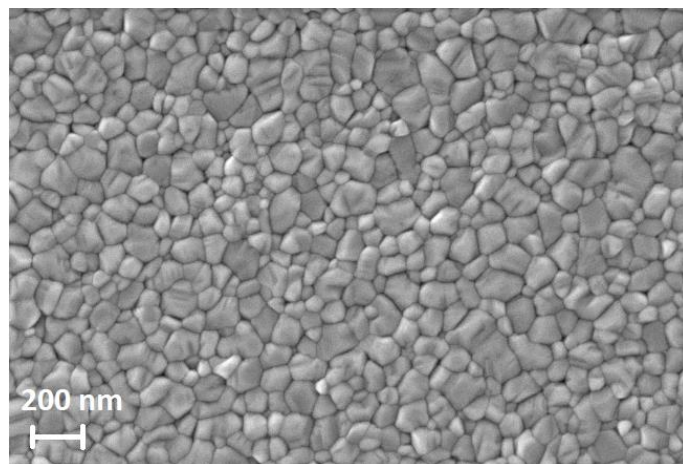


Figure S2. Top-view SEM micrograph corresponding to $P + 15\%$ MAPbBr₃.

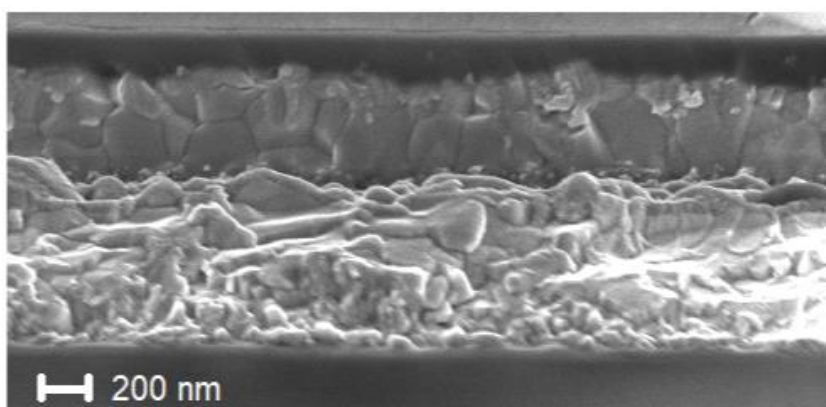


Figure S3. SEM cross-sectional micrograph corresponding to the PSC containing 15% MAPbBr₃

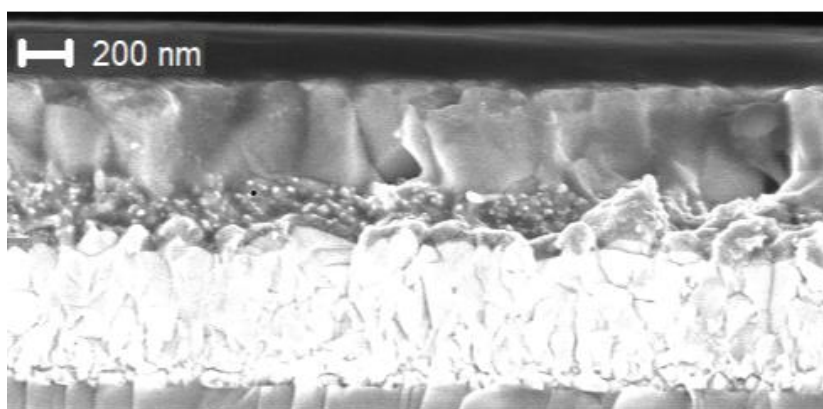


Figure S4. SEM cross-sectional micrograph corresponding to the PSC containing 20% MAPbBr₃

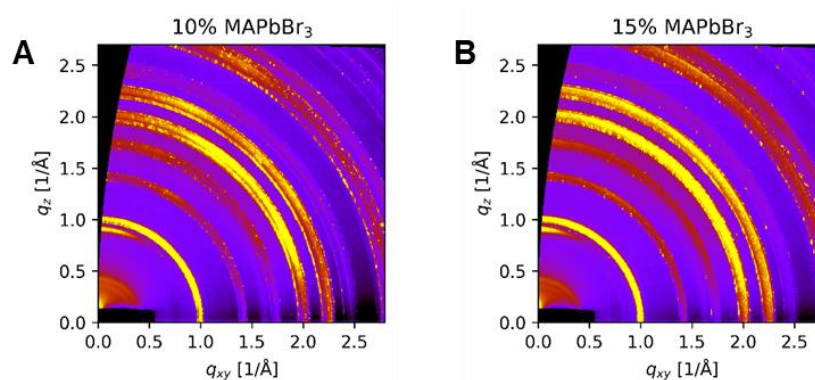


Figure S5. Reciprocal space maps obtained from GIWAXS of perovskite films with different amounts of MAPbBr₃ at an angle of incidence of 0.06°: (A) P + 10% MAPbBr₃ and (B) P+ 15% MAPbBr₃.

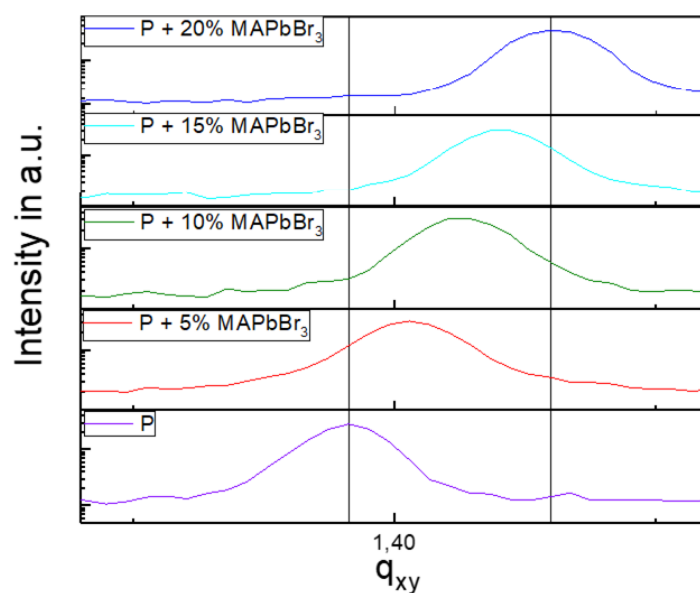


Figure S6. Zoom on a given XRD peak attributed to the perovskite phase illustrating the shift as a function of MAPbBr₃ content.

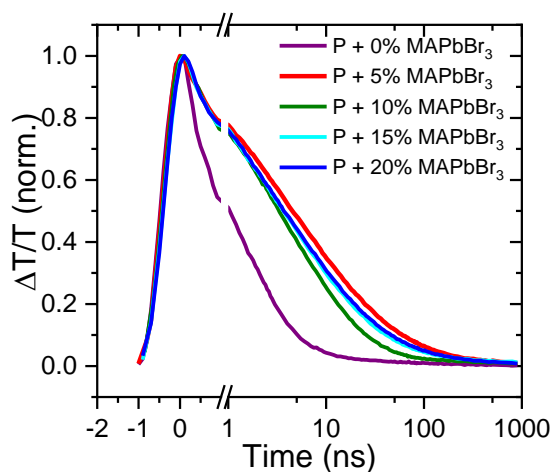


Figure S7. Kinetics of ground-state bleach of different stoichiometric perovskite films.

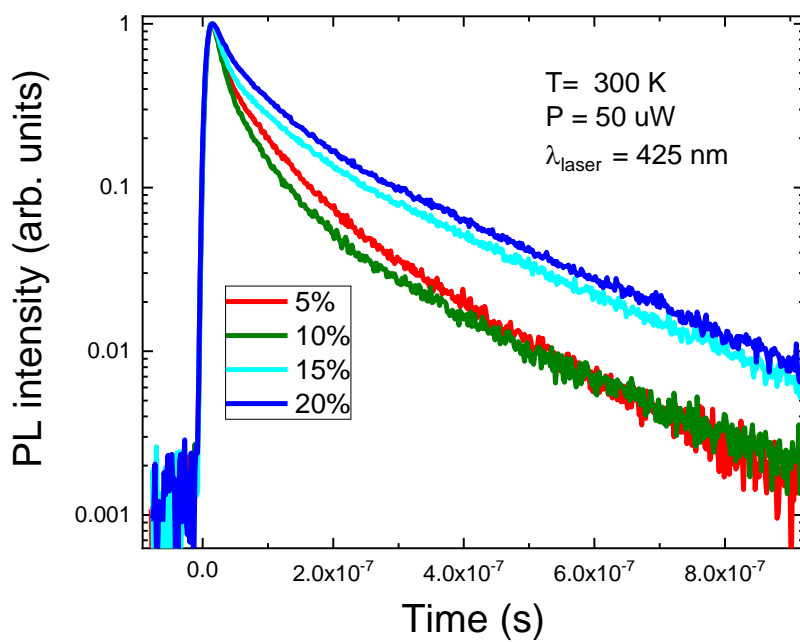


Figure S8. Time-resolved photoluminescence spectra of perovskite films with varying MAPbBr_3 content. The increased carriers' lifetime is clearly observed as the MAPbBr_3 content is increased. Thus, the introduction of MAPbBr_3 improves the perovskite film by reducing the non-radiative recombination rate and the trap state density.

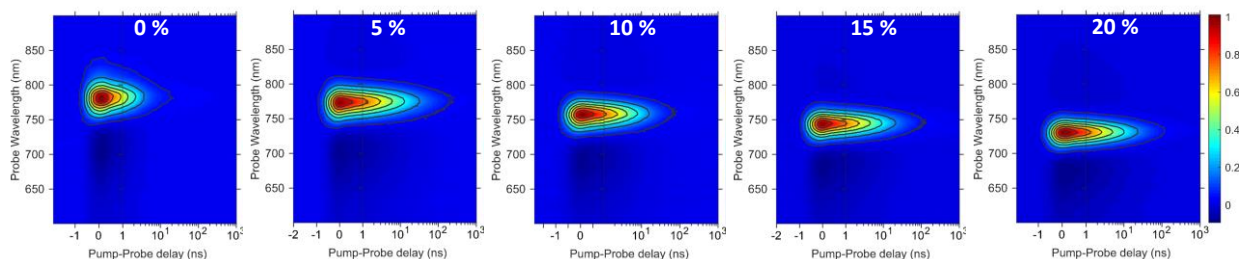


Figure S9. Full contour TA maps of perovskite films with varying MAPbBr₃ content. The shift in the bandgap is clearly observed as the GSB shifts with different stoichiometric ratio. The absence of any new GSB with delay in time reveals that the films do not have significant halide segregation.

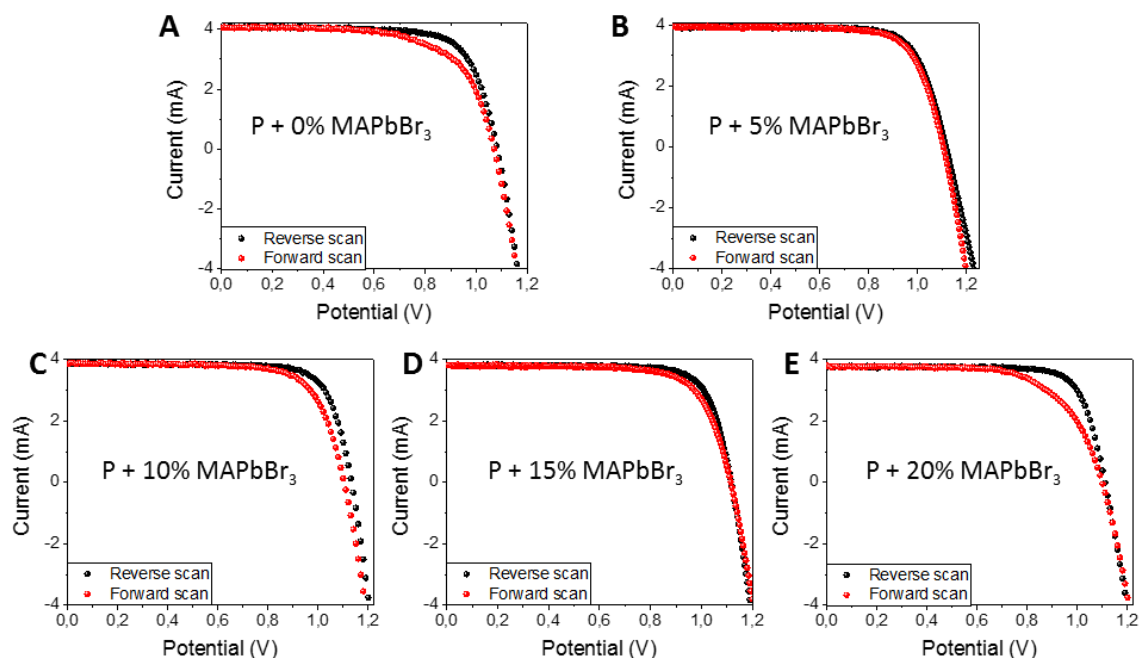


Figure S10. *J-V* hysteresis curves for the PSCs; A) *P*+0% MAPbBr₃, B) *P*+5% MAPbBr₃, C) *P*+10% MAPbBr₃, D) *P*+15% MAPbBr₃, E) *P*+20% MAPbBr₃.

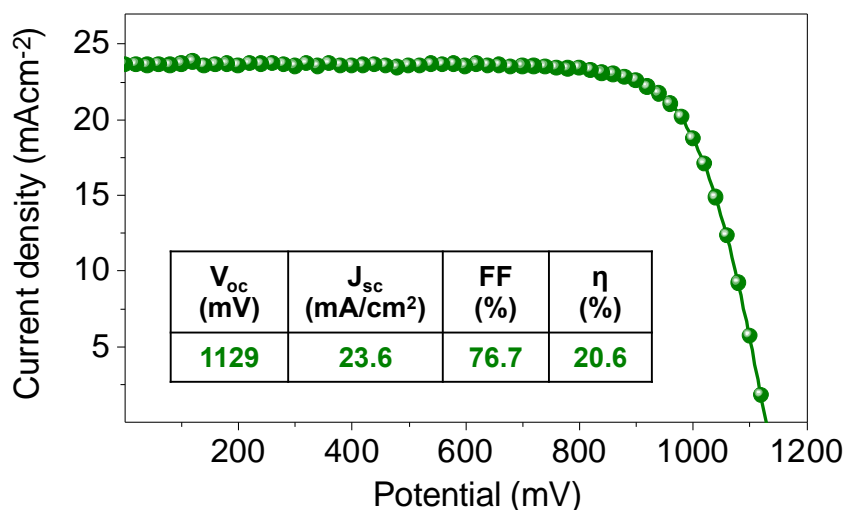


Figure S11. *J-V* data for the PSC containing 17% MAPbBr₃.

Table S2. Average photovoltaic parameters extracted from the *J-V* data (Figure 5D) corresponding to each perovskite composition observed from different batches.

MAPbBr ₃ conc. (%)	J_{SC} (mA cm ⁻²)	V_{OC} (V)	FF	PCE (%)
0	24.99±0.371	1.079±0.011	0.675±0.047	18.44±1.57
5	24.65±0.169	1.124±0.006	0.758±0.007	21.11±0.29
10	24.17±0.182	1.129±0.005	0.755±0.012	20.73±0.38
15	23.74±0.096	1.135±0.012	0.751±0.029	20.18±0.99
20	23.27±0.116	1.154±0.011	0.763±0.009	20.55±0.37

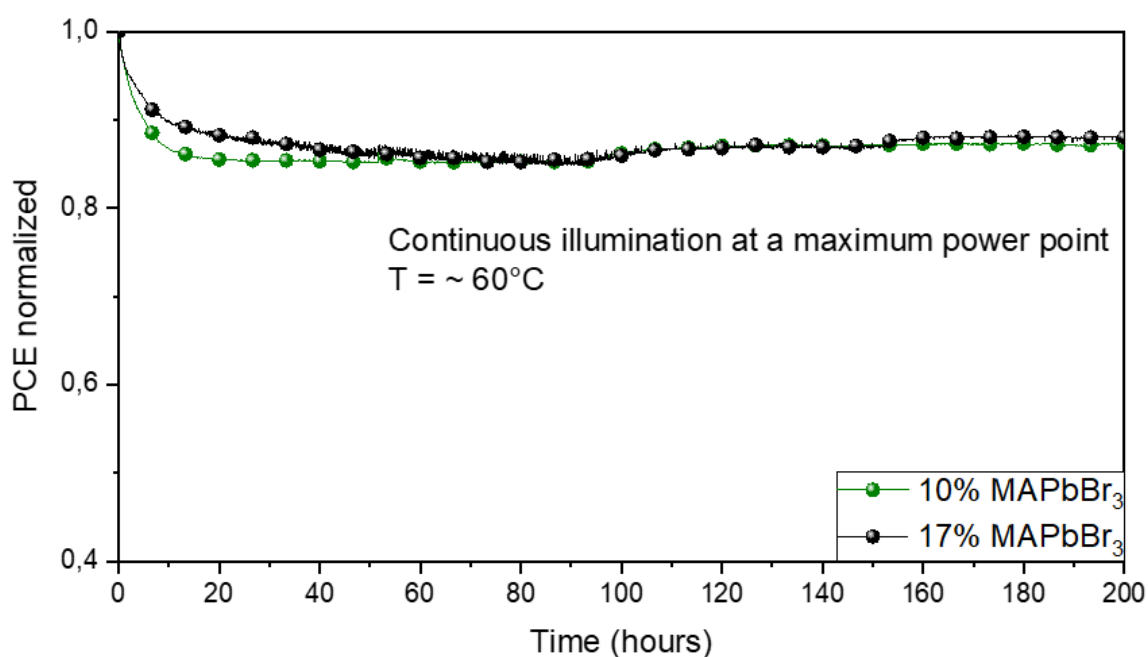


Figure S12. The plot of the operational stability of P+ 10% MAPbBr₃ and P+17% MAPbBr₃ PSCs.

References

- (1) Kojima, A.; Teshima, K.; Shirai, Y.; Miyasaka, T., Organometal Halide Perovskites as Visible-Light Sensitizers for Photovoltaic Cells. *J. Am. Chem. Soc.* **2009**, *131* (17), 6050-6051.

(2) Lee, M. M.; Teuscher, J.; Miyasaka, T.; Murakami, T. N.; Snaith, H. J., Efficient Hybrid Solar Cells Based on Meso-Superstructured Organometal Halide Perovskites. *Science* **2012**, 338 (6107), 643.

(3) Kim, H.-S.; Lee, C.-R.; Im, J.-H.; Lee, K.-B.; Moehl, T.; Marchioro, A.; Moon, S.-J.; Humphry-Baker, R.; Yum, J.-H.; Moser, J. E.; Grätzel, M.; Park, N.-G., Lead Iodide Perovskite Sensitized All-Solid-State Submicron Thin Film Mesoscopic Solar Cell with Efficiency Exceeding 9%. *Sci. Rep.* **2012**, 2, 591.

(4) Dar, M. I.; Jacopin, G.; Meloni, S.; Mattoni, A.; Arora, N.; Boziki, A.; Zakeeruddin, S. M.; Rothlisberger, U.; Grätzel, M., Origin of unusual bandgap shift and dual emission in organic-inorganic lead halide perovskites. *Sci. Adv.* **2016**, 2 (10), e1601156.

(5) Xing, G.; Mathews, N.; Lim, S. S.; Yantara, N.; Liu, X.; Sabba, D.; Grätzel, M.; Mhaisalkar, S.; Sum, T. C., Low-temperature solution-processed wavelength-tunable perovskites for lasing. *Nat. Mater.* **2014**, 13, 476.

(6) Stoumpos, C. C.; Malliakas, C. D.; Kanatzidis, M. G., Semiconducting Tin and Lead Iodide Perovskites with Organic Cations: Phase Transitions, High Mobilities, and Near-Infrared Photoluminescent Properties. *Inorg. Chem.* **2013**, 52 (15), 9019-9038.

(7) Dong, Q.; Fang, Y.; Shao, Y.; Mulligan, P.; Qiu, J.; Cao, L.; Huang, J., Electron-hole diffusion lengths > 175 μm in solution-grown $\text{CH}_3\text{NH}_3\text{PbI}_3$ single crystals. *Science* **2015**, 347 (6225), 967-970.

(8) Manser, J. S.; Christians, J. A.; Kamat, P. V., Intriguing Optoelectronic Properties of Metal Halide Perovskites. *Chem. Rev.* **2016**, 116 (21), 12956-13008.

(9) Noh, J. H.; Im, S. H.; Heo, J. H.; Mandal, T. N.; Seok, S. I., Chemical Management for Colorful, Efficient, and Stable Inorganic–Organic Hybrid Nanostructured Solar Cells. *Nano Lett.* **2013**, *13* (4), 1764-1769.

(10) Koh, T. M.; Fu, K.; Fang, Y.; Chen, S.; Sum, T. C.; Mathews, N.; Mhaisalkar, S. G.; Boix, P. P.; Baikie, T., Formamidinium-Containing Metal-Halide: An Alternative Material for Near-IR Absorption Perovskite Solar Cells. *J. Phys. Chem. C* **2014**, *118* (30), 16458-16462.

(11) Pellet, N.; Gao, P.; Gregori, G.; Yang, T.-Y.; Nazeeruddin, M. K.; Maier, J.; Grätzel, M., Mixed-Organic-Cation Perovskite Photovoltaics for Enhanced Solar-Light Harvesting. *Angew Chem.* **2014**, *53* (12), 3151-3157.

(12) Jeon, N. J.; Noh, J. H.; Yang, W. S.; Kim, Y. C.; Ryu, S.; Seo, J.; Seok, S. I., Compositional engineering of perovskite materials for high-performance solar cells. *Nature* **2015**, *517*, 476.

(13) Saliba, M.; Matsui, T.; Domanski, K.; Seo, J.-Y.; Ummadisingu, A.; Zakeeruddin, S. M.; Correa-Baena, J.-P.; Tress, W. R.; Abate, A.; Hagfeldt, A.; Grätzel, M., Incorporation of rubidium cations into perovskite solar cells improves photovoltaic performance. *Science* **2016**, *354* (6309), 206.

(14) Uchida, R.; Binet, S.; Arora, N.; Jacopin, G.; Alotaibi, M. H.; Taubert, A.; Zakeeruddin, S. M.; Dar, M. I.; Graetzel, M., Insights about the Absence of Rb Cation from the 3D Perovskite Lattice: Effect on the Structural, Morphological, and Photophysical Properties and Photovoltaic Performance. *Small* **2018**, *14* (36), 1802033.

(15) Yadav, P.; Dar, M. I.; Arora, N.; Alharbi, E. A.; Giordano, F.; Zakeeruddin, S. M.; Grätzel, M., The Role of Rubidium in Multiple-Cation-Based High-Efficiency Perovskite Solar Cells. *Adv. Mater.* **2017**, *29* (40), 1701077.

(16) Abdi-Jalebi, M.; Andaji-Garmaroudi, Z.; Cacovich, S.; Stavrakas, C.; Philippe, B.; Richter, J. M.; Alsari, M.; Booker, E. P.; Hutter, E. M.; Pearson, A. J.; Lilliu, S.; Savenije, T. J.; Rensmo, H.; Divitini, G.; Ducati, C.; Friend, R. H.; Stranks, S. D., Maximizing and stabilizing luminescence from halide perovskites with potassium passivation. *Nature* **2018**, *555*, 497.

(17) Liu, Y.; Akin, S.; Pan, L.; Uchida, R.; Arora, N.; Milić, J. V.; Hinderhofer, A.; Schreiber, F.; Uhl, A. R.; Zakeeruddin, S. M.; Hagfeldt, A.; Dar, M. I.; Grätzel, M., Ultrahydrophobic 3D/2D fluoroarene bilayer-based water-resistant perovskite solar cells with efficiencies exceeding 22%. *Sci. Adv.* **2019**, *5* (6), eaaw2543.

(18) Lee, J.-W.; Dai, Z.; Han, T.-H.; Choi, C.; Chang, S.-Y.; Lee, S.-J.; De Marco, N.; Zhao, H.; Sun, P.; Huang, Y.; Yang, Y., 2D perovskite stabilized phase-pure formamidinium perovskite solar cells. *Nat. Commun.* **2018**, *9* (1), 3021.

(19) Saidaminov, M. I.; Kim, J.; Jain, A.; Quintero-Bermudez, R.; Tan, H.; Long, G.; Tan, F.; Johnston, A.; Zhao, Y.; Voznyy, O.; Sargent, E. H., Suppression of atomic vacancies via incorporation of isovalent small ions to increase the stability of halide perovskite solar cells in ambient air. *Nat. Energy* **2018**, *3* (8), 648-654.

(20) Zhao, Y.; Tan, H.; Yuan, H.; Yang, Z.; Fan, J. Z.; Kim, J.; Voznyy, O.; Gong, X.; Quan, L. N.; Tan, C. S.; Hofkens, J.; Yu, D.; Zhao, Q.; Sargent, E. H., Perovskite seeding growth of formamidinium-lead-iodide-based perovskites for efficient and stable solar cells. *Nat. Commun.* **2018**, *9* (1), 1607.

(21) Min, H.; Kim, M.; Lee, S.-U.; Kim, H.; Kim, G.; Choi, K.; Lee, J. H.; Seok, S. I., Efficient, stable solar cells by using inherent bandgap of α -phase formamidinium lead iodide. *Science* **2019**, *366* (6466), 749-753.

(22) Saliba, M.; Matsui, T.; Seo, J.-Y.; Domanski, K.; Correa-Baena, J.-P.; Nazeeruddin, M. K.; Zakeeruddin, S. M.; Tress, W.; Abate, A.; Hagfeldt, A.; Grätzel, M., Cesium-containing triple cation perovskite solar cells: improved stability, reproducibility and high efficiency. , *Energy Environ. Sci.* **2016**, 9 (6), 1989-1997.

(23) Lee, J.-W.; Kim, D.-H.; Kim, H.-S.; Seo, S.-W.; Cho, S. M.; Park, N.-G., Formamidinium and Cesium Hybridization for Photo- and Moisture-Stable Perovskite Solar Cell. *Adv. Energy Mater.* **2015**, 5 (20), 1501310.

(24) Briggs, D.; Seah, M., Practical Surface Analysis (2nd Ed.), vol. 1, New York: John Wiley, **1996**.

(25) Pederson, L. R., Two-dimensional chemical-state plot for lead using XPS. *J. Electron Spectrosc. Relat. Phenom.* **1982**, 28 (2), 203-209.

(26) Bagus, P. S.; Illas, F.; Pacchioni, G.; Parmigiani, F., Mechanisms responsible for chemical shifts of core-level binding energies and their relationship to chemical bonding. *J. Electron Spectrosc. Relat. Phenom.* **1999**, 100 (1), 215-236.

(27) Dar, M. I.; Hinderhofer, A.; Jacopin, G.; Belova, V.; Arora, N.; Zakeeruddin, S. M.; Schreiber, F.; Grätzel, M., Function Follows Form: Correlation between the Growth and Local Emission of Perovskite Structures and the Performance of Solar Cells. *Adv. Funct. Mater.* **2017**, 27 (26), 1701433.

(28) Amat, A.; Mosconi, E.; Ronca, E.; Quarti, C.; Umari, P.; Nazeeruddin, M. K.; Grätzel, M.; De Angelis, F., Cation-Induced Band-Gap Tuning in Organohalide Perovskites: Interplay of Spin–Orbit Coupling and Octahedra Tilting. *Nano Lett.* **2014**, 14 (6), 3608-3616.

(29) Jones, T. W.; Osherov, A.; Alsari, M.; Sponseller, M.; Duck, B. C.; Jung, Y.-K.; Settens, C.; Niroui, F.; Brenes, R.; Stan, C. V.; Li, Y.; Abdi-Jalebi, M.; Tamura, N.; Macdonald, J. E.;

Burghammer, M.; Friend, R. H.; Bulović, V.; Walsh, A.; Wilson, G. J.; Lilliu, S.; Stranks, S. D., Lattice strain causes non-radiative losses in halide perovskites. *Energy Environ. Sci.* **2019**, *12* (2), 596-606.

(30) Ball, J. M.; Petrozza, A., Defects in perovskite-halides and their effects in solar cells. *Nat. Energy* **2016**, *1* (11), 16149.

(31) Abdi-Jalebi, M.; Dar, M. I.; Sadhanala, A.; Senanayak, S. P.; Franckevičius, M.; Arora, N.; Hu, Y.; Nazeeruddin, M. K.; Zakeeruddin, S. M.; Grätzel, M.; Friend, R. H., Impact of Monovalent Cation Halide Additives on the Structural and Optoelectronic Properties of $\text{CH}_3\text{NH}_3\text{PbI}_3$ Perovskite. *Adv. Energy Mater.* **2016**, *6* (10), 1502472.

(32) Arora, N.; Dar, M. I.; Abdi-Jalebi, M.; Giordano, F.; Pellet, N.; Jacopin, G.; Friend, R. H.; Zakeeruddin, S. M.; Grätzel, M., Intrinsic and Extrinsic Stability of Formamidinium Lead Bromide Perovskite Solar Cells Yielding High Photovoltage. *Nano Lett.* **2016**, *16* (11), 7155-7162.

(33) Shi, D.; Adinolfi, V.; Comin, R.; Yuan, M.; Alarousu, E.; Buin, A.; Chen, Y.; Hoogland, S.; Rothenberger, A.; Katsiev, K.; Losovyj, Y.; Zhang, X.; Dowben, P. A.; Mohammed, O. F.; Sargent, E. H.; Bakr, O. M., Low trap-state density and long carrier diffusion in organolead trihalide perovskite single crystals. *Science* **2015**, *347* (6221), 519-522.

(34) Yang, Z.; Chueh, C.-C.; Liang, P.-W.; Crump, M.; Lin, F.; Zhu, Z.; Jen, A. K. Y., Effects of formamidinium and bromide ion substitution in methylammonium lead triiodide toward high-performance perovskite solar cells. *Nano Energy* **2016**, *22*, 328-337.

(35) Zhang, Y.; Zhou, Z.; Ji, F.; Li, Z.; Cui, G.; Gao, P.; Oveisi, E.; Nazeeruddin, M. K.; Pang, S., Trash into Treasure: δ -FAPbI₃ Polymorph Stabilized MAPbI₃ Perovskite with Power Conversion Efficiency beyond 21%. *Adv. Mater.* **2018**, *30* (22), 1707143.

(36) Niu, T.; Lu, J.; Tang, M.-C.; Barrit, D.; Smilgies, D.-M.; Yang, Z.; Li, J.; Fan, Y.; Luo, T.; McCulloch, I.; Amassian, A.; Liu, S.; Zhao, K., High performance ambient-air-stable FAPbI₃ perovskite solar cells with molecule-passivated Ruddlesden–Popper/3D heterostructured film. *Energy Environ. Sci.* **2018**, *11* (12), 3358-3366.

(37) Eames, C.; Frost, J. M.; Barnes, P. R. F.; O'Regan, B. C.; Walsh, A.; Islam, M. S., Ionic transport in hybrid lead iodide perovskite solar cells. *Nature Commun.* **2015**, *6* (1), 7497.

(38) Arora, N.; Dar, M. I.; Hinderhofer, A.; Pellet, N.; Schreiber, F.; Zakeeruddin, S. M.; Grätzel, M., Perovskite solar cells with CuSCN hole extraction layers yield stabilized efficiencies greater than 20%. *Science* **2017**, *358* (6364), 768.

(39) Christians, J. A.; Schulz, P.; Tinkham, J. S.; Schloemer, T. H.; Harvey, S. P.; Tremolet de Villers, B. J.; Sellinger, A.; Berry, J. J.; Luther, J. M., Tailored interfaces of unencapsulated perovskite solar cells for >1,000 hour operational stability. *Nat. Energy* **2018**, *3* (1), 68-74.

Chapter 3 Formation of High-Performance Multi-Cation Halide Perovskites Photovoltaics by d-CsPbI₃/ d-RbPbI₃ Seed-assisted Heterogeneous Nucleation

This work has been published: T. Baumeler, E. A. Alharbi*, A. Krishna, A. Y. Alyamani, F. T. Eickemeyer, O. Ouellette, L. Pan, F. S. Alghamdi, Z. Wang, M. H. Alotaibi, B. Yang, M. Almalki, M. D. Mensi, H. Albrithen, A. Albadri, A. Hagfeldt, S. M. Zakeeruddin, M. Grätzel, Advanced Energy Materials, 2021, 11(16), 2003875*

Introduction

Over the last decade, organic-inorganic halide perovskite solar cells (PSCs) have garnered significant attention. Their high carrier mobility and long electron-hole diffusion length, small exciton binding energy, tunable bandgap, high absorption coefficient, and tolerance to defects make these materials suitable for a broad range of applications, ranging from photovoltaic devices to light-emitting diodes and lasers^{89–93}. Recently, certified power conversion efficiencies (PCE) of perovskite solar cells have reached 25.5% [1]. The chemical formula ABX₃ of organic-inorganic halide perovskites stands for a monovalent A cation, i.e. methylammonium (MA⁺ = CH₃NH₃⁺), formamidinium (FA⁺ = CH(NH₂)₂⁺), or Cs⁺, and Rb⁺, a divalent metal B cation (Pb²⁺, Ge²⁺ and Sn²⁺) and a halide anion X (I[−], Br[−], and Cl[−]). Tuning the perovskite bandgap and modulating the crystallinity by using elemental composition engineering in bulk or at the surface via incorporation of multiple A cations and halides improves their performance and stability^{94–98}. Perovskite films are commonly fabricated using different techniques such as the one-step method (antisolvent), two-steps method (sequential deposition), thermal evaporation, vapor-assisted deposition, and blade coating^{99–103}. In the case of the antisolvent method, a certain amount of non-polar solvent is dripped on the perovskite precursor solution during spin-casting to initiate the nucleation and subsequent crystal growth

of the perovskite. Achieving high reproducibility using this method is challenging, especially for large-area devices ¹⁰⁴. In contrast, sequential deposition starts first with the deposition of an inorganic component, such as PbI_2 , not soluble in alcohol solvents, followed by the coating of a layer of organic salts, which interact with the inorganic component, leading to their final conversion into a perovskite film. This has been demonstrated as an effective method to fabricate dense and uniform perovskite films and devices with a high PCE and is considered a reliable strategy to upscale devices to large modules size, owing to the better quality and higher reproducibility ^{100,105–108}. One of the most promising perovskite composition is α - FAPbI_3 due to its broader light absorption range with its reduced bandgap ^{109,110}. However, the perovskite cubic α -phase of FAPbI_3 is only thermodynamically stable above 400 K and turns into a yellow non-perovskite hexagonal phase (δ -phase) at room temperature ¹¹¹. It was found that the incorporation of smaller cations (such as MA^+ , Cs^+ , Rb^+) ^{94,95,97} or additives (such as PEA^+ , BA^+ , MACl) ^{112–115}, leads to more stable devices with improved PCEs. Cs/FA double cations-based perovskites have the potential to stabilize the perovskite phase and increase the thermal and moisture stability due to the contraction of the cuboctahedral volume ^{116–118}. For example, additives such as PEA^+ , BA^+ , MACl , or Rb^+ were found to work as stabilizers or crystallization aids that preserve the desirable photoactive perovskite α -phase of FAPbI_3 while improving the phase crystallinity and film quality ^{119–121}.

However, for the sequential deposition method, it is difficult to introduce Cs^+ or Rb^+ in the FAPbI_3 lattice due to the low solubility of CsX and/or RbX ($\text{X}=\text{I}, \text{Br}, \text{Cl}$) salts in alcohol solvents. This prevents adding these salts together with MA/FA cations in the second step of the process, which employs typically isopropanol (IPA) to dissolve the A cation halide. There have been few reports of incorporation of Cs^+ in the perovskite fabricated with sequential deposition where either CsI or δ - CsPbI_3 phase was added to PbI_2 ^{122,123} which lead to perovskites with high crystallinity, excellent optoelectronic properties, and high performance.

However, to the best of our knowledge, Rb^+ or Cs^+/Rb^+ mixtures so far have not been employed in the sequential deposition processes for the formation of perovskite films.

Herein, we report the systematic investigation of the role of multication-halide formulations in directing sequential deposition. For the first time, we examine the influence of $\delta\text{-RbPbI}_3$ and $\delta\text{-CsPbI}_3$ 1D polymorphs on the heterogeneous nucleation and conversion via the sequential deposition method and show the beneficial effect of quadruple cation formulation (RbCsMAFA) on the conversion of PbI_2 films into perovskite. The introduction of a mixture of $\delta\text{-RbPbI}_3$ and $\delta\text{-CsPbI}_3$ 1D polymorphs induces the formation of porous microstructure in the PbI_2 films, which facilitates the penetration of the A cations into the PbI_2 and leads to its rapid and complete conversion into the photoactive α -phase perovskite

Results and Discussion

We employed 1.15M solution of PbI_2 in 1 mL of dimethylformide (DMF) and 200 μL of dimethylsulfoxide (DMSO) as a starting solution. To this we added either 7 mol.% RbPbI_3 or 10 mol.% CsPbI_3 or a mixture both, i.e. 10 mol.% CsPbI_3 and 7 mol.% RbPbI_3 from 1.15M stock solutions of RbPbI_3 and CsPbI_3 in DMSO (see Supporting Informations for experimental details). We label these solutions as $\text{PbI}_2 \bullet 7\% \text{RbPbI}_3$, $\text{PbI}_2 \bullet 10\% \text{CsPbI}_3$, and $\text{PbI}_2 \bullet (7\% \text{RbPbI}_3 + 10\% \text{CsPbI}_3)$ respectively. We used these solutions during the first step of the sequential deposition to impregnate mesoporous TiO_2 layers and annealed them at 80°C for 2-3 min. After letting the films cool down to room temperature, we exposed them during the second step of our sequential perovskite preparation to the organic halide salts (52.2 mg FAI, 5.2 mg MABr, and 5.2 mg MACl) dissolved in 1 mL isopropanol (IPA) and annealed them at 100°C for 10 min and thereafter at 150°C for 20 min. Here methyl ammonium chloride (MACl) was used as an additive to improve the perovskite crystallization which sublimed during the annealing of the perovskite. The optimized compositions for the double, triple, and quadruple

A-cation perovskites are $\text{FA}_{0.91}\text{MA}_{0.09}\text{Pb}(\text{I}_{0.91}\text{Br}_{0.09})_3$, $\text{Rb}_{0.07}\text{FA}_{0.85}\text{MA}_{0.08}\text{Pb}(\text{I}_{0.92}\text{Br}_{0.08})_3$, $\text{Cs}_{0.09}\text{FA}_{0.83}\text{MA}_{0.08}\text{Pb}(\text{I}_{0.92}\text{Br}_{0.08})_3$ and $\text{Rb}_{0.06}\text{Cs}_{0.08}\text{FA}_{0.78}\text{MA}_{0.08}\text{Pb}(\text{I}_{0.92}\text{Br}_{0.08})_3$, and these are labeled below as Control, Target-Rb, Target-Cs, and Target-RbCs respectively. We present details on our optimization procedure in Figures S2, S3, S4 and S5. Humidity plays a key role in the nucleation and crystallization process of organic-inorganic perovskites as it activates the reaction of PbI_2 species with the halides¹²⁴. Hence, the perovskite films were annealed under an ambient atmosphere with relative humidity (RH) of $30\pm5\%$. Also, processing under RH of $30\pm5\%$ leads to a compact polycrystalline texture with full surface coverage and large grain size, features that are distinct from the small grain size and pinholes obtained from the films that were processed at a low humidity of $8\pm4\%$ (figure S6). This is explained by the fact that the presence of water facilitates the ionic dissociation of FAI/MABr and thus accelerates the reaction of PbI_2 with the halides¹²⁴. Furthermore, processing conditions are known to be critical to yield highly reproducible PSCs, especially using the sequential deposition method as they impact the morphology of the PbI_2 precursor films, which is of crucial importance for the efficiency and stability of the final perovskite solar cells^{125,126}. Employing $30\pm5\%$ RH, our method allows for producing highly efficient PSCs with very good reproducibility. We additionally found that optimizing the thickness of the mesoporous layer plays a key role in the conversion of PbI_2 into the perovskite (Fig. S7).

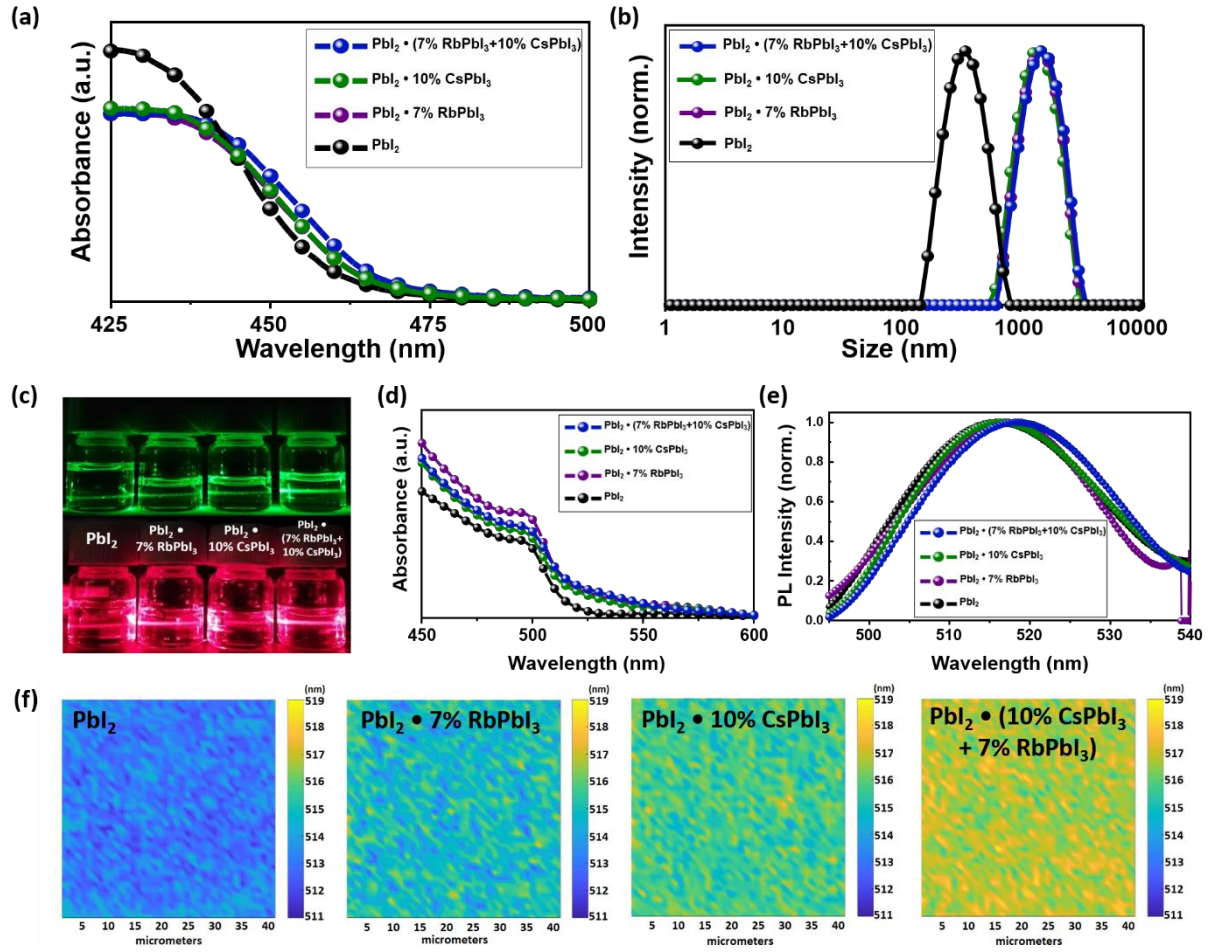
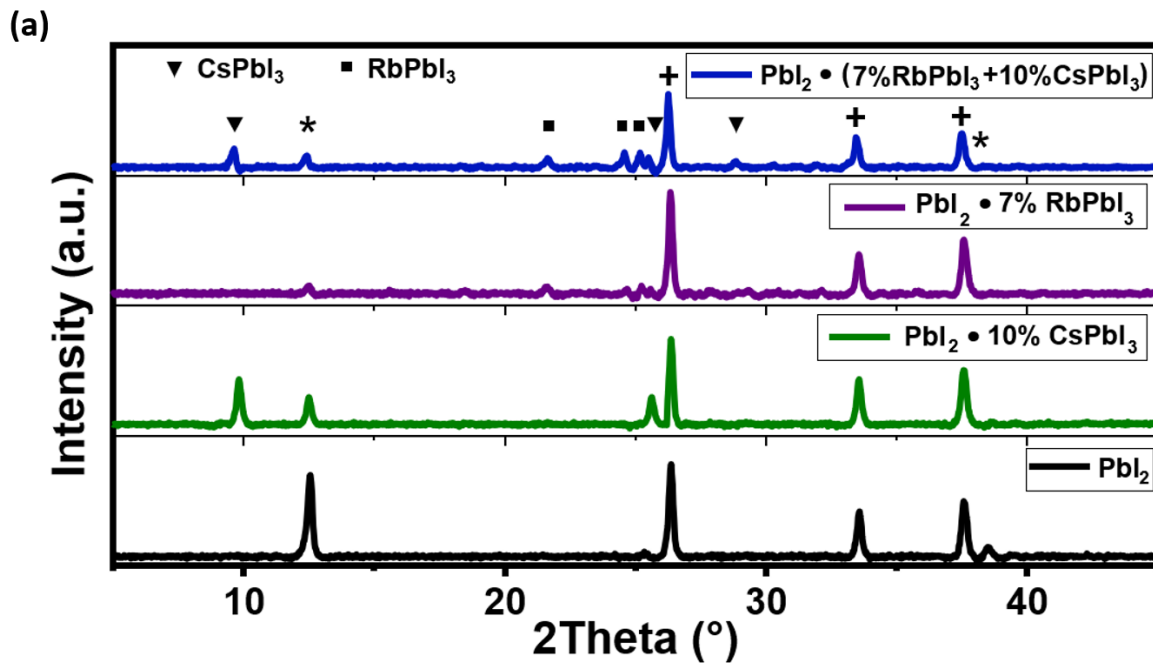


Figure 1. (a) UV-Vis spectra, (b) Dynamic light scattering spectra and (c) Tyndall effect of PbI_2 , $\text{PbI}_2 \cdot 7\% \text{RbPbI}_3$, $\text{PbI}_2 \cdot 10\% \text{CsPbI}_3$, and $\text{PbI}_2 \cdot 7\% \text{RbPbI}_3 + 10\% \text{CsPbI}_3$ precursor perovskite solutions, respectively. (d) UV-Vis spectra of the same condition as films and (e) corresponding photoluminescence spectra and (f) PL mapping of PbI_2 , $\text{PbI}_2 \cdot 7\% \text{RbPbI}_3$, $\text{PbI}_2 \cdot 10\% \text{CsPbI}_3$, and $\text{PbI}_2 \cdot 7\% \text{RbPbI}_3 + 10\% \text{CsPbI}_3$ films, respectively.

To understand the effect of δ - CsPbI_3 and δ - RbPbI_3 on the perovskite nucleation and growth we investigated the optical behaviour of their precursor solutions. Figures. 1a and 1d show their absorption spectra in solution and after deposition as solid films. Addition of the δ - RbPbI_3 and δ - CsPbI_3 polymorphs to the PbI_2 precursor solutions produces small red shift of their absorption and emission spectrum as well as a tail in the absorbance attributed to light scattering. Previous studies showed that perovskite precursors form colloids in the mother solution^{127,128}. The tailing of the absorbance towards longer wavelengths is likely to be caused by the formation of colloids with increased diameter. To gain further insight, we employed

dynamic light scattering (DLS) measurements (Fig.1b, Fig. S1a,b), which confirmed the presence of colloids in the precursor solutions, the PbI_2 particles having a size of ~ 350 nm. Upon the addition of the 7% RbPbI_3 , 10% CsPbI_3 , or (7% RbPbI_3 + 10% CsPbI_3) precursor solutions the PbI_2 colloids disappear and larger colloids of microscopic size (1480 nm) are observed. Furthermore, we confirmed the colloidal nature of the precursor solutions by observing the Tyndall effect in solutions illuminated with laser beams of red and green wavelengths as shown in Fig. 1c. We then performed photoluminescence (PL) mapping measurements on solid films prepared from the precursor solutions. The results shown in Fig.1f, reveal the persistence of colloidal particles in the intermediate phase PbI_2 films. The absorbance and photoluminescence of all these intermediate phase films red-shift upon the addition of RbPbI_3 and/or CsPbI_3 , showing the same trend as for the solutions (Fig.1d and Fig.1e).

We investigated the structure and the morphology of the perovskite and non-perovskite precursor films using X-ray diffraction (XRD) and scanning electron microscopy (SEM).



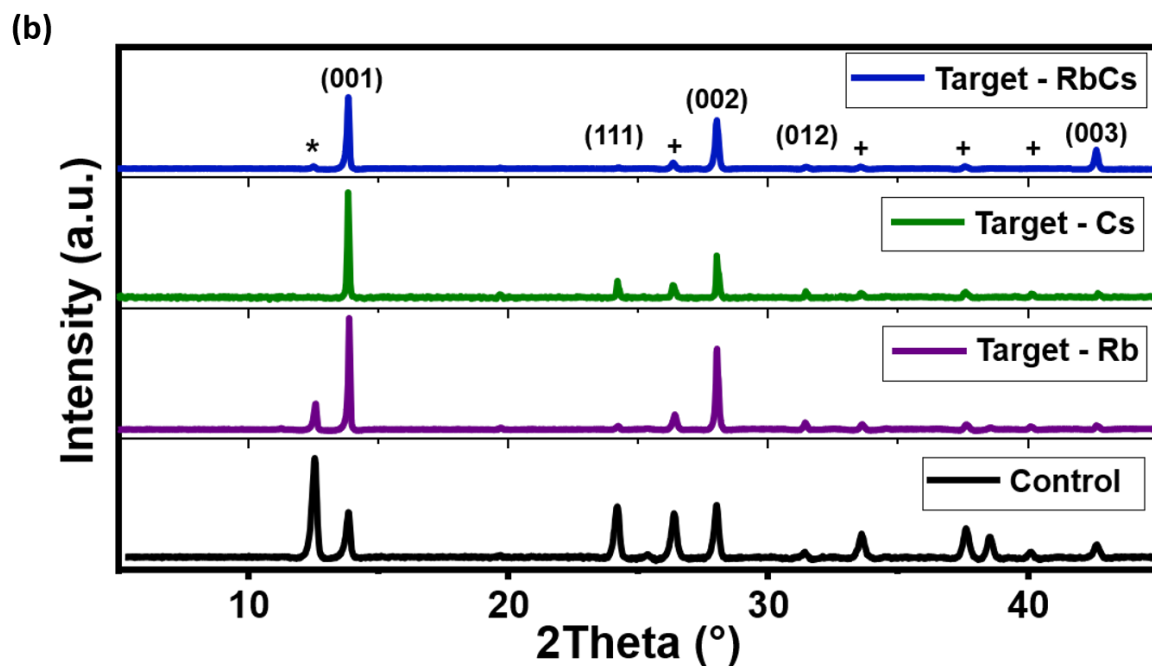


Figure 2. XRD patterns of (a) non-perovskite for PbI_2 , $\text{PbI}_2 \cdot 7\% \text{RbPbI}_3$, $\text{PbI}_2 \cdot 10\% \text{CsPbI}_3$, and $\text{PbI}_2 \cdot 7\% \text{RbPbI}_3 + 10\% \text{CsPbI}_3$ films, respectively, (Peaks marked with * and + are those assigned to PbI_2 and the FTO substrate respectively) and (b) Control, Target-Rb, Target-Cs, Target-RbCs perovskite films perovskite films.

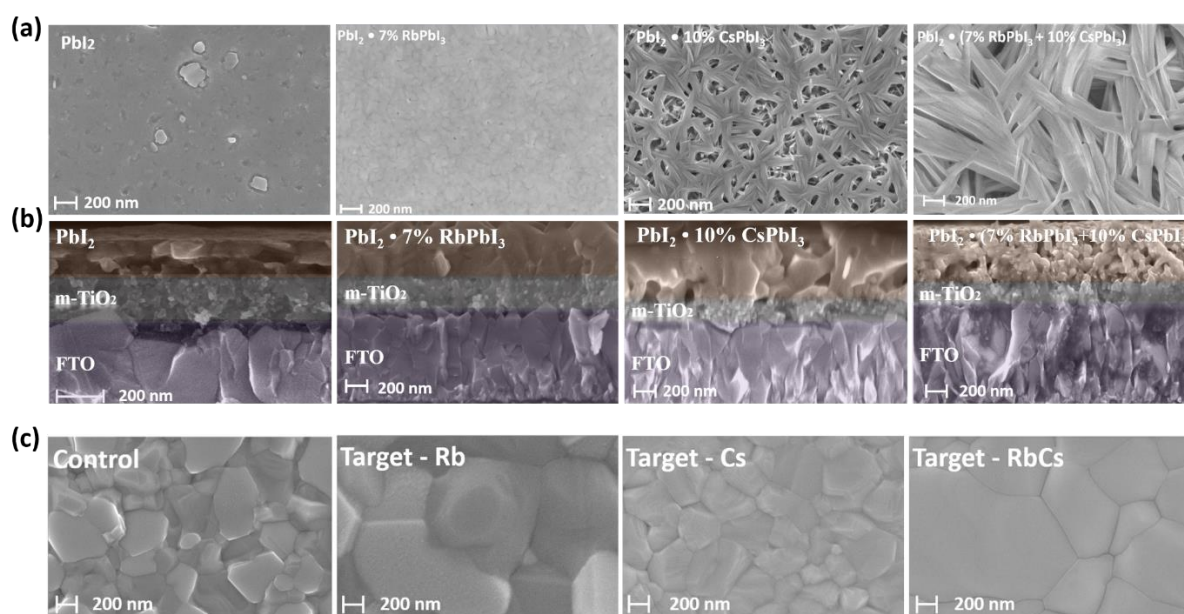


Figure 3. (a) SEM Top view and (b) cross-sectional images for PbI_2 , $\text{PbI}_2 \cdot 7\% \text{RbPbI}_3$, $\text{PbI}_2 \cdot 10\% \text{CsPbI}_3$, and $\text{PbI}_2 \cdot 7\% \text{RbPbI}_3 + 10\% \text{CsPbI}_3$ respectively films respectively and (c) SEM Top view pictures for Control, Target-Rb, Target-Cs, Target-RbCs perovskite film.

The XRD patterns of the PbI_2 films with and without the 7% RbPbI_3 , 10% CsPbI_3 and (7% $\text{RbPbI}_3 + 10\% \text{CsPbI}_3$) are shown in Fig.2a. The existence of 1D polymorphs of $\delta\text{-CsPbI}_3$ phase

in PbI_2 layer after the introduction of 10% CsPbI_3 can be observed at 25.5° . Fig.2a also shows some peaks at 21.5° , 24.6° , 25.2° , and 25.6° belonging to 1D orthorhombic RbPbI_3 ($\text{PbI}_2 \cdot 7\% \text{RbPbI}_3$). The same peaks are observed for the mixture of (7% RbPbI_3 + 10% CsPbI_3) together with the appearance of extra peaks at 25.5° and 28.8° belonging to the orthorhombic phase of CsPbI_3 ^{129–137}. It should be noted that the PbI_2 peak at 12.5° , which belongs to the (001) lattice phase of hexagonal (2H polytype) of PbI_2 ¹³⁸ is preserved in all compositions.

The XRD patterns of the corresponding perovskite films are shown in Fig.2b and Fig.S8a, S9a, S10a. The patterns of perovskites for the Control films reveals the presence of unreacted PbI_2 at 12.5° , whereas the PbI_2 peak was not observable for the Target-Cs and Target-RbCs perovskites (Fig.S8a, S9a, S10a). The suppression of the unreacted PbI_2 peaks indicates that Target-Cs and Target-RbCs indeed underwent complete conversion and exhibit enhanced crystallinity. Furthermore, the surface and cross-section morphology of the intermediate phase (first step) and of the final perovskite phase films on mesoporous TiO_2 was investigated via scanning electron microscopy (SEM). Top-view and cross-section SEM images of the PbI_2 film without and with various inorganic non-perovskite doping are shown in Fig.3a, Fig. 3b and Fig.S8b,S9b,S10b. The pristine PbI_2 and $\text{PbI}_2.7\%\text{RbPbI}_3$ film show a compact morphology, while the $\text{PbI}_2.10\%\text{CsPbI}_3$ and $\text{PbI}_2.(10\%\text{CsPbI}_3.7\%\text{RbPbI}_3)$ films exhibit a high degree of porosity and formation of nanorods. Previous work attributes the nanorods in the $\text{PbI}_2.10\%\text{CsPbI}_3$ films to $\delta\text{-CsPbI}_3$ ¹³⁹. The cross-section of $\text{PbI}_2.7\%\text{CsPbI}_3$ and $\text{PbI}_2.(10\%\text{CsPbI}_3.7\%\text{RbPbI}_3)$ show mesoscopic porous structure in contrast to the compact to pristine PbI_2 and $\text{PbI}_2.7\%\text{RbPbI}_3$ film. Such a mesoscopic network could be highly beneficial for facilitating the conversion of PbI_2 into the perovskite phase upon exposure to the organic salts.

The top-view SEM images of the perovskite films (Fig. 3c) indicate that the presence of Cs^+ or a mixture of Cs^+/Rb^+ cations there generates a drastic increase in the grain size as well as an

improvement in the homogeneity of the microstructure. This increase in grain size and phase purity indicates that the Target-Cs and Target-RbCs intermediate phase in the PbI_2 layer promotes the growth of perovskite grains via the increase of the porosity of the PbI_2 films. The high porosity of PbI_2 films enables the efficient penetration of FA/MA cations and the subsequent conversion of the PbI_2 films into the cubic α perovskite structure in agreement with the XRD characterization. By comparison, in the Control and Target-Rb perovskite films, several residual unreacted PbI_2 particles are observable on the top of the perovskite layer, whereas there is no residual PbI_2 in the Target-Cs and Target-RbCs films. We concluded that the addition of $\delta\text{-CsPbI}_3/\delta\text{-RbPbI}_3$ leads to a porous mesoscopic network, which facilitates the conversion into alpha perovskite leading to improved optoelectronic properties.

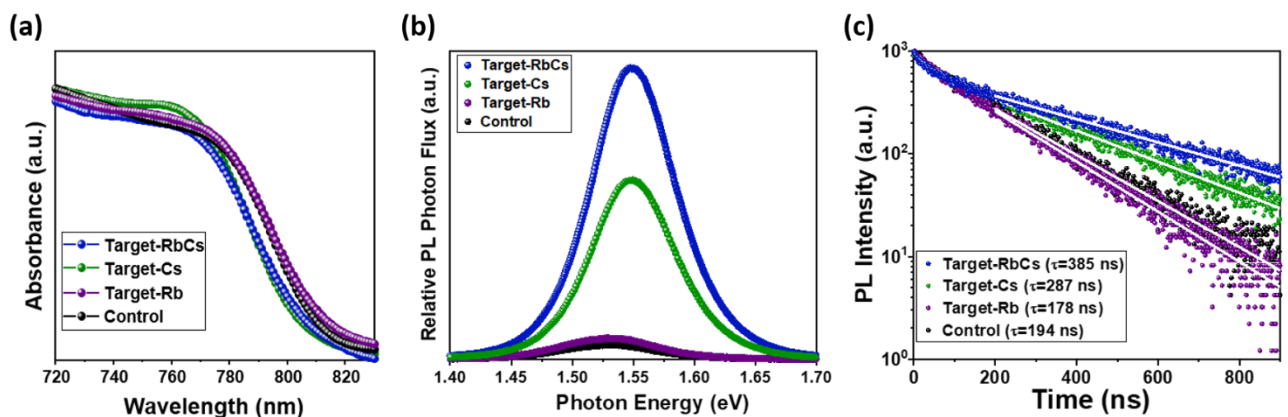


Figure 4. (a) Absorbance spectrum, (b) steady-state photoluminescence (PL), and (c) Time-resolved photoluminescence (TRPL) measurements of the different perovskite films, the solid lines are monoexponential fits for $t > 200$ ns.

Fig.4a shows the absorbance spectra of Control, Target-Rb, Target-Cs, and Target-RbCs perovskite films. A blueshift is observed in the absorbance spectra upon CsPbI_3 incorporation. The incorporation of the smaller Cs^+ ions into the double cation crystal lattice reduces the effective radius of the triple cations $(\text{Cs}_x(\text{FA}_{0.91}\text{MA}_{0.09})_{1-x})$ as compared to double cations. As a result, the tolerance factor is driven towards a cubic lattice structure, and an increase in the optical bandgap is observed, which is consistent with previous work⁹⁴. However, the undoped

Control perovskite and rubidium-doped (Target-Rb) perovskite films show an unchanged absorbance onset (Fig.4a), which is in good agreement with previous reports ^{128,140,141}, as Rb⁺ ions are not incorporated into the perovskite lattice but rather act as film quality enhancer and/or surface passivation layer ^{142–146}.

Relative steady-state photoluminescence (PL) photon flux spectra are shown in Fig. 4b, measured in the same measurement geometry so that the relative intensities can be compared. The PL spectra show an emission peak at 1.53 eV for Control, and Target-Rb, while all Cs-containing compositions Target-Cs and Target-CsRb exhibit a blue-shifted emission (Fig.4b and Fig.S8c, S9c, S10c). Furthermore, Target-Cs and Target-RbCs compositions show an emission peak at 1.55 eV, in agreement with the absorbance results as well as with external quantum efficiency (EQE) from the inflection point as shown in Fig. S17. Target-RbCs show the highest PL signal indicating the lowest non-radiative recombination rate, followed by Target-Cs, Target-Rb, and Control.

Next, we carried out time-resolved photoluminescence (TRPL) measurements to evaluate the charge carrier dynamics (Fig.4c) for Control, Target-Rb, Target-Cs, and Target-RbCs films. We performed our experiments at low fluences ($<5\text{ nJ/cm}^2$) so that bimolecular and Auger recombination is negligible ¹⁴⁷. All the TRPL traces show a monoexponential decay after $t > 200\text{ ns}$. This decay is due to non-radiative bulk and interface recombination. We cannot distinguish between these two mechanisms with this TRPL experiment, but we can give an upper limit for the monomolecular bulk recombination constant k_1 assuming zero interface recombination velocity. In that way, the upper limits of k_1 for Control, Target-Rb, Target-Cs and Target-RbCs are $2.58 \cdot 10^6\text{ s}^{-1}$, $2.81 \cdot 10^6\text{ s}^{-1}$, $1.74 \cdot 10^6\text{ s}^{-1}$, and $1.3 \cdot 10^6\text{ s}^{-1}$, respectively. This suggests that there is a decrease in non-radiative recombination in target Cs and target CsRb perovskites, which is in good agreement with the steady-state PL measurements.

Table 1. Chemical composition at the surface and in the bulk of the perovskite layer determined by XPS.

Depth	Rb/Cs	Br/I	Cs/Pb	Chemical composition
0 nm	0.903	0.0085	0.04	$\text{Rb}_{0.04}\text{Cs}_{0.04}\text{FA}_{0.91}\text{MA}_{0.01}\text{Pb}(\text{Br}_{0.01}\text{I}_{0.99})_3$
30 nm	0.406	0.0077	0.06	$\text{Rb}_{0.02}\text{Cs}_{0.05}\text{FA}_{0.92}\text{MA}_{0.01}\text{Pb}(\text{Br}_{0.01}\text{I}_{0.99})_3$

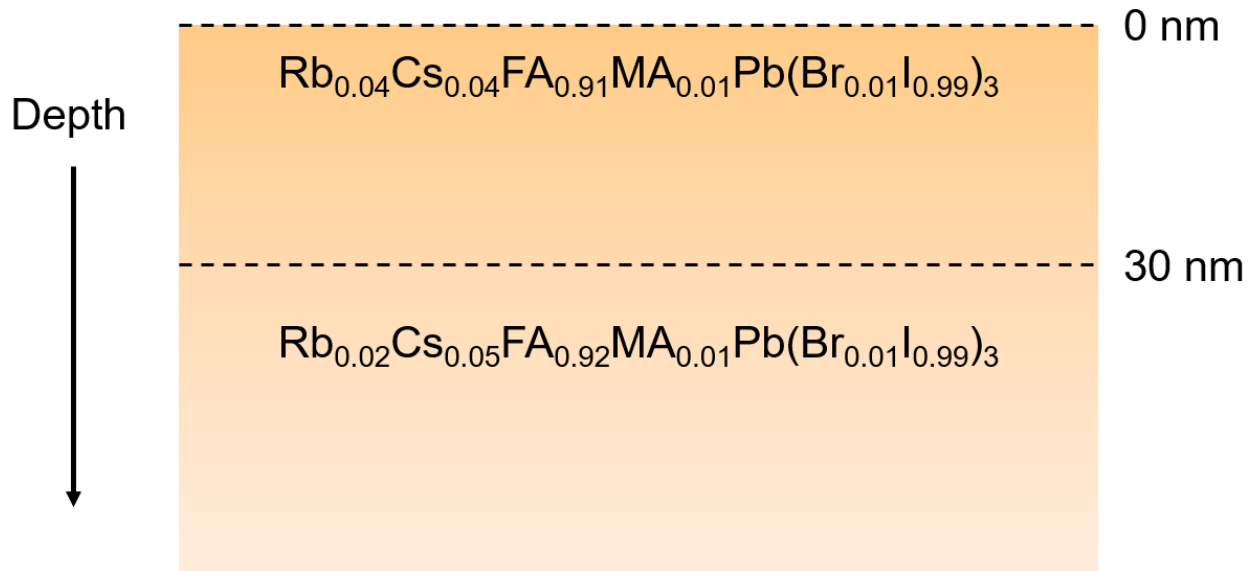


Figure 5. Scheme of the chemical composition at the surface and in the bulk of the perovskite layer from XPS measurement.

The elemental distribution of the composition with the longest carrier lifetime (Target-RbCs) was investigated using X-ray photoelectron spectroscopy (XPS). The XPS spectra (Fig.5, Fig.S11,S12) show that the elemental distribution differs between the surface (0 nm) and the bulk (30 nm) of the perovskite film (Table 1). As was expected^{143,144,148,149}, rubidium cations are not easily incorporated into the crystal lattice but rather preferentially act as surface defects passivation. In contrast to rubidium, the cesium cations are preferentially concentrated towards

the bulk of the perovskite films. We note that the I/Br ratio is decreased to only ~1%, which is in good agreement with the low bandgap of Target-RbCs (1.55 eV) estimated by PL and EQE measurements. Elemental ratios are summarized in Table 1 for the surface and the bulk. These results are consistent with previous reports^{128,140,150–152}.

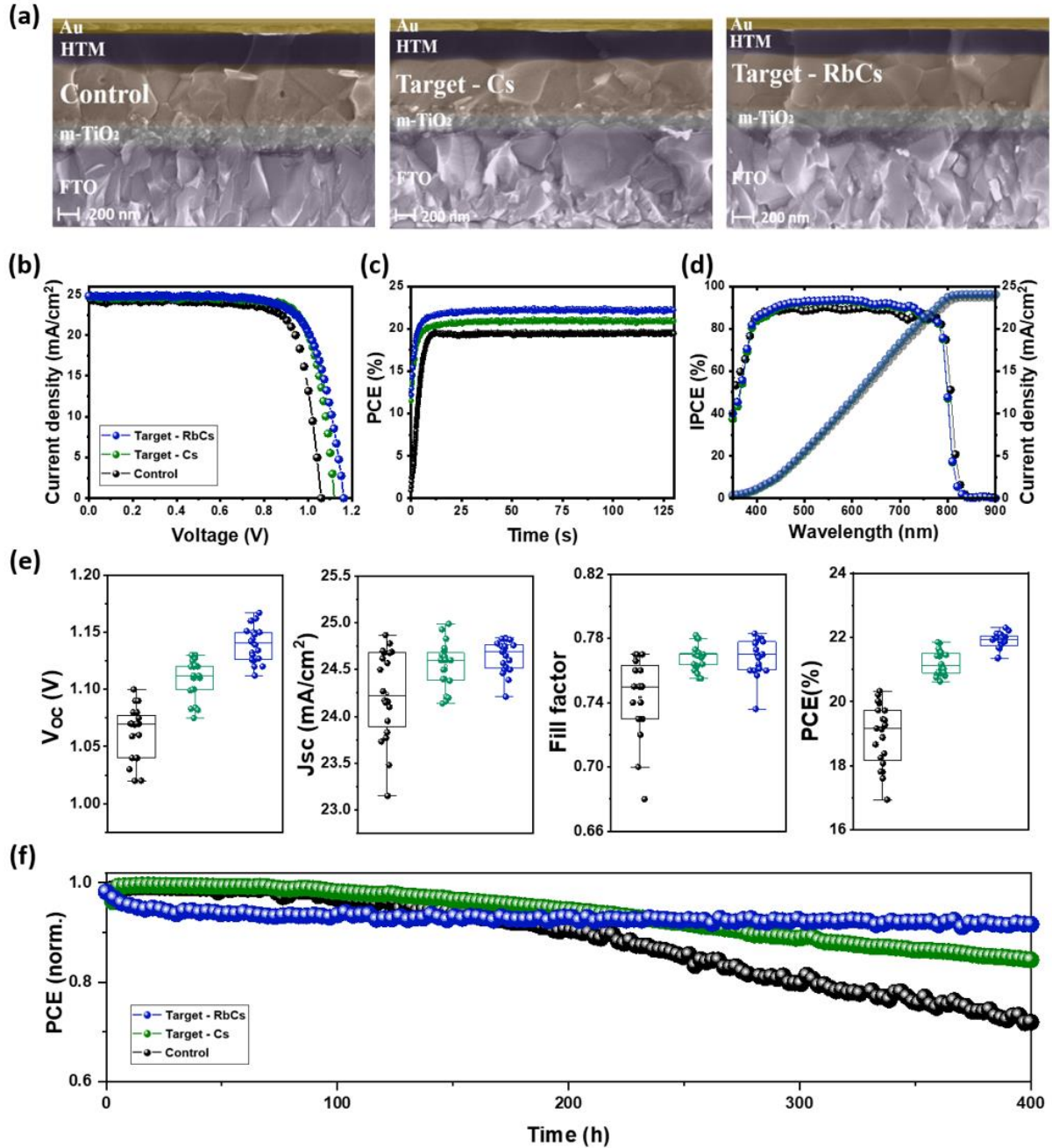


Figure 6. (a) Cross-sectional SEM images, (b) J-V curves of the devices, (c) maximum power point tracking, (d) IPCE spectra and photocurrent integrated over the standard AM 1.5G solar spectrum, (e) J-V metrics of devices, and (f) Operational stability in a nitrogen environment at room temperature

under continuous illumination (LED source, approximated 1 Sun) at maximum power point for Control, Target-Cs, Target-RbCs.

To examine the photovoltaic performance of these perovskites, we fabricated complete devices in a FTO/c-TiO₂/mp-TiO₂/perovskite/spiro-OMeTAD/Au architecture (see Fig.S13, S14, S15 for a comparison of all compositions). Fig.6a shows the cross-sectional SEM images of the full devices based on Control, Target-Cs and Target-RbCs perovskites. The champion Control perovskite device shows a PCE of 20.42%, V_{OC} of 1.06 V, a J_{SC} of 24.30 mA·cm⁻², and FF of 77%; the champion device for Target-Cs yields an enhanced PCE of 21.63%, with V_{oc} = 1.12 V, J_{sc} = 24.80 mA·cm⁻², and FF of 78%, while Target-RbCs shows a PCE of 22.30%, J_{sc} of 24.82 mA·cm⁻², V_{oc} = 1.15 V and FF of 78% as shown in Fig.6b. The ideality factor n_{id} was extracted from the illumination intensity as a function of the V_{oc} (Fig. S18). The Control, Target-Cs, and Target-RbCs devices show a n_{id} of 1.56, 1.45 and 1.44, respectively. The improvement in V_{oc} is in coherence with the PL, TRPL, and ideality factor which shows suppression in non-radiative recombination. To the best of our knowledge, this is the highest efficiency to be achieved in RbCsFAMA-based perovskite solar cells fabricated via sequential deposition on a mesoscopic architecture.

The hysteresis for the best devices is shown in Fig.S16. In Target-Cs and Target-RbCs a small PCE difference between forward and reverse scans is observed, with hysteresis index (HI = (PCE_{backward} - PCE_{forward})/PCE_{backward}) of 0.07 and 0.02 respectively, whereas the Control device exhibits a higher hysteresis in J-V scans with a HI of 0.13. The higher difference of hysteresis in the Control device is mainly due to the higher trap density in the perovskite film^{94,95,143}. Fig.6c shows the stabilized power output for the best performing devices during maximum power point tracking (MPP) in ambient air (10% RH (relative humidity)) under one sun illumination for 130 sec. The stabilized PCE upon MPP tracking for Control, Target-Cs and Target-RbCs are 19.5%, 21.2% and 22.1%, respectively.

The incident photon-to-current efficiency (IPCE) spectra and integrated current density are shown in Fig.6d. In agreement with absorbance spectra, a small blue shift in the onset of the IPCE spectra is detected for Target-Cs and Target-RbCs devices as compared to Control, while integrated current densities agree with the J_{sc} -values derived from the J-V measurements 24.04 $\text{mA}\cdot\text{cm}^{-2}$, 24.01 $\text{mA}\cdot\text{cm}^{-2}$ and 23.97 $\text{mA}\cdot\text{cm}^{-2}$. The statistical distribution of the photovoltaic characteristics (J_{sc} , V_{oc} , FF, and PCE) from at least 20 devices of each composition is presented in Fig.6e. The statistical distribution shows Target-Cs and Target-RbCs-based devices are much more reproducible than Control-based devices.

Operational stability remains a major concern in perovskite solar cells ^{153,154}. Therefore, the devices based on Control, Target-Cs, and Target-RbCs were subjected to light soaking in simulated solar irradiation at their maximum power for 400 hours under a nitrogen atmosphere at room temperature (Fig.6f). Devices fabricated with Control, Target-Cs and Target-RbCs perovskite retained ~72%, ~85%, and ~92% of the initial performance after 400 hr, respectively. This showed that our strategy to produce quadruple cation perovskite not only improves performance but also enhances the device stability.

Conclusion

In summary, we demonstrated the importance of the multi-cation halide composition engineering of perovskite solar cells fabricated by sequential deposition. Utilizing a mix of fully 1D inorganic photoinactive phase ($\delta\text{-RbPbI}_3/\delta\text{-CsPbI}_3$) resulted in an improvement of the perovskite crystallization via the creation of a mesoscopic porous network in the PbI_2 film, which enabled the facilitated penetration of the A-cations into PbI_2 and the subsequent conversion into efficient α cubic photoactive perovskite structures. XPS revealed that rubidium cations are mostly located at the surface of the perovskite film as well as the ratio of MAPbBr_3 is decreased to only ~1%, which is in good agreement with the low bandgap of Target-RbCs

(1.55 eV) estimated by PL/EQE measurements. There is significant enhancement of the open-circuit voltage from 1.06 V to 1.12 V, and 1.15 V, leading to a PCE of 20.42%, 21.63%, and 22.30% for Control, Target-Cs, and Target-RbCs, respectively. The Target-RbCs based device show high operational stability and retains more than 90% of its initial PCE after 400 hr illumination under MPP tracking. This work exemplifies the importance of tuning the crystallization in perovskite solar cells and has the potential to stimulate other successful developments in the future.

Experimental Section

Solar cell preparation: Fluorine-doped tin oxide (FTO)-glass substrates (TCO glass, NSG 10, Nippon sheet glass, Japan) were etched from the edges by using Zn powder and 4 M HCl and then, were cleaned by ultrasonication in Hellmanex (2%, deionized water), rinsed thoroughly with de-ionized water and ethanol, and then treated in oxygen plasma for 15 min. A 30 nm blocking layer (TiO_2) was deposited on the cleaned FTO by spray pyrolysis at 450 °C using a commercial titanium diisopropoxide bis(acetylacetonate) solution (75% in 2-propanol, Sigma-Aldrich) diluted in anhydrous ethanol (1:9 volume ratio) as precursor and oxygen as a carrier gas. A mesoporous TiO_2 layer was deposited by spin-coating a diluted paste in ethanol (1:6 wt. ratio) or (1:8.5 wt. ratio) or (1:10.5 wt. ratio) (Dyesol 30NRD: ethanol) (3000 rpm, acceleration 2000 rpm for 20 s) onto the substrate containing TiO_2 compact layer, and then sintered at 450 °C for 30 min in dry air.

Fabrication of perovskite films: 1.15 M PbI_2 or CsPbI_3 or RbPbI_3 or a mixture solution precursor were stirred at 70 °C for 12 h. PbI_2 , $\text{PbI}_{2-x}\%\text{CsPbI}_3$ ($x=0,5,10,15$ and 20%) or $\text{PbI}_{2-x}\%\text{RbPbI}_3$ ($x=0,7,10,15$ and 20%) or $\text{PbI}_{2-x}\%\text{CsPbI}_3.y\%\text{RbPbI}_3$ ($x=10\%$ and $y=0,7,10,15$ and 20%) solutions were spin-coated on FTO/c- TiO_2 /meso- TiO_2 substrate at 4000 r.p.m. for 45 s and then heated at 80 °C for 2-3 min to remove the solvents. After cooling down, the

FAI/MABr/MACl mixture solution was spin-coated on top of the PbI_2 or $\text{PbI}_{2.x}\%\text{CsPbI}_3$ or $\text{PbI}_{2.x}\%\text{RbPbI}_3$ or a mixture of $\text{PbI}_{2.10}\%\text{CsPbI}_{3.y}\%\text{RbPbI}_3$ at 2500 r.p.m. for 45 s followed by annealing at 100 °C for 10 min and 150 °C for 20 min with a relative humidity $\sim 30\pm 5\%$ to fabricate perovskite film. The HTM was deposited in by spin-coating at 4000 rpm for 30 s in a dry box with controlled humidity $\sim 8\pm 4\%$. The HTM was doped with bis(trifluoromethylsulfonyl)imide lithium salt (17.8 μl prepared by dissolving 520 mg LiTFSI in 1 ml of acetonitrile), and 28.8 μl of 4-tert-butylpyridine. Finally, a ~ 80 nm gold (Au) layer was thermally evaporated.

Device characterization: The current-voltage (J-V) characteristics of the perovskite devices were recorded with a digital source meter (Keithley model 2400, USA). A 450 W xenon lamp (Oriel, USA) was used as the light source for photovoltaic (J-V) measurements. The spectral output of the lamp was filtered using a Schott K113 Tempax sunlight filter (Präzisions Glas & Optik GmbH, Germany) to reduce the mismatch between the simulated and actual solar spectrum to less than 2%. The photo-active area of 0.16 cm^2 was defined using a dark-colored metal mask.

Incident photon-to-current efficiency (IPCE): was recorded under a constant white light bias of approximately 5 mW cm^{-2} supplied by an array of white light emitting diodes. The excitation beam coming from a 300 W Xenon lamp (ILC Technology) was focused through a Gemini-180 double monochromator (Jobin Yvon Ltd) and chopped at approximately 2 Hz. The signal was recorded using a Model SR830 DSP Lock-In Amplifier (Stanford Research Systems).

Scanning electron microscopy (SEM): was performed on a ZEISS Merlin HR-SEM.

X-ray powder diffractions were recorded on an X'Pert MPD PRO (Panalytical) equipped with a ceramic tube (Cu anode, $\lambda = 1.54060$ Å), a secondary graphite (002) monochromator and a RTMS X'Celerator (Panalytical).

UV-Vis measurements (UV-vis) were performed on a Varian Cary 5.

Photoluminescence spectra (PL) were obtained with a Florolog 322 (Horiba Jobin Yvon Ltd) in the wavelength range from 500 nm to 850 nm by exciting at 460 nm.

Time-resolved photoluminescence (TRPL) was measured with a spectrometer (FluoroLog-3, Horiba) working in a time-correlated single-photon counting mode with <ns time resolution. A picosecond pulsed diode laser head NanoLED N-670L (Horiba) emitting <200 ps duration pulses at 670 nm with a maximum repetition rate of 1 MHz was used as excitation source.

Long term light soaking test: Stability measurements were performed with a Biologic MPG2 potentiostat under a full AM 1.5 Sun-equivalent white LED lamp. The devices were measured with a maximum power point (MPP) tracking routine under continuous illumination at room temperature. The MPP was updated every 10 s by a standard perturb and observe method. Every minute a JV curve was recorded in order to track the evolution of individual JV parameters.

X-ray photoelectron spectroscopy (XPS): was carried out using a PHI VersaProbe II scanning XPS microprobe with Al K α X-ray source. The spherical capacitor analyser was set at 45° take-off angle with respect to the sample surface. Bulk composition analysis was done after argon plasma etching. Data were processed using the PHI Multipak software.

Supplementary Information

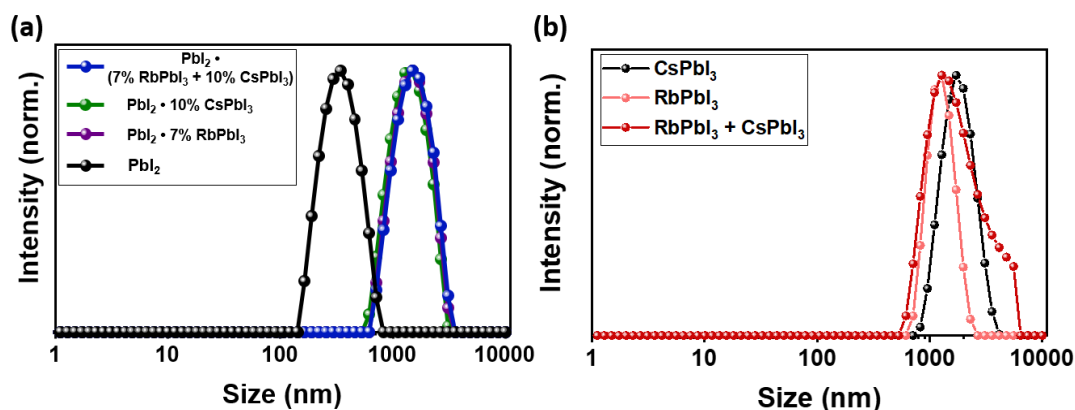


Figure S1. Dynamic Light scattering spectra of perovskite precursor solution (a) the variation of colloids: PbI_2 , $\text{PbI}_2 \bullet 7\% \text{RbPbI}_3$, $\text{PbI}_2 \bullet 10\% \text{CsPbI}_3$ and $\text{PbI}_2 \bullet (7\% \text{RbPbI}_3 + 10\% \text{CsPbI}_3)$, respectively and (b) CsPbI_3 , RbPbI_3 and mixture of pure 10:7 CsPbI_3 : RbPbI_3 without PbI_2 .

Figures from S2 to S7, the first step was prepared using the following composition: $\text{PbI}_2 \bullet 10\% \text{CsPbI}_3$ (Target-Cs)

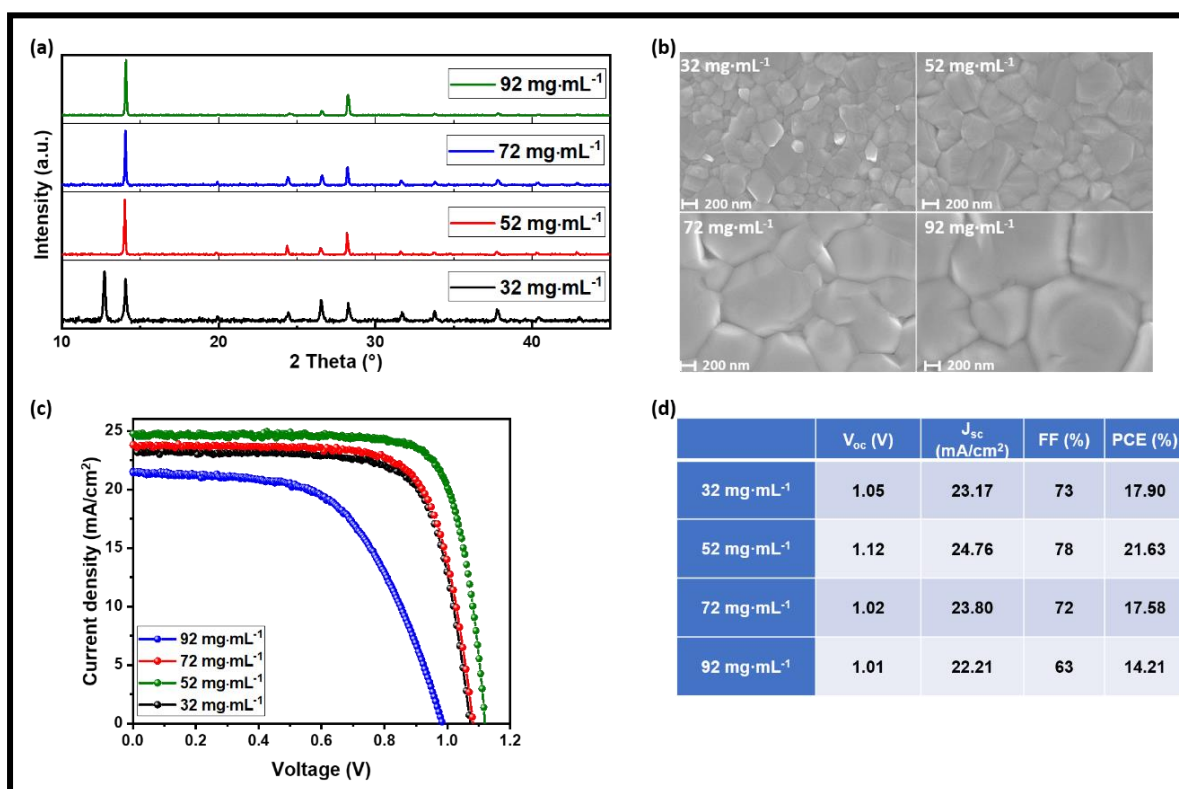


Figure S2 Optimization of different concentrations (a) XRD, (b) SEM, (c) J-V curves and (d) J-V summarized results.

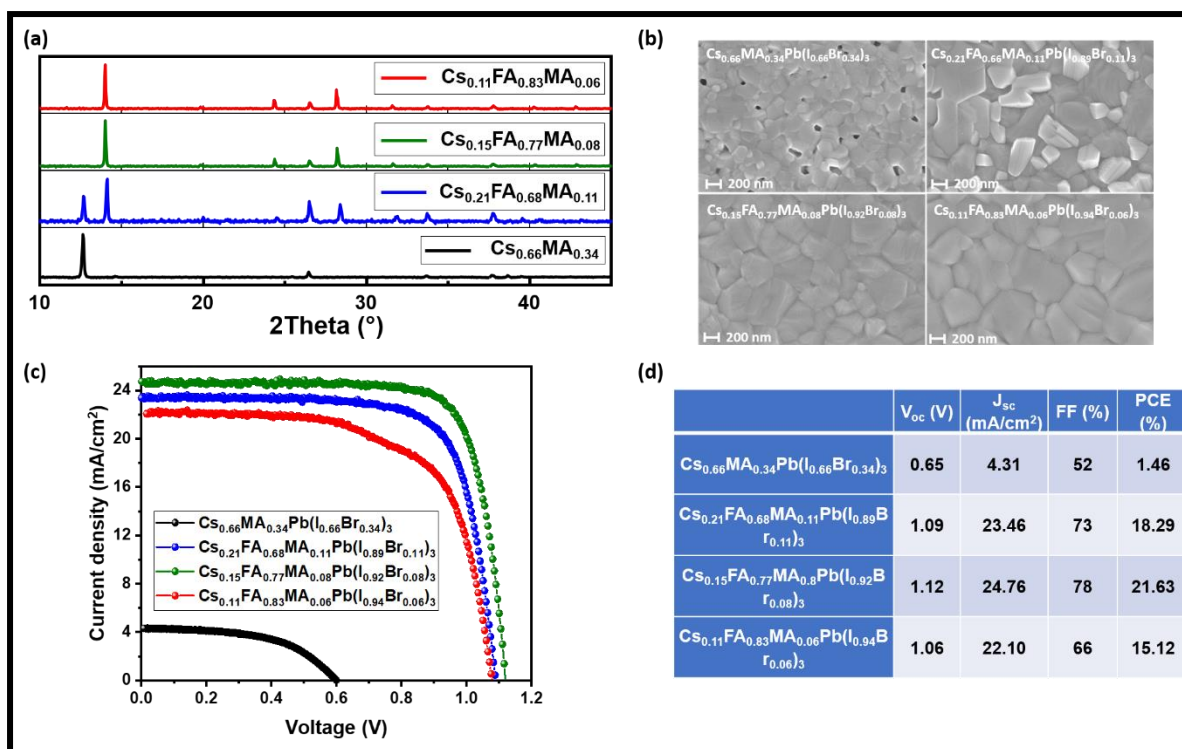


Figure.S3 Optimization of ratio of FAI (a) XRD, (b) SEM, (c) J-V curves and (d) J-V summarized results.

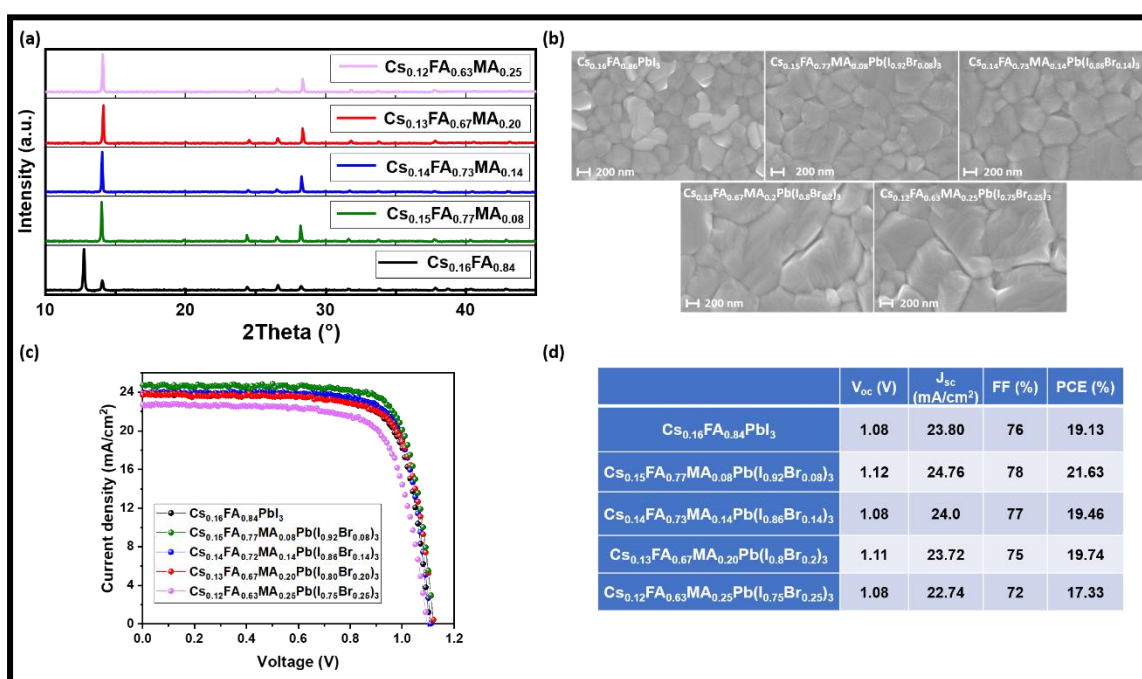


Figure.S4 Optimization of ratio of MABr (a) XRD, (b) SEM, (c) J-V curves and (d) J-V summarized results.

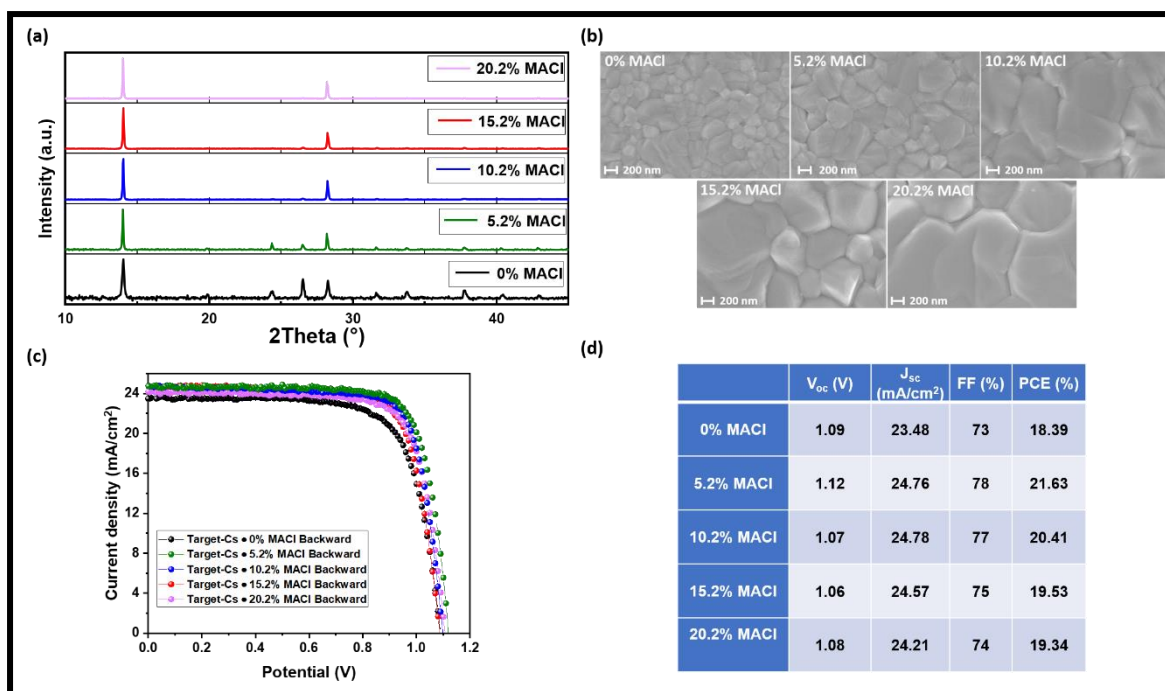


Figure.S5 Optimization of the addition of MACl (a) XRD, (b) SEM, (c) J-V curves and (d) J-V summarized results.

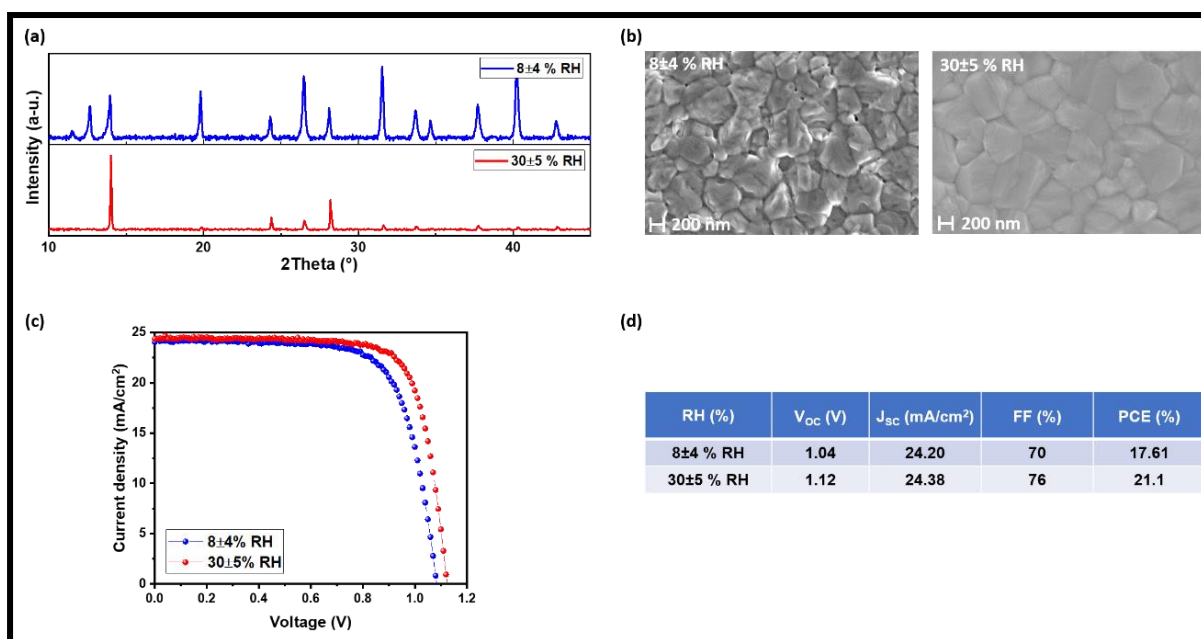


Figure.S6 Effect of relative humidity on the crystallization of perovskite films and device.

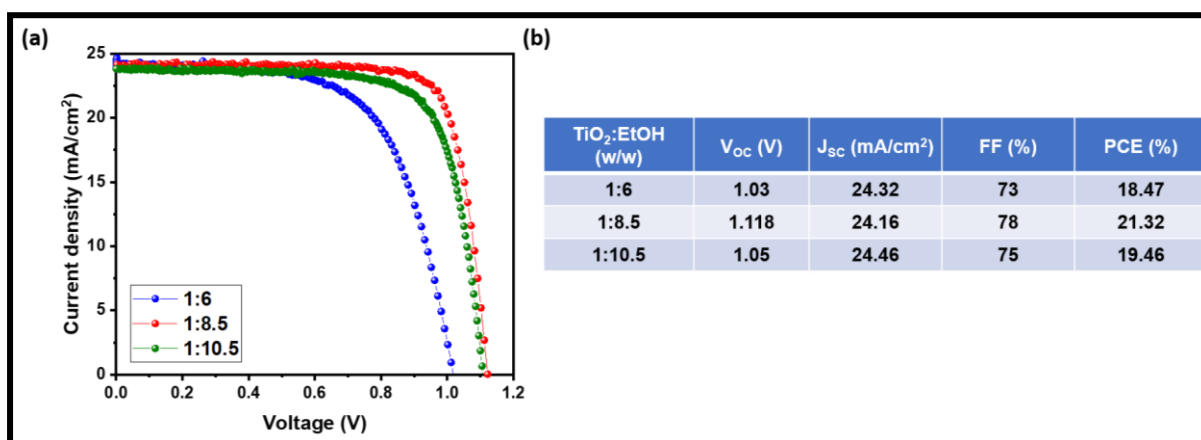


Figure.S7 Influence of the mesoporous TiO₂ solution concentration on the perovskite devices. The concentration of the solution determines the thickness of the final TiO₂ layer

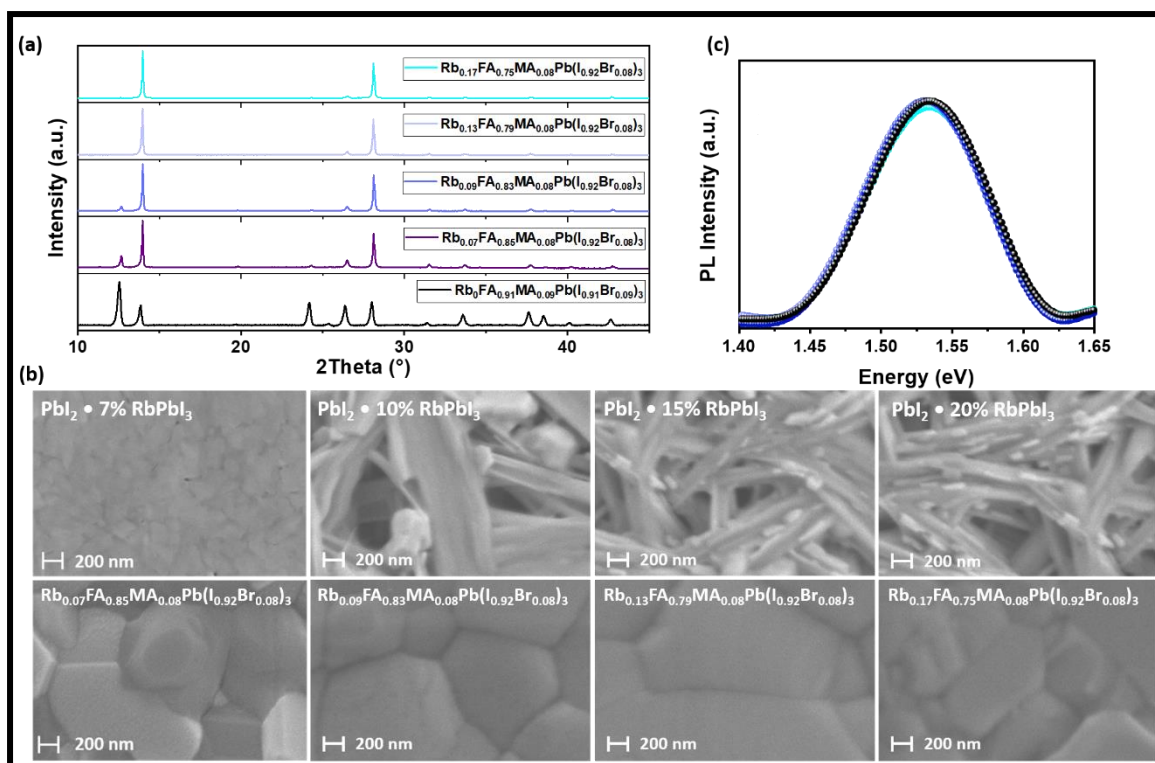


Figure.S8 (a) XRD and (b) PL of $Rb_x \cdot FA_{91}MA_9$. (c) SEM of $PbI_2 \cdot Rb_x$ and $Rb_x \cdot FA_{91}MA_9$.

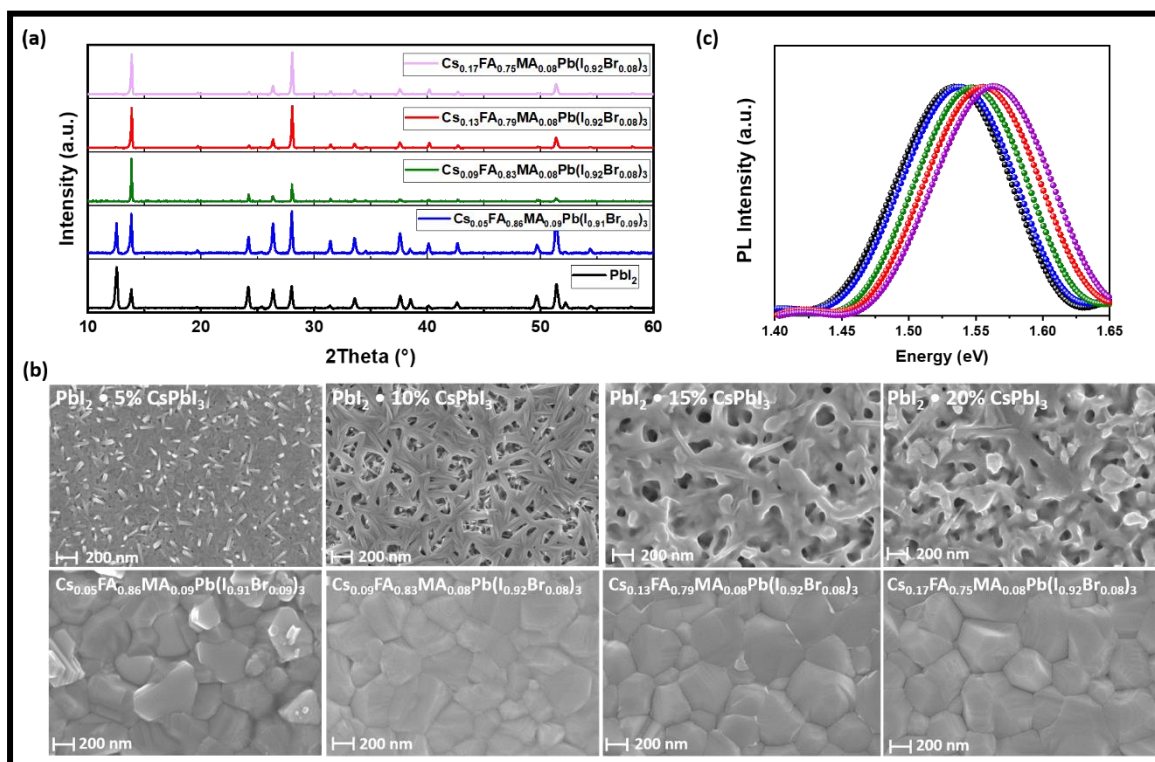


Figure.S9 (a) XRD and (b) PL of $Cs_x \cdot FA_{91}MA_9$. (c) SEM of $PbI_2 \cdot Cs_x$ and $Rb_x \cdot FA_{91}MA_9$.

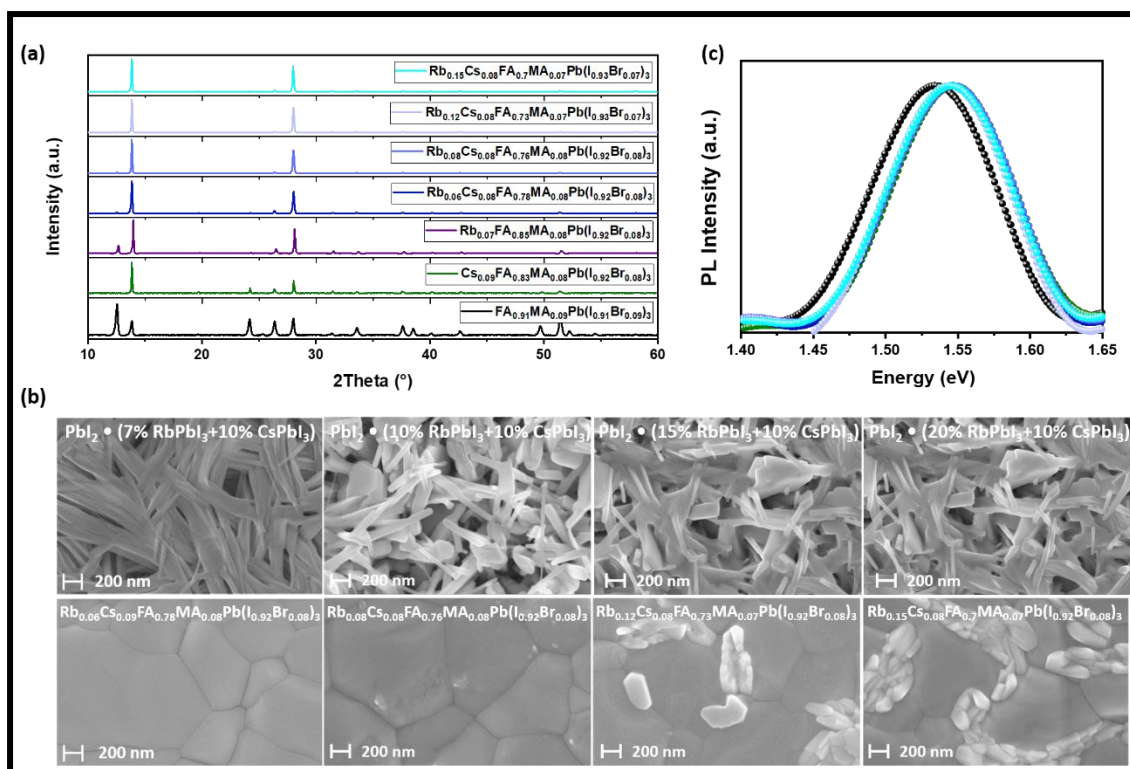


Figure.S10 (a) XRD and (b) PL of $\text{Rb}_x \cdot \text{Cs}_{10}\text{FA}_{91}\text{MA}_9$. (c) SEM of $\text{PbI}_2 \cdot (\text{Rb}_x + \text{Cs}_{10})$ and $\text{Rb}_x \cdot \text{Cs}_{10}\text{FA}_{91}\text{MA}_9$.

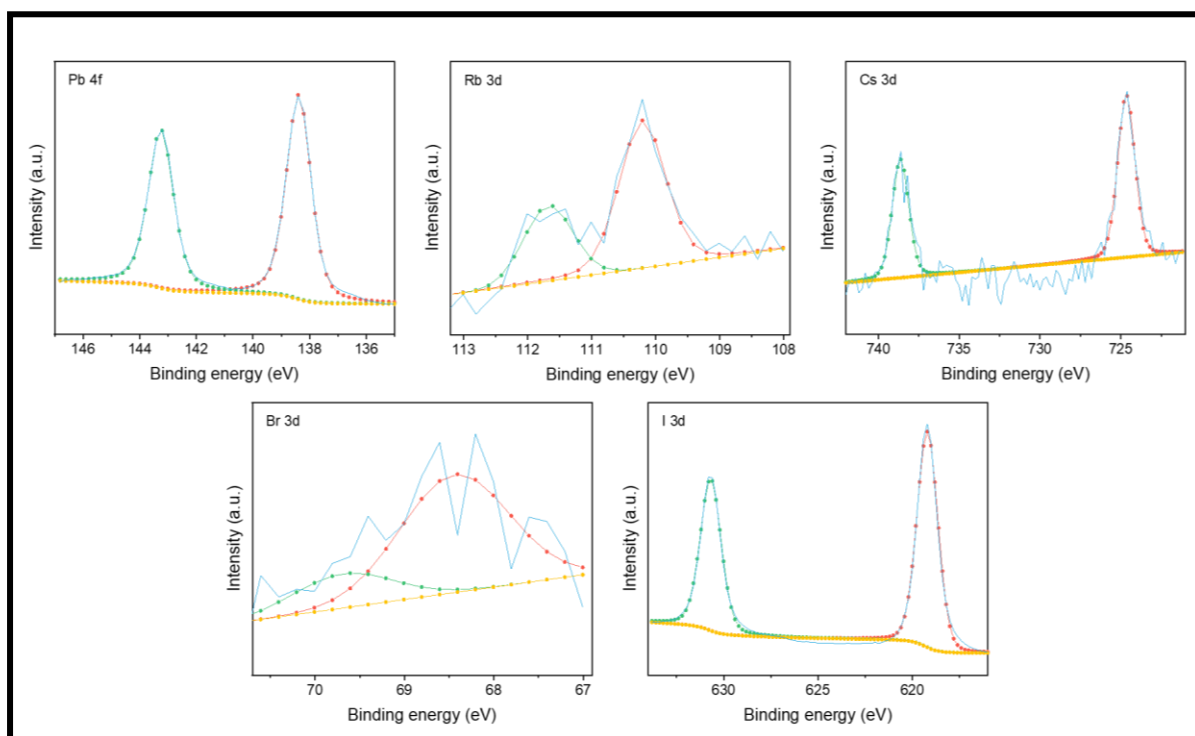


Figure S11 XPS spectra of the perovskite films at 0 nm (at the surface)

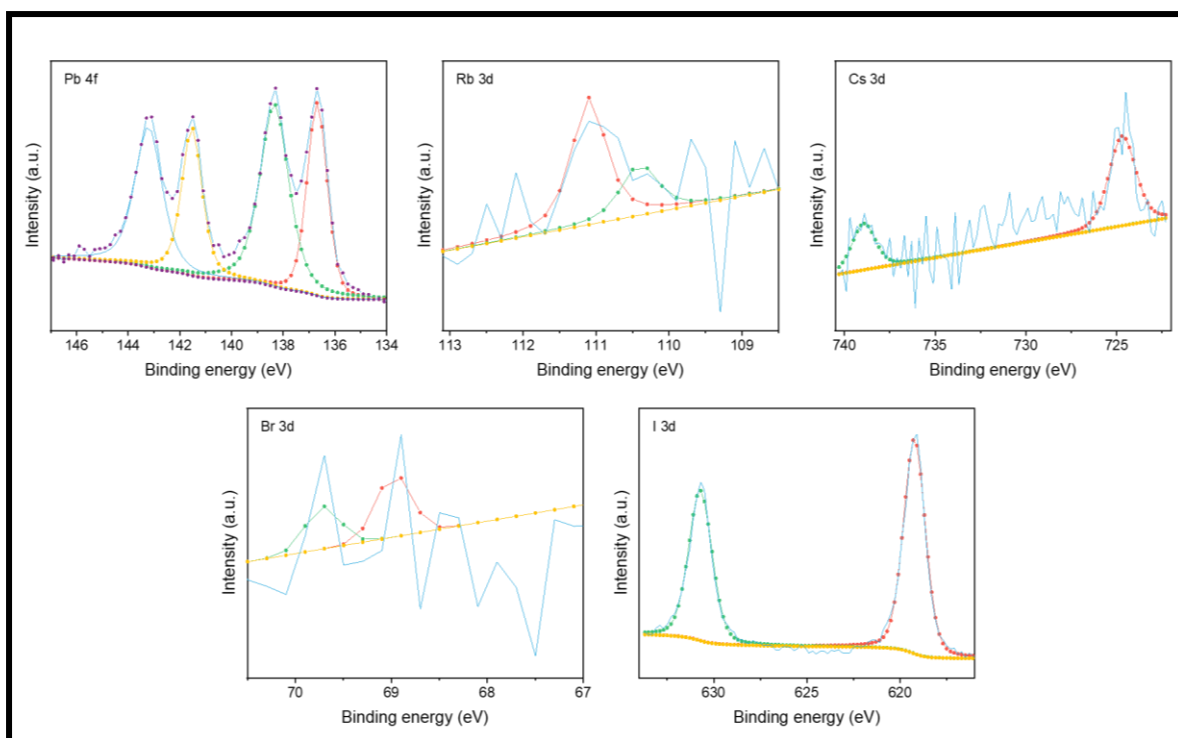


Figure S12 XPS spectra of the perovskite films at 30 nm (in the bulk)

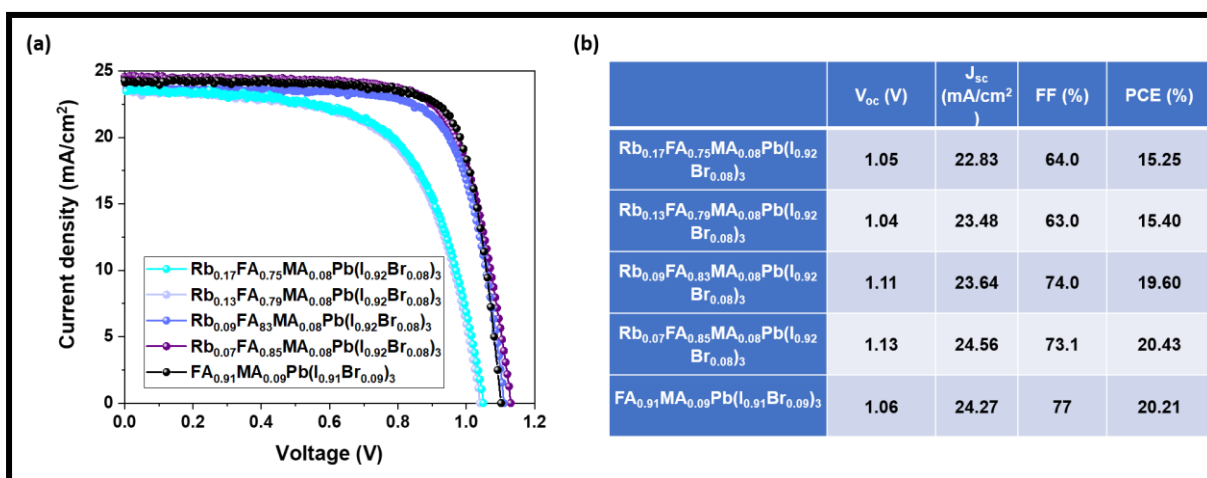


Figure S13. J-V curves and summarized results of $y\%$ $RbPbI_3 \cdot FA_{91}MA_9Pb(I_{91}Br_9)_3$ ($y = 7, 10, 15$ and 20).

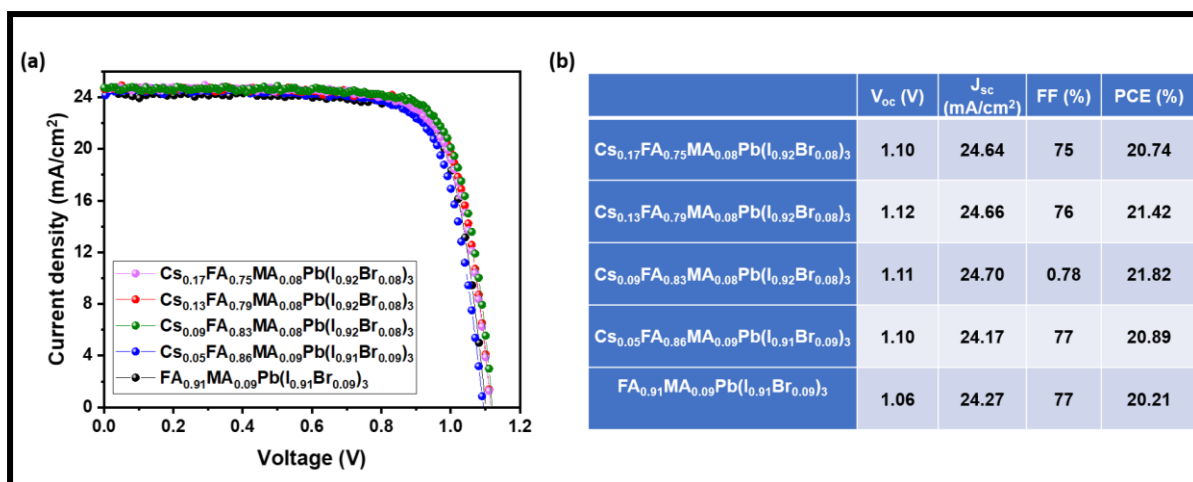


Figure S14. *J-V curves and summarized results of $x\%$ CsPbI₃•FA₉₁MA₉Pb(I₉₁Br₉)₃ ($x = 5, 10, 15$ and 20%).*

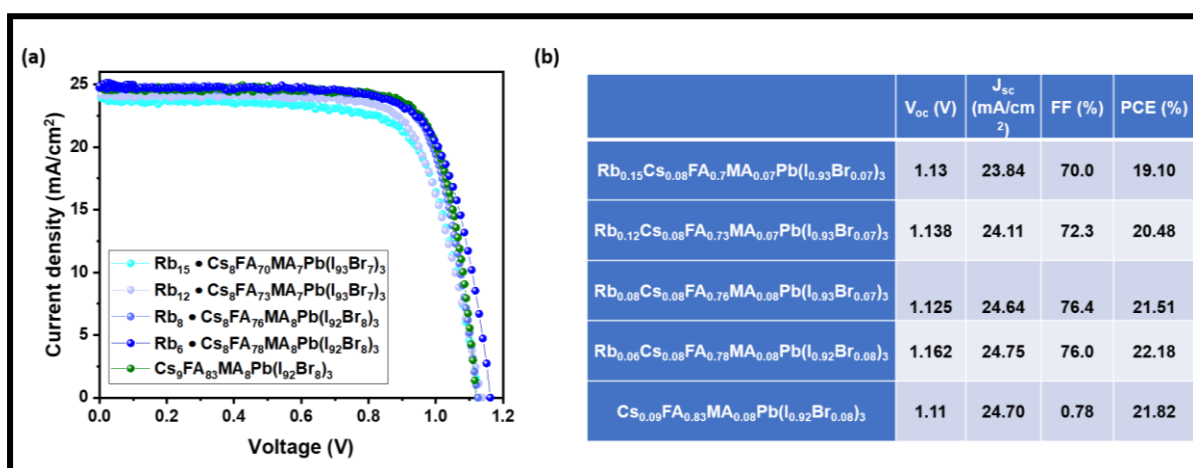


Figure S15. *J-V curves and summarized results of $y\%$ RbPbI₃•Target-Cs ($y = 7, 10, 15$ and 20).*

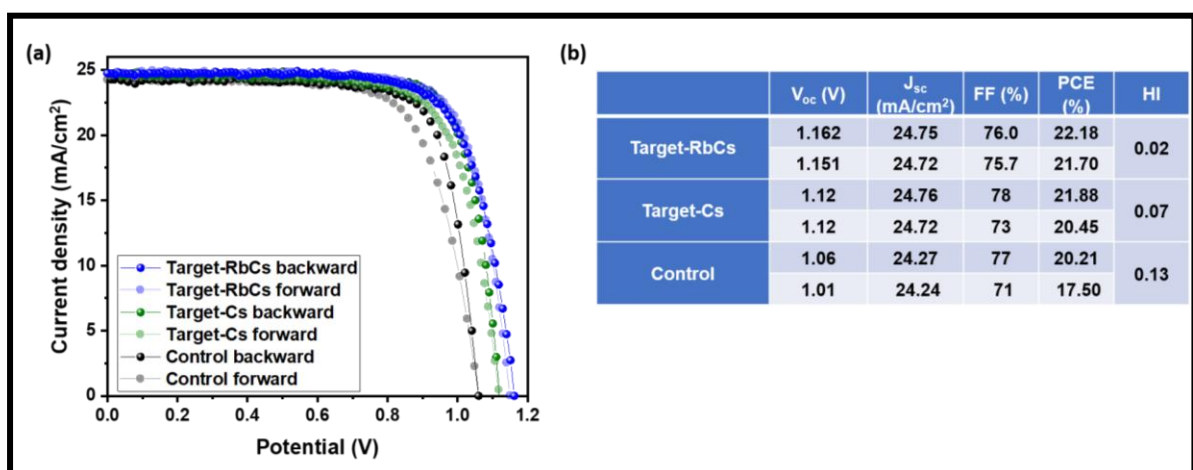


Figure S16. *J-V curves at forward and reverse scans and summarized results of Control, Target-Cs and Target-RbCs.*

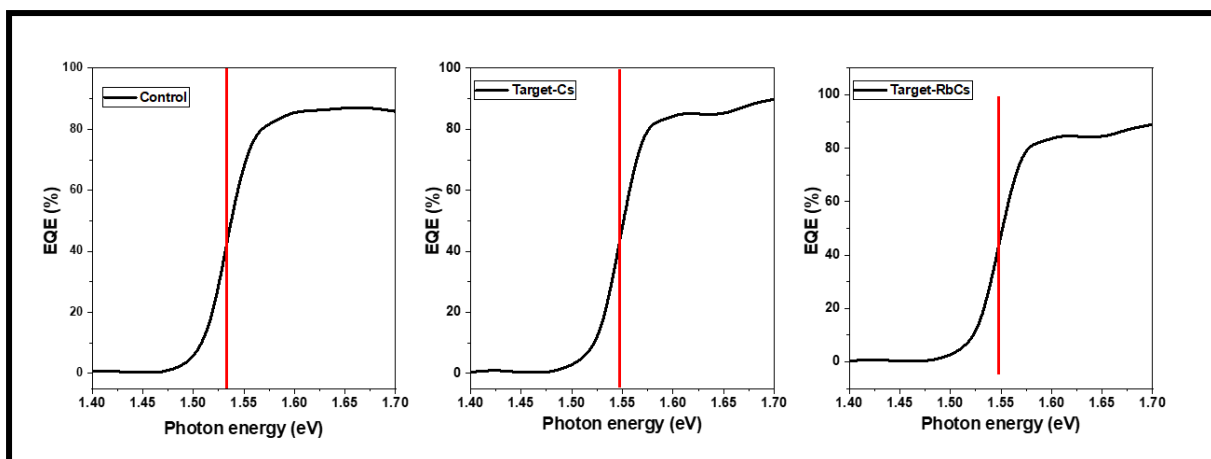


Figure S17. Bandgap extracted from EQE of solar cells.

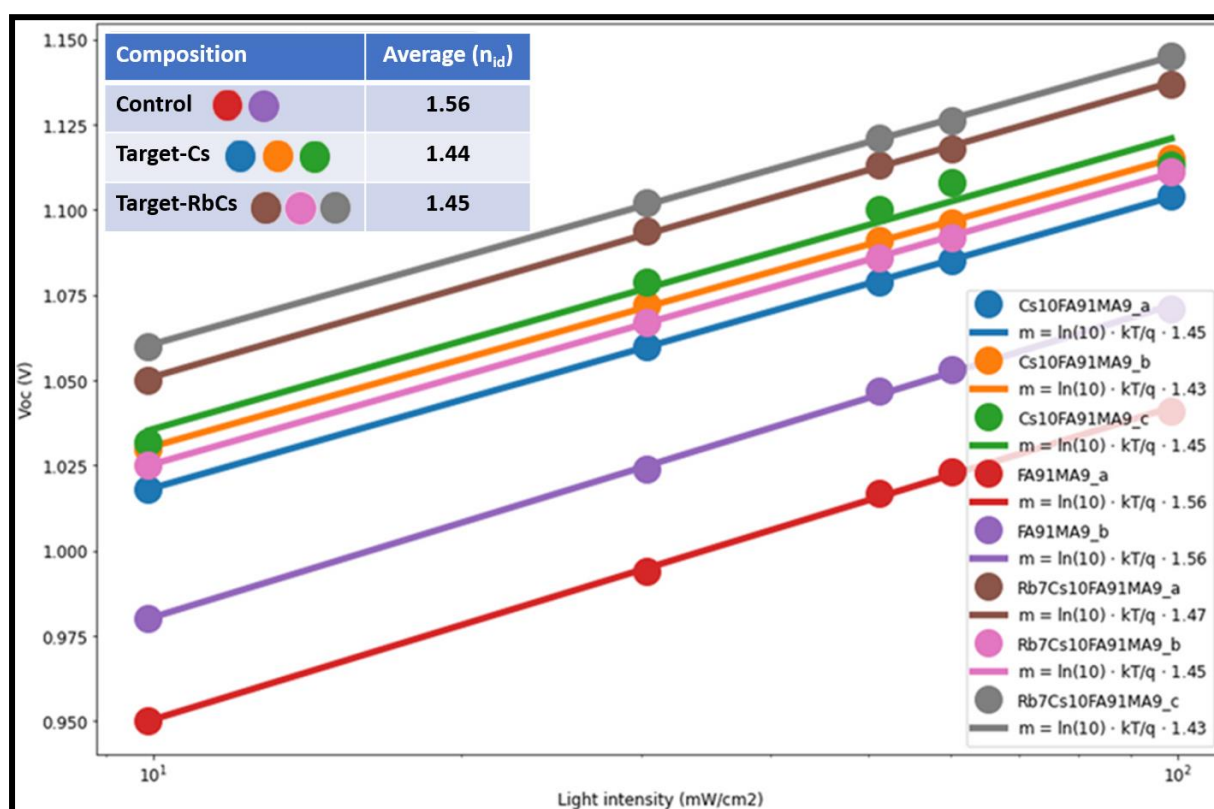


Figure S18. Ideality factor of solar cells.

References

1. Global primary energy consumption by source.
https://ourworldindata.org/grapher/global-energy-consumption-source?country=~OWID_WRL.
2. Morris, C. R. The dawn of innovation : the first American Industrial Revolution. 368 (2012).
3. Britannica, E. of the encyclopedia. 'Edwin Drake - American oil driller'. *Encyclopedia Britannica*.
4. Deese, D. A. Energy: Economics, Politics, and Security. *Int. Secur.* **4**, 140 (1979).
5. Hawks, J., Hunley, K., Lee, S. H. & Wolpoff, M. Population bottlenecks and Pleistocene human evolution. *Mol. Biol. Evol.* **17**, 2–22 (2000).
6. van Ruijven, B. J., De Cian, E. & Sue Wing, I. Amplification of future energy demand growth due to climate change. *Nat. Commun.* **10**, 1–12 (2019).
7. Watari, T. *et al.* Total material requirement for the global energy transition to 2050: A focus on transport and electricity. *Resour. Conserv. Recycl.* **148**, 91–103 (2019).
8. Perez, R. & Perez, M. A fundamental look at energy reserves for the planet.
9. Twidale, S. Flows through Russia's Yamal-Europe gas pipeline turn eastwards | Reuters. *Reuters* <https://www.reuters.com/business/energy/russias-yamal-europe-gas-pipeline-halts-westbound-flows-data-2022-03-15/> (2022).
10. Crude oil - 2022 Data - 1983-2021 Historical - 2023 Forecast - Price - Quote - Chart.
<https://tradingeconomics.com/commodity/crude-oil>.
11. De Broglie, L. Recherches sur la théorie des Quanta.
12. Singh, N., Kaushik, S. C. & Misra, R. D. Exergetic analysis of a solar thermal power system. *Renew. Energy* **19**, 135–143 (2000).
13. *Thermal, Mechanical, and Hybrid Chemical Energy Storage Systems*. (Elsevier, 2021).

doi:10.1016/C2019-0-00430-X.

14. Becquerel, E. Comptes rendus hebdomadaires. *Comptes rendus l'Académie des Sci.* (1839).
15. Kuzemsky, A. L. Band Theory and Electronic Properties of Solids. *Stat. Mech. Phys. Many-Particle Model Syst.* 297–318 (2017) doi:10.1142/9789813145641_0012.
16. Luque, A. & Hegedus, S. Handbook of Photovoltaic Science and Engineering. *Handb. Photovolt. Sci. Eng.* (2005) doi:10.1002/0470014008.
17. Kirk, A. P. Solar Photovoltaic Cells: Photons to Electricity. *Sol. Photovolt. Cells Photons to Electr.* 1–123 (2014) doi:10.1016/C2014-0-03052-3.
18. Jobayer Hossain, M., Hossain, J. & Mohammad. Novel High Efficiency Quadruple Junction Solar Cell with Current Matching and Optimized Quantum Efficiency. *arXiv arXiv:1904.01108* (2019).
19. Tress, W. Perovskite Solar Cells on the Way to Their Radiative Efficiency Limit – Insights Into a Success Story of High Open-Circuit Voltage and Low Recombination. *Adv. Energy Mater.* **7**, 1602358 (2017).
20. Nelson, J. The Physics of Solar Cells. *Phys. Sol. Cells* (2003) doi:10.1142/P276.
21. Drud Nielsen, L. Distributed Series Resistance Effects in Solar Cells. *IEEE Trans. Electron Devices* **29**, 821–827 (1982).
22. Araújo, G. L., Cuevas, A. & Ruiz, J. M. The Effect of Distributed Series Resistance on the Dark and Illuminated Current-Voltage Characteristics of Solar Cells. *IEEE Trans. Electron Devices* **33**, 391–401 (1986).
23. Charles, J. P., Abdelkrim, M., Muoy, Y. H. & Mialhe, P. A practical method of analysis of the current-voltage characteristics of solar cells. *Sol. Cells* **4**, 169–178 (1981).
24. Lorenzo, E. *et al.* Solar Electricity: Engineering of Photovoltaic Systems. 316 (1994).
25. Gueymard, C. A., Myers, D. & Emery, K. Proposed reference irradiance spectra for

solar energy systems testing. *Sol. Energy* **73**, 443–467 (2002).

26. Solar Spectra | Grid Modernization | NREL. <https://www.nrel.gov/grid/solar-resource/spectra.html>.

27. Lashkaryov, V. E. INVESTIGATIONS OF A BARRIER LAYER BY THE THERMOPROBE METHOD. *Izv. Akad. Nauk SSSR, Ser. Fiz* **5**, 442–446 (1941).

28. Ohl, R. S. Light-sensitive electric device. (1941).

29. Chapin, D. M., Fuller, C. S. & Pearson, G. L. A new silicon p-n junction photocell for converting solar radiation into electrical power [3]. *Journal of Applied Physics* vol. 25 676–677 (1954).

30. Green, M. *et al.* Solar cell efficiency tables (version 57). *Prog. Photovoltaics Res. Appl.* **29**, 3–15 (2021).

31. Stoppato, A. Life cycle assessment of photovoltaic electricity generation. *Energy* **33**, 224–232 (2008).

32. Kim, G. *et al.* Transparent Thin-Film Silicon Solar Cells for Indoor Light Harvesting with Conversion Efficiencies of 36% without Photodegradation. *ACS Appl. Mater. Interfaces* **12**, 27122–27130 (2020).

33. Muteri, V. *et al.* Review on Life Cycle Assessment of Solar Photovoltaic Panels. *Energies* 2020, Vol. 13, Page 252 **13**, 252 (2020).

34. Luceño-Sánchez, J. A., Díez-Pascual, A. M. & Capilla, R. P. Materials for Photovoltaics: State of Art and Recent Developments. *Int. J. Mol. Sci.* 2019, Vol. 20, Page 976 **20**, 976 (2019).

35. Nakamura, M. *et al.* Cd-Free Cu(In,Ga)(Se,S)₂ thin-film solar cell with record efficiency of 23.35%. *IEEE J. Photovoltaics* **9**, 1863–1867 (2019).

36. National Renewable Energy Laboratory of the United States of America (NREL) National Center for Photovoltaics. Best Research-Cell Efficiencies chart.

<https://www.nrel.gov/pv/assets/pdfs/best-research-cell-efficiencies.20200925.pdf>.

37. First Solar, Inc. - First Solar Achieves Yet Another Cell Conversion Efficiency World Record. <https://investor.firstsolar.com/news/press-release-details/2016/First-Solar-Achieves-Yet-Another-Cell-Conversion-Efficiency-World-Record/default.aspx>.
38. Ali, A. M. *et al.* A computational study on the energy bandgap engineering in performance enhancement of CdTe thin film solar cells. *Results Phys.* **7**, 1066–1072 (2017).
39. Geisz, J. F., Steiner, M. A., García, I., Kurtz, S. R. & Friedman, D. J. Enhanced external radiative efficiency for 20.8% efficient single-junction GaInP solar cells. *Appl. Phys. Lett.* **103**, 041118 (2013).
40. Kotulak, N. A. & Barner, K. E. Growth and analysis of gallium phosphide on silicon for very high efficiency solar cells. (2011).
41. Wang, W. *et al.* Device Characteristics of CZTSSe Thin-Film Solar Cells with 12.6% Efficiency. *Adv. Energy Mater.* **4**, 1301465 (2014).
42. Bag, S. *et al.* Low band gap liquid-processed CZTSe solar cell with 10.1% efficiency. *Energy Environ. Sci.* **5**, 7060–7065 (2012).
43. Kojima, A., Teshima, K., Shirai, Y. & Miyasaka, T. Organometal halide perovskites as visible-light sensitizers for photovoltaic cells. *J. Am. Chem. Soc.* **131**, 6050–6051 (2009).
44. Kim, M. *et al.* Conformal quantum dot–SnO₂ layers as electron transporters for efficient perovskite solar cells. *Science* (80-.). **375**, 302–306 (2022).
45. Liu, F. *et al.* Organic Solar Cells with 18% Efficiency Enabled by an Alloy Acceptor: A Two-in-One Strategy. *Adv. Mater.* **33**, (2021).
46. Hazen, R. M. Perovskites. *Sci. Am.* **258**, 74–80 (1988).
47. Miyasaka, T. Hybrid Perovskite Solar Cells. *Hybrid Perovskite Sol. Cells* (2021) doi:10.1002/9783527825851.
48. Schooley, J. F., Hosler, W. R. & Cohen, M. L. Superconductivity in Semiconducting

SrTi₃. *Phys. Rev. Lett.* **12**, 474–475 (1964).

49. Pedersen, L. A. & Libby, W. F. Unseparated rare earth cobalt oxides as auto exhaust catalysts. *Science* (80-.). **176**, 1355–1356 (1972).

50. Kobayashi, K. I., Kimura, T., Sawada, H., Terakura, K. & Tokura, Y. Room-temperature magnetoresistance in an oxide material with an ordered double-perovskite structure. *Natur* **395**, 677–680 (1998).

51. Philipp, J. B. *et al.* Spin-dependent transport in the double-perovskite Sr₂CrWO₆. *Appl. Phys. Lett.* **79**, 3654 (2001).

52. Kojima, A., Teshima, K., Miyasaka, T. & Shirai, Y. Novel Photoelectrochemical Cell with Mesoscopic Electrodes Sensitized by Lead-halide Compounds (2).

53. Hao, F. *et al.* Solvent-Mediated Crystallization of CH₃NH₃SnI₃ Films for Heterojunction Depleted Perovskite Solar Cells. *J. Am. Chem. Soc.* **137**, 11445–11452 (2015).

54. Sun, P. P., Li, Q. S., Yang, L. N. & Li, Z. S. Theoretical insights into a potential lead-free hybrid perovskite: substituting Pb²⁺ with Ge²⁺. *Nanoscale* **8**, 1503–1512 (2016).

55. Park, B.-W. *et al.* Bismuth Based Hybrid Perovskites A₃Bi₂I₉ (A: Methylammonium or Cesium) for Solar Cell Application. *Adv. Mater.* **27**, 6806–6813 (2015).

56. Saparov, B. *et al.* Thin-Film Preparation and Characterization of Cs₃Sb₂I₉: A Lead-Free Layered Perovskite Semiconductor. *Chem. Mater.* **27**, 5622–5632 (2015).

57. Cortecchia, D. *et al.* Lead-Free MA₂CuCl_xBr_{4-x} Hybrid Perovskites. *Inorg. Chem.* **55**, 1044–1052 (2016).

58. Zhou, C. *et al.* Low dimensional metal halide perovskites and hybrids. *Mater. Sci. Eng. R Reports* **137**, 38–65 (2019).

59. Goldschmidt, V. M. Die Gesetze der Krystallochemie. *Naturwissenschaften* **14**, 477–485 (1926).

60. Kieslich, G., Sun, S. & Cheetham, A. K. Solid-state principles applied to organic–

inorganic perovskites: New tricks for an old dog. *Chem. Sci.* **5**, 4712–4715 (2014).

61. Rudd, P. N. & Huang, J. Metal Ions in Halide Perovskite Materials and Devices. *Trends Chem.* **1**, 394–409 (2019).

62. Jono, R. & Segawa, H. Theoretical Study of the Band-gap Differences among Lead Triiodide Perovskite Materials: CsPbI₃. *Chem. Lett.* **48**, 877–880 (2019).

63. Goetz, K. P., Taylor, A. D., Paulus, F. & Vaynzof, Y. Shining Light on the Photoluminescence Properties of Metal Halide Perovskites. *Adv. Funct. Mater.* **30**, (2020).

64. Li, C., Soh, K. C. K. & Wu, P. Formability of ABO₃ perovskites. *J. Alloys Compd.* **372**, 40–48 (2004).

65. Dolgos, M. *et al.* Chemical control of octahedral tilting and off-axis A cation displacement allows ferroelectric switching in a bismuth-based perovskite. *Chem. Sci.* **3**, 1426–1435 (2012).

66. Li, C. *et al.* Formability of ABX₃ (X = F, Cl, Br, I) halide perovskites. *Acta Crystallogr. B.* **64**, 702–707 (2008).

67. Filip, M. R. & Giustino, F. The geometric blueprint of perovskites. *PNAS* **115**, 5397–5402 (2018).

68. Umebayashi, T. *et al.* Electronic structures of lead iodide based low-dimensional crystals. *Phys. Rev. B* **67**, 155405 (2003).

69. Walsh, A. Principles of Chemical Bonding and Band Gap Engineering in Hybrid Organic–Inorganic Halide Perovskites. *J. Phys. Chem. C* **119**, 5755–5760 (2015).

70. Zhao, B. *et al.* High Open-Circuit Voltages in Tin-Rich Low-Bandgap Perovskite-Based Planar Heterojunction Photovoltaics. *Adv. Mater.* **29**, 1604744 (2017).

71. Stoumpos, C. C. *et al.* Hybrid germanium iodide perovskite semiconductors: Active lone pairs, structural distortions, direct and indirect energy gaps, and strong nonlinear optical properties. *J. Am. Chem. Soc.* **137**, 6804–6819 (2015).

72. Abdelhady, A. L. *et al.* Heterovalent Dopant Incorporation for Bandgap and Type Engineering of Perovskite Crystals. *J. Phys. Chem. Lett.* **7**, 295–301 (2016).
73. Weller, M. T., Weber, O. J., Frost, J. M. & Walsh, A. Cubic Perovskite Structure of Black Formamidinium Lead Iodide, α -[HC(NH₂)₂]PbI₃, at 298 K. *J. Phys. Chem. Lett.* **6**, 3209–3212 (2015).
74. Lu, H. *et al.* Vapor-assisted deposition of highly efficient, stable black-phase FAPbI₃ perovskite solar cells. *Science* (80-.). **370**, (2020).
75. Kim, B., Kim, J. & Park, N. First-principles identification of the charge-shifting mechanism and ferroelectricity in hybrid halide perovskites. *Sci. Reports 2020 101* **10**, 1–7 (2020).
76. Breternitz, J., Tovar, M. & Schorr, S. Twinning in MAPbI₃ at room temperature uncovered through Laue neutron diffraction. *Sci. Rep.* **10**, 16613 (2020).
77. Bertolotti, F. *et al.* Coherent Nanotwins and Dynamic Disorder in Cesium Lead Halide Perovskite Nanocrystals. *ACS Nano* **11**, 3819–3831 (2017).
78. Murugadoss, G. *et al.* Crystal stabilization of α -FAPbI₃ perovskite by rapid annealing method in industrial scale. *J. Mater. Res. Technol.* **12**, 1924–1930 (2021).
79. Kim, J., Lee, S. H., Lee, J. H. & Hong, K. H. The role of intrinsic defects in methylammonium lead iodide perovskite. *J. Phys. Chem. Lett.* **5**, 1312–1317 (2014).
80. Ball, J. M. & Petrozza, A. Defects in perovskite-halides and their effects in solar cells. *Nat. Energy 2016 111* **1**, 1–13 (2016).
81. Yang, S. *et al.* Stabilizing halide perovskite surfaces for solar cell operation with wide-bandgap lead oxysalts. *Science* (80-.). **365**, 473–478 (2019).
82. Wang, F., Bai, S., Tress, W., Hagfeldt, A. & Gao, F. Defects engineering for high-performance perovskite solar cells. *npj Flex. Electron. 2018 21* **2**, 1–14 (2018).
83. Lei, Y., Xu, Y., Wang, M., Zhu, G. & Jin, Z. Origin, Influence, and Countermeasures

of Defects in Perovskite Solar Cells. *Small* **17**, (2021).

84. Liu, N. & Yam, C. Y. First-principles study of intrinsic defects in formamidinium lead triiodide perovskite solar cell absorbers. *Phys. Chem. Chem. Phys.* **20**, 6800–6804 (2018).

85. Bi, E., Song, Z., Li, C., Wu, Z. & Yan, Y. Mitigating ion migration in perovskite solar cells. *Trends Chem.* **3**, 575–588 (2021).

86. Liu, M., Johnston, M. B. & Snaith, H. J. Efficient planar heterojunction perovskite solar cells by vapour deposition. *Nature* **501**, 395–398 (2013).

87. Zhou, H. *et al.* Interface engineering of highly efficient perovskite solar cells. *Science* (80-.). **345**, 542–546 (2014).

88. Chen, Q. *et al.* Planar heterojunction perovskite solar cells via vapor-assisted solution process. *J. Am. Chem. Soc.* **136**, 622–625 (2014).

89. Green, M. A., Ho-Baillie, A. & Snaith, H. J. The emergence of perovskite solar cells. *Nature Photonics* vol. 8 506–514 (2014).

90. Zhao, Y. & Zhu, K. CH₃NH₃Cl-assisted one-step solution growth of CH₃NH₃PbI₃: Structure, charge-carrier dynamics, and photovoltaic properties of perovskite solar cells. *J. Phys. Chem. C* **118**, 9412–9418 (2014).

91. Saliba, M. *et al.* Cesium-containing triple cation perovskite solar cells: Improved stability, reproducibility and high efficiency. *Energy Environ. Sci.* **9**, 1989–1997 (2016).

92. Saliba, M. *et al.* Incorporation of rubidium cations into perovskite solar cells improves photovoltaic performance. *Science* (80-.). **354**, 206–209 (2016).

93. Alharbi, E. A. *et al.* Perovskite Solar Cells Yielding Reproducible Photovoltage of 1.20 V. *Research* **2019**, 8474698 (2019).

94. Alharbi, E. A. *et al.* Atomic-level passivation mechanism of ammonium salts enabling highly efficient perovskite solar cells. *Nat. Commun.* **10**, 1–9 (2019).

95. Mahesh, S. *et al.* Revealing the origin of voltage loss in mixed-halide perovskite solar

cells. *Energy Environ. Sci.* **13**, 258–267 (2020).

96. Kadro, J. M., Nonomura, K., Gachet, D., Grätzel, M. & Hagfeldt, A. Facile route to freestanding CH₃NH₃PbI₃ crystals using inverse solubility. *Sci. Rep.* **5**, 1–6 (2015).

97. Burschka, J. *et al.* Sequential deposition as a route to high-performance perovskite-sensitized solar cells. *Nature* **499**, 316–319 (2013).

98. Malinkiewicz, O. *et al.* Perovskite solar cells employing organic charge-transport layers. *Nat. Photonics* **8**, 128–132 (2014).

99. Ball, J. M., Lee, M. M., Hey, A. & Snaith, H. J. Low-temperature processed meso-superstructured to thin-film perovskite solar cells. *Energy Environ. Sci.* **6**, 1739–1743 (2013).

100. Kim, J. H., Williams, S. T., Cho, N., Chueh, C. C. & Jen, A. K. Y. Enhanced Environmental Stability of Planar Heterojunction Perovskite Solar Cells Based on Blade-Coating. *Adv. Energy Mater.* **5**, (2015).

101. Jeon, N. J. *et al.* Solvent engineering for high-performance inorganic-organic hybrid perovskite solar cells. *Nat. Mater.* **13**, 897–903 (2014).

102. Yang, W. S. *et al.* High-performance photovoltaic perovskite layers fabricated through intramolecular exchange. *Science* (80-.). **348**, 1234–1237 (2015).

103. Im, J. H., Jang, I. H., Pellet, N., Grätzel, M. & Park, N. G. Growth of CH₃ NH₃ PbI₃ cuboids with controlled size for high-efficiency perovskite solar cells. *Nat. Nanotechnol.* **9**, 927–932 (2014).

104. Seo, J. *et al.* Benefits of very thin PCBM and LiF layers for solution-processed p-i-n perovskite solar cells. *Energy Environ. Sci.* **7**, 2642–2646 (2014).

105. Kim, Y. Y. *et al.* Fast two-step deposition of perovskite via mediator extraction treatment for large-area, high-performance perovskite solar cells. *J. Mater. Chem. A* **6**, 12447–12454 (2018).

106. Eperon, G. E. *et al.* Formamidinium lead trihalide: A broadly tunable perovskite for

efficient planar heterojunction solar cells. *Energy Environ. Sci.* **7**, 982–988 (2014).

107. Li, Z. *et al.* Stabilizing Perovskite Structures by Tuning Tolerance Factor: Formation of Formamidinium and Cesium Lead Iodide Solid-State Alloys. *Chem. Mater.* **28**, 284–292 (2016).

108. Jeon, N. J. *et al.* Compositional engineering of perovskite materials for high-performance solar cells. *Nature* **517**, 476–480 (2015).

109. Lee, J. W. *et al.* 2D perovskite stabilized phase-pure formamidinium perovskite solar cells. *Nat. Commun.* **9**, 1–10 (2018).

110. Yoo, H. S. & Park, N. G. Post-treatment of perovskite film with phenylalkylammonium iodide for hysteresis-less perovskite solar cells. *Sol. Energy Mater. Sol. Cells* **179**, 57–65 (2018).

111. Liu, G. *et al.* Efficient solar cells with enhanced humidity and heat stability based on benzylammonium-caesium-formamidinium mixed-dimensional perovskites. *J. Mater. Chem. A* **6**, 18067–18074 (2018).

112. Niu, T. *et al.* High performance ambient-air-stable FAPbI₃ perovskite solar cells with molecule-passivated Ruddlesden-Popper/3D heterostructured film. *Energy Environ. Sci.* **11**, 3358–3366 (2018).

113. Yi, C. *et al.* Entropic stabilization of mixed A-cation ABX₃ metal halide perovskites for high performance perovskite solar cells. *Energy Environ. Sci.* **9**, 656–662 (2016).

114. Stranks, S. D. & Snaith, H. J. Metal-halide perovskites for photovoltaic and light-emitting devices. *Nature Nanotechnology* vol. 10 391–402 (2015).

115. Liu, T. *et al.* Cesium Halides-Assisted Crystal Growth of Perovskite Films for Efficient Planar Heterojunction Solar Cells. *Chem. Mater.* **30**, 5264–5271 (2018).

116. Kim, M. *et al.* Methylammonium Chloride Induces Intermediate Phase Stabilization for Efficient Perovskite Solar Cells. *Joule* **3**, 2179–2192 (2019).

117. Duong, T. *et al.* Structural engineering using rubidium iodide as a dopant under excess lead iodide conditions for high efficiency and stable perovskites. *Nano Energy* **30**, 330–340 (2016).
118. Zhang, M. *et al.* High-Efficiency Rubidium-Incorporated Perovskite Solar Cells by Gas Quenching. *ACS Energy Letters* vol. 2 438–444 (2017).
119. Zhou, N. *et al.* CsI Pre-Intercalation in the Inorganic Framework for Efficient and Stable FA_{1-x}Cs_xPbI₃(Cl) Perovskite Solar Cells. *Small* **13**, (2017).
120. Zhou, W. *et al.* Thermal Conductivity: Thermal Conductivity of Amorphous Materials (Adv. Funct. Mater. 8/2020). *Adv. Funct. Mater.* **30**, 2070048 (2020).
121. Xu, Y. *et al.* The Effect of Humidity upon the Crystallization Process of Two-Step Spin-Coated Organic-Inorganic Perovskites. *ChemPhysChem* **17**, 112–118 (2016).
122. Pathak, S. *et al.* Atmospheric influence upon crystallization and electronic disorder and its impact on the photophysical properties of organic-inorganic perovskite solar cells. *ACS Nano* **9**, 2311–2320 (2015).
123. Ko, H. S., Lee, J. W. & Park, N. G. 15.76% efficiency perovskite solar cells prepared under high relative humidity: Importance of PbI₂ morphology in two-step deposition of CH₃NH₃PbI₃. *J. Mater. Chem. A* **3**, 8808–8815 (2015).
124. Yan, K. *et al.* Hybrid Halide Perovskite Solar Cell Precursors: Colloidal Chemistry and Coordination Engineering behind Device Processing for High Efficiency. *J. Am. Chem. Soc.* **137**, 4460–4468 (2015).
125. Zhao, Y. *et al.* Perovskite seeding growth of formamidinium-lead-iodide-based perovskites for efficient and stable solar cells. *Nat. Commun.* **9**, 1–10 (2018).
126. Jung, M. H., Rhim, S. H. & Moon, D. TiO₂/RbPbI₃ halide perovskite solar cells. *Sol. Energy Mater. Sol. Cells* **172**, 44–54 (2017).
127. Lim, D.-H., Ramasamy, P., Kwak, D.-H. & Lee, J.-S. Solution-phase synthesis of

rubidium lead iodide orthorhombic perovskite nanowires. *Nanotechnology* **28**, 255601 (2017).

128. Zhang, T. *et al.* Bication lead iodide 2D perovskite component to stabilize inorganic a-CsPbI₃ perovskite phase for high-efficiency solar cells. *Sci. Adv.* **3**, e1700841 (2017).

129. Wang, Y. *et al.* Thermodynamically stabilized β -CsPbI₃-based perovskite solar cells with efficiencies $\geq 18\%$. *Science* **365**, 591–595 (2019).

130. Meng, H. *et al.* Chemical Composition and Phase Evolution in DMAI-Derived Inorganic Perovskite Solar Cells. *ACS Energy Lett.* **5**, 263–270 (2020).

131. Burwig, T., Fränzel, W. & Pistor, P. Crystal Phases and Thermal Stability of Co-evaporated CsPbX₃ (X = I, Br) Thin Films. *J. Phys. Chem. Lett.* **9**, 4808–4813 (2018).

132. Trots, D. M. & Myagkota, S. V. High-temperature structural evolution of caesium and rubidium triiodoplumbates. *J. Phys. Chem. Solids* **69**, 2520–2526 (2008).

133. Han, B. *et al.* Stable, Efficient Red Perovskite Light-Emitting Diodes by (α , δ)-CsPbI₃ Phase Engineering. *Adv. Funct. Mater.* **28**, 1804285 (2018).

134. Lim, D.-H., Ramasamy, P., Kwak, D.-H. & Lee, J.-S. Solution-phase synthesis of rubidium lead iodide orthorhombic perovskite nanowires. *Nanotechnology* **28**, 255601 (2017).

135. Mohammed, M. S., Salman, G. D. & Hassoon, K. I. Growth and Characterizes of PbI₂ Films By Vacuum Evaporation Method. *Al-Mustansiriyah J. Sci.* **30**, 60 (2019).

136. Xu, X. *et al.* Porous and Intercrossed PbI₂-CsI Nanorod Scaffold for Inverted Planar FA-Cs Mixed-Cation Perovskite Solar Cells. *ACS Appl. Mater. Interfaces* (2019) doi:10.1021/acsami.8b20933.

137. Yang, W. S. *et al.* Iodide management in formamidinium-lead-halide-based perovskite layers for efficient solar cells. *Science* (80-.). **356**, 1376–1379 (2017).

138. Jiang, Q. *et al.* Enhanced electron extraction using SnO₂ for high-efficiency planar-structure HC(NH₂)₂ PbI₃-based perovskite solar cells. *Nat. Energy* **2**, 1–7 (2017).

139. Kubicki, D. J. *et al.* Phase Segregation in Cs-, Rb- and K-Doped Mixed-Cation

(MA)_x(FA)_{1-x}PbI₃ Hybrid Perovskites from Solid-State NMR. *J. Am. Chem. Soc.* **139**, 14173–14180 (2017).

140. Yadav, P. *et al.* The Role of Rubidium in Multiple-Cation-Based High-Efficiency Perovskite Solar Cells. *Adv. Mater.* **29**, 1701077 (2017).

141. Uchida, R. *et al.* Insights about the Absence of Rb Cation from the 3D Perovskite Lattice: Effect on the Structural, Morphological, and Photophysical Properties and Photovoltaic Performance. *Small* **14**, 1802033 (2018).

142. Lee, J. W. *et al.* Formamidinium and cesium hybridization for photo- and moisture-stable perovskite solar cell. *Adv. Energy Mater.* **5**, (2015).

143. Xia, X. *et al.* Spray reaction prepared FA_{1-x}Cs_xPbI₃ solid solution as a light harvester for perovskite solar cells with improved humidity stability. *RSC Adv.* **6**, 14792–14798 (2016).

144. Kirchartz, T., Márquez, J. A., Stolterfoht, M. & Unold, T. Photoluminescence-Based Characterization of Halide Perovskites for Photovoltaics. *Adv. Energy Mater.* **10**, 1904134 (2020).

145. Abdi-Jalebi, M. *et al.* Potassium-and rubidium-passivated alloyed perovskite films: Optoelectronic properties and moisture stability. *ACS Energy Lett.* **3**, 2671–2678 (2018).

146. Jong, U.-G. *et al.* First-principles study on the chemical decomposition of inorganic perovskites CsPbI₃ and RbPbI₃ at finite temperature and pressure. (2018).

147. Philippe, B. *et al.* Chemical Distribution of Multiple Cation (Rb⁺, Cs⁺, MA⁺, and FA⁺) Perovskite Materials by Photoelectron Spectroscopy. *Chem. Mater.* **29**, 3589–3596 (2017).

148. Jiang, Q. *et al.* Enhanced electron extraction using SnO₂ for high-efficiency planar-structure HC(NH₂)₂ PbI₃-based perovskite solar cells. *Nat. Energy* **2**, 1–7 (2017).

149. Yang, W. S. *et al.* High-performance photovoltaic perovskite layers fabricated through intramolecular exchange. *Science (80-.)*. **348**, 1234–1237 (2015).

150. Domanski, K., Alharbi, E. A., Hagfeldt, A., Grätzel, M. & Tress, W. Systematic

investigation of the impact of operation conditions on the degradation behaviour of perovskite solar cells. *Nat. Energy* **3**, 61–67 (2018).

151. Tress, W. *et al.* Performance of perovskite solar cells under simulated temperature-illumination real-world operating conditions. *Nat. Energy* **4**, 568–574 (2019).

Chapter 4 Quantifying Stabilized Phase Purity in

Formamidinium-Based Multiple-Cation Hybrid Perovskites

*This work has been published: L. Merten, A. Hinderhofer, T. Baumeler, N. Arora, J. Hagenlocher, S. M. Zakeeruddin, M. I. Dar, M. Grätzel, F. Schreiber, Chem. Mater. **2021**, 33, 8, 2769-2776*

Introduction

During the last decade, huge efforts were expended in the material class of hybrid organic-inorganic perovskites by the solar cell community, leading to a substantial rise in photovoltaic efficiency and a promising perspective for relatively cheap and easy to manufacture perovskite materials for solar energy.¹ For optimization of solar cell devices, material composition and structure are of crucial importance. Indeed, the composition of organic-inorganic hybrid perovskites is variable to a large extent, providing means and need for structural optimization, which in turn has a great impact on performance improvement.

In the hybrid lead halide materials APbX_3 , where X is iodide, bromide or chloride anion, different kinds and mixtures of A cations have been investigated. The most commonly used organic molecular cation is methylammonium (MA^+), which is able to form a lead halide perovskite structure at room temperature.² In particular, the material MAPbI_3 has been widely explored due to its relatively small band gap that allows absorption of visible light.³ An even narrower bandgap, which facilitates a greater amount of harvested solar energy, is exhibited by hybrid perovskites based on the formamidinium (FA^+) cation.^{4,5} In addition, FA^+ is supposed to be more thermally stable⁴ than the MA^+ cation and has the potential of outperforming the insufficient environmental⁶⁻⁸ and operational⁹ stability of MAPbI_3 , which is a major drawback for hybrid perovskite solar cells. Unfortunately, the FAPbI_3 system at room temperature exhibits a large proportion of non-photoactive (“yellow”) hexagonal δ -phase.^{5,10,11} For optical applications such as solar cells, a high phase purity of the optically active cubic (“black”)

perovskite modification would be desirable. In order to exploit the excellent light-harvesting and enhanced stability of the FA^+ cation, efforts have been made to stabilize the cubic phase of FAPbI_3 at room temperature.¹² This can be achieved, for example, by blending the precursors FAI and MABr ^{13,14}, which yield a mixed ion perovskite upon reaction with PbI_2 . Addition of Cs^+ to the mixture has proven to reduce the occurrence of δ -phase even further¹⁵⁻¹⁹ and to positively affect the crystallization process.^{15,16,20-22} Also an excess of PbI_2 has been shown to assist the suppression of δ -phase and even benefit device performance.²³ However, the presence of a segregated PbI_2 phase might negatively affect charge carrier lifetimes²⁴ and long-term environmental stability of the material.²⁵ This has been addressed by the addition of Rb^+ , which has proven beneficial in stabilizing the cubic FAPbI_3 phase^{10,26-29} and reducing residual PbI_2 ^{10,27} by reacting with excess material, and has also been explored in quadruple cation compositions of FA^+ , MA^+ , Cs^+ and Rb^+ .^{20,26,30,31,22}

In this paper, a quantitative comparison of the structural properties of hybrid lead iodide perovskites containing different cation compositions is made. In particular, the effects of including the inorganic cations Cs^+ and Rb^+ into an optimized mixture¹³ of organic cations FA^+ and MA^+ under excess lead iodide conditions were examined with regard to the occurrence of different crystal phases. For that purpose, four compositionally differing samples were prepared: The parent compound, produced from a mixture of 83 % FAPbI_3 and 17 % MAPbBr_3 , a similar composition with the addition of excess PbI_2 , a triple mixture of FA^+ , MA^+ and Cs^+ cations, as well as the quadruple composition of FA^+ , MA^+ , Cs^+ , Rb^+ . Although a considerable amount of research on multiple cation perovskites has been conducted by now, this report is to the best of our knowledge the first to provide quantitative data comparing the effects of excess lead iodide, Cs^+ and Rb^+ on the phase composition of perovskite thin films.

Results and discussion

Incorporation of Cs^+ and Rb^+ into organic-inorganic hybrid lead iodide perovskite thin films has been shown to improve the film quality and phase purity of the desired cubic perovskite phase.^{10,15,16,21,22,26-28,30} To investigate the crystal structure of samples containing different cation compositions, two-dimensional reciprocal space maps were recorded, which are shown in Figure 1 (a)-(d). All films exhibit Bragg reflections of the cubic perovskite modification. Additional features corresponding to hexagonal phases of FAPbI_3 and PbI_2 can be found dependent on the cation composition.

Azimuthal integration of the radially distributed intensity in the reciprocal space maps visualizes the relative total peak intensities (Figure 1 (e)). In the double cation compound, labelled as FA:MA, the intensity of the hexagonal phases 4H and 6H, occurring at small values of the scattering vector Q , is almost equal compared to the cubic phase. Also in the corresponding reciprocal space map, the Bragg peaks from hexagonal phases and PbI_2 are clearly visible. The 4H and 6H hexagonal phases contain corner- and face-sharing lead halide octahedra and can be considered as intermediates between the 2H hexagonal δ -phase of FAPbI_3 , featuring only face-sharing octahedra, and the cubic perovskite phase comprising exclusively corner-sharing lead halide octahedra.³⁴

The sample containing excess PbI_2 exhibits stronger cubic phase peaks and less hexagonal phase, but also a distinct amount of segregated lead iodide crystal phase, which is represented by the strong signal at $Q=0.91 \text{ \AA}^{-1}$. However, the corresponding peak in the radial profile is rather broad and exhibits two additional shoulders due to an overlap with the signals from hexagonal phases, which are obviously still present in the material.

Addition of Cs^+ reduces both PbI_2 and hexagonal phase signals to a large degree, but small features of 4H and PbI_2 phases are still distinguishable at the corresponding positions of the

green curve in Figure 1 (e) and also in the reciprocal space map in Figure 1 (c). These are further diminished upon the incorporation of Rb^+ into the mixture, indicating a beneficial effect of using both inorganic cations. The quadruple cation composition almost exclusively displays the cubic perovskite modification, as can be seen in Figure 1 (d), where the distinct perovskite diffraction signals are marked. Nearly no residual hexagonal or PbI_2 phases can be found.

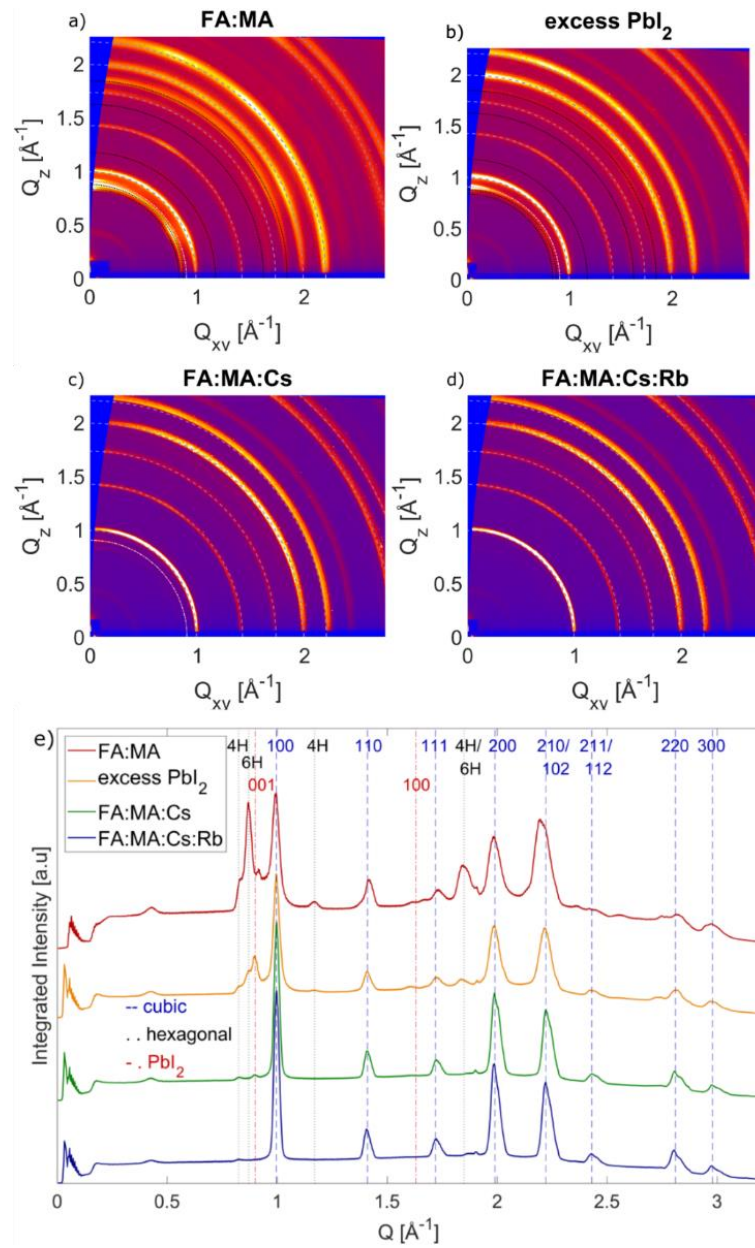


Figure 1. (a)-(d) 2D reciprocal space maps of samples with different compositions. Ring-shaped diffraction features indicate a random orientation of perovskite crystallites. Blue dashed lines mark

perovskite signals, hexagonal phases are labelled in black, and PbI_2 is denoted by pink lines. Incidence angle was 0.14° for measurement of all Q -maps. (e) Radial intensity distribution extracted from reciprocal space maps. Peaks are indexed according to literature³⁴, displaying cubic perovskite crystal structure. Additional hexagonal and PbI_2 phases³⁶ can be found for certain samples, as explained in the text.

Quantification of the respective amounts of hexagonal and PbI_2 phases (Figure 2) was performed via integration of diffraction signals ascribed to the respective phases and using structure factor calculations, as described in the experimental section. We chose two different angles of incidence, 0.1° and 0.2° (Figure S2), to distinguish between surface and bulk properties. The incident angle of 0.1° was determined to be just below the critical angle and therefore is supposed to reflect largely surface properties of the films. Increasing the incident angle increases also the penetration depth of the X-rays into the material and is expected to reflect a larger amount of the bulk film properties, which is therefore depicted by a 0.2° angle of incidence.

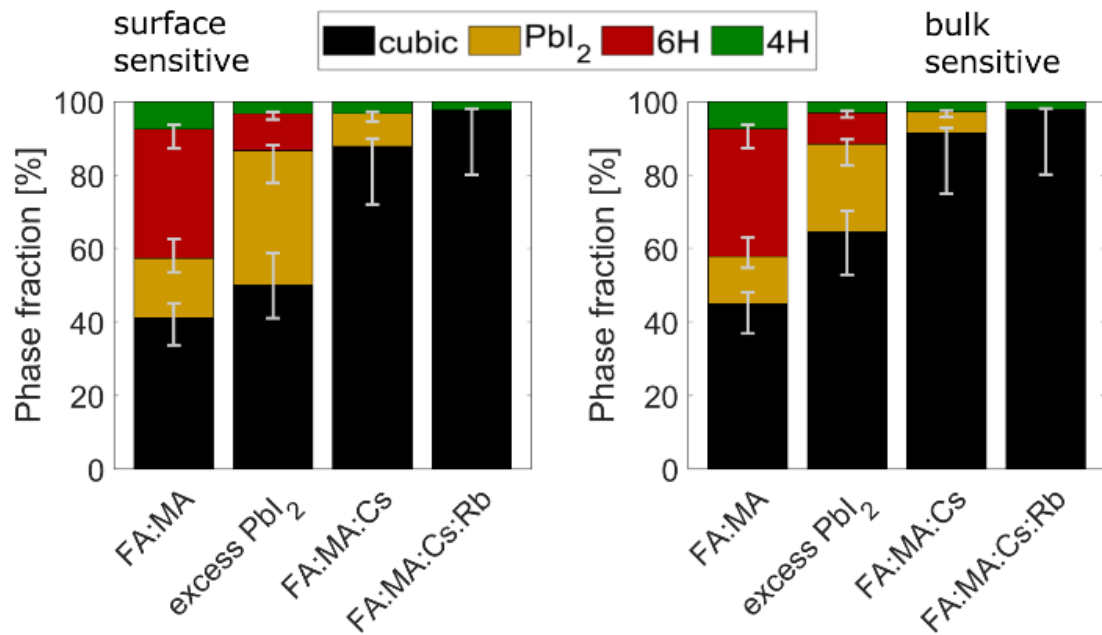


Figure 2. Molar phase fractions of cubic, hexagonal and PbI_2 phases depending on the film composition, determined from peak integration of radial intensity profiles extracted from reciprocal space maps at incident angles of 0.1° (left, surface-sensitive) and 0.2° (right, bulk sensitive). Error bars were estimated due to compositional uncertainties and experimental statistics.

The trends in phase composition with varying cation mixture are consistent for both incident angles. FA:MA binary mixtures exhibit a huge amount of 6H hexagonal polymorph, making

up about 35 % of the total investigated material volume, which is close to the content of the desired cubic phase. This could be extremely detrimental to the performance of the final device and might even be a potential trigger for further transition of the material to the photoinactive δ -phase. Also, a significant contribution of 4H polymorph and PbI_2 phase can be observed in the binary sample. Excess PbI_2 reduces the amount of hexagonal polymorphs significantly, but occurs as a separate PbI_2 phase, which consequently can be observed in a higher fraction than in simple FA:MA mixtures. The quantity of excess PbI_2 phase can be successfully reduced upon addition of Cs^+ and Rb^+ into the mixture, as can the appearance of hexagonal polymorphs. Solely adding Cs^+ , though reducing the intensities of impurity phases, still leaves residual PbI_2 and 4H phases in the films. The addition of both Cs^+ and Rb^+ , however, effectively suppresses excess PbI_2 phase and 6H phase, while the 4H phase is reduced to a marginal amount of around 2 % of the total material. This shows that even though the addition of Cs^+ has a beneficial effect on the phase composition of mixed perovskites, it is not sufficient to fully suppress impurity phases, especially a considerable amount of excess PbI_2 is still present. An even higher phase purity can be obtained by adding both Cs^+ and Rb^+ to yield a quadruple cation mixed perovskite, almost exclusively (97.8 %) consisting of the cubic perovskite modification. Cs^+ has been shown before to suppress the formation of hexagonal phases during the crystallization process^[1], while its effect on the excess lead iodide phase, even though it is reduced, does not suffice to prevent PbI_2 phase formation. On the contrary, Rb^+ has been reported to reduce PbI_2 phase impurities even under excess lead iodide conditions.^[27] Hence, using both Cs^+ and Rb^+ has a joint effect and enables a high purity cubic perovskite film.

Comparing the composition near the surface to the bulk material, a general trend of increasing proportions of hexagonal and PbI_2 phases as compared to the cubic perovskite phase with lowering the probing depth can be observed. Especially for the excess lead iodide phase, this effect is strongly pronounced and suggests the location of PbI_2 preferably near the film surface.

Decreasing intensities of the undesired phases with larger probing depth indicate that the bulk of the film contains less of PbI_2 and hexagonal phases than areas near the surface, while for PbI_2 the preference of surface areas seems the most pronounced and the fraction of hexagonal phases is only slightly lower in the bulk than near the surface, suggesting an almost equal distribution throughout the film. The prevalence of PbI_2 close to the surface might be due to an increased vulnerability of the perovskite surface toward degradation.

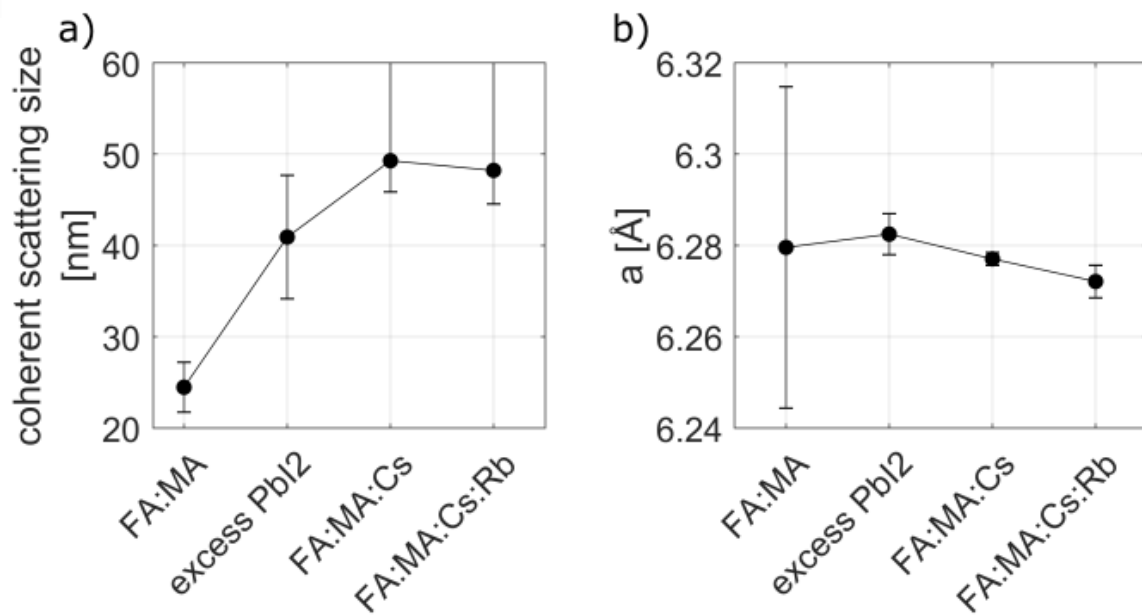


Figure 3. (a) Minimum coherently scattering island size as a function of composition, determined from gaussian fits of peak widths (FWHM) of XRR data (Figure S1). Averaging was performed over different crystallographic directions, as similar trends could be observed for all of them. (b) Unit Cell Parameters as a function of composition, determined from gaussian fits of peak positions observed in the XRR data.

Improved purity of the perovskite phase upon inorganic cation addition is not only suggested by the disappearance of the peaks which were ascribed to impurity phases, i.e. lead iodide and hexagonal polymorphs. Also, a general peak sharpening can be observed, indicative of an improvement in crystal structure by enhanced crystallite size. Figure 3 (a) shows sizes of homogeneous scattering domains determined from peak widths (FWHM) of XRR data, averaged over different crystallographic directions. Consistent with the peak sharpening, which can be observed in the 2-dimensional Q -maps in Figure 1, calculations confirm an increase in

crystallite size upon addition of excess lead iodide as well as inorganic cations. Here, adding Cs^+ had an even more enlarging effect than lead iodide, leading to an increase in crystallite size by at least a factor of two. However, the resolution limit of the experimental setup does not allow for the determination of coherently scattering island sizes larger than 50 nm, so the crystalline domains for the triple and quadruple cation composition might be even larger.

While on the incorporation of Cs^+ into the perovskite crystal lattice a broad consensus is achieved,^{15,16,37-39} the question whether or not Rb^+ can also be integrated into the mixed perovskite crystal lattice is still discussed.^{26-28,30-32,37-40} To address this issue, lattice parameters of the cubic perovskite structure were determined for the different compositions. Figure 3 (b) depicts the cubic unit cell parameter a as a function of composition. Data from X-ray reflectivity (Figure S1) was used to calculate the unit cell size from the positions of diffraction signals. From the calculated lattice parameters, it can be observed that excess PbI_2 leads to a small increase in the unit cell size compared to the simple MA:FA mixture, which might be due to partial substitution of bromide ions in the mixture with the larger iodide.

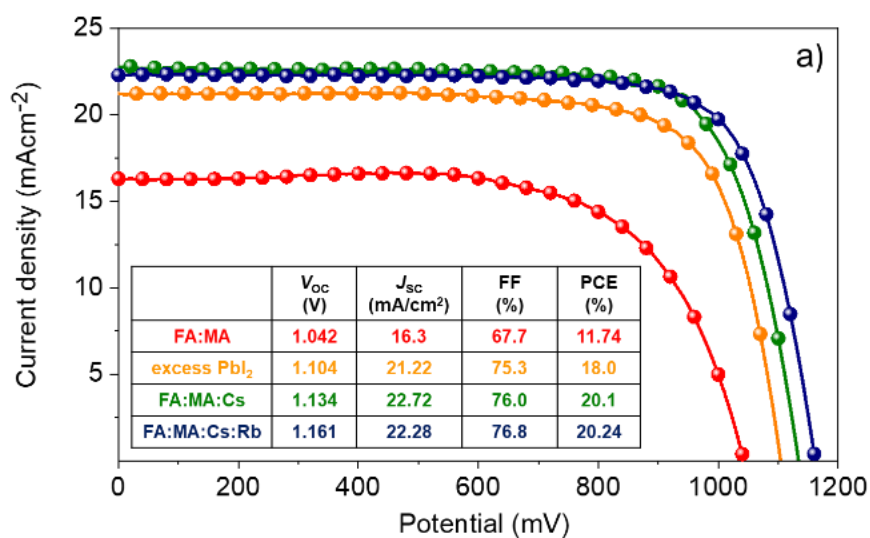
Addition of Cs^+ slightly shrinks the lattice, suggesting incorporation of the smaller inorganic cation in the hybrid perovskite, partially substituting for the larger organic cations FA^+ and MA^+ and thus decreasing the effective average cation radius.

Upon introduction of Rb^+ into the material, a still smaller unit cell size is observed. Besides possible incorporation of the smaller Rb^+ cation into the perovskite lattice, there might be several reasons for that. Rb^+ has been found to interact strongly with iodide, leading to the formation of Rb- and I-rich side phases⁴¹ and increasing the Br ratio in the perovskite phase, which also might cause a smaller lattice constant. Furthermore, since Cs^+ has been observed to influence the distribution of Rb^+ ions in the film³¹, the presence of Rb^+ might reversely also alter the distribution of Cs^+ in the material. The apparent lattice contraction upon Rb^+

incorporation possibly could be also ascribed to those side effects and does not provide sufficient proof of incorporation of Rb^+ into the perovskite lattice.

Detailed investigation of the azimuthally distributed intensity along the diffraction rings descending from the perovskite structure also revealed a small, but still noticeable influence of cation composition on the orientational order of crystallites. An explicitly preferred orientation could be observed only for the (110) plane at an angle of 60° relative to the substrate (compare Figure S3). This finding is consistent with the previously reported orientation of the (202) plane parallel to the substrate⁴². However, the degree of orientational alignment is rather low in all samples, while it is strongest in the pure FA:MA mixture. Addition of excess PbI_2 or inorganic cations obviously affects the orientational alignment of crystallites and leads to randomization of orientation.

The impact of compositional engineering involving the incorporation of MA^+ , Cs^+ and Rb^+ cations and a mixture thereof into FAPbI_3 phase on the power conversion efficiencies (PCEs) of perovskite solar cells (PSCs) was evaluated under standard illumination conditions. For details, we refer to the experimental section.



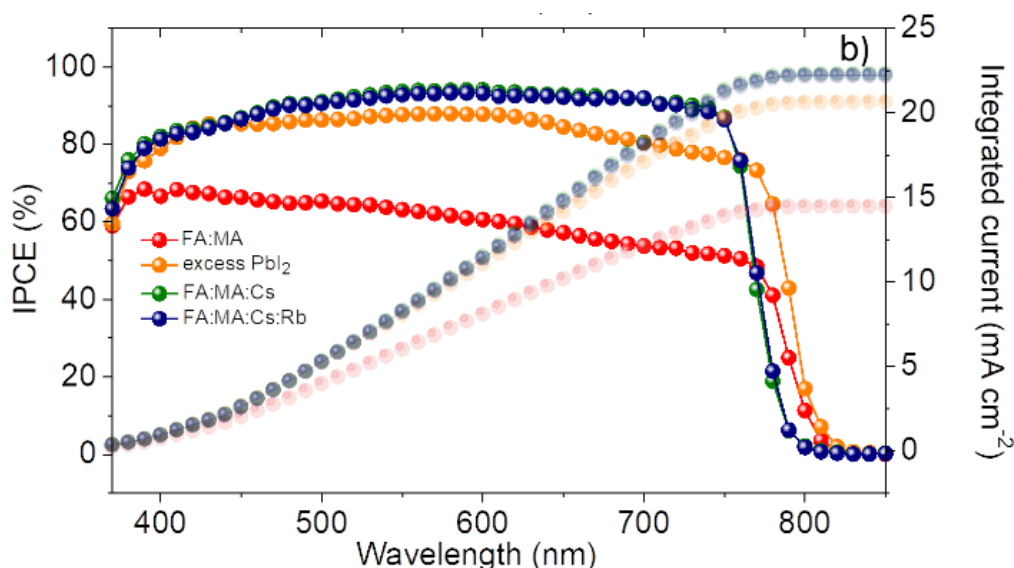


Figure 4. a) Current density-voltage (J - V) characteristics measured under standard simulated AM1.5 illumination at a scan rate of 100 mV/s (reverse scan, with an illumination area of 0.16 cm²) corresponding to the devices based on the following architecture FTO/c-TiO₂/m-TiO₂/Perovskite/Spiro/Au. Inset: PV metrics derived from the J - V curve. b) Incident Photon-to-Current Conversion Efficiency (IPCE) as a function of monochromatic wavelength recorded for devices with different compositions and the integrated current density obtained from the respective IPCE spectrum.

As shown in Figure 4, PSC containing a light absorption layer composed of FA_{1-x}MA_xPb(I_{3-x}Br_x) ($x \approx 17\%$) yielded a PCE of 12 %, with current density (J_{SC}) of 16.3 mA/cm², open-circuit voltage (V_{OC}) of 1.042 V and fill factor (FF) of 68 %. Adding excess amount of PbI₂ to FA_{1-x}MA_xPb(I_{3-x}Br_x) increased the PCE to 18 % (J_{SC} of 21.22 mA/cm², V_{OC} of 1.104 V and FF of 75 %), and by incorporating Cs⁺ into the FA_{1-x}MA_xPb(I_{3-x}Br_x) lattice, the PCE value was further improved to 20 %. As summarised in the inset of Figure 4, Cs⁺ incorporation improved the J_{SC} and V_{OC} , whereas the introduction of RbI into Cs-containing FA_{1-x}MA_xPb(I_{3-x}Br_x) precursor solution majorly increased the V_{OC} to 1.161 V, further supported by the average device metrics collected from a batch presented in Figure S5. The trend exhibited by the J_{SC} values extracted from the J - V curves and hysteresis data (Table S6) is further substantiated by the corresponding incident photon-to-current conversion efficiency (IPCE) spectra (Figure 4b). Comparative analysis of the IPCE spectra illustrates that introduction of Cs⁺ increases the bandgap with respect to double-cation compositions, whereas Rb⁺ incorporation in the

precursor solution does not change the IPCE onset.³⁹ Furthermore, the stabilized power output data (Figure S4) also collaborated with the PCE values obtained through *J-V*-measurements. Overall, the observed trend agrees with the literature.^{43,44}

Particularly, to understand the observed trend in the V_{OC} , we recorded steady-state and time-resolved photoluminescence (PL) (Figure 5). Steady-state PL (Figure 5a) revealed that the excess PbI_2 does not influence the bandgap of double-cation perovskite and with the introduction of Cs^+ , the bandgap increases expectedly, while the introduction Rb^+ does not alter the bandgap of Cs-containing triple-cation based perovskite, collaborating well with the IPCE data (Figure 4b).³⁹ Time-resolved PL (Figure 5b) brought out that the charge-carrier combination slightly improved when excess PbI_2 was used. With the introduction of inorganic cations, the lifetime of charge-carrier increased further as τ_{10} (τ_{10} , when PL intensity drops by an order of magnitude) increased from 430 ns to 600 and 770 ns, respectively, when Cs^+ and ($Cs^+ + Rb^+$) cations were introduced. The presence of long-lived charge carrier infers the reduction in non-radiative recombination, and the formation of high-quality perovskite films that enable the fabrication of PSCs yielding improved photovoltages, similar to previous reports.^{16,27}

Conclusion

In summary, a detailed investigation and quantification of the effects of mixing multiple cations in a hybrid lead halide perovskite including excess lead iodide conditions was conducted. The organic cations FA^+ and MA^+ , as well as the inorganic cations Cs^+ and Rb^+ were used. Adding the smaller inorganic cations to yield triple or quadruple cation hybrid perovskites significantly improved the phase purity of the black photoactive cubic perovskite modification, enhancing its fraction from about 45 % in the double cation $FA:MA$ mixture to 97.8 % in the quadruple cation material. Consequently, a reduction of hexagonal and PbI_2 phases in the perovskite thin

films was observed. The quadruple mixture displayed the lowest amount of impurity phases, i.e. only about 2 % of 4H phase, indicating a beneficial effect of adding both Cs^+ and Rb^+ . The phase composition also showed variations as a function of probing depth, such that especially PbI_2 was found preferentially near the film surface compared to the bulk of the film. Addition of excess PbI_2 , as well as Cs^+ and Rb^+ also affected the crystal structure of the cubic perovskite, manifesting in a reduced amount of orientational order, a modification of lattice constants and a significant increase of crystallite size. Finally, owing to improved phase purity of the photoactive layer, desired absorption and emission features were obtained, which led to the realization of photovoltaic performance exceeding 20% from the PSCs employing triple and quadruple cation materials.

Experimental section

Perovskite Film Preparation and Device Fabrication

The perovskite films were deposited using a single-step deposition method from the precursor solution containing FAI (1.0 M) (Greatcell Solar), PbI_2 (1.1 M) (TCI), MABr (0.2 M) (Greatcell Solar), and PbBr_2 (0.2 M) (TCI) in anhydrous dimethylformamide (99.8 %, Acros)/dimethylsulphoxide (99.7 %, Acros) (4:1 (v:v)). After that, CsI and RbI (abcr, GmbH, ultra-dry; 99.998 %), (5 % volume, 1.5 M DMSO) was added to the precursor solution. The precursor solution was spin-coated in a two-step programme at 1000 and 6000 r.p.m. for 10 and 30 s, respectively, onto the mesoporous TiO_2 films. During the second step, 100 μl of chlorobenzene (99.8 %, Acros) was dropped on the spinning substrate 10 s prior to the end of the program. This was followed by annealing the films at 100°C for 45 min. The substrates were cooled for a few minutes and subsequently, a 200 nm thick layer of spiro-OMeTAD (Merck) was spin-coated onto the perovskite layer and the devices were completed by thermal evaporation of a 70-80 nm thick gold back contact layer under high vacuum. The deposition of perovskite and

spiro-OMeTAD was carried out in a dry air glove box under controlled atmospheric conditions with humidity < 1 %. The photovoltaic performance of the devices was evaluated under standard illumination conditions. All experimental procedures are reported elsewhere.^{15, 26, 32}

X-Ray Diffraction Measurements

Experimental X-ray data was recorded at ESRF beamline ID10 with photon energy $E = 22$ keV. To account for preferred orientation, typically observed for perovskite thin films, we used GIWAXS to record reciprocal space maps³³ by employing a 2D Pilatus 300K detector. All measurements were performed under a nitrogen atmosphere.

Determination of Relative Phase Fractions

To determine the fractions of different phases, intensities of the first Bragg peaks of each phase were used, located at $Q=0.82 \text{ \AA}^{-1}$ for 4H phase, $Q=0.87 \text{ \AA}^{-1}$ for 6H, $Q=0.91 \text{ \AA}^{-1}$ for PbI_2 , and $Q=0.99 \text{ \AA}^{-1}$ for the cubic phase. To normalize and compare the actual phase amounts, structure factor calculations were performed using the atomic positions in the crystal structures.^{34,35} In addition, Lorentz- and polarisation corrections were applied. Radially integrated intensity profiles of reciprocal space maps at two different angles of incidence were used to distinguish bulk and surface composition, as described in the main text.

Supporting Information

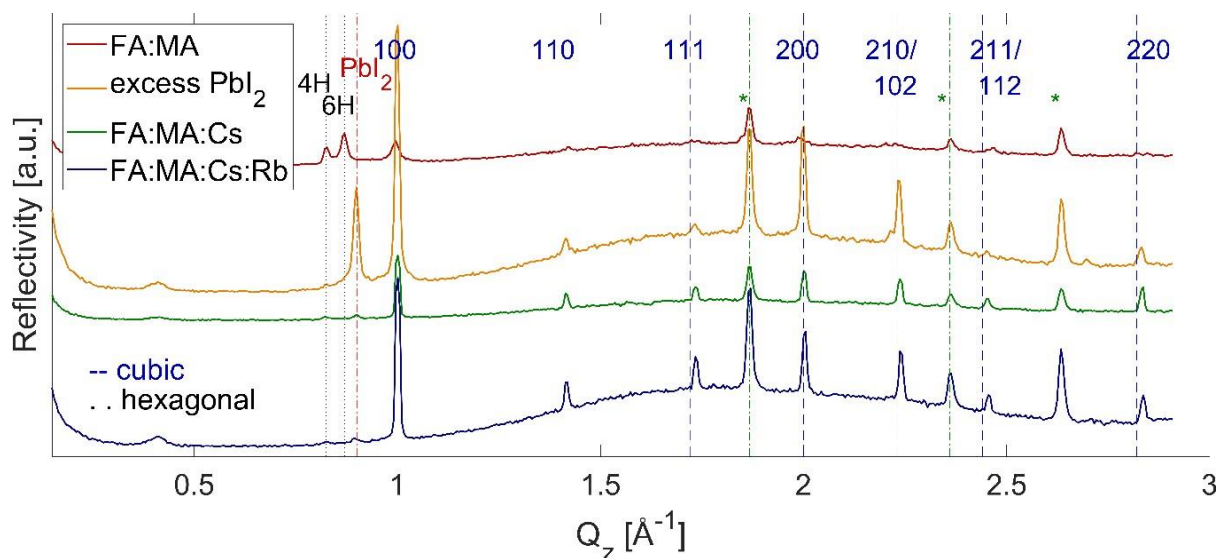
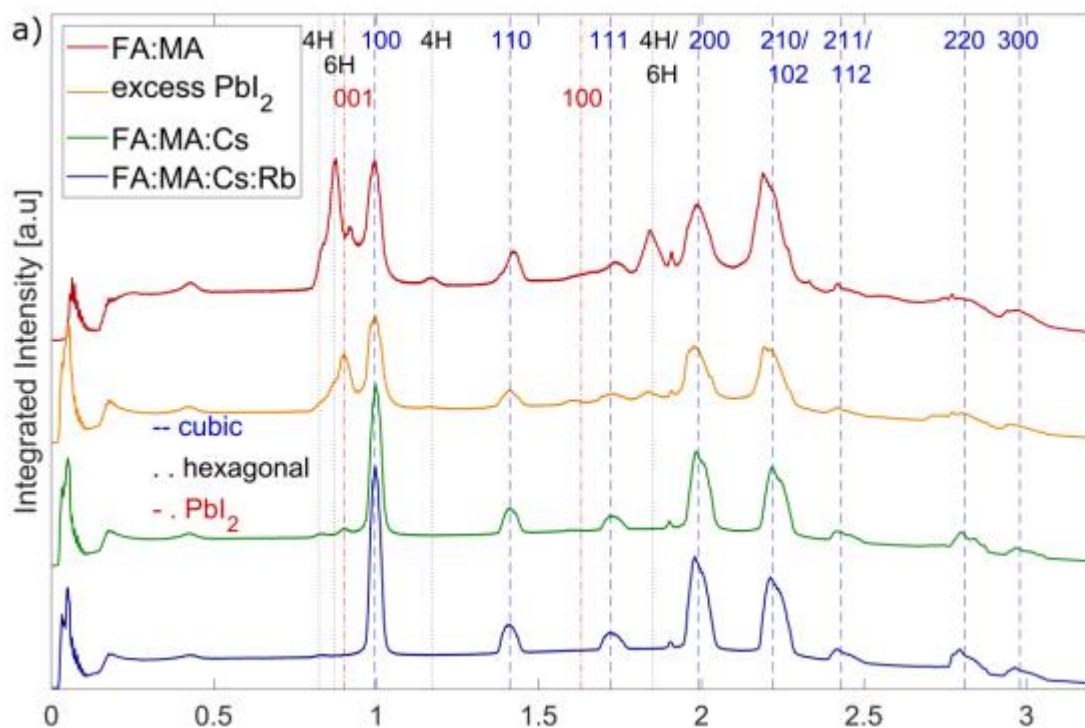


Figure S1. Out-of-plane scans of samples with different compositions, showing out-of-plane crystal structure. Peak indications after reported cubic perovskite structures and hexagonal polymorphs⁴⁵, TiO_2 peaks originate from the substrate⁴⁶ and are marked by asterisks. In the binary mixture of FA^+ and MA^+ (red curve), additional hexagonal phase is visible, as well as a PbI_2 signal⁴⁷ in the sample containing excess PbI_2 (yellow curve). Addition of Cs^+ and Rb^+ effectively suppresses hexagonal and PbI_2 phases (green and blue curves).



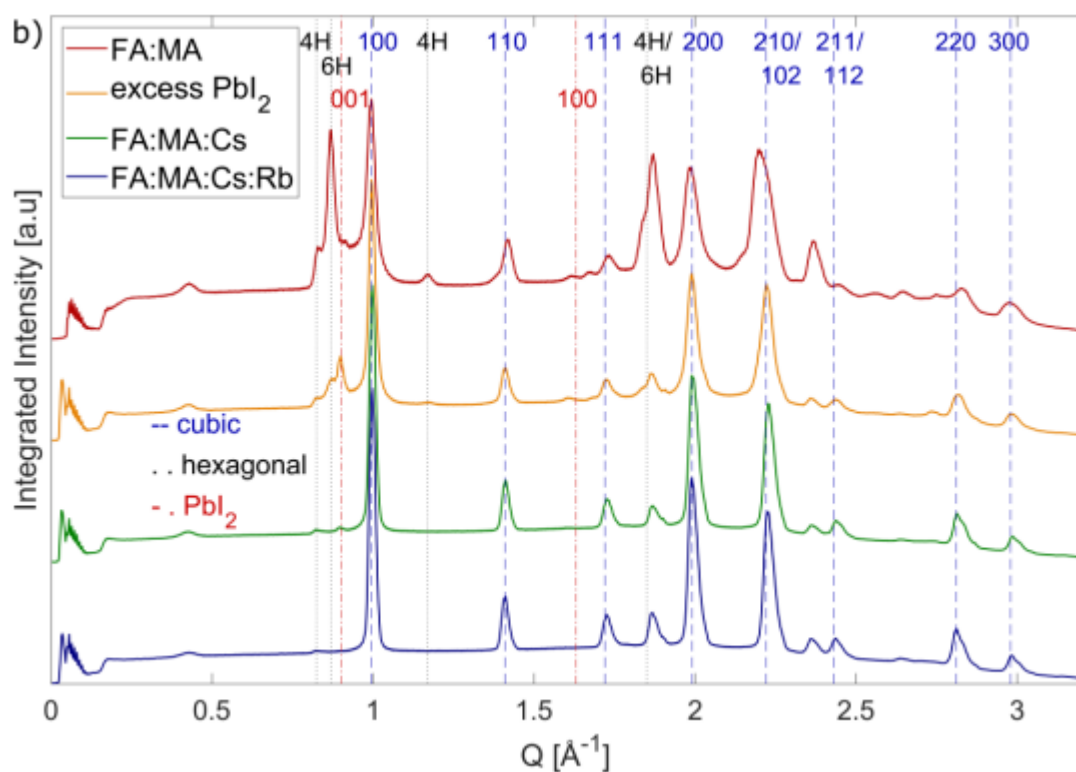


Figure S2. Radial intensity profiles extracted from reciprocal space maps at incident angles of (a) 0.1° (surface sensitive) and (b) 0.2° (bulk sensitive).

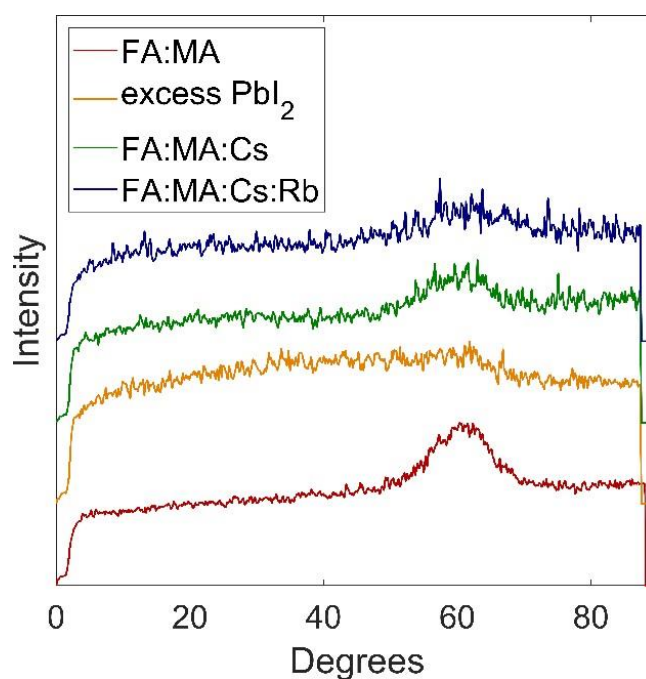


Figure S3. Intensity of (110) diffraction signal as a function of azimuthal angle. Only for this crystallographic plane a clearly preferred orientation can be found, which is most pronounced for the FA:MA 85:15 sample. Incident angle was 0.14° .

Table S1. Lattice parameters assuming cubic perovskite structure as derived from gaussian fits of peak positions in the XRR data.

Cation composition	FA:MA	FA:MA, excess PbI ₂	FA:MA:Cs	FA:MA:Rb
Cubic lattice parameter [Å]	6.279 ±0.035	6.282 ±0.004	6.277 ±0.001	6.272 ±0.004

Table S2. Molar fractions [%] of different phases near the sample surface, obtained from radial profiles of GIWAXS images measured at 0.10° angle of incidence

	FA:MA	Excess PbI ₂	FA:MA:Cs	FA:MA:Cs:Rb
4H	7.488	03.3219	3.2832	2.2658
6H	35.1326	10.0612	0	0
PbI ₂	16.2573	36.5485	8.8732	0
cubic	41.1221	50.0684	87.8435	97.7342

Table S3. Molar fractions [%] of different phases in the bulk of the sample, obtained from radial profiles of GIWAXS images measured at 0.20° angle of incidence

	FA:MA	Excess PbI ₂	FA:MA:Cs	FA:MA:Cs:Rb
4H	7.4171	3.0501	2.7755	2.2176
6H	34.7226	8.4926	0	0
PbI ₂	12.8938	23.9578	5.8347	0
Cubic	44.9666	64.4995	91.3897	97.7824

Table S4. Weight fractions [%] of different phases near the sample surface, obtained from radial profiles of GIWAXS images measured at 0.10° angle of incidence

	FA:MA	Excess PbI ₂	FA:MA:Cs	FA:MA:Cs:Rb
4H	7.7974	3.6473	3.3559	2.2658
6H	36.5845	11.0468	0	0
PbI ₂	12.7965	30.3328	6.8557	0
cubic	42.8215	54.9731	89.7884	97.7342

Table S5. Weight fractions [%] of different phases in the bulk of the sample, obtained from radial profiles of GIWAXS images measured at 0.20° angle of incidence

	FA:MA	Excess PbI ₂	FA:MA:Cs	FA:MA:Cs:Rb
4H	7.6581	3.2396	2.8156	2.2176
6H	35.851	9.0201	0	0
PbI ₂	10.063	19.2343	4.4741	0
Cubic	46.4279	68.506	92.7103	97.7824

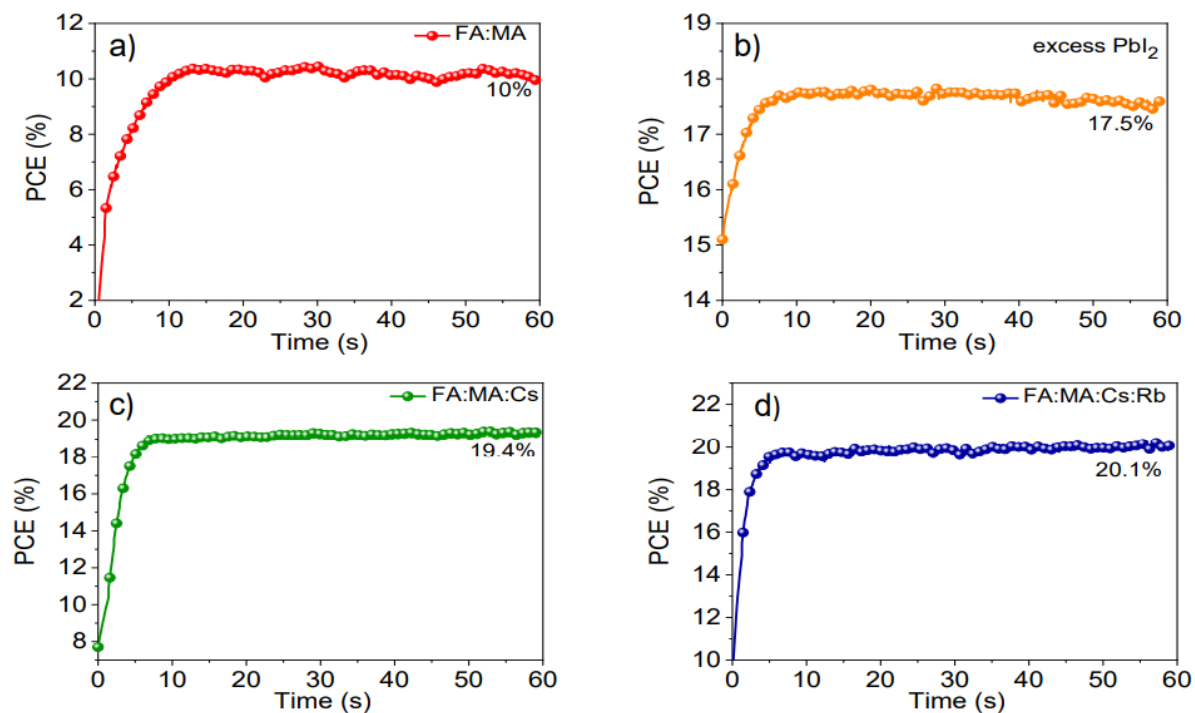


Figure S4. Maximum power point tracking showing stabilized efficiencies for devices with different compositions.

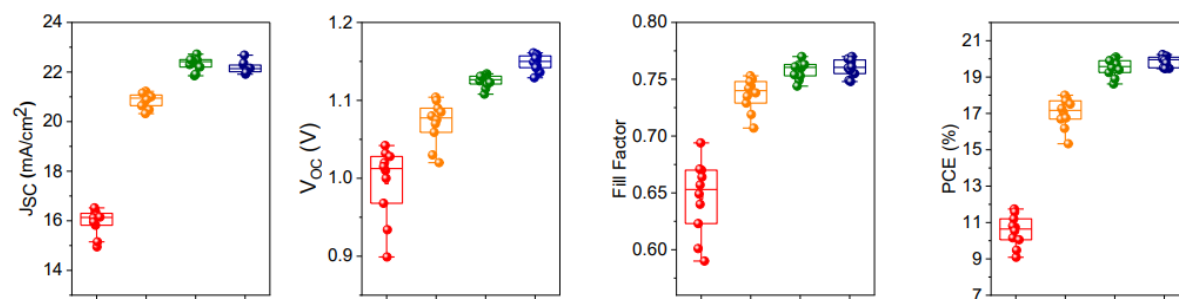


Figure S5. Photovoltaic metrics for devices with different compositions.

Table S6. Photovoltaic parameters extracted from the J-V curves for devices with different compositions recorded in reverse (from V_{OC} to J_{SC}) and forward (from J_{SC} to V_{OC}) scanning directions. All J-V curves were recorded under standard simulated AM 1.5 illumination at a scan rate of 100 mV/s, with an illuminated area of 0.16 cm^2

		V_{OC} (V)	J_{SC} (mA/cm ²)	FF (%)	PCE (%)
FA:MA	Reverse	1.042	16.30	67.7	11.74
	Forward	1.03	15.71	63.4	10.46
Excess Pbl₂	Reverse	1.104	21.22	75.3	18.0
	Forward	1.096	20.96	72.9	17.1
FA:MA:Cs	Reverse	1.134	22.72	76.0	20.1
	Forward	1.125	22.61	74.9	19.5
FA:MA:Cs:Rb	Reverse	1.161	22.28	76.8	20.24
	Forward	1.161	22.27	75.9	20.03

References

- [1] N. Arora, M. I. Dar, S. Akin, R. Uchida, T. Baumeler, Y. Liu, S. M. Zakeeruddin, and M. Graetzel, ‘Low-Cost and Highly Efficient Carbon-Based Perovskite Solar Cells Exhibiting Excellent Long-Term Operational and UV Stability’, *Small* **2019**, 15, 1904746.
- [2] D. Weber, ‘CH₃NH₃PbX₃, ein Pb(II)-System mit kubischer Perowskit-struktur’, *Z. Naturforsch.* **1978**, 33b, 1443-1445
- [3] T. Baikie, Y. Fang, J. M. Kado, M. Schreyer, F. Wei, S. G. Mhaisalkar, M. Graetzel, and T. J. White, ‘Synthesis and crystal chemistry of the hybrid perovskite (CH₃NH₃)PbI₃ for solid-state sensitised solar cell applications’, *J. Mater. Chem. A* **2013**, 1, 5628
- [4] G. E. Eperon, S. D. Stranks, C. Menelaou, M. B. Johnston, L. M. Herz, and H. J. Snaith, ‘Formamidinium lead trihalide: a broadly tunable perovskite for efficient planar heterojunction solar cells’, *Energ. Environ. Sci.* **2014**, 7, 982.

[5] T. M. Koh, K. Fu, Y. Fang, S. Chen, T. C. Sum, N. Mathews, S. G. Mhaisalkar, P. P. Boix, and T. Baikie, 'Formamidinium-Containing Metal-Halide: An Alternative Material for Near-IR Absorption Perovskite Solar Cells', *J. Phys. Chem. C*, **2013**, 118, 16458-16462.

[6] B. Conings, J. Drijkoningen, N. Gauquelin, A. Babayigit, J. D'Haen, L. D'Olieslaeger, A. Ethirajan, J. Verbeeck, J. Manca, E. Mosconi, F. D. Angelis, and H.-G. Boyen, 'Intrinsic Thermal Instability of Methylammonium Lead Trihalide Perovskite', *Adv. Energy Mater.* **2015**, 5, 1500477.

[7] J. C.-R. Ke, A. S. Walton, D. J. Lewis, A. Tedstone, P. O'Brien, A. G. Thomas, and W. R. Flavell, 'In situ investigation of degradation at organometal halide perovskite surfaces by X-ray photoelectron spectroscopy at realistic water vapour pressure', *Chem. Commun.* **2017**, 53, 5231.

[8] E. J. Juarez-Perez, L. K. Ono, M. Maeda, Y. Jiang, Z. Hawash, and Y. Qi, 'Photodecomposition and thermal decomposition in methylammonium halide lead perovskites and inferred design principles to increase photovoltaic device stability', *J. Mater. Chem. A*, **2018**, 6, 9604.

[9] D. Bryant, N. Aristidou, S. Pont, I. Sanchez-Molina, T. Chotchunangatchaval, S. Wheeler, J. R. Durrant, and S. A. Haque, 'Light and oxygen induced degradation limits the operational stability of methylammonium lead triiodide perovskite solar cells', *Energ. Environ. Sci.* **2016**, 9, 1655.

[10] S.-H. Turren-Cruz, M. Saliba, M. T. Mayer, H. Juarez-Santesteban, X. Mathew, L. Nienhaus, W. Tress, M. P. Erodici, M.-J. Sher, M. G. Bawendi, M. Graetzel, A. Abate, A. Hagfeldt, and J.-P. Correa-Baena, 'Enhanced charge carrier mobility and lifetime suppress

hysteresis and improve efficiency in planar perovskite solar cells', *Energ. Environ. Sci.* **2018**, 11, 78.

[11] C. C. Stoumpos, C. D. Malliakas, and M. G. Kanatzidis, 'Semiconducting Tin and Lead Iodide Perovskites with Organic Cations: Phase Transitions, High Mobilities, and Near-Infrared Photoluminescent Properties', *Inorg. Chem.* **2013**, 52, 9019.

[12] S. Akin, N. Arora, S. M. Zakeeruddin, M. Graetzel, R. H. Friend, and M. I. Dar, 'New Strategies for Defect Passivation in High-Efficiency Perovskite Solar Cells', *Adv. Energy Mater.* **2019**, 1903090.

[13] N. J. Jeon, J. H. Noh, W. S. Yang, Y. C. Kim, S. Ryu, J. Seo, and S. I. Seok, 'Compositional engineering of perovskite materials for high-performance solar cells', *Nature* **2015**, 517, 476.

[14] N. Pellet, P. Gao, G. Gregori, T.-Y. Yang, M. K. Nazeeruddin, J. Maier, and M. Graetzel, 'Mixed-Organic-Cation Perovskite Photovoltaics for Enhanced Solar-Light Harvesting' *Angew. Chem. Int. Edit.* **2014**, 53, 3151.

[15] M. Saliba, T. Matsui, J.-Y. Seo, K. Domanski, J.-P. Correa-Baena, M. K. Nazeeruddin, S. M. Zakeeruddin, W. Tress, A. Abate, A. Hagfeldt, and M. Graetzel, 'Cesium-containing triple cation perovskite solar cells: improved stability, reproducibility and high efficiency', *Energ. Environ. Sci.* **2016**, 9, 1989.

[16] T. Matsui, J.-Y. Seo, M. Saliba, S. M. Zakeeruddin, and M. Graetzel, 'Room-Temperature Formation of Highly Crystalline Multication Perovskites for Efficient, Low-Cost Solar Cells', *Adv. Mater.* **2017**, 29, 1606258.

[17] Z. Li, M. Yang, J.-S. Park, S.-H. Wei, J. J. Berry, and K. Zhu, 'Stabilizing Perovskite Structures by Tuning Tolerance Factor: Formation of Formamidinium and Cesium Lead Iodide Solid-State Alloys', *Chem. Mater.* **2015**, 28, 284

[18] D. P. McMeekin, G. Sadoughi, W. Rehman, G. E. Eperon, M. Saliba, M. T. Horantner, A. Haghighirad, N. Sakai, L. Korte, B. Rech, M. B. Johnston, L. M. Herz, and H. J. Snaith, 'A mixed-cation lead mixed-halide perovskite absorber for tandem solar cells', *Science* **2016**, 351, 151.

[19] C. Yi, J. Luo, S. Meloni, A. Boziki, N. Ashari-Astani, C. Graetzel, S. M. Zakeeruddin, U. Roethlisberger, and M. Graetzel, 'Entropic stabilization of mixed A-cation ABX₃ metal halide perovskites for high performance perovskite solar cells', *Energ. Environ. Sci.* **2016**, 9, 656.

[20] H. Shen, T. Duong, J. Peng, D. Jacobs, N. Wu, J. Gong, Y. Wu, S. K. Karuturi, X. Fu, K. Weber, X. Xiao, T. P. White, and K. Catchpole, 'Mechanically-stacked perovskite/CIGS tandem solar cells with efficiency of 23.9 % and reduced oxygen sensitivity', *Energ. Environ. Sci.* **2018**, 11, 394.

[21] Ming-Chun Tang, Yuanyuan Fan, Dounya Barrit, Ruipeng Li, Hoang X. Dang, Siyuan Zhang, Timothy J. Magnanelli, Nhan V. Nguyen, Edwin J. Heilweil, Christina A. Hacker, Detlef-M. Smilgies, Kui Zhao, Aram Amassian, and Thomas D. Anthopoulos, 'Efficient Hybrid Mixed-Ion Perovskite Photovoltaics: In Situ Diagnostics of the Roles of Cesium and Potassium Alkali Cation Addition', *Sol. RRL* **2020**, 4, 2000272.

[22] Hoang X. Dang, Kai Wang, Masoud Ghasemi, Ming-Chun Tang, Michele De Bastiani, Erkan Aydin, Emilie Dauzon, Dounya Barrit, Jun Peng, Detlef-M. Smilgies, Stefaan De Wolf, and Aram Amassian, 'Multi-cation Synergy Suppresses Phase Segregation in Mixed-Halide Perovskites', *Joule* **2019**, 3, 1746.

[23] D. Bi, W. Tress, M. I. Dar, P. Gao, J. Luo, C. Renevier, K. Schenk, A. Abate, F. Giordano, J.-P. C. Baena, J.-D. Decoppet, S. M. Zakeeruddin, M. K. Nazeeruddin, M. Graetzel, and A. Hagfeldt, 'Efficient luminescent solar cells based on tailored mixed-cation perovskites', *Science Advances* **2016**, 2, e1501170.

[24] S. I. Seok, M. Graetzel, and N.-G. Park, 'Methodologies toward Highly Efficient Perovskite Solar Cells', *Small* **2018**, 14, 1704177.

[25] H. Zhang, J. Mao, H. He, D. Zhang, H. L. Zhu, F. Xie, K. S. Wong, M. Graetzel, and W. C. H. Choy, 'A Smooth $\text{CH}_3\text{NH}_3\text{PbI}_3$ Film via a New Approach for Forming the PbI_2 Nanostructure Together with Strategically High $\text{CH}_3\text{NH}_3\text{I}$ Concentration for High Efficient Planar-Heterojunction Solar Cells', *Adv. Energy Mater.* **2015**, 5, 1501354.

[26] M. Saliba, T. Matsui, K. Domanski, J.-Y. Seo, A. Ummadisingu, S. M. Zakeeruddin, J.-P. Correa-Baena, W. R. Tress, A. Abate, A. Hagfeldt, and M. Gratzel, 'Incorporation of rubidium cations into perovskite solar cells improves photovoltaic performance', *Science* **2016**, 354, 206.

[27] T. Duong, H. K. Mulmudi, H. Shen, Y. Wu, C. Barugkin, Y. O. Mayon, H. T. Nguyen, D. Macdonald, J. Peng, M. Lockrey, W. Li, Y.-B. Cheng, T. P. White, K. Weber, and K. Catchpole, 'Structural engineering using rubidium iodide as a dopant under excess lead iodide conditions for high efficiency and stable perovskites', *Nano Energy* **2016**, 30, 330.

[28] M. Zhang, J. S. Yun, Q. Ma, J. Zheng, C. F. J. Lau, X. Deng, J. Kim, D. Kim, J. Seidel, M. A. Green, S. Huang, and A. W. Y. Ho-Baillie, 'High-Efficiency Rubidium-Incorporated Perovskite Solar Cells by Gas Quenching', *ACS Energy Lett.* **2017**, 2, 438.

[29] Y. H. Park, I. Jeong, S. Bae, H. J. Son, P. Lee, J. Lee, C.-H. Lee, and M. J. Ko, 'Inorganic Rubidium Cation as an Enhancer for Photovoltaic Performance and Moisture Stability of $\text{HC}(\text{NH}_2)_2\text{PbI}_3$ Perovskite Solar Cells', *Adv. Funct. Mater.* **2017**, 27, 1605988.

[30] T. Duong, Y. Wu, H. Shen, J. Peng, X. Fu, D. Jacobs, E.-C. Wang, T. C. Kho, K. C. Fong, M. Stocks, E. Franklin, A. Blakers, N. Zin, K. McIntosh, W. Li, Y.-B. Cheng, T. P. White, K. Weber, and K. Catchpole, 'Rubidium Multication Perovskite with Optimized Bandgap for Perovskite-Silicon Tandem with over 26% Efficiency', *Adv. Energy Mater.* **2017**, 7, 1700228.

[31] B. Philippe, M. Saliba, J.-P. Correa-Baena, U. B. Cappel, S.-H. Turren-Cruz, M. Graetzel, A. Hagfeldt, and H. Rensmo, 'Chemical Distribution of Multiple Cation (Rb^+ , Cs^+ , MA^+ , and FA^+) Perovskite Materials by Photoelectron Spectroscopy', *Chem. Mater.* **2017**, 29, 3589.

[32] P. Yadav, M. I. Dar, N. Arora, E. A. Alharbi, F. Giordano, S. M. Zakeeruddin, and M. Graetzel, 'The Role of Rubidium in Multiple-Cation-Based High-Efficiency Perovskite Solar Cells', *Adv. Mater.* **2017**, 29, 1701077.

[33] A. Greco, A. Hinderhofer, M. I. Dar, N. Arora, J. Hagenlocher, A. Chumakov, M. Graetzel, and F. Schreiber, 'Kinetics of Ion-Exchange Reactions in Hybrid Organic-Inorganic Perovskite Thin Films Studied by In Situ Real-Time X-ray Scattering', *J. Phys. Chem. Lett.* **2018**, 9, 6750.

[34] P. Gratia, I. Zimmermann, P. Schouwink, J.-H. Yum, J.-N. Audinot, K. Sivula, T. Wirtz, and M. K. Nazeeruddin, 'The Many Faces of Mixed Ion Perovskites: Unraveling and Understanding the Crystallization Process', *ACS Energy Lett.* **2017**, 2, 2686.

[35] R. S. Mitchell, 'Structural polytypism of lead iodide and its relationship to screw dislocations', *Z. Kristallogr.* **1959**, 111, 372-384.

[36] A. Ummadisingu and M. Graetzel, 'Revealing the detailed path of sequential deposition for metal halide perovskite formation', *Science Advances* **2018**, 4, e1701402.

[37] D. J. Kubicki, D. Prochowicz, A. Hofstetter, S. M. Zakeeruddin, M. Graetzel, and L. Emsley, 'Phase Segregation in Cs-, Rb- and K-Doped Mixed-Cation (MA)_x(FA)_{1-x}PbI₃ Hybrid Perovskites from Solid-State NMR' *J. Am. Chem. Soc.* **2017**, 139, 14173.

[38] Y. Hu, M. F. Aygüler, M. L. Petrus, T. Bein, and P. Docampo, 'Impact of Rubidium and Cesium Cations on the Moisture Stability of Multiple-Cation Mixed-Halide Perovskites', *ACS Energy Lett.* **2017**, 2, 2212-2218.

[39] R. Uchida, S. Binet, N. Arora, G. Jacopin, M. H. Alotaibi, A. Taubert, S. M. Zakeeruddin, M. I. Dar, and M. Graetzel, 'Insights about the Absence of Rb Cation from the 3D Perovskite Lattice: Effect on the Structural, Morphological, and Photophysical Properties and Photovoltaic Performance', *Small* **2018**, 14, 1802033.

[40] I. J. Park, S. Seo, M. A. Park, S. Lee, D. H. Kim, K. Zhu, H. Shin, and J. Y. Kim, 'Effect of Rubidium Incorporation on the Structural, Electrical, and Photovoltaic Properties of Methylammonium Lead Iodide-Based Perovskite Solar Cells', *ACS Appl. Mater. Inter.* **2017**, 9, 41898.

[41] M. Abdi-Jalebi, Z. Andaji-Garmaroudi, A. J. Pearson, G. Divitini, S. Cacovich, B. Philippe, H. Rensmo, C. Ducati, R. H. Friend, and S. D. Stranks, 'Potassium- and Rubidium-

Passivated Alloyed Perovskite Films: Optoelectronic Properties and Moisture Stability', *ACS Energy Lett.* **2018**, 3, 2671.

[42] M. I. Dar, A. Hinderhofer, G. Jacopin, V. Belova, N. Arora, S. M. Zakeeruddin, F. Schreiber, and M. Graetzel, 'Function Follows Form: Correlation between the Growth and Local Emission of Perovskite Structures and the Performance of Solar Cells', *Adv. Funct. Mater.* **2017**, 27, 1701433.

[43] N. Arora, M. I. Dar, A. Hinderhofer, N. Pellet, F. Schreiber, S. M. Zakeeruddin, and M. Graetzel, 'Perovskite solar cells with CuSCN hole extraction layers yield stabilized efficiencies greater than 20%', *Science* **2017**, 358, 768.

[44] M. Abdi-Jalebi, M. I. Dar, S. P. Senanayak, A. Sadhanala, Z. Andaji-Garmaroudi, L. M. Pazos-Outon, J. M. Richter, A. J. Pearson, H. Sirringhaus, M. Graetzel, and R. H. Friend, 'Charge extraction via graded doping of hole transport layers gives highly luminescent and stable metal halide perovskite devices', *Science Advances* **2019**, 5, eaav2012.

[45] P. Gratia, I. Zimmermann, P. Schouwink, J.-H. Yum, J.-N. Audinot, K. Sivula, T. Wirtz, and M. K. Nazeeruddin, 'The Many Faces of Mixed Ion Perovskites: Unraveling and Understanding the Crystallization Process', *ACS Energy Lett.* 2017, 2, 2686.

[46] J.-H. Im, C.-R. Lee, J.-W. Lee, S.-W. Park, and N.-G. Park, '6.5% efficient perovskite quantum-dot-sensitized solar cell', *Nanoscale* 2011, 3, 4088.

[47] A. Ummadisingu and M. Graetzel, 'Revealing the detailed path of sequential deposition for metal halide perovskite formation', *Science Advances* 2018, 4, e1701402

Chapter 5 Post-engineering via inorganic salts to reach highly efficient and stable perovskite solar cells

This work is ready for submission/publication

Introduction

Metal halide perovskite (MHPs) solar cells are attracting tremendous attention from both the industry and academia as they represent one of the most promising emerging photovoltaic technologies.^[1–4] From an initial power conversion efficiency (PCE) of 3.8% in 2009^[5], single-junction perovskite solar cells (PSCs) rapidly evolved to reach nowadays a record PCE value of 25.7%.^[6] MHPs are a class of material with the general formula ABX_3 ; A stands for a monovalent cation, whether organic ($HC(NH_2)_2^+$, FA^+ or $CH_3NH_3^+$, MA^+) or inorganic (Cs^+ , Rb^+), B for a divalent metal cation (Pb^{2+} or Sn^{2+}) and X for a monovalent halide anion (I^- , Br^- , Cl^-). Among a wide range of different perovskite compositions, the cubic α -phase of formamidinium lead iodide (α -FAPbI₃) represents the best candidate for highly efficient single-junction solar cells fabrication due to its narrow bandgap of 1.45 to 1.53 eV^[7–9], close to the optimum value given by the Shockley-Queisser limit, which allows for broad solar light absorption and higher thermal stability relative to MAPbI₃.^[10] The introduction of inorganic cesium and/or rubidium cations in FA-rich perovskite compositions has proven to be an efficient strategy to improve the fabrication of perovskite solar cells. Indeed, the introduction of Cs^+ in the bulk of the perovskite lattice decreases the phase impurities in the overall perovskite structure and confers higher stability and reproducibility, whereas Rb^+ helps to lower non-radiative, trap-assisted recombination.^[11,12] Unfortunately, these ions detrimentally change the optoelectronic properties of the perovskite, by increasing its band gap. Given the

energy of the pure material's band gap, this moves it further away from the optimum Shockley-Queisser band gap for single-junction solar cells.^[13] Where the most efficient PSCs based on α -FAPbI₃ attain 25.5% PCE.^[14] Moreover, heteroatoms often tend to create inhomogeneities in the perovskite crystal lattice, which are a major source of degradation and promote non-radiative recombination over the long term.^[15,16] Apart from heteroatoms, the simple fabrication method via solution process and ionic nature of hybrid perovskite causes several drawbacks which yield perovskite films with a rather low phase purity and a high defect density. This is especially present at the perovskite surface and grain boundaries.^[17,18] The vacancies, in particular iodide or cation vacancies, provide a diffusion pathway for cation and halide ions, thus, compromising photovoltaic performance and long-term operational stability.^[19–29] To mitigate these issues, different strategies have been explored, such as compositional engineering, Lewis acid/base,^[30,31] polymers,^[32,33] organic solvents,^[34,35] organic halide salts,^[36,37] and ionic liquids. However, most passivation research has so far involved mostly organic salts as the passivation agents, while the more stable inorganic ones have been overlooked.

Herein, we investigate the effect of two most used different inorganics with different halides namely as CsX and RbX (X=I,Br,Cl⁻) as an additive for surface passivation instead of adding them into the bulk of perovskite layer to mitigate the defects at the interface of perovskite/HTM as well as to enhance the stability. Based on our device optimizations, we found a power conversion efficiency (PCE) of 24.1% with a high fill factor (FF) of 82.2% and 1.16 V open-circuit voltage (V_{oc}) upon the passivation via CsI, whereas control devices delivered a V_{oc} of 1.12 V, 80.5% FF and 22.73 % PCE. CsI-passivated devices exhibit improved operational stability as compared to the control. Afterwards, we analyzed in-depth the effect of CsI passivation on the structural and optical properties of FAPbI₃-rich perovskite by X-Ray diffraction (XRD), X-Ray photoelectron, angle-resolved photoelectron spectroscopy

(XPS, ARXPS), time-resolved photoluminescence (PL, TRPL), photoluminescence quantum yield (PLQY) and time-resolved electroabsorption spectroscopy (TREAS) and Kelvin probe force microscopy (KPFM).

Results and Discussion

To begin with, we prepared perovskite precursor solutions based on rich α -FAPbI₃. We added a small amount of 2% MAPbBr₃ to stabilize the phase of FAPbI₃ as double-cation (FAPbI₃)_{0.98}(MAPbBr₃)_{0.02}, triple-cation Cs_{0.05}FA_{0.93}MA_{0.02}Pb(I_{0.98}Br_{0.02})₃ and quadruple-cation Rb_{0.03}Cs_{0.05}FA_{0.93}MA_{0.02}Pb(I_{0.98}Br_{0.02})₃ perovskite films, labeled as control, CsFAMA and Rb.CsFAMA, respectively. Perovskite films were deposited by spin-coating onto the mesoporous TiO₂ (mp-TiO₂) layer by a one-step method using chlorobenzene as antisolvent. In the first strategy, we carried out an investigation on the effect of mixed cation- halide on the photovoltaic performance. The champion device using CsFAMA showed a PCE of 22.05% with a J_{SC} of 24.6 mA·cm⁻², a V_{OC} of 1.13 V and FF of 78.7%, while using Rb.CsFAMA produced a PCE of 22.4% with a J_{SC} of 24.82 mA·cm⁻², a V_{OC} of 1.16 V and FF of 77.4% and a PCE of 22.7% with a J_{SC} of 25.0 mA·cm⁻², a V_{OC} of 1.12 V and FF of 80.5% achieved by the control as shown in **Figure 1a**. Next strategy, we excluded CsX or RbX (X = F⁻, Cl⁻, Br⁻, I⁻) with different halides from the bulk addition (that is, mixed with precursor solution) and used them as passivated agents on the control ((FAPbI₃)_{0.98}(MAPbBr₃)_{0.02}). For simplicity, we named them as CsX-passivated and RbX-passivated, respectively. This strategy showed a dramatic improvement in the performance with champion PCE of 24.1%, a J_{SC} of 25.15 mA·cm⁻², a V_{OC} of 1.164 V and FF of 82.2% via CsI-passivation, whereas RbI-passivation showed a PCE of 22.95% with a J_{SC} of 24.9 mA·cm⁻², a V_{OC} of 1.15 V and FF of 80.0%, as presented in **Figure 1b**, **Figure S1,S2**. To gain insight on the band gap of these two different strategies, we recorded the incident photon-to-current efficiency (IPCE) spectra ,integrated

current density and the inflection point (**Figure 1c,d and Figure S3a,b**) for Control, CsFAMA, Rb.CsFAMA, CsI-Passivated and RbI-Passivated devices. Control, CsI-passivated and RbI-passivated films exhibited an unchanged bandgap of 1.52 eV, whereas CsFAMA and Rb.CsFAMA showed a bandgap of 1.55 eV. Interestingly, and as shown by the onset of the IPCE spectra, (**Figure 1c**) Cs^+ ions do not change the band gap from the control value of 1.52 eV when passivation is applied. This suggests that Cs^+ does not diffuse into the bulk of the perovskite film but rather act as a surface defect passivator which is in a good agreement with the angle resolved XPS (ARXPS) measurements, shown in **Figure S4**. In the ARXPS experiment, the sample is sequentially tilted with respect to the analyzer. In turn - due to a purely geometrical effect - the effective escape depth of the photoelectron decreases as the tilt angle increases. This implies that species over-represented at the surface proportionally increase with the tilt angle, and with respect to species that are beneath the surface (or uniformly distributed in the depth). The comparison of the relative abundance of elements at different angles reveals that Cs^+ was concentrated at the surface and not incorporated into the bulk of the perovskite lattice upon passivation as observed by the inflection point from IPCE. After screening the effect of these CsI and RbI as mixture and passivated, we can see that the best results are obtained with CsI-Passivated. From here on, we performed an in-depth investigation on the impact of the CsI-Passivated using multi characterization techniques to unravel its effect on the device's photophysics and determine the impact on device stability. In addition, the statistical distribution of the photovoltaic characteristics (J_{sc} , V_{oc} , FF, and PCE) is presented in **Figure 1e** for Control and CsI-passivated. Then, we measured backward and forward JV scans to examine the hysteresis in the Control, CsI-passivated and RbI-Passivated devices (**Figure S5 a,b,c**). The Control device shows a PCE of 22.73 % in the backward scan and 22.01% in the forward scan, RbI-passivated exhibits a PCE of 22.95% in the backward and 21.87% in the forward scan and CsI-passivated represents a PCE of 24.1% in the backward and

23.55% in the forward scan which translated to a hysteresis index ($HI = [(PCE_{backward} - PCE_{forward})/(PCE_{backward})] \times 100$) of 3.17%, 4.70% and 2.28% for the Control, RbI-passivated and CsI-Passivated devices respectively. Furthermore, we carried out the stability test on the Control and CsI-Passivated by subjecting them at MPP for 600 hours under continuous one sun illumination at room temperature under nitrogen environment. The Control and CsI-Passivated devices retained 90 % and 80 % of the initial performance as shown in Figure 1f, respectively.

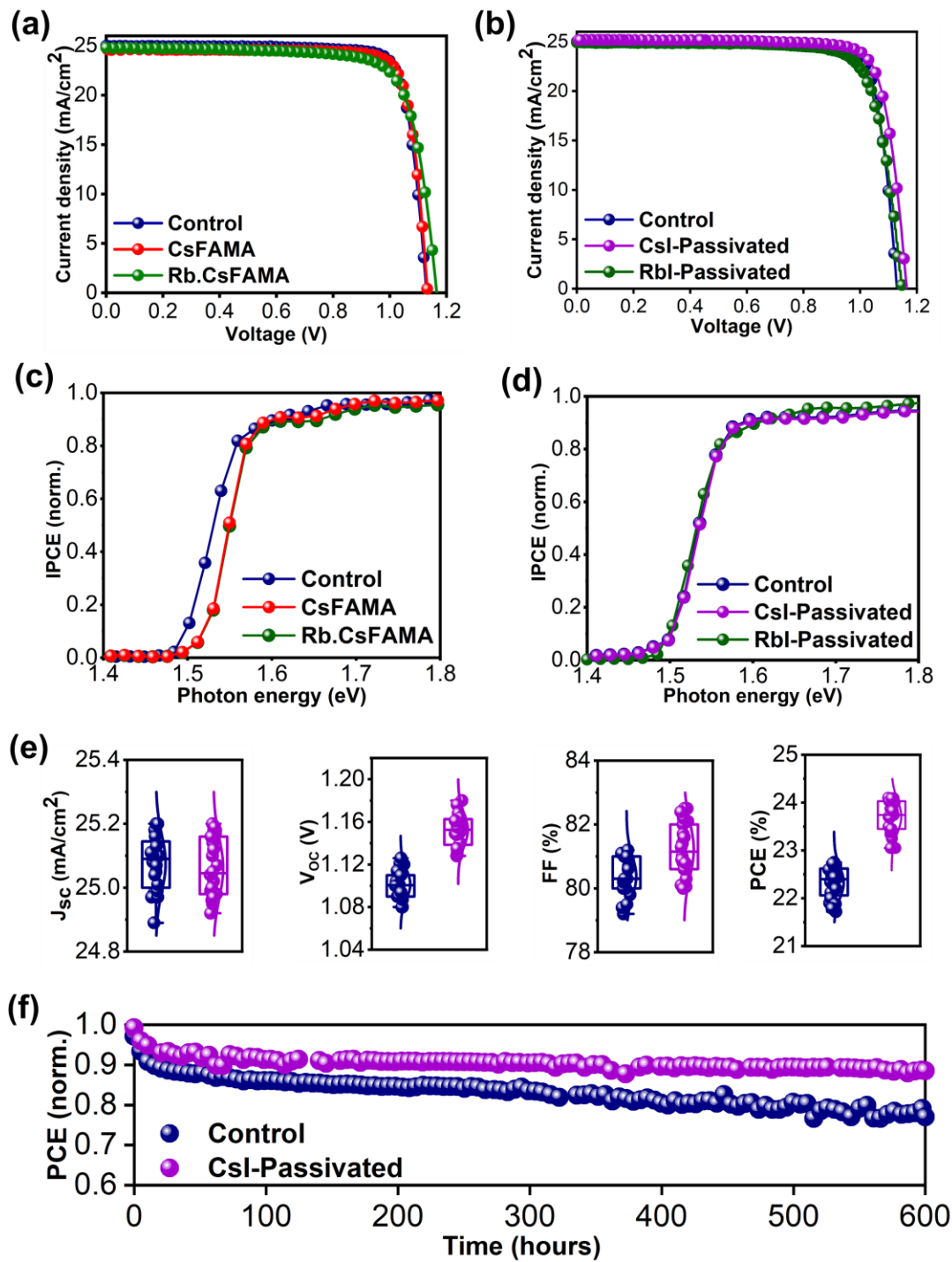


Figure 26. (a) J-V characteristic curves and (c) inflection point extracted from IPCE spectra for Control, CsFAMA and Rb.CsFAMA showing the detrimental effect of the adjunction of Rb^+ and Cs^+ in the perovskite lattice on the photovoltaic performance and typical blue-shift on the absorption of Cs-containing films in the IPCE spectra. (b) J-V characteristic curves and (d) inflection point extracted from IPCE spectra for Control, CsI, and RbI samples. The passivated samples show a superior V_{oc} . (e) Photovoltaic statistics for a batch of 13 control and 13 CsI-passivated devices highlighting the clear superior and reproducible V_{oc} of passivated films and (f) MPP tracking during the operational stability test in a nitrogen environment at room temperature under continuous simulated AM1.5 sunlight.

To analyze the influence of CsI-passivated on the structure of the perovskite absorber layer, XRD was acquired and is shown in **Figure 2a**. The CsI-Passivated completely removes the signal of PbI_2 at 12.6° in the XRD pattern. This suggests a complete conversion of the reactants into the perovskite phase. Furthermore, X-ray photoelectron spectroscopy (XPS) measurements (**Figure 2b**) demonstrate that upon CsI-Passivated addition, the residual metallic lead Pb^0 , which is often observed in MHPs, and is seen in the control films, is totally transformed to Pb^{2+} .^[38] This is a key parameter, as metallic lead aggregates to form deep-level traps, a known source of non-radiative recombination and degradation.^[39] **Figure 3a** shows the surface morphology of both Control and CsI-Passivated perovskite films. CsI-Passivated perovskite film are uniform and highly crystalline with much larger perovskite grains as compared to the non-treated perovskite (Control) as shown in **Figure 3a**. In **Figure 3b** and **Figure S6**, the Kelvin Probe Force (KPFM) microscopy measurements of the control and CsI-Passivated exhibit the striking effect of cesium iodide in mitigating surface inhomogeneities, i.e. defects, in the surface potential of the perovskite film. The CsI-Passivated treatment yields films showing a homogeneous surface with potential variations of less than 10 mV, whereas the untreated films (Control) exhibit differences close to 30 mV. Moreover, the atomic force microscopy (AFM) measurements reveals that both conditions result in very similar topography as shown in **Figure S7**.

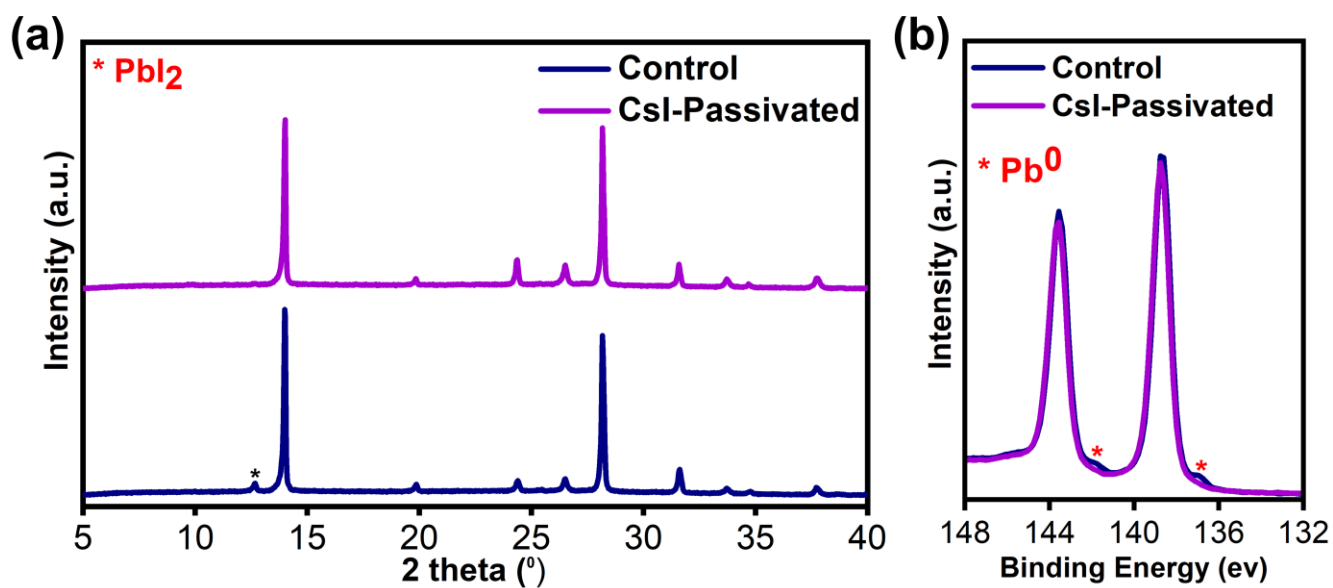


Figure 27. (a) XRD patterns of Control and CsI perovskite films on FTO highlighting the suppression of PbI_2 signal upon CsI passivation (b) XPS Pb 4f spectra of Control and CsI showing the suppression of residual unreacted Pb^0 upon CsI passivation.

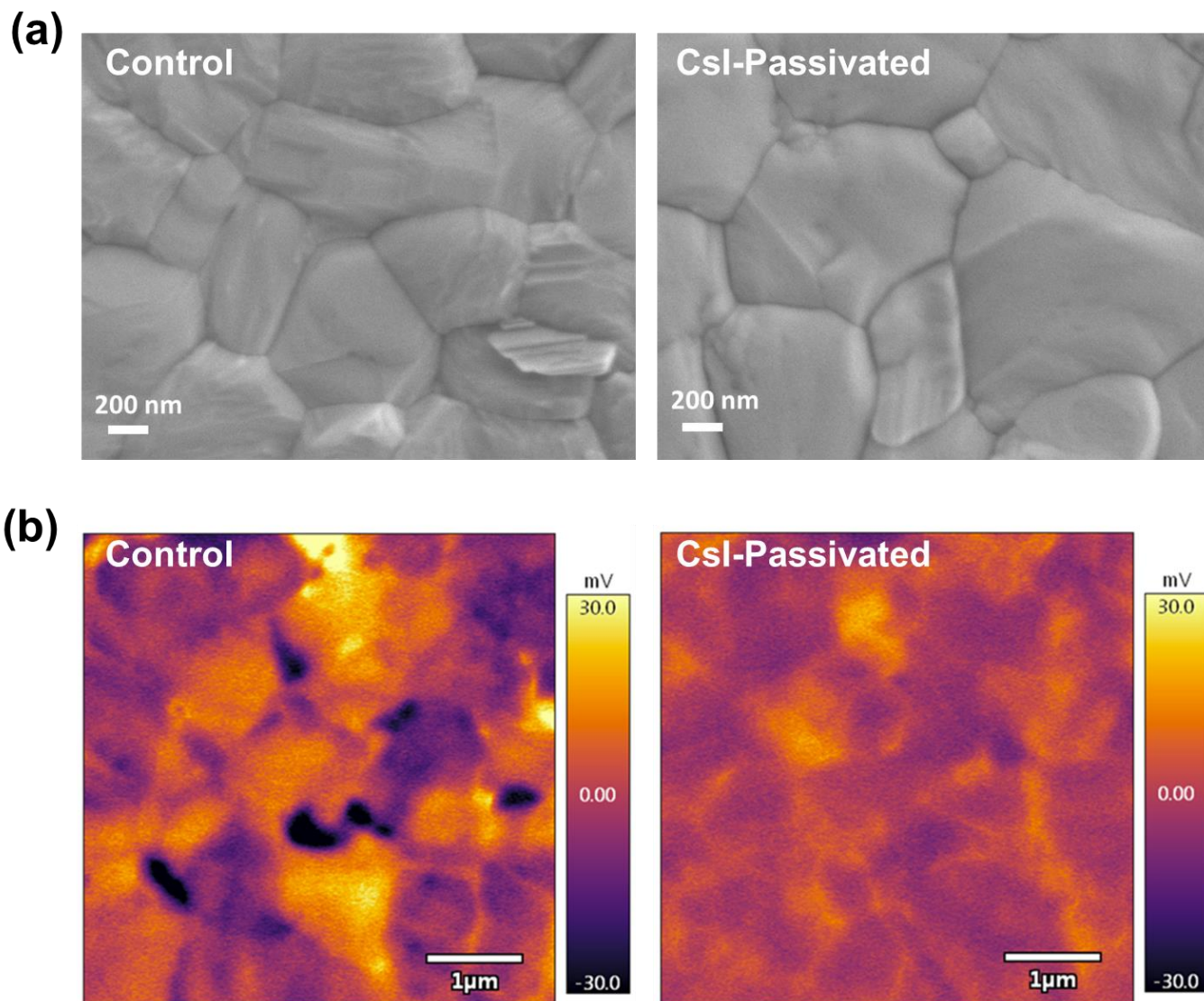


Figure 3 (a) Top-view SEM micrographs of Control and CsI conditions exhibiting much bigger grain size (around 1 μm) for CsI-passivated perovskite (b) KPFM measurements of Control and CsI, respectively, showing a much more homogeneous surface potential for CsI perovskite films compared to Control.

Next, we carried out an in-depth investigation of the optoelectronic properties of the Control and CsI-Passivated. We performed time-resolved electroabsorption spectroscopy (TREAS) to get insights into the intrinsic charge carrier mobility and lifetime. **Figure 4a and Figure S8,S9** show TREAS displayed two different domains in both the Control and CsI-Passivated. The first (linear) domain corresponds to the intragrain charge carrier separation and shows a rather similar time constant for both conditions. The second (logarithmic) domain shows the increase of the signal owing to the accumulation of charge at the perovskite surface and can thus be used to determine charge carriers mobilities in the perovskite films. Time

constants of $\tau = 2.57$ ps and $\tau = 2.10$ ps were recorded for the control and CsI-Passivated films, respectively. The mobility being inversely proportional to this time constant ($\mu = \frac{l}{\tau[E]_0}$; where μ is the mobility, $l = (l_{e^-} + l_{h^+})/2$ the charges transit distance, averaged here as half the perovskite layer thickness, τ the logarithmic domain time constant and $[E]_0$ the bias applied accounting for the voltage drop across the Al_2O_3 insulating layer),^[40] TREAS demonstrate the CsI-Passivated leads to the higher mobility of charges, with a determined mobility of $24.2 \text{ cm}^2\text{V}^{-1}\text{s}^{-1}$ for CsI-Passivated vs. $19.8 \text{ cm}^2\text{V}^{-1}\text{s}^{-1}$ for Control films. We assumed equal mobility for holes and electrons. The lifetimes were calculated at $1.05 \cdot 10^3$ ns and $1.0 \cdot 10^3$ ns for the control and CsI-passivated films via TRPL, respectively, which is in good agreement with TREAS. To further verify this, we analyzed the diode characteristics of the devices. In figure 4c, we measured the ideality factor (n_{id}) by taking the dependence of V_{OC} as a function of incident light intensity. With the treated device (CsI-Passivated) the n_{id} decreases from 1.54 (Control) to 1.27, which indicates a substantial reduction of non-radiative recombination. To further confirm the role of nonradiative recombination, we measured absolute photoluminescence (PL) photon fluxes $\Phi_{PL}(E)$ of Control and CsI-Passivated films following established methods.^[41] Stunningly, the PLQY improved from 0.4% for the untreated perovskite films to as high as 8% for CsI-passivated films as shown in **Figure 3d** with an exhibition of increased Quasi-Fermi levels splitting (QFLS) of 1.20 V compared to 1.13 V for Control film (Figure 3d). Overall, these results, acquired from PV devices, n_{id} , TREAS, TRPL and PLQY indicate that the CsI-Passivated improves the quality of perovskite and reduces the non-radiative recombination rate and increases the charge carrier mobility, leading to the observed improvements in both V_{OC} and FF.

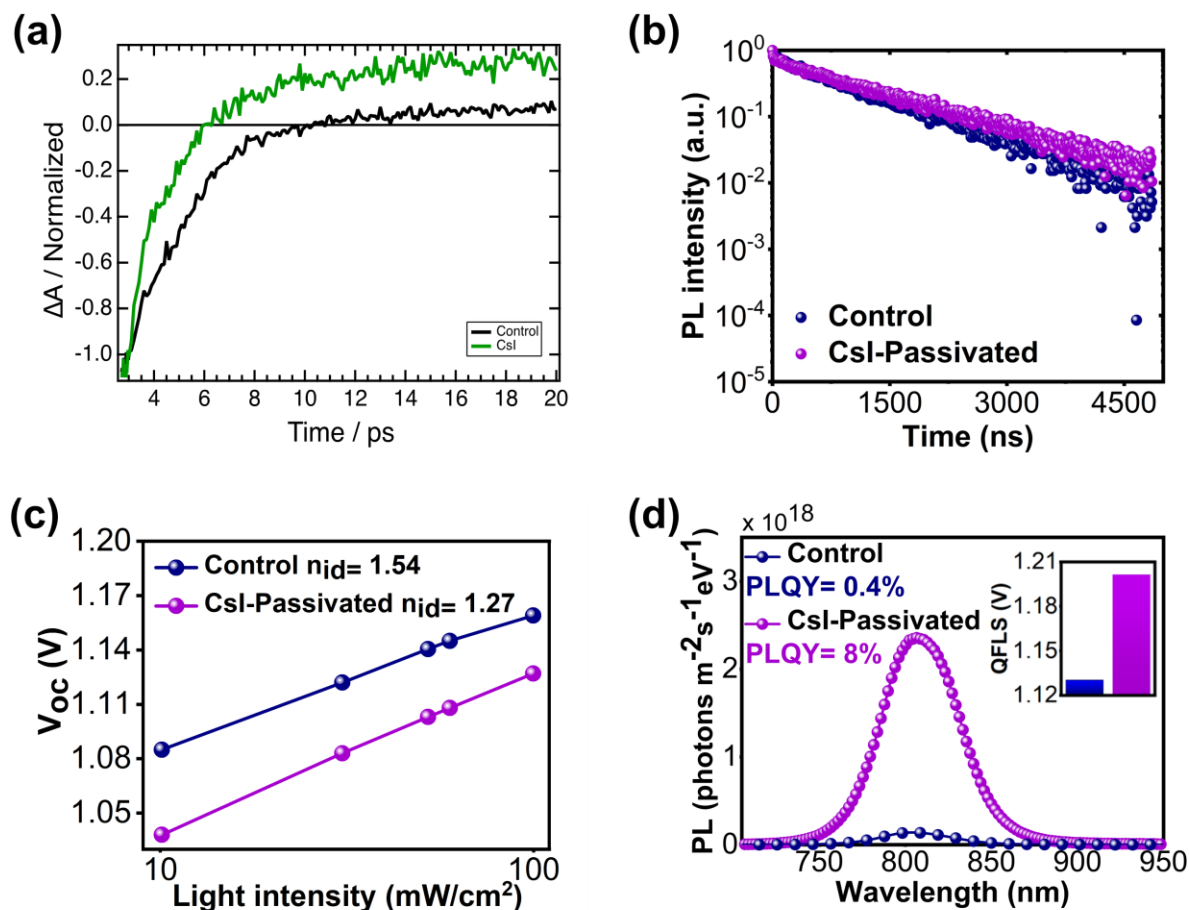


Figure 4. (a) TREAS measurements of the control and CsI films on TiO_2 . The higher free charge carrier mobility for CsI films (24.2 vs $19.8 \text{ cm}^2\text{V}^{-1}\text{s}^{-1}$) suggests lower defects (b) TRPL measurements of the control and CsI films on glass. Charge carriers lifetime is improved in CsI-treated films compared to the control. (c) ideality factor of Control and CsI solar cells (d) PLQY measurements of Control and CsI films exhibiting a PLQY of 0.4 and 8% respectively, showing an impressive 18x increase upon CsI passivation. (inset: Quasi-Fermi level splitting of the control and CsI film. The larger QFLS of the CsI-passivated films attests to their higher quality).

Conclusion

In summary, we applied CsI as passivator instead of stabilizer to suppress the defects at the interface of perovskite/HTM to obtain highly efficient and stable perovskite based on rich $\alpha\text{-FAPbI}_3$. The objective was to remove Cs^+ ions from the perovskite composition to prepare stable and robust perovskite solar cells without sacrificing the optimum J - V parameters delivered by the pure $\alpha\text{-FAPbI}_3$ perovskite composition. As a result, CsI-passivated devices achieved a PCE exceeding 24% which also exhibits a remarkable improvement in structural,

morphological, and optoelectronic properties as well as device operational stability based on our in-depth experimental investigation. Results suggest that CsI passivation efficiently suppresses non-radiative recombination by passivating defects at the surface of the perovskite, yielding higher QFLS and in turn, V_{OC} . The facile strategy provided in this work has the potential to stimulate other successful developments in the future.

Experimental Section/Methods

Solar cells preparation:

Fluorine-doped tin oxide (FTO)-glass substrates (TCO glass, NSG 10, Nippon sheet glass, Japan) were etched from the edges by using Zn powder and 4 M HCl and then, were cleaned by ultrasonication in Hellmanex (2%, deionized water), rinsed thoroughly with de-ionized water and ethanol, and then treated in oxygen plasma for 15 min. An approximately 30 nm thick blocking layer (TiO_2) was deposited on the cleaned FTO by spray pyrolysis at 450 °C using a commercial titanium diisopropoxide bis(acetylacetonate) solution (75% in 2-propanol, Sigma-Aldrich) diluted in anhydrous ethanol (1:9 volume ratio) as precursor and oxygen as a carrier gas. A mesoporous TiO_2 layer was deposited by spin-coating a diluted paste in ethanol (1:6 wt. ratio) (Dyesol 30NRD:ethanol) at 5000 rpm for 15 s and sintered at 450°C for 30 min in dry atmosphere.

Fabrication of perovskite films:

The perovskite films were deposited using a single-step deposition method from the precursor solution, which was prepared in an argon atmosphere by dissolving FAI, MABr, PbI_2 in anhydrous dimethylformamide/dimethyl sulfoxide (4:1 (volume ratio)) to achieve the desired composition: $(FAPbI_3)_{0.98}(MAPbBr_3)_{0.02}$ with 3% PbI_2 excess and 44 mg MAI. The perovskite films were then passivated by dynamically spin-coating (6000 rpm for 45 s) a 3 mg.mL⁻¹ solution of EAI (EAI = ethylammonium iodide = $CH_3CH_2NH_3^+ I^-$) in isopropanol. CsX

(X = Br⁻, Cl⁻, I⁻) and RbX (X = Br⁻, Cl⁻, I⁻) were deposited on the surface of EAI-passivated films by spin-coating solutions (in MeOH) following the same procedure. The HTM was deposited by spin-coating at 5000 rpm for 30 s. The HTM was doped with bis(trifluoromethylsulfonyl)imide lithium salt (17.8 μ l prepared by dissolving 520 mg LiTFSI in 1 ml of acetonitrile), and 28.8 μ l of 4-tert-butylpyridine. Finally, an approximately 80 nm gold (Au) layer was thermally evaporated.

Device characterization:

The current-voltage (J-V) characteristics of the perovskite devices were recorded with a digital source meter (Keithley model 2400, USA). A 450 W xenon lamp (Oriel, USA) was used as the light source for photovoltaic (J-V) measurements. The spectral output of the lamp was filtered using a Schott K113 Tempax sunlight filter (Präzisions Glas & Optik GmbH, Germany) to reduce the mismatch between the simulated and actual solar spectrum to less than 2%. The photo-active area of 0.16 cm² was defined using a dark-colored metal mask.

Incident photon-to-current efficiency (IPCE):

The IPCE was recorded under a constant white light bias of approximately 5 mW cm⁻² supplied by an array of white light emitting diodes. The excitation beam coming from a 300 W Xenon lamp (ILC Technology) was focused through a Gemini- 180 double monochromator (Jobin Yvon Ltd) and chopped at approximately 2 Hz. The signal was recorded using a Model SR830 DSP Lock-In Amplifier (Stanford Research Systems).

Scanning electron microscopy (SEM):

SEM micrograph measurements were performed on a ZEISS Merlin HR-SEM.

X-ray powder diffractions (XRD):

XRD patterns of the perovskite films were recorded on an X'Pert MPD PRO (Panalytical) equipped with a ceramic tube (Cu anode, $\lambda = 1.54060 \text{ \AA}$), a secondary graphite (002) monochromator and a RTMS X'Celerator (Panalytical).

Atomic force microscopy (AFM) and kelvin probe force microscopy (KPFM):

AFM/KPFM were performed with an Asylum Research Cypher using Pt coated tips (AC240TM, Olympus) under ambient condition and at the room temperature. The films were measured on the grounded FTO substrate for the KPFM characterizations. The resulting images were processed by flattening.

Photoluminescence Quantum Yield (PLQY):

The PLQY was acquired following the procedure suggested by de Mello.²⁰³ The samples were excited using a continuous-wave laser (OBIS LX, 660 nm) whose power was adjusted to match the photogeneration rate under 1 sun of illumination (0.324 mW, 0.786 mm effective beam full width at half-maximum (fwhm)). The signal was collected using an integrating sphere (Gigahertz Optik, UPB-150-ARTA) connected via a multimode, 400 μm diameter optical fiber (Thorlabs BFL44LS01) to a spectrometer (Andor, Kymera 193i). The system was spectrally calibrated using an irradiance calibration standard lamp (Gigahertz Optik, BN-LH250-V01).

Time-resolved photoluminescence (TRPL):

The TRPL of perovskite films on glass was measured with a spectrometer (FluoroLog-3, Horiba) working in a time-correlated single-photon counting mode with <ns time resolution. A picosecond pulsed diode laser head NanoLED N-670L (Horiba) emitting <200 ps duration pulses at 670 nm with a maximum repetition rate of 1 MHz was used as excitation source.

Electroabsorption (EA) and time-resolved electroabsorption spectroscopy (TREAS)

measurements:

EA and TREAS measurements were carried out using a femto-second pump probe spectrometer based on a Ti:sapphire laser (Clark-MXR, CPA-2001) delivering 778 nm pulses with a pulse duration of 150 fs and a 1 kHz repetition rate. The difference between the two techniques is that TREAS involves pumping the sample, whereas EA just uses the probe beam. The 389 nm pump beam for TREAS measurements was generated by passing part of the fundamental through a beta barium borate (BBO) crystal in order to generate the second harmonic at 389 nm. In both EA and TREAS the probe beam, consisting of a broadband white light continuum (400 – 750 nm), was generated by passing part of the fundamental through a 4 mm sapphire window. Measurements were carried out in reflection mode, and the probe beam was split into a signal and reference beam to account for shot-to-shot fluctuations. The signal and reference beams were dispersed into two spectrographs (SR163, Andor Instruments) and detected shot-to-shot at 1 kHz using 512x68 pixel back-thinned CCD cameras (Hamamatsu S07030-0906). Square pulses generated by a function generator (Tektronix AFG 2021, from -10 to 10 V, 100 μ s pulse duration) were used to modulate the electric field across the sample at 500 Hz. The current responses across the samples were recorded using a 50 Ω series load with a 400 MHz bandpass oscilloscope (Tektronix TDS 3044B).

X-ray photoelectron spectroscopy (XPS and Angle-Resolved X-ray photoelectron spectroscopy (ARXPS):

XPS and ARXPS measurements were carried out using a PHI VersaProbe II scanning XPS microprobe with Al K α X-ray source. For XPS measurements, the spherical capacitor analyser was set at 45° take-off angle with respect to the sample surface. Bulk composition analysis was done after argon plasma etching. Data were processed using the PHI Multipak software.

Long term light soaking test:

Stability measurements were performed with a Biologic MPG2 potentiostat under a full AM 1.5 Sun-equivalent white LED lamp. The devices were measured with a maximum power point

(MPP) tracking routine under continuous illumination at room temperature. The MPP was updated every 10 s by a standard perturb and observe method. Every minute a *JV* curve was recorded in order to track the evolution of individual *JV* parameters.

Supporting Information

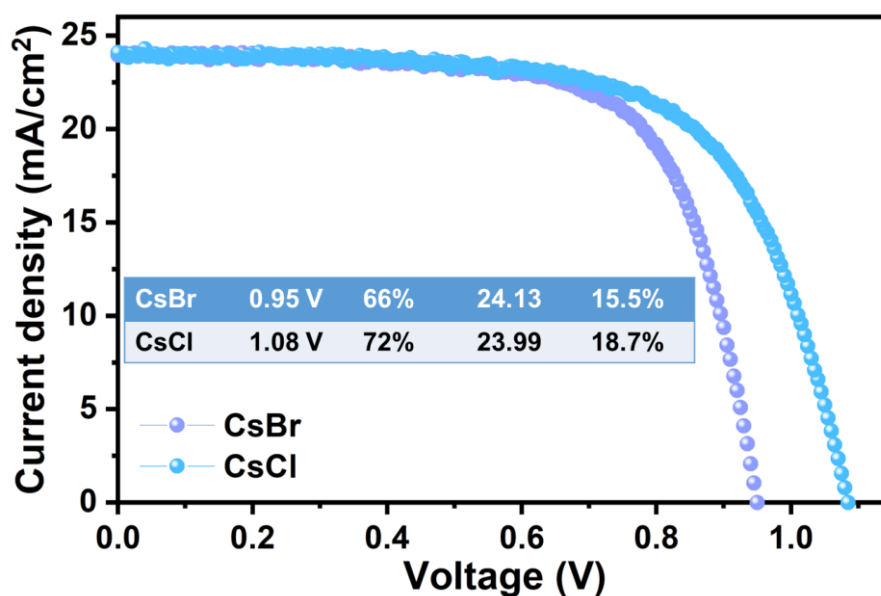


Figure S1. J-V characteristic curves of the control perovskite films passivated with CsX salts (X = Br⁻, Cl⁻, I⁻)

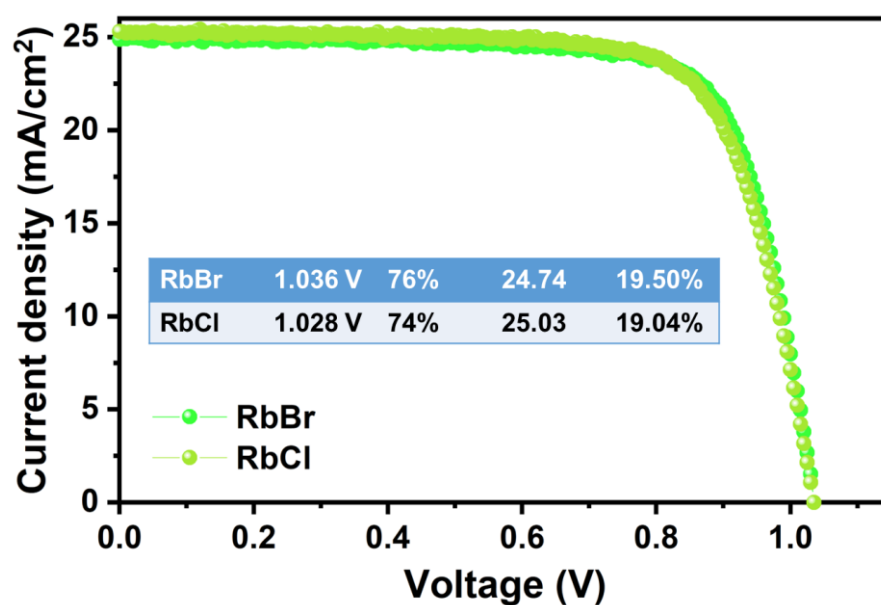


Figure S2. J-V characteristic curves of the control perovskite films passivated with RbX salts (X = Br⁻, Cl⁻, I⁻) with CsI displayed for comparison

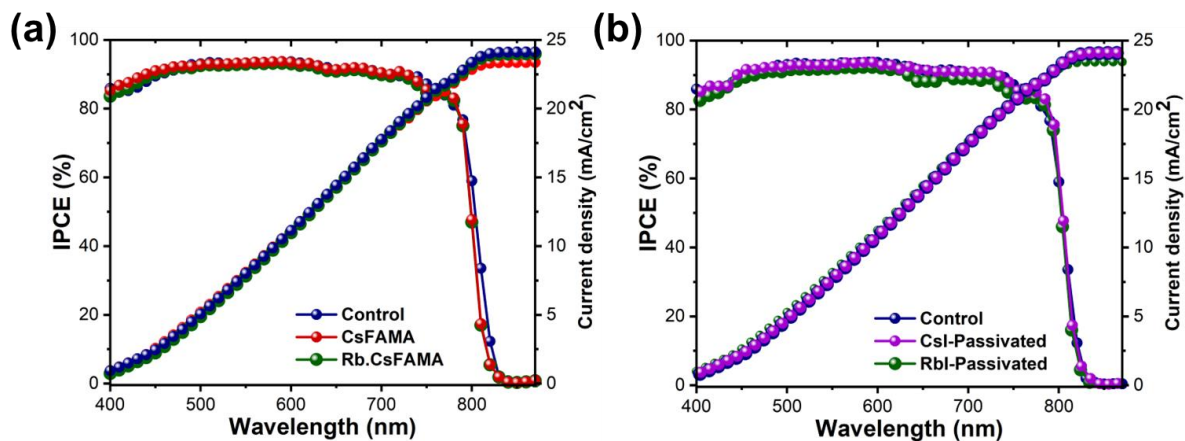


Figure S3 IPCE spectra for Control, CsFAMA and Rb.CsFAMA (a) showing the detrimental effect of the adjunction of Rb and Cs on the photovoltaic performance and typical blue-shift on the absorption of Cs-containing films and IPCE spectra of Control, CsI and RbI-passivated films (b) showing no shift upon CsI passivation, suggesting no incorporation of Cs⁺ ions in the perovskite lattice

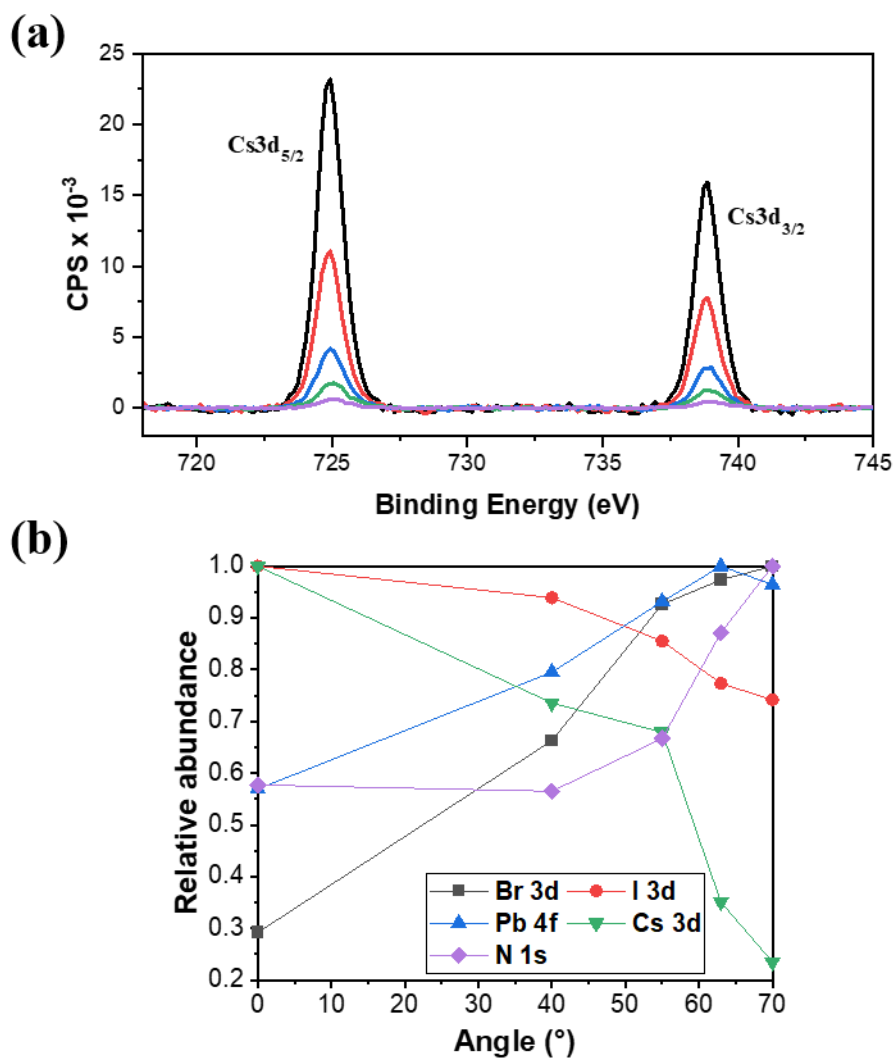
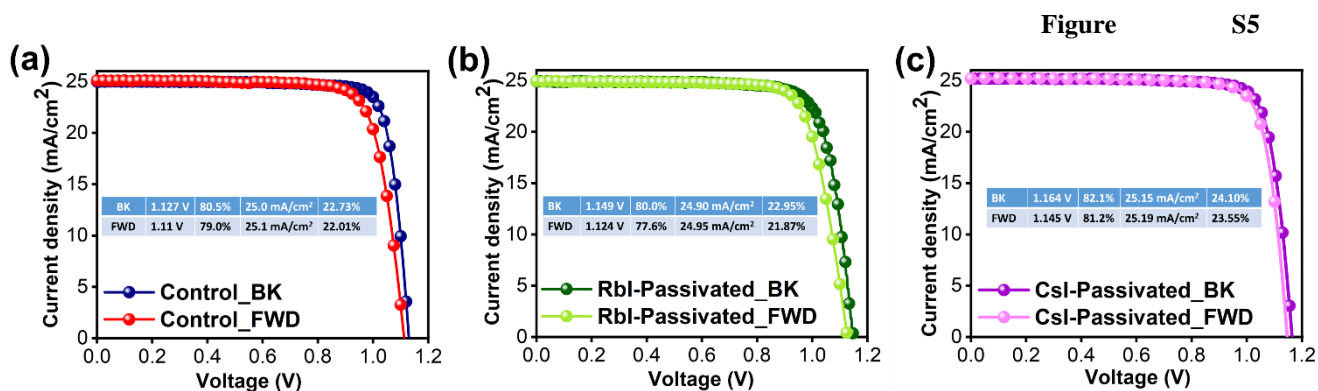


Figure S4. (a) ARXPS spectra of Cs 3d measured at 0, 40, 55, 63 and 70 degrees (b) relative abundance of Cs(3d), Pb(4f), N(1s), I(3d) and Br(3d) in function of the ARXPS angle showing the gradient of cesium concentration within the first few nanometers of CsI perovskite film. Cs 3d signal intensity decreases as the ARXPS angle is reduced.



Backward and forward *JV* scans of Control (A), RbI-passivated (B) and CsI-passivated (C)

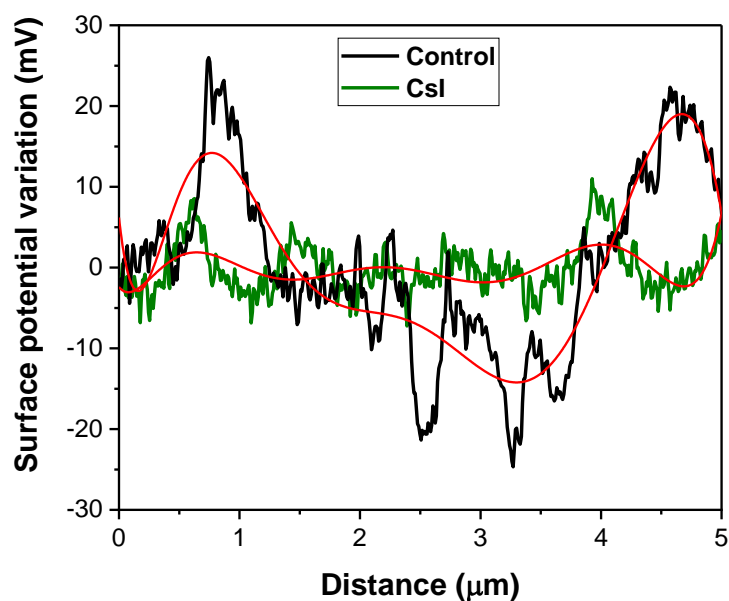


Figure S6. Surface potential variation of the control and CsI films measured by KPFM

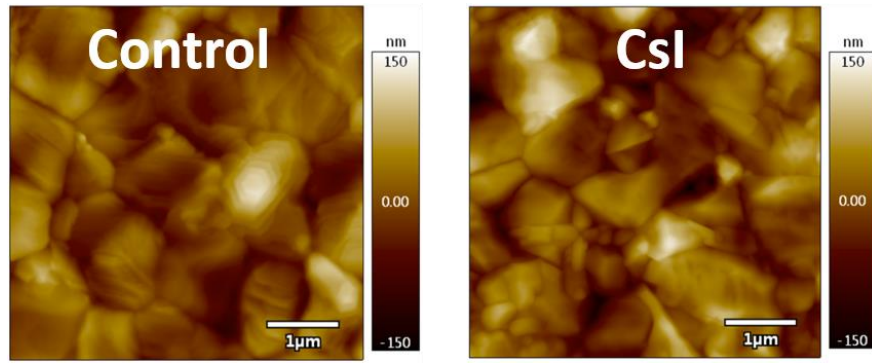


Figure S7. AFM measurement of the control and CsI perovskite films exhibiting similar roughness

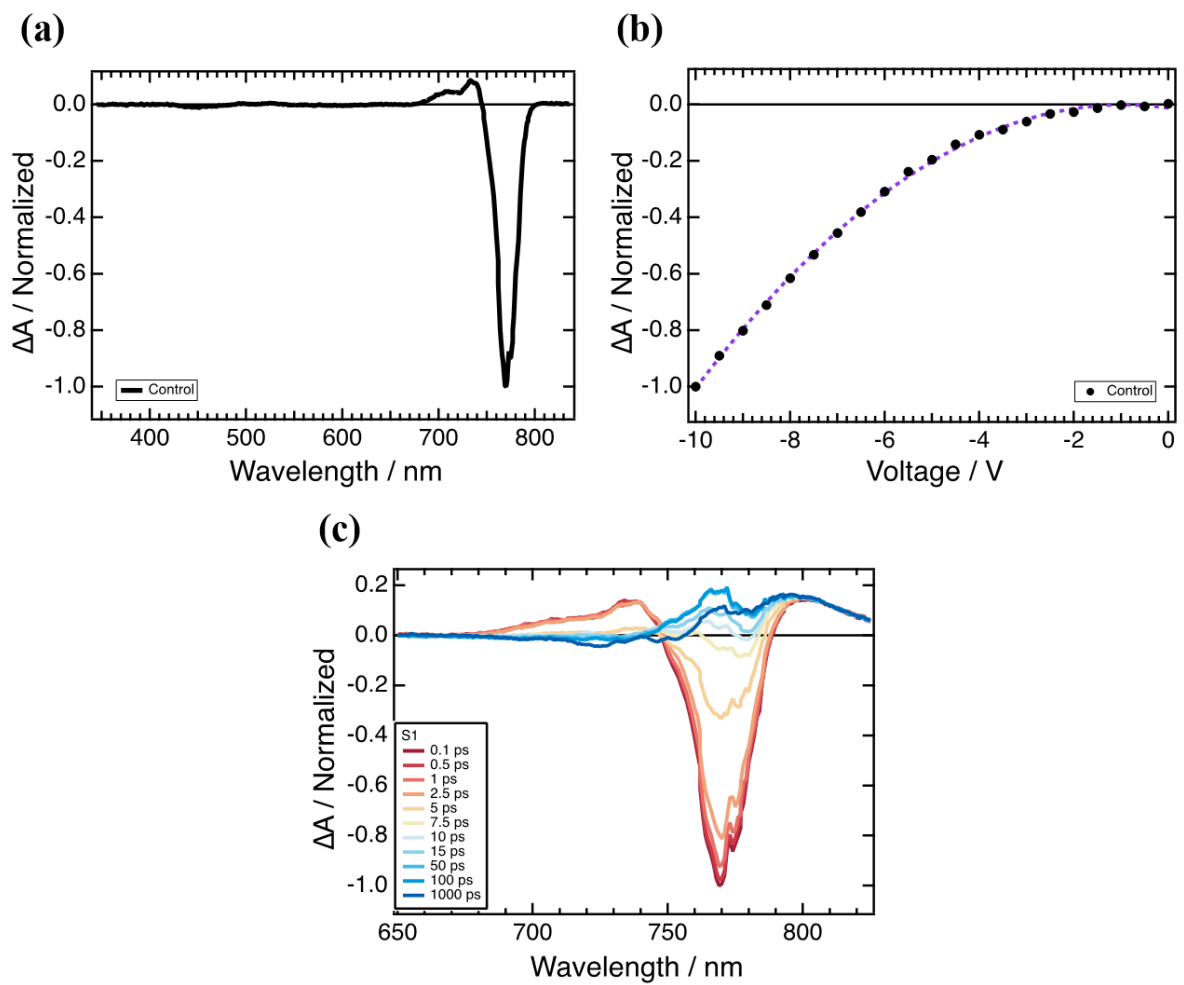


Figure S8. EA and TREAS plots for the control perovskite film

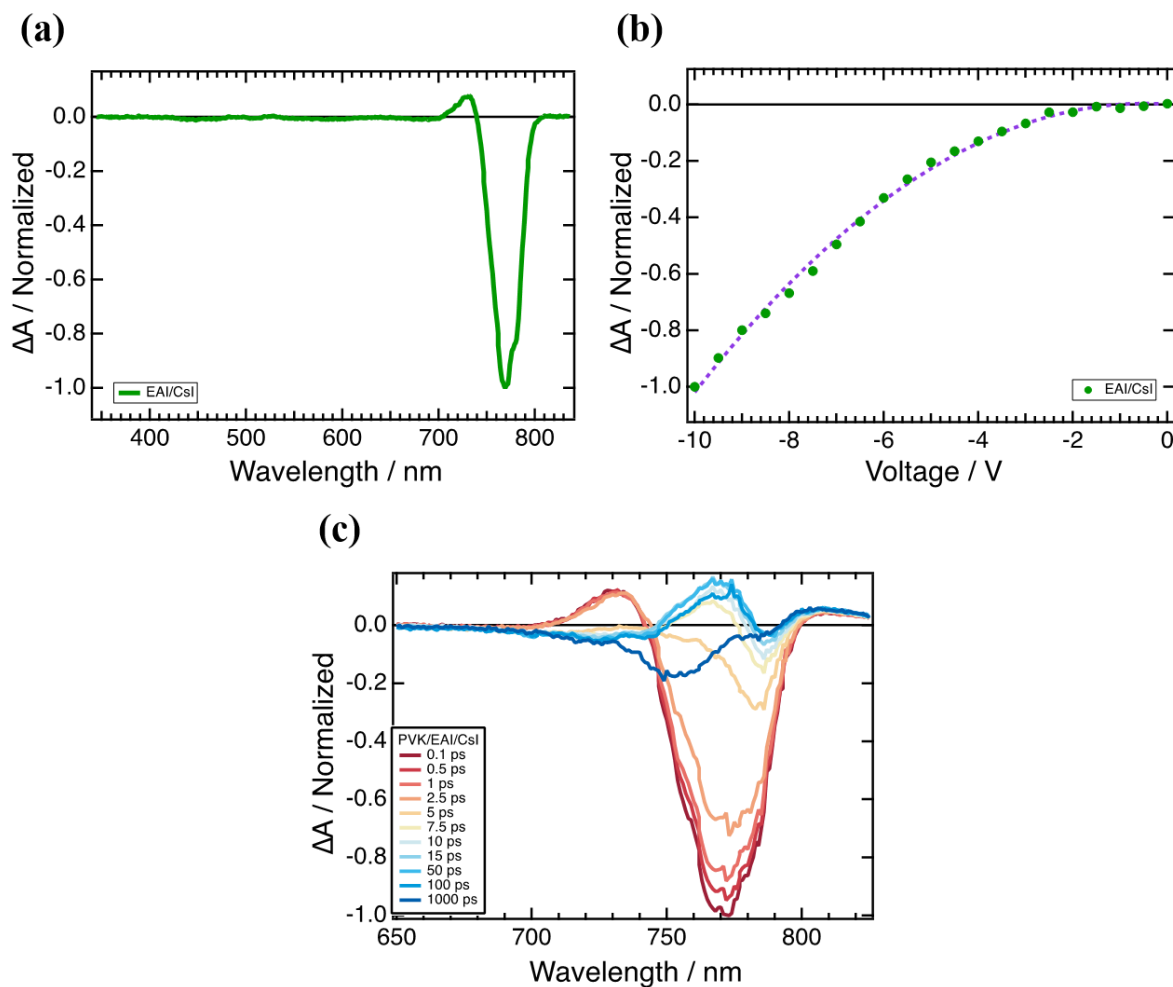


Figure S9. EA and TREAS plots for the CsI-passivated perovskite film

References

- [1] M. Grätzel, *Nat. Mater.* **2014**, *13*, 838.
- [2] N. G. Park, M. Grätzel, T. Miyasaka, K. Zhu, K. Emery, *Nat. Energy* **2016**, *1*, 1.
- [3] J. P. Correa-Baena, M. Saliba, T. Buonassisi, M. Grätzel, A. Abate, W. Tress, A. Hagfeldt, *Science (80-.)*. **2017**, *358*, 739.
- [4] M. A. Green, A. Ho-Baillie, H. J. Snaith, *Nat. Photonics* **2014**, *8*, 506.
- [5] A. Kojima, K. Teshima, Y. Shirai, T. Miyasaka, *J. Am. Chem. Soc.* **2009**, *131*, 6050.
- [6] National Renewable Energy Laboratory of the United States of America (NREL) National Center for Photovoltaics, "Best Research-Cell Efficiencies chart," can be

found under <https://www.nrel.gov/pv/assets/pdfs/best-research-cell-efficiencies.20200925.pdf>, **n.d.**

- [7] Q. Han, S. H. Bae, P. Sun, Y. T. Hsieh, Y. Yang, Y. S. Rim, H. Zhao, Q. Chen, W. Shi, G. Li, Y. Yeng, *Adv. Mater.* **2016**, 28, 2253.
- [8] G. E. Eperon, S. D. Stranks, C. Menelaou, M. B. Johnston, L. M. Herz, H. J. Snaith, *Energy Environ. Sci.* **2014**, 7, 982.
- [9] A. Amat, E. Mosconi, E. Ronca, C. Quarti, P. Umari, M. K. Nazeeruddin, M. Grätzel, F. De Angelis, *Nano Lett.* **2014**, 14, 3608.
- [10] E. Smecca, Y. Numata, I. Deretzis, G. Pellegrino, S. Boninelli, T. Miyasaka, A. La Magna, A. Alberti, *Phys. Chem. Chem. Phys.* **2016**, 18, 13413.
- [11] M. Saliba, T. Matsui, J. Y. Seo, K. Domanski, J. P. Correa-Baena, M. K. Nazeeruddin, S. M. Zakeeruddin, W. Tress, A. Abate, A. Hagfeldt, M. Grätzel, *Energy Environ. Sci.* **2016**, 9, 1989.
- [12] P. Yadav, M. I. Dar, N. Arora, E. A. Alharbi, F. Giordano, S. M. Zakeeruddin, M. Grätzel, *Adv. Mater.* **2017**, 29, 1701077.
- [13] W. Shockley, H. J. Queisser, *R. ell, Cit. J. Appl. Phys* **1961**, 32, 510.
- [14] M. Kim, J. Jeong, H. Lu, T. K. Lee, F. T. Eickemeyer, Y. Liu, I. W. Choi, S. J. Choi, Y. Jo, H.-B. Kim, S.-I. Mo, Y.-K. Kim, H. Lee, N. G. An, S. Cho, W. R. Tress, S. M. Zakeeruddin, A. Hagfeldt, J. Y. Kim, M. Grätzel, D. S. Kim, *Science (80-.).* **2022**, 375, 302.
- [15] J. P. Correa-Baena, Y. Luo, T. M. Brenner, J. Snider, S. Sun, X. Li, M. A. Jensen, N. T. P. Hartono, L. Nienhaus, S. Wieghold, J. R. Poindexter, S. Wang, Y. S. Meng, T. Wang, B. Lai, M. V. Holt, Z. Cai, M. G. Bawendi, L. Huang, T. Buonassisi, D. P. Fenning, *Science (80-.).* **2019**, 363, 627.
- [16] D. J. Kubicki, D. Prochowicz, A. Hofstetter, S. M. Zakeeruddin, M. Grätzel, L. Emsley, *J. Am. Chem. Soc.* **2017**, 139, 14173.
- [17] Q. Jiang, Y. Zhao, X. Zhang, X. Yang, Y. Chen, Z. Chu, Q. Ye, X. Li, Z. Yin, J. You, *Nat. Photonics* **2019**, 13, 460.
- [18] Y. Yang, S. Feng, W. Xu, M. Li, L. Li, X. Zhang, G. Ji, X. Zhang, Z. Wang, Y. Xiong,

- L. Cao, B. Sun, X. Gao, *ACS Appl. Mater. Interfaces* **2017**, 9, 23141.
- [19] N. G. Park, K. Zhu, *Nat. Rev. Mater.* **2020**, 5, 333.
- [20] M. Saliba, T. Matsui, K. Domanski, J. Y. Seo, A. Ummadisingu, S. M. Zakeeruddin, J. P. Correa-Baena, W. R. Tress, A. Abate, A. Hagfeldt, M. Grätzel, *Science (80-.)*. **2016**, 354, 206.
- [21] R. J. Stoddard, A. Rajagopal, R. L. Palmer, I. L. Braly, A. K. Y. Jen, H. W. Hillhouse, *ACS Energy Lett.* **2018**, 3, 1261.
- [22] S. H. Turren-Cruz, A. Hagfeldt, M. Saliba, *Science (80-.)*. **2018**, 362, 449.
- [23] M. M. Tavakoli, P. Yadav, D. Prochowicz, M. Sponseller, A. Osherov, V. Bulović, J. Kong, *Adv. Energy Mater.* **2019**, 9, DOI 10.1002/aenm.201803587.
- [24] L. Shi, M. P. Bucknall, T. L. Young, M. Zhang, L. Hu, J. Bing, D. S. Lee, J. Kim, T. Wu, N. Takamure, D. R. McKenzie, S. Huang, M. A. Green, A. W. Y. Ho-Baillie, *Science (80-.)*. **2020**, 368, DOI 10.1126/science.aba2412.
- [25] Y. Yun, F. Wang, H. Huang, Y. Fang, S. Liu, W. Huang, Z. Cheng, Y. Liu, Y. Cao, M. Gao, L. Zhu, L. Wang, T. Qin, W. Huang, *Adv. Mater.* **2020**, 32, DOI 10.1002/adma.201907123.
- [26] J. Burschka, N. Pellet, S. J. Moon, R. Humphry-Baker, P. Gao, M. K. Nazeeruddin, M. Grätzel, *Nature* **2013**, 499, 316.
- [27] J. Jeong, M. Kim, J. Seo, H. Lu, P. Ahlawat, A. Mishra, Y. Yang, M. A. Hope, F. T. Eickemeyer, M. Kim, Y. Jin Yoon, I. Woo Choi, B. Primera Darwich, S. Ju Choi, Y. Jo, J. Hee Lee, B. Walker, S. M. Zakeeruddin, L. Emsley, U. Rothlisberger, A. Hagfeldt, D. Suk Kim, M. Grätzel, J. Young Kim, *Nature* **2021**, 592, 381.
- [28] L. Merten, A. Hinderhofer, T. Baumeler, N. Arora, J. Hagenlocher, S. M. Zakeeruddin, M. I. Dar, M. Grätzel, F. Schreiber, *Chem. Mater.* **2021**, acs. chemmater.0c04185.
- [29] X. Zheng, B. Chen, J. Dai, Y. Fang, Y. Bai, Y. Lin, H. Wei, X. C. Zeng, J. Huang, *Nat. Energy* 2017 27 **2017**, 2, 1.
- [30] Y. Lin, L. Shen, J. Dai, Y. Deng, Y. Wu, Y. Bai, X. Zheng, J. Wang, Y. Fang, H. Wei, W. Ma, X. Cheng Zeng, X. Zhan, J. Huang, Y. Lin, L. Shen, Y. Deng, Y. Bai, X. Zheng, Y. Fang, H. Wei, J. Huang, J. Dai, X. C. Zeng, Y. Wu, W. Ma, J. Wang, X.

- Zhan, *Adv. Mater.* **2017**, 29, 1604545.
- [31] W. Tress, K. Domanski, B. Carlsen, A. Agarwalla, E. A. Alharbi, M. Graetzel, A. Hagfeldt, *Nat. Energy* **2019**, 4, 568.
- [32] M. Kim, S. G. Motti, R. Sorrentino, A. Petrozza, *Energy Environ. Sci.* **2018**, 11, 2609.
- [33] Y. Liu, S. Akin, L. Pan, R. Uchida, N. Arora, J. V. Milić, A. Hinderhofer, F. Schreiber, A. R. Uhl, S. M. Zakeeruddin, A. Hagfeldt, M. I. Dar, M. Grätzel, *Sci. Adv.* **2019**, 5, eaaw2543.
- [34] R. Wang, J. Xue, L. Meng, J.-W. Lee, Z. Zhao, P. Sun, L. Cai, T. Huang, Z. Wang, Z.-K. Wang, Y. Duan, J. L. Yang, S. Tan, Y. Yuan, Y. Huang, Y. Yang, *Joule* **2019**, 3, 1464.
- [35] S. Zhang, S. Wu, W. Chen, H. Zhu, Z. Xiong, Z. Yang, C. Chen, R. Chen, L. Han, W. Chen, *Mater. Today Energy* **2018**, 8, 125.
- [36] E. A. Alharbi, A. Y. Alyamani, D. J. Kubicki, A. R. Uhl, B. J. Walder, A. Q. Alanazi, J. Luo, A. Burgos-Caminal, A. Albadri, H. Albrithen, M. H. Alotaibi, J. E. Moser, S. M. Zakeeruddin, F. Giordano, L. Emsley, M. Grätzel, *Nat. Commun.* **2019**, 10, 1.
- [37] M. Yang, T. Zhang, P. Schulz, Z. Li, G. Li, D. H. Kim, N. Guo, J. J. Berry, K. Zhu, Y. Zhao, *Nat. Commun.* **2016**, 7, 12305.
- [38] E. A. Alharbi, A. Krishna, T. P. Baumeler, M. Dankl, G. C. Fish, F. Eickemeyer, O. Ouellette, P. Ahlawat, V. Škorjanc, E. John, B. Yang, L. Pfeifer, C. E. Avalos, L. Pan, M. Mensi, P. A. Schouwink, J. E. Moser, A. Hagfeldt, U. Rothlisberger, S. M. Zakeeruddin, M. Grätzel, *ACS Energy Lett.* **2021**, 6, 3650.
- [39] D. Luo, R. Su, W. Zhang, Q. Gong, R. Zhu, *Nat. Rev. Mater.* **2019**, 5, 44.
- [40] A. A. Paraecattil, J. De Jonghe-Risse, V. Pranculis, J. Teuscher, J. E. Moser, *J. Phys. Chem. C* **2016**, 120, 19595.
- [41] J. C. De Mello, H. F. Wittmann, R. H. Friend, *Adv. Mater.* **1997**, 9, 230.

Conclusion

Presently, the world is craving for renewable energy sources. Living standards are continuously raising worldwide and many countries are still in the process (or even at the beginning) of their development. Global population is raising dramatically fast as well, and political instability in the Middle East and in Eastern Europe panics the markets. On top of that, global warming effects start to be strongly felt, and an unprecedented catastrophe is to be feared from an ecological point of view. We are thus on the verge of an energy crisis and hence, the need for novel and renewable energy sources is more crucial than ever. Also, the dependence of most countries to foreign energy raises questions of security and independence. Thus, the development of a technology that can be universally adapted would prove really relevant. In this regard, perovskite solar cells (PSCs) represent a very promising candidate due to their incredible rise in power conversion efficiency in a very short time span and the relatively low costs associated to their fabrication. However, some issues subsist and still prevent their large scale, industrial development. Research and development is therefore of prime importance.

In this thesis, efforts have been put to bring some valuable contribution in understanding and bringing perovskite solar cells one step further and closer to a commercial reality.

In chapter 2, we studied the perovskite layer itself by engineering state-of-the-art perovskite composition of the time (2018-19), that is the triple cation (CsFAMA) configuration which, at the time, contained 83% of FAPbI₃, 17 % of MAPbBr₃, with an additional 5 % of Cs⁺ (Cs₅(FA₈₃MA₁₇)₉₅Pb(I₈₃Br₁₇)₃). We aimed at improving its power conversion efficiency without impacting on the operational stability. Our strategy was to increased the ratio of the most-efficient FAPbI₃ vs. the less efficient MAPbBr₃ in order to boost the efficiency of the resulting perovskite films while still benefiting from the stabilization features of MAPbBr₃. We probed the PCE and stability of PSCs of compositions CsI_{0.05}(FA_{1-y}MA_y)_{0.95}Pb(I_{1-y}Br_y)₃ (y=0, 0.05,

0.10, 0.15, 0.20) in order to find out the composition, which demonstrates the best compromise between the stabilization features and the loss of photocurrent associated with MAPbBr₃, while simultaneously improving the overall photovoltaic performance of FA-dominant PSCs. We demonstrated by SEM and XRD measurements that MAPbBr₃ increases the nucleation density and influences the preferred orientation of perovskite grains, but most crucially plays an important role in lowering the hexagonal non-perovskite phase compared to composition without MAPbBr₃. However, we also showed that minimum amount of MAPbBr₃ (that is PSCs containing 5% MAPbBr₃) was enough to benefit from these features. The composition CsI_{0.05}(FA_{0.95}MA_{0.05})_{0.95}Pb(I_{0.95}Br_{0.05})₃ demonstrated the lowest trade-off between photovoltage and photocurrent and reach the highest PCE of 21.6 %, an increase compared to that of state-of-the-art PSCs containing 17% MAPbBr₃. Also, this composition demonstrated the best operational stability. Nowadays, established highly efficient FAPbI₃-rich perovskite compositions involve about 2 % MAPbBr₃, proving the relevance of our study at the time. Finally, this work demonstrated a facile example of compositional engineering of the perovskite in a way to improve the performance of resulting solar cells.

In chapter 3, we continued our journey of improving PSCs by engineering the preparation method of multi-cation PSCs. Indeed, the control of the crystal growth plays a crucial role in controlling the quality of the resulting perovskite films. We added a mixture of orthorhombic 1D polymorphs of δ -RbPbI₃ and δ -CsPbI₃ to the PbI₂ solution in the sequential deposition method and demonstrated that it induces the formation of porous mesostructured hexagonal films. Thanks to the porosity created, the penetration and subsequent heterogeneous nucleation of FA/MA cations within the PbI₂ film was greatly improved. As a result, the conversion into the desired cubic α -structure of perovskite was enhanced and films prepared using this method demonstrated superior crystallinity and optoelectronics properties. Also, we showed that cesium was fully introduced in the bulk of the perovskite lattice, whereas rubidium remained

mainly on the surface, passivating surface traps. The champion PSCs showed a PCE of 22.3 % compared to 20.4 % for the control devices. Also, it retained more than 90% of its initial efficiency after more than 400 hours under continuous 1-sun illumination at its maximum power point. This work demonstrated the importance of engineering the preparation method as well and brings a simple but very efficient example on how it can help to considerably improve the efficiency and stability of resulting PSCs.

In Chapter 4, we conducted an important study of the impact of inorganic cations Rb^+ and Cs^+ and of the use of excess PbI_2 on the phase purity of perovskite films and discussed their implications on the optoelectronic and photovoltaic qualities of the resulting PSCs. More in details, we compared and quantified the methods of stabilizing FA-based perovskites involving the additional blending of excess lead iodide and the smaller inorganic cations cesium and rubidium, which can lead to an improvement in phase purity of the black cubic α -perovskites. We demonstrated by advanced XRD techniques (synchrotron XRD, 2D GIWAXS reciprocal space maps) that adding the smaller inorganic Rb^+ and Cs^+ cations to yield triple- or quadruple-cation hybrid perovskites drastically improves the phase purity of the black photoactive cubic α -perovskite. The fraction of photoactive phase was enhanced from 45 % for the regular FA:MA composition to 98 % upon the addition of Cs^+ and Rb^+ . Furthermore, we showed that the addition of these cations, as well as the use of some PbI_2 excess, affected the cubic perovskite structure by lowering the amount of oriental order and decreasing significantly the crystallite size. Finally, devices prepared using Rb.CsFAMA quadruple-cation recipe demonstrated the highest photovoltaic performance with improved optoelectronic properties over the other conditions. This work, focused more on an analytical point of view of the multi-cation perovskite solar cells rather than in a performance-based one, provides a very important contributions in the understanding of the effects of these inorganic cations in multi-cation perovskite recipes. It brings to the perovskite community some fundamental evidence of the

mechanisms and importance of inorganic additives towards the realization of phase-pure perovskite films.

In Chapter 5, we aimed at removing the inorganic cations from the bulk of the perovskite in order to maximize its light-harvesting properties and yield higher performing devices. The idea was to use Cs^+ and Rb^+ as passivation agents, that is on the surface of the perovskite, in order to take advantage of their stabilization features of the cubic perovskite phase (black α -phase), but without introducing in the bulk, that is, keeping the band gap energy of resulting perovskite films unchanged and closer to pure FAPbI_3 films. We showed by XRD and XPS that the passivation of EAI-passivated $(\text{FAPbI}_3)_{0.98}(\text{MAPbBr}_3)_{0.02}$ with CsI leads to the disappearance of PbI_2 and Pb^0 aggregates, which are converted into the desired perovskite cubic black α -phase. It resulted in films exhibiting a highly homogeneous surface potential and showing a PLQY increase of 1800 % to over 8%, underlying the drastically lowered non-radiative recombination and thus, the enhanced crystallinity and optoelectronic properties of as-prepared perovskite films. Photoluminescence, XPS and external quantum efficiency measurements demonstrated that Cs^+ was not included in the bulk of the perovskite and that the films prepared showed a band gap energy of 1.52 eV vs. 1.55 eV for the standard EAI-passivated triple cation recipe. It resulted in highly efficient PSCs surpassing 24 % PCE and with improved operational stability.

All in all, we demonstrated in this thesis various engineering methods to improve PSCs and contribute towards making them a viable source of cheap and environmentally friendly energy for our society. We showed in Chapter 2 an example of the compositional engineering of the perovskite layer, whereas in Chapter 3 we demonstrated how the preparation methods can also be tuned. Both works resulted in more efficient and stable devices. In Chapter 4, we focused on analysing the effects of the engineering realized in chapters 2 & 3 on the phase purity of the resulting perovskite and linked these crystallographic findings to the optoelectronic

improvements measured. Chapter 4 was a successful tentative to move a step beyond by removing the stabilizing agents from the bulk of the perovskite and employing them on the surface instead. It resulted in great performance with an improvement in PCE from about 22 % to over 24 % and superior stability.

Altogether, this thesis represents a small step in the development of PSCs, which itself is a small steps towards a sustainable future. The findings developed herein demonstrate solid engineering examples and open ways to inspire other researchers around the globe. Great challenges remain, though, especially on the stability (and to some extent to the toxicity), before making PSCs a successful industrial reality.

Curriculum Vitae

Thomas Paul Baumeler

thomas.baumeler@epfl.ch

OrcID: <https://orcid.org/0000-0002-9771-7440>

4, Chemin du Murgier • 2350 Saignelégier, CH-Switzerland •
(+41) 78-668-57-35



EDUCATION

Ecole polytechnique fédérale de Lausanne , School of Basic Sciences	Lausanne, Switzerland
• Ph.D., Chemistry and Chemical Engineering	Expected April 28, 2022
• MSc, Molecular and Biological Chemistry	February 2018
• BA, Chemistry and Chemical engineering	May 2015

RESEARCH EXPERIENCE

Ecole polytechnique fédérale de Lausanne	Lausanne, Switzerland
<i>Graduate Student with Prof. Michael Graetzel</i>	May 2018-present

Development of highly efficient and stable hybrid organic-inorganic perovskite solar cells

- Stabilization of photoactive cubic α -FAPbI₃ perovskite for highly efficient perovskite solar cells via compositional engineering & passivation
- Demonstrating the creation of microporous PbI₂ films via the adjunction of 1D δ -CsPbI₃/ δ -RbPbI₃ polymorphs in the sequential deposition method to facilitate the heterogeneous nucleation and the penetration of cations which improves the subsequent conversion of PbI₂ into desired multication cubic α -structure
- Development of unexpensive and efficient low-temperature processed hole transport materials for highly efficient stable perovskite solar cells

Project in molecular sciences with Prof. Michael Graetzel	September 2017 – February 2018
--	--------------------------------

- Development of Copper electrolytes for ambient light and outdoor applications of dye-sensitized solar cells
- Decomposition of the relations between compositional, structural and opto-electronical features of perovskite solar cells

Ecole polytechnique fédérale de Lausanne Valais/Wallis	Sion, Switzerland
<i>Interdisciplinary project with Prof. Andreas Züttel</i>	February 2017 – May 2017

Development of metal-organic frameworks (MOFs) for CO₂ capture

- MOFs synthesis and purification
- Development of a mini-reactor for CO₂ capture measurements
- CO₂ capture measurements

RESEARCH SKILLS and TECHNIQUES

- Optoelectronic characterization of semiconductor thin films (UV-Vis, photoluminescence, time-resolved photoluminescence, photoluminescence quantum yield, ultrafast photoelectron spectroscopy)

- Morphological, structural and compositional analysis of nanomaterials and thin films (X-ray diffraction, scanning electron microscopy, X-ray photoelectron spectroscopy)
- Synthesis and deposition of perovskite thin films (spin-casting, antisolvent method, sequential deposition, compositional engineering, additives engineering)
- Perovskite solar cells fabrication and engineering
- Photodiodes PV metrics characterization (*JV*, stabilized photoconversion efficiency, maximum powerpoint tracking, external quantum efficiency)

TEACHING ACTIVITIES

Ecole polytechnique fédérale de Lausanne,
Mentor, Mentoring for Science program

Lausanne, Switzerland
February 2019 – May 2020

- Guided first-year Master students in chemistry to pursue a semester project ("*Advanced analytical chemistry project*", 30 ECTS) on the chemical analysis of selected metals in water by atomic absorption spectroscopy
- Guided third-year bachelor chemistry and chemical engineering students for a project (12 ECTS) in molecular sciences

Teaching Assistant, Chemistry

September 2015 - Present

Over 600 hours of teaching assistantship for the following courses/laboratory work:

- Artificial photosynthesis - EPFL Chemistry Master's degree course
- Advanced analytical separation methods – EPFL Chemistry Bachelor's degree course
- Organic chemistry – EPFL Chemistry Bachelor's degree course
- Advanced general chemistry - **Université de Lausanne** forensics sciences Bachelor's degree course
- General chemistry – EPFL general Bachelor's degree course
- Laboratory work in advanced analytical separation methods – EPFL Chemistry Bachelor's degree lab work
- Introduction to Laboratory practices – EPFL Chemistry Bachelors' degree course

PRIZES, AWARDS, FELLOWSHIPS

Ecole polytechnique fédérale de Lausanne,

Lausanne, Switzerland
November 2020

- Award for my "*Excellent contribution to the teaching*" from the EPFL Basic Sciences Institute of chemical sciences and engineering's teaching Committee

PERSONAL SKILLS

Languages skills

- French : level C2 ; native language
- English : level C1
- German : level B2
- Spanish : level A2

Digital competences

- Microsoft Office
- LaTeX
- OriginPro
- ImageJ
- C/C++ programming